UTS UNIVERSITY OF TECHNOLOGY SYDNEY

Modelling alkali-silica reaction effects for condition assessment and capacity evaluation of reinforced concrete structures

by Thuc Nhu Nguyen

Thesis submitted in fulfilment of the requirements for
the degree of

Doctor of Philosophy

under the supervision of Professor Jianchun Li,
Dr. Nadarajah Gowripalan, Dr. Yang Yu & Dr. Leandro Sanchez

University of Technology Sydney
Faculty of Engineering and Information Technology

February 2021

Certificate of Original Authorship

I, **Thuc Nhu Nguyen** declare that this thesis, is submitted in fulfilment of the requirements for the award of **Doctor of Philosophy**, in the School of Civil and Environmental Engineering, Faculty of Engineering and Information Technology at the University of Technology Sydney.

This thesis is wholly my own work unless otherwise referenced or acknowledged. In addition, I certify that all information sources and literature used are indicated in the thesis.

This document has not been submitted for qualifications at any other academic institution.

This research is supported by the Australian Government Research Training Program.

Signature: Production Note:
Signature removed prior to publication.

Date: 20th February 2021

Dedication

To my father, who strongly encourages and believes in my journey, with love!

Acknowledgement

To come to the completion of this thesis, I am indebted to many persons who have given generous support through various means over the last four years.

First of all, I would like to express my heartfelt gratitude to my principal supervisor Prof. Jianchun Li for giving me the opportunity to work on this exciting project and for his excellent supervision and support throughout my PhD candidature at UTS. I am truly grateful to him for allowing me to freely explore the research work while giving me suggestions for further improvement. I am also thankful to my co-supervisor Dr Nadarajah Gowripalan for sharing his precious experience and knowledge in several insightful discussions both within and beyond the scope of my PhD. I also take this opportunity to thank Dr Yang Yu for being not only my co-supervisor but also a friend who always offers his help.

I would like to extend my sincere gratitude to Prof Vute Sirivivatnanon for being a great mentor and offering continuing support throughout my time in Sydney. I am grateful to see such a role model as him, who always being kind and supportive to students and colleagues.

I would like to acknowledge the Australian Research Council Research Hub for Nanoscience Based Construction Materials Manufacturing (ARC NanoComm Hub) and Transport for New South Wales (TfNSW) for providing financial support for this project.

I would like to extend my thank to my external supervisor Professor Leandro Sanchez for giving me the opportunity to work with uStructure research group at the University of Ottawa, where I have gained invaluable experience, an understanding of ASR, and more importantly, the “crack” friendships. I am grateful to him for his valuable advice and continuing support since the first date we met. Likewise, I am thankful to Dr Emre

Erkmen from Concordia University for helping me to make the visit trip to Canada possible and for making my time there enjoyable both in and out of his office. In this regard, I would like to thank UTS HDR Research Collaboration Grant and Mitacs Globalinks Grant for providing the financial support for my visit and collaboration with the research teams in Canada.

I would like to thank all the friends I have met in Australia and Canada during my PhD for making this journey much more fun and enjoyable. Special thanks to several Vietnamese friends and Mrs Van Le, who helped me since my first day in Australia and have made me less homesick.

Finally, I extremely grateful to my beloved parents and siblings for their love and unwavering support in my every endeavour. To my beloved wife, I could not say thank you enough for being with me through low or high moments in this PhD journey and in this life.

THUC NHU NGUYEN

Table of Contents

List of Abbreviations

ACR	Alkali-carbonate reaction
AMBT	Accelerated Mortar Bar Test
ANN	Artificial Neural Network
ASR	Alkali-silica reaction
ASTM	American Society for Testing and Materials
BR	Bayesian Regularization
CPT	Concrete Prism Test
DRI	Damage rating index
FEM	Finite element modelling
FEA	Finite element analysis
HAPC	High-alkali Portland cement
ISE	Institution of Structural Engineers
LAPC	Low-alkali Portland cement
LM	Levenberg-Marquardt
NN	Neural network
RC	Reinforced concrete
RVE	Representative Volume Element
SCM	Supplementary cementing material

List of Figures

List of Tables

Abstract

Alkali-silica reaction (ASR) is one of the most harmful distress mechanisms affecting concrete infrastructure worldwide. ASR is a chemical reaction that generates a secondary product, which induces expansive pressure within the reacting aggregate particles and adjacent cement paste upon moisture uptake. This in turn leads to cracking, loss of material integrity, and consequently compromises serviceability and capacity of the structure. In Australia, several concrete structures of various types such as dams, bridges and railway sleepers have been identified as affected by the reaction to varying extents. To date, the majority of experts agree that new concrete structures can be constructed in such a way to avoid ASR-induced effects by using either non-reactive aggregates classified by national and international standards, or supplementary cementitious materials to mitigate the reaction. However, there is currently a lack of a comprehensive plan for diagnosis and prognosis of existing concrete structures affected by ASR. This is despite its importance in providing efficient rehabilitation methods and management strategies for the infrastructure.

When investigating existing structures affected by ASR, two crucial questions need to be answered prior to specifying management strategies, i.e., (i) the current state of damage and its effects on structural capacity and serviceability; and (ii) the prediction of damage progress and its impact on the structure in the coming months or years. In this regard, two main effects of the deleterious ASR - expansion and mechanical properties degradation of the concrete - need to be evaluated prior to assessing the condition and capacity of the affected structures suffering from ASR. This study aimed to provide different modelling approaches for evaluating the degradation of mechanical properties, expansion of concrete in the field, and eventually assessing the structural behaviour of ASR affected structural members and structures.

First, a critical review on mechanical properties of concrete suffering from ASR is provided. Due to significant reduction in modulus of elasticity and its wide variation, two different models were implemented to provide better understanding and evaluations of the reduction in the modulus of elasticity. An artificial neural network (ANN) model was

proposed to investigate impacts of different factors (i.e., reactive aggregates, alkali content, design strength in addition to the expansion) to the modulus of elasticity and subsequently to provide a better estimation of the reduction. In another approach, a computational homogenization model was developed to model the impact of ASR-induced cracking in concrete on its stiffness. The proposed model was able to quantify the impact of ASR-induced internal cracking on the reduction of concrete stiffness.

Second, a novel semi-empirical model was proposed for forecasting expansion of unrestrained concrete in the field based on results of laboratory testing such as from the concrete prism test (CPT). The model accounted for effects of the reactive aggregate type and nature, alkali leaching, alkali contribution from aggregates and environmental conditions (i.e. temperature, relative humidity) on the ASR expansion. The semi-empirical model is capable of accounting for the effects of environmental conditions in the field for forecasting ASR-induced expansion of concrete field blocks. This is shown by excellent model outcomes for concrete blocks from three outdoor sites in Canada and the USA, which were made by different reactive aggregates and alkali contents.

Finally, as a continuation of the semi-empirical model, a finite element (FE) model was developed for modelling expansion and load-carrying capacity of reinforced concrete members. Two well-known empirical models to account for stress-dependency of the ASR expansion were adopted to account for the effect of reinforcement restraints on the ASR expansion development in reinforced concrete members. The model was implemented in the commercial FEA package ABAQUS/Implicit using different developed user subroutines, and the concrete damaged plasticity model. Impact of the variation in residual mechanical properties on expansion advancement and load-carrying capacity of reinforced concrete members was also investigated.

By providing different numerical investigations on the degradation of mechanical properties, expansion of the field concrete and consequently the structural capacity, this study provided a comprehensive approach for assessing condition and capacity of existing reinforced concrete structures suffering from ASR.

Chapter 1: Introduction

This chapter establishes the background on alkali-silica reaction and its effects on concrete material and structures, and then highlights the importance of modelling approaches in assessing conditions of existing structures affected by ASR. Furthermore, an overview of Australia's experience in minimising the risk of damage to concrete structures due to ASR is briefly introduced. The research scope and objectives are then explained, followed by an outline of how the thesis is structured.

1.1. Background

1.1.1. Alkali-silica reaction in concrete and its consequences

Alkali-silica reaction (ASR), one of the most harmful distress mechanisms affecting concrete material and structures, was first identified and studied by T.E. Stanton in the 1940s in California and thereafter have been found affecting numerous concrete structures worldwide (Sims & Poole 2017; Stanton 1940). ASR is a chemical reaction between certain reactive silica phases from the aggregates and the alkali hydroxides (i.e., Na+, K+ and OH-) in the concrete pore solution originating mainly from cement. This reaction generates a secondary product, the so-called ASR gel that swells under moisture uptake, leading to important crack formation followed by reductions in mechanical properties and adverse impacts on long-term performance (i.e., durability and serviceability) of concrete structures (Fournier et al. 2010; ISE 1992). A typical mechanism of ASR damage in concrete is shown in Figure 1.1 (Deschenes, Bayrak & Folliard 2009).

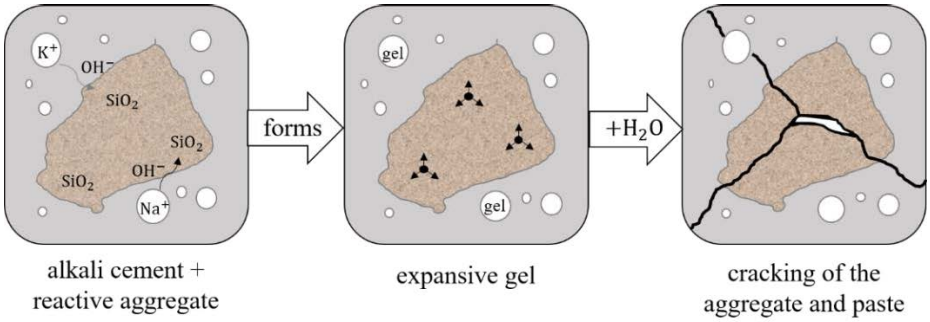

Figure 1.1: Alkali-silica reaction in concrete (adapted from Deschenes, Bayrak & Folliard (2009)

In terms of the chemical process, the reaction is affected by several factors such as concentration of reactants, and surrounding environments represented by exposure conditions. The key parameters influencing ASR in the concrete could be listed as temperature, moisture condition, alkali content (mainly from cement), aggregate type (mineralogy and size) and porosity (Larive 1997; Lindgård et al. 2012; Sanchez 2014). Different types of reactive aggregate have different mineralogy properties and reactivity levels. In addition, raising the exposure temperature increases the reaction rate, while moisture and alkalis are essential for the reaction (Larive 1997).

In terms of physical effects, ASR causes expansion, cracking and changes in the concrete's mechanical properties. For instance, according to ISE (1992), the modulus of elasticity, compressive strength and tensile strength may reduce by as much as 65%, 60%, 40% at the expansion level of 0.5%, respectively. The reduction in the mechanical properties is smaller at lower expansion values. The development of cracks in concrete due to ASR could unfavourably affect the resistance of concrete to other environmental loadings. All these effects could consequently induce an adverse impact on serviceability and load-carrying capacity of the affected concrete structures (ISE 1992). Therefore, forecasting and evaluating ASR-induced expansion, cracking, and degradation of

mechanical properties become crucial tasks in the appraisal and prognosis of existing structures suffering from ASR.

After first being identified by Stanton (1940), ASR has been found to affect concrete structures in several countries (Sims & Poole 2017). It elicits essential tasks on monitoring, condition assessment and load capacity evaluation of these structures. On investigating these structures, two crucial questions need to be answered for an efficient rehabilitation and management strategies: (i) the current damage state and its effects on structural capacity and serviceability; and (ii) the prediction of damage progression and its impact to the structure in the future. Many challenges are yet to be addressed for answering these questions due to inherent complexities of both ASR characteristics and structural aspects such as geometry, reinforcement configuration, restraints and loading. The most reliable approach to answer these questions is a series of field investigations such as detailed field inspection, monitoring and full-scale load test, along with an extensive laboratory testing on core samples (i.e., sampling for petrography, mechanical testing and residual expansion testing). These tests, however, are expensive and not always feasible for a long-term investigation. In this context, modelling approaches such as employing empirical, analytical, and numerical models become an important and effective tool to reduce the burden and reliance on the laboratory and field tests. These modelling approaches are able to account for the above-mentioned inherent complexities of ASR characteristics and structural aspects. In addition, numerical analyses are very useful for the interpretation of measured data.

1.1.2. Australia's experience in assessment of ASR effects in concrete structures

In Australia, several concrete structures of various types such as dams, bridges and railway sleepers have been identified as affected by the alkali-silica reaction. For instance, Carse (1993) and Carse (2003) reported several structures affected by ASR in different regions in Queensland, Australia. The expansion level induced on these structures could be as high as 0.8% to 1.2%. This high expansion level could cause significant damage and consequences on structural capacity and serviceability. In addition, the author also highlighted important role of rainfall on the development of ASR, in which high rainfall regions are favourable for concrete to expand due to ASR.

Another example is shown in Figure 1.2 for a bridge affected by ASR in Perth, WA (HB79 2015). In this context, several studies have been conducted in the last few decades to investigate different aspects of alkali-silica reactions, such as aggregate reactivity, mitigation of the reaction in concrete, and diagnosis and prognosis of existing structures suffering from ASR. Two Australian standards, AS-1141.60.1 (2014) and AS-1141.60.2 (2014), prepared in 2014 for accelerated mortar bar test and concrete prism test, respectively, show high reliability in the assessment of aggregate reactivity (Sirivivatnanon, Mohammadi & South 2016). Handbook 79, which is the guideline for minimising the risk of ASR damage in concrete structures in Australia, provides different approaches to minimise ASR risks in both newly constructed and existing concrete structures (HB79 2015).

Figure 1.2: Causeway bridge affected by ASR in Perth, WA (HB79 2015)

Until now, most experts agree that new concrete structures can be constructed without or with negligible ASR by using either non-reactive aggregates classified by national and international standards or supplementary cementitious materials to mitigate the reaction. However, a comprehensive approach for the diagnosis and prognosis of existing concrete structures affected by ASR is still currently lacking. Yet it is accepted that this task is important if efficient rehabilitation solutions and management strategies for the infrastructure are to be provided. In terms of numerical modelling, there is limited information provided in HB79 to assist engineers and asset owners in modelling approach and implementation to assess ASR effects on structural behaviour. It strongly suggests the need to develop a modelling procedure to assess ASR effects in concrete structures so that better decisions on a rehabilitation and management plan are made.

1.2. Research scope and objectives

This study was designed to investigate different aspects of ASR effects on reinforced concrete structures, such as expansion, cracking, reduction in mechanical properties and consequently their impact on the structural load-carrying capacity, using various means of modelling. A key investigation is modelling expansion of reinforced concrete members

in the field by using laboratory measurements along with considering environmental conditions in the field. In addition, ASR effect on mechanical properties of concrete was investigated via different modelling approaches. Afterwards, the load-carrying capacity of structures undergoing ASR was evaluated as a continuation of the numerical modelling for expansion and taking into account the changes occurring in mechanical properties.

The objective of this PhD study was to develop modelling approaches to assess the effects of ASR to reinforced concrete structures for condition assessment and capacity evaluation. The following primary sub-objectives are set to achieve this overarching objective:

1. To develop a model procedure for forecasting evolution of free expansion of concrete due to ASR in the field using laboratory measurements;
2. To develop a numerical model to estimate ASR expansion of reinforced concrete based on the measured/estimated free expansion by accounting for the restraints from reinforcement;
3. To investigate ASR effects on the mechanical properties of concrete, focusing on the modulus of elasticity by employing different modelling approaches such as machine learning and computational homogenization;
4. To evaluate ASR effects on the load-carrying capacity of reinforced concrete structures, taking into account both the expansion and possible reduction in mechanical properties of concrete.

1.3. Thesis structure

The thesis consists of 6 chapters, including this introductory chapter, a literature review chapter, three main chapters and a final chapter for conclusions and recommendations.

This introductory chapter presents an overview of ASR, research scope and objectives, and how the thesis is organised. The literature review chapter provides a state-of-the-art review of the investigated topics. Three main chapters set out to achieve the four objectives presented above. Details of these three chapters, i.e. Chapter 3 to Chapter 5 are provided as follows.

In ***Chapter 3***, a critical review on mechanical properties of concrete suffering from ASR is provided. Due to significant effects of ASR on the modulus of elasticity of the concrete, different methods were implemented to better evaluate the reduction in the modulus of elasticity. A machine learning model was proposed to investigate impacts of various factors such as proportions of reactive aggregates, alkali content, exposed temperature and concrete strength, in addition to the expansion to the modulus of elasticity. The model also aims to deliver a better estimation of the reduction in the modulus of elasticity of concrete. In addition, a computational homogenization model was developed to model the impact of ASR-induced cracking in concrete on its stiffness. The proposed model was able to link the measurement of internal cracking to the reduction of concrete stiffness.

Chapter 4 presents the development of a semi-empirical approach to correlate ASR-induced expansion in the laboratory and in the field, which accounts for effects of the reactive aggregate type and nature, alkali leaching, alkali contribution from aggregates and environmental conditions (i.e., temperature, relative humidity). First, laboratory test data of ASR-affected concrete containing a wide range of reactive aggregates, alkali content/leaching as well as exposure conditions were gathered to develop and calibrate the model parameters for an ideal expansion curve without leaching. The model was then utilised to forecast ASR-induced expansion of concrete blocks incorporating different

reactive aggregates and alkali contents and exposed to three different outdoor conditions in Canada and the USA.

As a continuation of the semi-empirical model developed in the previous chapter, ***Chapter 5*** presents a numerical modelling framework for the ASR expansion of reinforced concrete. Two different ASR constitutive models were adopted to account for the effect of confinements on the ASR expansion development. The model was implemented in the commercial FEA package ABAQUS using different developed user subroutines, and the concrete damaged plasticity model. Impacts of changes in mechanical properties due to ASR on the expansion evolution were also investigated. The FE model was further implemented to assess the load-carrying capacity of reinforced concrete members suffering from ASR. The consequence of both ASR-induced expansion and changes in mechanical properties to load-carrying capacity is studied.

Several stand-alone scientific manuscripts have been either published or prepared for publication from the content of this thesis. The list of publications and manuscripts is as follows in chronological order:

1. ***Thuc Nhu Nguyen***, Leandro L.M. Sanchez, Jianchun Li, Benoit Fournier, and Vute Sirivivatnanon. "Correlating ASR-induced expansion from short-term laboratory testings to long-term field performance: a novel semi-empirical model" (in preparation, to be submitted to *Construction and Building Materials*), 2021.
2. ***Thuc Nhu Nguyen***, Leandro F.M. Sanchez, Jianchun Li, Nadarajah Gowripalan, Vute Sirivivatnanon. "An integrated modelling approach for ASR expansion of reinforced concrete in the field" (in preparation, to be submitted to *Engineering Structures*), 2021.

3. ***Thuc Nhu Nguyen***, R. Emre Erkmen, Leandro F.M. Sanchez, and Jianchun Li. "Stiffness degradation of concrete due to alkali-silica reaction: A computational homogenization approach". *ACI Materials Journal, 2020*, vol. 117, no. 6, pp. 65-76.
4. ***Thuc Nhu Nguyen***, R. Emre Erkmen, Leandro F.M. Sanchez, and Jianchun Li. "A probabilistic homogenization approach for the computation of stiffness degradation in ASR-affected concrete", accepted to be presented at the *16th International Conference on Alkali Aggregate Reaction in Concrete*, Lisbon, Portugal, 2021.
5. ***Thuc Nhu Nguyen***, Yang Yu, Jianchun Li, Nadarajah Gowripalan, and Vute Sirivivatnanon. "Elastic modulus of ASR affected concrete: an evaluation using Artificial Neural Network". *Computers and Concrete, 2019*, vol. 24, no. 6, pp. 541-553.
6. ***Thuc Nhu Nguyen***, Yang Yu, Jianchun Li, Nadarajah Gowripalan, and Vute Sirivivatnanon. "Evaluation of elastic modulus reduction due to ASR", *Concrete in Australia*, *2019*, vol. 45, no. 2, pp. 47-52.
7. ***Thuc Nhu Nguyen***, Yang Yu, Jianchun Li, Nadarajah Gowripalan, and Vute Sirivivatnanon. "Mechanical properties of ASR affected concrete: a critical review". *Concrete 2019 Conference*, Sydney, Australia, 2019.
8. ***Thuc Nhu Nguyen***, Yang Yu, Jianchun Li, and Vute Sirivivatnanon. "An Optimised Support Vector Machine Model for Elastic Modulus Prediction of Concrete Subject to Alkali Silica Reaction". In Wang C., Ho J., Kitipornchai S. (eds.), *ACMSM25*. *Lecture Notes in Civil Engineering*, vol. 37, pp. 899-909. Springer, Singapore, 2019.

Chapter 2: Literature review

This chapter presents a comprehensive review on the effects of ASR in reinforced concrete structures such as degradation of mechanical properties, cracking and expansion, and their consequences for structural capacity. The review starts by proving current practices and state-of-the-art on evaluating these effects for condition assessment and capacity evaluation of the affected structures, thereafter focusing on modelling approaches. Following the comprehensive review, challenges and needs for further investigations on each of the reviewed ASR effects are discussed in great detail.

2.1. Introduction

After the first identification by Stanton (1940), ASR was found to undermine concrete structures in several countries worldwide (Sims & Poole 2017). It necessitated important tasks to be done on monitoring, condition assessment and load capacity evaluation of these structures. On investigating these structures, two crucial questions need to be answered for an efficient rehabilitation and management solution: (i) current damage condition and its effects on structural behaviour (in terms of structural capacity and serviceability); and (ii) predicting the damage's progress and impact on the structure in subsequent months or years. To address these questions, the most reliable approach to answer these questions is conducting a series of field investigations (detailed field inspection, monitoring and full-scale load test) along with an extensive laboratory test experiment (sampling for petrography, mechanical testing and residual expansion testing). These tests, however, are expensive and not always feasible for a long-term investigation. In this context, numerical modelling becomes an important and effective tool to reduce the burden and reliance on laboratory and field testings, which enable

considerations of the complexities of ASR characteristics and structural aspects. In addition, numerical analyses can greatly assist in interpreting the measured data.

In general, in order to address the two questions stated above, two crucial measurements/or estimations are: firstly, the extent of ASR development in concrete represented by the expansion level; and secondly, the subsequent degradation of mechanical properties (Hariri-Ardebili, Saouma & Merz 2018). Knowing the up-to-date expansion level and concrete mechanical properties of each structural members, makes it feasible to conduct a numerical analysis for the structural behaviour of affected structures. In addition, enabling forecasting of the potential expansion in the future is the key to making a prognosis of the damage and providing better rehabilitation and management solutions for the structures. For this reason, it is important to have a reliable estimation of the ASR expansion of concrete in the field, and a better understanding of how it affects concrete's mechanical properties.

2.2. Degradation of concrete mechanical properties due to ASR

Ongoing deleterious reaction causes cracking in concrete and consequently results in an adverse impact on its mechanical properties. Due to the importance of mechanical properties on assessing the integrity of deteriorated structures, various studies regarding mechanical properties degradation of concrete caused by ASR have been done in recent decades (Esposito et al. 2016; Giaccio et al. 2008; Larive 1997; Sanchez 2014). Evaluating the extent of degradation is commonly evaluated with respect to the ASR expansion level. Most research agrees that ASR causes degradation of each property, i.e., compressive strength, tensile strength and elastic modulus at different extents. According to the lower bound proposed in the Institution of Structural Engineers guidance (ISE

1992), compressive strength, tensile strength and modulus of elasticity can be reduced up to, respectively, 40%, 60% and 65% at 0.5% of expansion compared to those of unaffected concrete. However, based on the experimental investigations in several studies, the deterioration in mechanical properties with respect to the expansion level greatly varies from one study to another.

In order to provide an overview of mechanical properties degradation with reference to the ASR expansion level, experimental data from several studies were collected for a preliminary investigation (Ahmed, Burley & Ridgen 1999; Esposito et al. 2016; Gautam et al. 2017a; Giaccio et al. 2008; Giannini 2012; Kagimoto, Yasuda & Kawamura 2014; Kubo & Nakata 2012; Larive 1997; Mohammed, Hamada & Yamaji 2003; Multon 2003; Ng & Clark 1992; Pleau et al. 1989; Sanchez et al. 2017; Sargolzahi et al. 2010; Smaoui, Bissonnette, et al. 2005; Swamy & AlL-Asali 1989). The data were plotted in Figure 2.1: along with the lower bound of mechanical properties reduction proposed in ISE (1992). Each property was normalised to the value of unaffected concrete to represent the residual property with respect to the ASE expansion level.

First, the data indicate that ASR exerts an adverse impact on concrete mechanical properties. In each study, there is a clear pattern in the reduction as the expansion increases. Yet, the extents of degradation are different from each study, and vary from one property to another. Many studies show an increase in compressive strength at the expansion level of less than 0.2% before reducing at higher expansion levels, while splitting tensile strength reveals an overall reduction trend from a low expansion level. Especially, most of these experimental studies show that modulus of elasticity underwent a significant reduction compared to splitting tensile strength or compressive strength. This is the reason why the elastic modulus has been commonly considered an important

indicator of ASR-affected concrete deterioration (Esposito et al. 2016; Islam & Ghafoori 2018; Jones & Clark 1998; Sanchez et al. 2017). For instance, Islam & Ghafoori (2018) proposed a procedure to evaluate the reactivity of aggregate by assessing the reduction in elastic modulus of concrete.

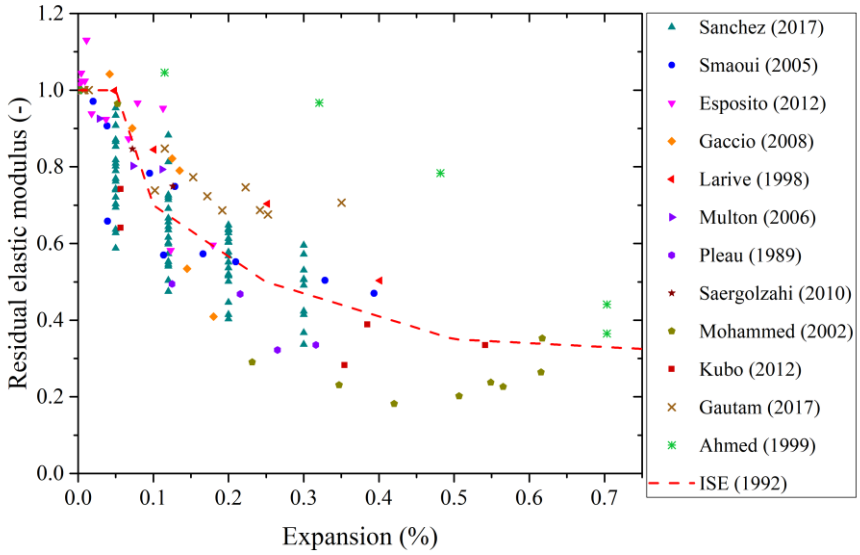

(a) Modulus of elasticity

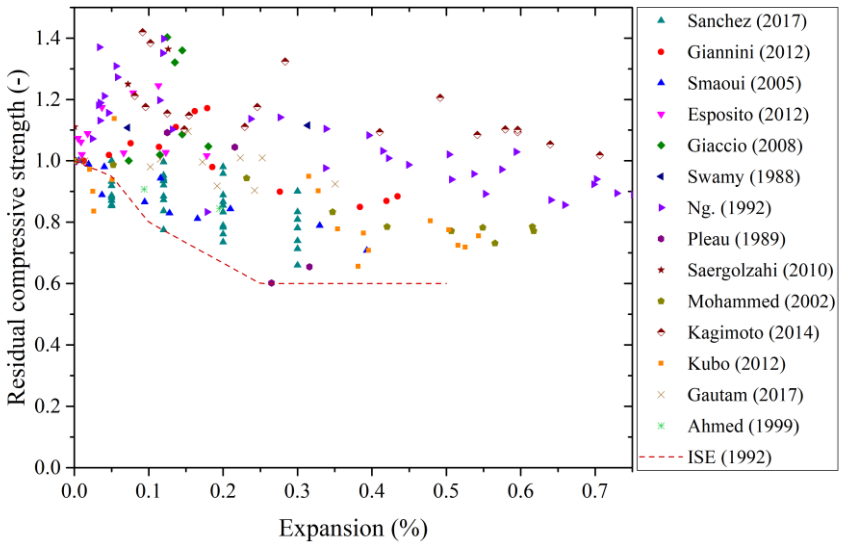

(b) Compressive strength

Figure 2.1: Mechanical properties degradation in relation to ASR-induced expansion.

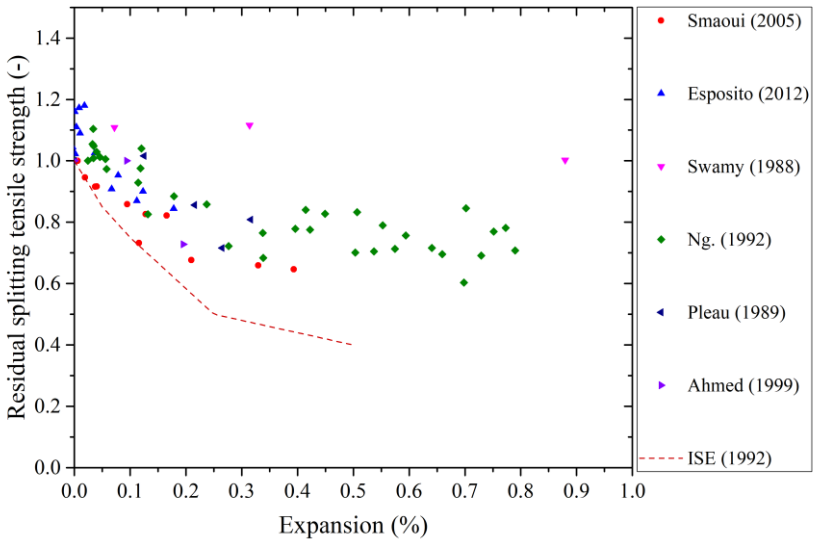

(c) Splitting tensile strength

Figure 2.1: Continued.

Using the proposed lower bounds ISE (1992) to estimate residual material properties as a conservative evaluation, has emerged as a safety margin for evaluating compressive and splitting tensile strength. However, it is not applicable to the elastic modulus where many experimental testing groups provided greater reductions than the lower bound. Furthermore, the strength and stiffness of free expansion specimens present a considerable variation at any specific expansion level. For instance, the elastic modulus at the expansion of 0.1% could vary from 45% to 90% of the undamaged value. These variations can be due to differences in several influencing factors from each study, i.e., testing condition (temperature and humidity), type of reactive aggregate (size, rock type and reactivity), proportion of reactive aggregate and designed strength of concrete (Gautam & Panesar 2017; Gautam et al. 2017a; Lindgård et al. 2012; Sanchez 2014; Smaoui, Bérubé, et al. 2005). Therefore, while assessment of compressive and tensile strength can be conducted by using the ISE's lower bound, it is necessary to assess the impact of certain key factors on changes in the elastic modulus, so it is better understood.

Another fundamental question on evaluating the modulus of elasticity reduction is how ASR-induced cracking in concrete affects the modulus of elasticity of concrete. In practice, cracking is commonly observed in concrete affected by ASR, as shown in Figure 2.2(a). Orientation and distribution of cracks usually indicate anisotropy in the stress state of concrete, while their quantity either in the aggregate particles or the cement paste could represent the level of ASR damage.

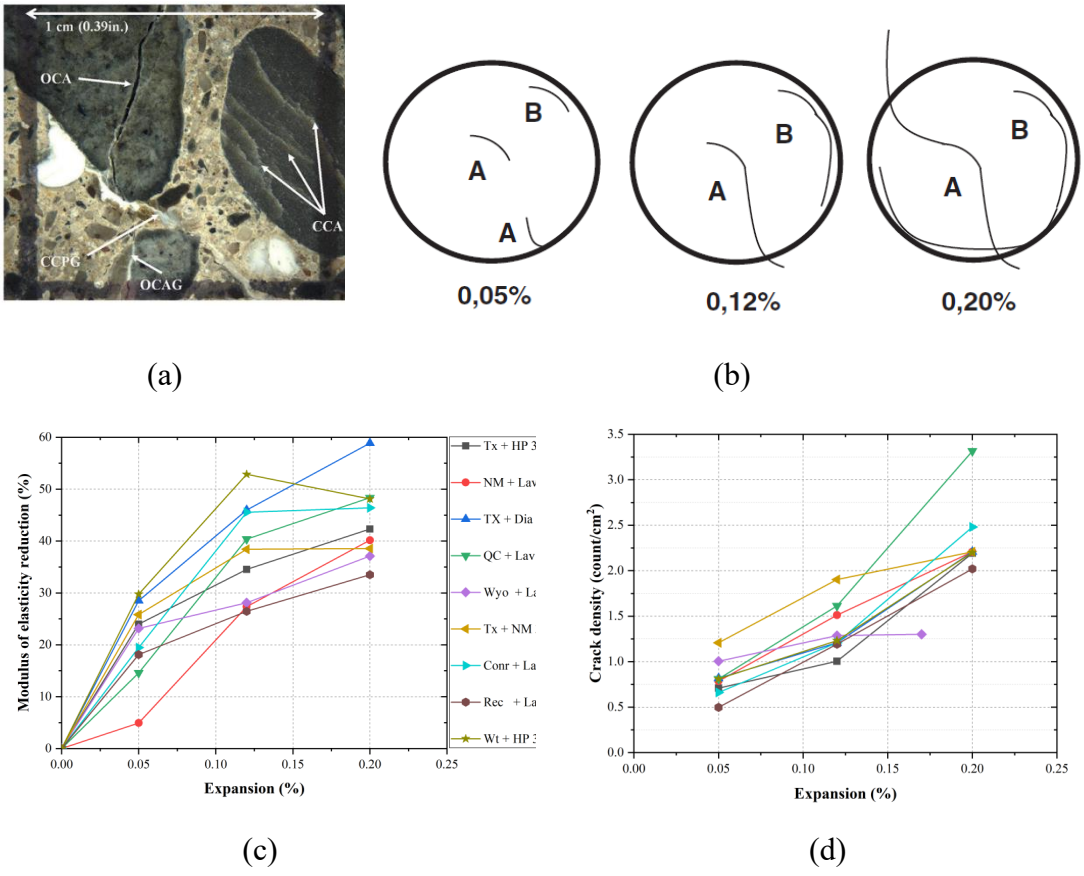

Figure 2.2: Crack development due to ASR: (a) Open cracks in aggregate and cement paste; (b) Qualitative crack development model at different levels of expansion, (c) Reduction in modulus of elasticity, and (d) Increase in crack density observed in concrete (Sanchez et al. 2015).

An example of the correlation between crack density observed in concrete, and the modulus of elasticity at three different expansion levels is shown in Figure 2.2(c-d)

adapted from Sanchez (2014). It shows that there is an obvious correlation between the development of cracks in concrete due to ASR and subsequent loss in the modulus of elasticity. Based on experimental observations, Sanchez et al. (2015) also proposed a qualitative description of ASR-induced crack generation and propagation as a function of its induced expansion development (see Figure 2.2(b)). By taking advantage of computational modelling, it is possible to link these cracking stages to the reduction in modulus of elasticity and possibly scale up to modelling ASR effects at the structural level.

2.3. Forecasting of ASR expansion of unrestrained concrete in the field

In numerical analyses of reinforced concrete structures, the advancement of expansion in unrestrained concrete, otherwise known as free expansion, is adopted along with considering the effects of restraints/confinements, applied loading and other aspects (i.e., creep, shrinkage, thermal expansion) to simulate the overall behaviour of affected structures. Therefore, free expansion is a key part of numerical modelling at the structural level to assess the progress of ASR damage and its implications for the structures. Most numerical models for structural assessment usually assume that the maximum possible expansion can be found by validating numerical results using structural monitoring data (Hariri-Ardebili, Saouma & Merz 2018; Pourbehi, van Zijl & Strasheim 2019). Accurate data for the validation is yet not always available due to the absence of a suitable reference at the non-damage stage of investigated structures. Another approach is correlating laboratory expansion measurement to the field performance by considering differences in environmental conditions. Despite several analytical/numerical expansion models being developed, a practical and reliable forecasting model for ASR-induced free expansion of

concrete in the field is lacking (Larive 1997; Multon & Sellier 2016; Ulm et al. 2000). It is worth noting that observations from several laboratory-field experimental campaigns confirmed a significant difference in free expansions of concrete tested in the laboratory and exposed in the field. In this regard, questions have been posed on which factors affect the laboratory-field performance and how to better estimate the field performance based on laboratory measurements prior to conducting the numerical analysis on the behaviour of reinforced concrete structures.

In the last few decades, several laboratory test procedures such as accelerated mortar bar test (AMBT) and concrete prism test (CPT), i.e., from ASTM International, Canadian Standards Association CSA, European RILEM and Australian Standard test methods, have been developed to assess the potential alkali-reactivity of concrete aggregates and the efficiency of preventive measures before being applied to field structures. Several comparative laboratory and field experimental studies have established reliable benchmarks and examined the reliability of laboratory standard tests for the above-mentioned applications (Fournier et al. 2018). Despite the robustness and applicability of these standards/protocols in identifying potential reactivity of a large number of aggregates, the majority of experts agree that many limitations still remain in classifying borderline reactive aggregates as well as in determining preventive measures levels required (i.e., control of concrete alkali content, use of supplementary cementing materials (SCMs) and lithium-based admixtures) (Doug Hooton et al. 2013; Fournier et al. 2019; Ideker et al. 2012; Thomas et al. 2006). More importantly, the observations from comparative laboratory-field studies show that expansion levels obtained from the laboratory- and the field-exposed specimens diverge greatly, in which the field blocks commonly present significantly higher expansion than the laboratory ones (Doug Hooton

et al. 2013; Fournier et al. 2019; Ideker et al. 2012). An example from Thomas et al. (2006) is shown in Figure 2.3, where the authors tested for expansion of concrete containing different proportions of a high-alkali cement (1.15% $Na2O_e$) and a reactive flint sand (25% of the total aggregate) from both laboratory testings (i.e., CPT and AMBT) and field blocks. The concrete blocks display double the ASR-induced expansions than laboratory specimens at two years. The authors also emphasised that this difference could be significantly higher since the expansion of CPT specimens reached the ultimate expansion after two years, while the blocks after 8-9 years kept expanding further. This poor laboratory-field expansion correlation could be of greater concern, as the ambiguous test results could deliver misleading information for the long-term prognosis of ASR-affected concrete structures.

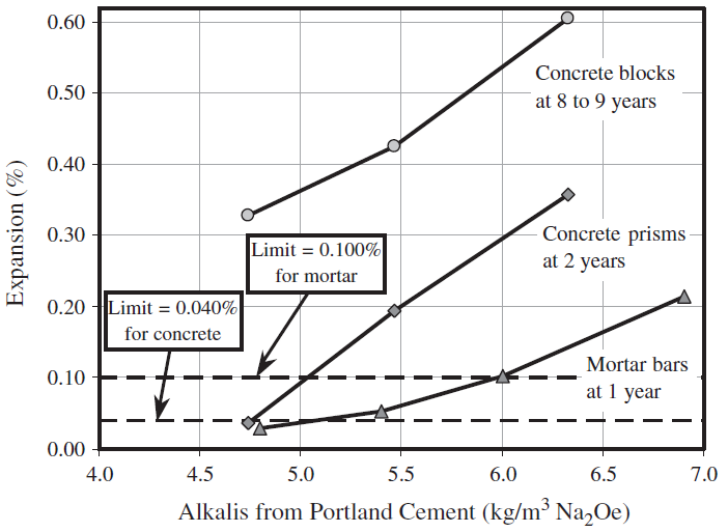

Figure 2.3: Laboratory versus field test results of concrete varying alkali content (Thomas et al. 2006).

The aforementioned limitations of laboratory test procedures still require intensive and extensive studies to improve laboratory-field correlations and thus provide better predictions of ASR prognosis in field structures. Likewise, ongoing research has been

focusing on developing alternative tests and improving the current test methods to limit or eliminate the leaching of alkalis in concrete, such as the miniature concrete prism test (MCPT) (AASHTO 2019) and the concrete cylinder test (CCT) (Chopperla 2019). On the other hand, given the current level of understanding of the laboratory-field expansion correlation and relatively large database available, mathematical modelling of ASR-induced expansion of field structures/structural members based on laboratory observations is necessary. It will enable further analysis of ASR structural implications and ensure better decisions on the rehabilitation of ASR-affected concrete infrastructure. In this context, several empirical, analytical and numerical approaches have been proposed to offer predictive information on ASR-induced expansion of affected structures in the field. These include thermo-chemo-mechanical models (Saouma & Perotti 2006a; Ulm et al. 2000), finite element inverse analysis (Sellier et al. 2009), multi-scale chemical analysis (Multon & Sellier 2016), analytical modelling (Kawabata et al. 2016), etc. Yet, to the best of the author's knowledge, the applicability of the vast majority of proposed models is still limited in current practice. This situation is due to either the highly complexity of the models or even the lack of their validation with the experimental database comprising a wide range of concrete mixtures and reactive aggregates.

2.4. Modelling ASR expansion of reinforced concrete structures

For reinforced concrete structures affected by ASR, presence of reinforcement could change the expansion behaviour of concrete in comparison to free expansion (Doug Hooton et al. 2013; ISE 1992). It is often observed that ASR-induced expansion is commonly inhibited in the direction along the steel reinforcement, where is increasingly occurs in other less restrained directions, thus leading to the development of cracking along the main reinforcement. As an example, Figure 2.4(a) depicts a comparison

between expansion advancement in non-reinforced and reinforced concrete beams tested at an exposure site located in Kingston, Ontario, Canada (MTO 2018). There is an obvious divergence in the expansion of the reinforced beam versus the non-reinforced beam after a few years of exposure. Another example is depicted in Figure 2.4(b) from ISE (1992), which was obtained from different experimental testings, and it shows a significant reduction in expansion of reinforced concrete compared to the non-reinforced concrete (i.e., free expansion) as the reinforcement ratio increases. For instance, using 1% of steel reinforcement in concrete could reduce expansion in the reinforcement direction up to as much as 80% of the free expansion (ISE 1992).

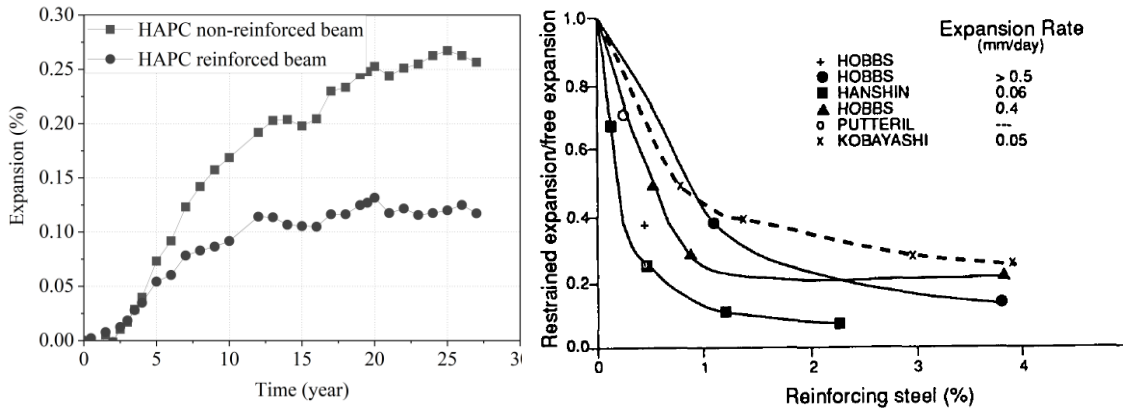

(a) (b)

Figure 2.4: Effect of reinforcement on ASR expansion: (a) from ISE (1992), and (b) from MTO (2018).

Due to this significant effect of reinforcement restraints, some studies on reinforced concrete specimens established empirical expansion-reinforcement ratios for estimating ASR expansion in reinforced concrete members (Aryan et al. 2020; Doug Hooton et al. 2013; Graff 2017). The impact of reinforcement restraint on ASR expansion, however, varies from one to another. The expansion rate may also contribute to the variation as shown in Figure 2.4(b), in which a high expansion rate tends to induce a higher reduction of the expansion due to reinforcement confinement. On this issue, the confinement effect

of reinforcement could be different for concrete in the field, where expansion rate is typically and significantly lower than that from laboratory-accelerated testings.

In addition, a series of experimental tests documented by Multon & Toutlemonde (2006) showed "expansion transfer" behaviour, in which expansions were transferred from a more restrained direction to other less or non-restrained directions. Results also indicated that the ASR volumetric expansion was virtually constant at whatever restrained level in one or two directions tested. The same expansion transferring behaviour was observed due to multiaxial reinforcement layout and ratios as in the experimental testings set by Allford (2016) and Giannini (2012). For instance, Giannini (2012) tested for expansion of non-reinforced and reinforced concrete blocks in the field, where main reinforcement was arranged only in the longitudinal direction of the blocks. The author observed almost the same total expansion from three orthogonal directions from the non-reinforced and reinforced concrete blocks, yet, expansion in the longitudinal direction fell from 85% to less than 40% of those measured in transverse directions.

This observation highlights the same transferring behaviour of the expansion due to reinforcement restraints. In this regard, it is difficult to simply apply the empirical restrained expansion-reinforcement ratio relationships in actual structures due to more complicated arrangements of reinforcement in different directions as well as the applied stress and boundary conditions. It is known that confinement in one direction could affect expansion in other orthogonal directions. Therefore, it is necessary to employ a numerical modelling approach, which enable considerations of both three-dimensional ASR expansion development and structures' complexities. In recent years, several models have been proposed for expansion and damage assessment modelling, such as Saouma & Perotti (2006b), Comi, Fedele & Perego (2009), Morenon et al. (2017); Roth (2020).

Recently, different numerical benchmarks for modelling ASR expansion were reported in a RILEM state-of-the-art report (Saouma 2020). However, most current studies focused on modelling of massive structures such as dam instead of thoroughly addressing the expansion behaviour of reinforced concrete members. As such, it is necessary to have modelling practices that can assess ASR-induced expansion and progress of damage in reinforced concrete members.

2.5. Structural performance of reinforced concrete structures suffering from ASR: experimental observation and numerical modelling

The rise of cracking, expansion and degradation of mechanical properties due to ASR may adversely impact on serviceability and load-carrying capacity of structures. Several studies have investigated the extent of ASR-induced impact on the flexural and shear capacity of concrete members at different ASR levels (Bach, Thorsen & Nielsen 1993; Deschenes, Bayrak & Folliard 2009; Fan & Hanson 1998; Giannini 2012; Hiroi et al. 2016; Liu et al. 2017; Monette, Gardner & Grattan-Bellew 2002). It is interestingly observed that load-carrying capacity of ASR-affected structures is not compromised, especially for shear capacity (Bach, Thorsen & Nielsen 1993; Deschenes, Bayrak & Folliard 2009; Giannini 2012; Liu et al. 2017). An exception is evident in Swamy & AlL-Asali (1989), where affected reinforced concrete beams lost up to nearly 25% of their flexural strength at the expansion level of 0.518% measured on the beams. These studies did, however, agree that the impact on load-carrying capacity would become significant if the specimens were subjected to longer periods of exposure and underwent high expansion levels (Deschenes, Bayrak & Folliard 2009; Giannini 2012). Deschenes, Bayrak & Folliard (2009). As such, besides adverse impacts on the material performance concrete such as cracking and degradation of mechanical properties, there is a certain

favourable effect of ASR on the capacity of structures at low expansion levels. According to ISE (1992), there is a favourable prestressing effect of restrained ASR expansion, such as from the reinforcement. The same observation was also reported in Huang et al. (2014) and Hansen et al. (2016). Two most important questions herein are (i) to what extent does the prestressing effect contribute to the capacity of affected structures; and (ii) can this favourable outcome be maintained or decayed as the expansion increases? Investigation on the prestressing effect in relation to the expansion advancement and degradation in mechanical properties is necessary.

Another important aspect of modelling structural behaviour of existing concrete structures subjected to ASR is forecasting expansion advancement of concrete in the field. As stated previously, this is a key input to the numerical modelling to assess ASR damage evolution and its implications for affected structures. For instance, Hariri-Ardebili, Saouma & Merz (2018) conducted a numerical simulation for an existing segmental bridge affected by ASR in Switzerland. To perform a risk-informed assessment, the authors assumed the future expansion of concrete for the next 50 years, in which maximum free volumetric expansion of the concrete varied widely from about 0.4% to 2% as shown in Figure 2.5(a). This uncertainty of the maximum possible expansion led to a very wide range of structural response, as depicted in Figure 2.5(b). This broad variation highlights the importance of having accurate forecasting for expansion of concrete in the field.

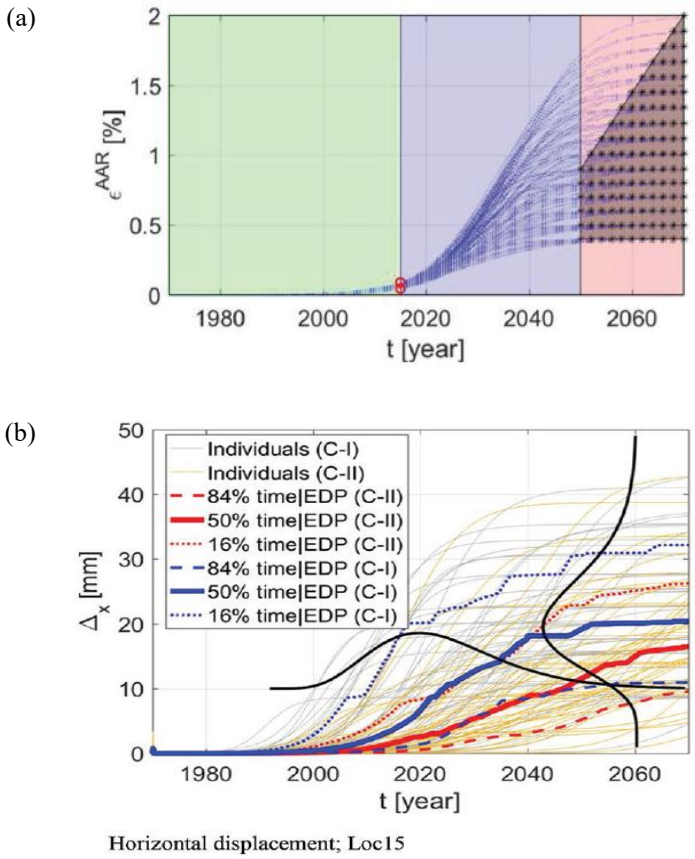

Figure 2.5: Modelling for condition assessment of a bridge as described by Hariri-Ardebili, Saouma & Merz (2018): (a) domain of uncertainties in the expansion advancement; and (b) structural displacement.

2.6. Research questions to be addressed

Based on the literature review on the relevant themes, several research questions need to be addressed so that ASR effects are better understood regarding condition assessment and capacity evaluation of concrete structures compromised by ASR. The questions are as follows:

1. ***Chapter 3*** was designed to address three important questions regarding the reduction in modulus of elasticity of concrete due to ASR: *(i) what are the factors affecting the degradation in modulus of elasticity of ASR-affected concrete?; (ii) how can a better*

estimation of the modulus of elasticity be provided?; and (iii) how does cracking affect mechanical properties? In this chapter, a machine learning approach was proposed to investigate the impact of different factors such as reactive aggregates, alkali content, and strength in addition to the expansion to the modulus of elasticity, so that reduction could be better estimated. In addition, a computational homogenization was developed to link the measurement of cracking in concrete to the reduction of modulus of elasticity.

2. In ***Chapter 4,*** two main research questions are asked regarding forecasting of the ASR expansion in the field: *(i) what are the main reasons leading to poor laboratory-field expansion correlation?; and (ii) how can this correlation be improved to provide a better estimation of concrete expansion in the field based on laboratory measurements?* This chapter presents a novel semi-empirical approach to correlate ASR-induced expansion of unrestrained concrete tested in the laboratory and in the field. It accounts for the effect of the reactive aggregate type and nature, alkali leaching, alkali contribution from aggregates and environmental conditions (i.e., temperature, relative humidity). The model was utilised for forecasting ASR-induced expansion of concrete blocks incorporating different reactive aggregates and alkali contents, and exposure to three different outdoor conditions in Canada and the USA.
3. ***Chapter 5*** seeks to answer two important questions about the effects of ASR on expansion and capacity of reinforced concrete structures: *(i) how can the expansion of unrestrained concrete as estimated from the novel semi-empirical model proposed in Chapter 4 be correlated to the expansion of reinforced concrete members?; and (ii) to what extent do ASR-induced expansion and degradation in mechanical properties affect the load-carrying capacity of reinforced concrete structures?* As a continuation of the semi-empirical model developed in Chapter 4, this chapter presents a numerical modelling framework for ASR expansion and load-carrying of

reinforced concrete. The model was implemented in the commercial FEA package ABAQUS as a practical engineering approach using different user subroutines and the concrete damaged plasticity model. Impacts of changes in mechanical properties due to ASR on the expansion advancement and load-carrying were then investigated.

2.7. Summary

In this chapter, a critical review on the evaluation of ASR-induced expansion, mechanical properties degradation and load-carrying capacity was presented. ASR and its effects have been intensively studied in the last 80 years since it was first identified, yet there are still many challenges in assessing and forecasting consequences of ASR in reinforced concrete structures. Several research questions have been identified regarding important aspects for the assessment and prognosis tasks of the ASR-affected structures such as evaluation of mechanical properties degradation, forecasting expansion of concrete in the field and modelling for structural capacity. All of the three main chapters were designed to address key research questions so that practical approaches could be implemented for condition assessment and capacity evaluation of concrete structures suffering from ASR.

Chapter 3: Evaluating degradation of mechanical properties of concrete due to ASR

As highlighted in Chapter 2, more attention needs to be paid for evaluation of the reduction in modulus of elasticity of concrete due to ASR. This chapter firstly presents an artificial neural network model to investigate the effects of contributing factors and provide a better understanding and estimation of the reduction. Then, a computational homogenization approach was proposed to evaluate impacts of cracking in concrete due to ASR on its stiffness.

3.1. Artificial Neural Network approach for modulus of elasticity of concrete affected by concrete

3.1.1. Introduction

In most of the previous studies, the degradation of mechanical properties also was at different levels according to different reactive aggregate types and nature which vary in size, rock type and reactivity level (Giaccio et al. 2008; Sanchez et al. 2015; Smaoui, Bissonnette, et al. 2005). Sanchez et al. found that concrete mixes of reactive sands present earlier reductions of mechanical properties than that of reactive coarse aggregates concrete (Sanchez 2014). Reactive aggregates have been used in several countries worldwide which are different in rock type and their reactivity. In research of Kubo & Nakata (2012), the reductions on the modulus of elasticity were greater than the lower bound proposed by ISE (1992). The author explained that typical reactive aggregates found in concrete structures deteriorated by ASR in Japan show rapid expansion and normal Portland cement made in Japan has faster hydration of cement than that of cement made in other countries. On the reactivity of aggregate, it is commonly evaluated through accelerated mortar bar test (AMBT) or concrete prism test (CPT) on standard mix design

and aggregate grading based on the measured expansion at specific accelerated conditions and durations (AS-1141.60.1 2014; AS-1141.60.2 2014). However, for experimental studies in the literature, the utilisation of reactive aggregate for investigation of mechanical properties of ASR-affected concrete subjected to expansion measurements did not follow the same testing standard. Therefore, the effect of reactivity of different aggregate types on mechanical properties degradation is difficult to assess from the available databases.

Additional alkali is commonly added to mixing water of concrete mixes to accelerate the ASR rate in the laboratory testing. The total amount of alkali content in a concrete mix is 1.25%, as recommended by many standards (AS-1141.60.1 2014; AS-1141.60.2 2014; ASTM-C1293 2015). However, this number in the previous experimental testings for mechanical properties degradation due to ASR is different from one to others. Many studies indicate that of increasing alkali content in concrete can cause a negative effect on concrete properties (Jawed & Skalny 1978; Shayan & Ivanusec 1989; Smaoui, Bérubé, et al. 2005). Jawed & Skalny (1978) suggests that increasing alkali content in the concrete reduce early and ultimate strengths. By investigating the effect of NaOH in concrete containing reactive aggregate, Shayan & Ivanusec (1989) concluded that microstructure of concrete with higher alkali content was less dense compared to low alkali content concrete. Experimental study of Smaoui, Bérubé, et al. (2005) observed that the high alkali concrete presents more reticular and porous microtexture, causing a reduction in strength and stiffness of concrete. The temperature and mix proportion, which have been intensively investigated in relation to concrete properties, are crucial parameters in concrete strength design. The testing condition such as temperature and moisture affect not only the ASR-induced expansion as in ASR accelerated condition but also the strength

evolution over time as curing procedure. In addition, mix proportion and designed strength also contribute to the strength and stiffness development of concrete material.

Due to wide variations of these influencing factors in experimental testing from the literature, it is difficult to compare and evaluate the degradation of mechanical properties due to ASR by considering only the expansion. In addition to the expansion, the effects of different influencing factors on mechanical properties of ASR-affected concrete need to be further intensively studied to get a fundamental understanding.

In recent decades, artificial intelligence (AI) has been widely employed in the area of concrete material and structures. They are able to build up a highly nonlinear relationship between input and output variables by learning algorithm from data themselves. Many AI-based models have been successfully developed for estimation of concrete properties and structural behaviour, such as artificial neural networks (ANN) (Sonebi et al. 2016), support vector machine (SVM) (Yu et al. 2018), genetic programming (GP) (Gandomi et al. 2013), and adaptive network-based fuzzy inference system (ANFIS) (Yu et al. 2018). Among all the AI techniques, artificial neural networks (ANN) is the most known technique and broadly applied to deal with concrete properties and durability prediction (Hodhod, Said & Ataya 2018). The method has been used to predict different properties and deterioration of concrete, such as concrete compressive strength (Ashteyat & Ismeik 2018; Ongpeng et al. 2017), elastic modulus of recycled aggregate concrete (Duan, Kou & Poon 2013), creep and shrinkage (Bal & Buyle-Bodin 2013; Hodhod, Said & Ataya 2018), and permeability of concrete (Kong, Chen & Du 2016). Furthermore, an important superiority of the ANN is that several algorithms have been proposed to evaluate the relative impact of the input variables on the prediction process (Gevrey, Dimopoulos & Lek 2003).

By taking advantages of the ANN, it can help to provide a better solution to tackle the challenge of evaluation of the modulus of elasticity degradation of ASR-affected concrete. In this study, based on a comprehensive database collected from experimental studies in the literature, ANN was utilised for evaluating the loss in modulus of elasticity of ASR-affected concrete in correlation to the ASR expansion level and other information on the mix proportion, reactive aggregate, exposure condition and initial strength of undamaged concrete. To the best of the authors' knowledge, the utilisation of AI in predicting concrete modulus of elasticity reduction due to ASR is proposed for the first time in this study. The motivation is to develop a highly accurate prediction model based on the comprehensive database, which can be used for prediction of the modulus of elasticity reduction in a large range of ASR-induced expansion. Firstly, an optimization study was conducted by a selection of input variables, examining two training algorithms and determining an optimal number of hidden neurons to obtain an optimal network. Then, to demonstrate a superior performance of the proposed ANN model, it was compared to the existing empirical models that are widely used in the current practice for the modulus of elasticity estimation of ASR-affected concrete. Eventually, it is important to give explanatory insight into the predictive progress to identify the contribution of influencing factors to the loss in modulus of elasticity of concrete due to ASR. The relative importance of each influencing factor as model input variable was determined by means of outstanding methods such as neural interpretation diagram, connection weights approach and partial derivatives.

3.1.2. Empirical models for modulus of elasticity of ASR affected concrete

In past decades, several empirical models for estimating modulus of elasticity of ASR affected concrete has been proposed based on ASR chemical damage laws as well as

available experimental data. These models were then utilised in evaluating the ASR-induced damage as well as in numerical modelling for assessing structural behaviour (Ferche et al. 2017; Hariri-Ardebili, Saouma & Merz 2018; Kawabata et al. 2017). However, due to the complicated mechanism of ASR in concrete, empirical models for degradation of concrete mechanical properties still have not been fundamentally established (Esposito et al. 2016). Most of these models are curve fitting based on the currently available data. In addition, it is worth to note that all these empirical models predict the modulus of elasticity as functions of only ASR-induced expansion.

Esposito et al. (2016) proposed a continuous piecewise linear function and fitted with a comprehensive available data set on mechanical properties of the ASR-affected concrete collected from the literature using a weighted least-squares fitting process, as shown in Eq. (3.1).

$$\beta_{Ec} = \frac{E}{E^{ref}} = \begin{cases} q_1 + m_1\varepsilon & if\ \varepsilon \leq 0.05\% \\ q_m + m_m\varepsilon & if\ 0.05\% < \varepsilon \leq 0.1\% \\ q_h + m_h\varepsilon & if\ 0.1\% < \varepsilon \leq 0.5\% \\ q_e + m_e\varepsilon & if\ \varepsilon > 0.5\% \end{cases} \quad (3.1)$$

In which, E_{ref} is the estimated modulus of elasticity at the reference expansion of 0.05%; q and m are linear coefficients for each level of expansion, which obtained from linear regression from collected experimental data. To meet continuity condition of the curve, the following relationship was constructed: $q_m = q_l + 0.05 \times (m_l - m_m)$; $q_h = q_m + 0.1 \times (m_m - m_h)$; $q_e = q_h + 0.5 \times (m_h - m_e)$. The prediction accuracy of this model was then compared to the S-shape curve modified from Saouma & Perotti (2006b):

$$\beta_{Ec} = \frac{E}{E^{ref}} = \beta_0 - (\beta_0 - \beta_\infty)\xi \quad (3.2)$$

where β_0 and β_∞ are normalized modulus of elasticity at non-expansive and asymptotic expansion condition, respectively; ξ is a sigmoid curve representing the volumetric expansion as a function of time and temperature, more details are found in Saouma & Perotti (2006b). The comparative study results showed that the proposed continuous piecewise linear function achieved higher accuracy in estimation of modulus of elasticity of ASR affected concrete compared to the modified S-shape curve. However, Esposito et al. (2016) also concluded that the observed estimation error was still very high; therefore, further fundamental investigations should systematically be conducted to obtain better models.

Recently, Kawabata et al. (2017) and Martin et al. (2017) adopted the chemical damage rule from Seignol et al. (2009), then fitted to a certain set of collected data from the literature. The chemical damage rule takes into account cement-paste microcracking induced by ASR by introducing damage parameters, shown as follows.

$$E_c = E_{c0} \times (1 - d) \tag{3. 3}$$

$$d = d_{max}(1 - \exp(-\omega \times \langle \varepsilon - \varepsilon_0 \rangle^+)) \tag{3. 4}$$

where, d represents the ASR-induced damage; d_{max} and ω are the maximum damage and rate of damage evolution, respectively; ε is the expansion level, ε_0 is the chemical expansion above which concrete matrix starts cracking. This damage rule was subsequently applied to evaluate the damage in ASR-affected concrete in both experimental and numerical studies (Kawabata et al. 2017; Martin et al. 2017).

In this study, three empirical models from Esposito et al. (2016), Kawabata et al. (2017) and Martin et al. (2017) was adopted to estimate the elastic modulus reduction due to ASR of 177 experimental tests from reliable literature sources. The results from these

empirical models were then compared to prediction results from the proposed ANN-based model in this study.

3.1.3. Data collection and description

3.1.3.1. Data collection

In order to gain an insight into the effects of ASR on concrete mechanical properties and to develop a highly accurate ANN model, a database has been established based on a large number of experimental research data published in the open literature. The dataset, collected from 13 studies with 45 concrete mixes, consists of 177 testing groups of elastic moduli at different levels of the ASR-induced expansion (Esposito et al. 2016; Gautam et al. 2017a; Giaccio et al. 2008; Giannini 2012; Kagimoto, Yasuda & Kawamura 2014; Kubo & Nakata 2012; Larive 1997; Mohammed, Hamada & Yamaji 2003; Multon 2003; Pleau et al. 1989; Sanchez et al. 2017; Sargolzahi et al. 2010; Smaoui, Bissonnette, et al. 2005). All these testings were conducted on the plain concrete specimens under free expansion conditions.

3.1.3.2. Model input and output description

Along with ASR-induced expansion, several other factors that affect both the ASR mechanism and properties of ASR-affected concrete need to be taken into consideration in the estimation of the residual modulus of elasticity. An appropriate selection of input variables is essential. In this study, the expansion level and other seven influencing factors are considered as eight input variables of the first ANN model. They include information on mix proportion, proportion of reactive sand and coarse aggregate, exposure condition, proportion of sodium oxide equivalent, initial compressive strength at the undamaged condition, and maximum measured expansion. The impact of all the input variables is

able to be evaluated based on weight factors after achieving high performance from this first model. Table 3.1 shows the ranges of all the input and output variables. More details of the selected input variables are described as follows.

Table 3.1: Model variables and variation range

Type	Model variable description	Symbol	Variation range [min, max]
Input	1. Cement content (kg/m^3)	C	[300, 424]
	2. Fine reactive aggregate/cement ratio	FRAC	[0, 2.85]
	3. Coarse reactive aggregate/cement ratio	CRAC	[0, 3.42]
	4. Exposure temperature (^{o}C)	T	[38, 50]
	5. Proportion of sodium oxide equivalent (%)	ALKALI	[1.17, 2.87]
	6. Initial compressive strength at "non-expansive" condition (MPa)	CS	[18.2, 58.5]
	7. Maximum measured expansion (%)	MAXEXP	[0.072, 0.916]
	8. Measured expansion (%)	EXP	[0.001, 0.916]
Output	Normalised modulus of elasticity	β_{Ec}	[0.163, 1.130]

Mix proportion and the use of reactive aggregate

It is well known that the proportion of different ingredients such as cement, water, fine and coarse aggregates are the key factor in design and determination of concrete modulus of elasticity (Duan, Kou & Poon 2013). In this study, cement content (C) and the proportion of aggregates are selected to represent the effect of mix proportion. Different from the aggregate contents in concrete without ASR, reactive aggregate content, which

is the main cause of ASR mechanism, should be paid more attention in assessment of ASR affected concrete material and structures (Nayıra, Erdoğdu & Kurbetcib 2017).

Reactive aggregate is the source of reactive non-crystalline silica for the alkali-silica reaction in concrete. In most of the previous studies, the degradation of mechanical properties also was at different levels according to different reactive aggregate types and nature which vary in size, rock type and reactivity level (Gao et al. 2011; Giaccio et al. 2008; Sanchez et al. 2015; Smaoui, Bissonnette, et al. 2005). Sanchez et al. (2017) found that concrete mixes of reactive sands present earlier reductions of mechanical properties than that of reactive coarse aggregates concrete (Sanchez 2014). In the proposed model, fine and coarse reactive aggregates are considered as two separate input variables to evaluate the effect the reactive aggregate size (FRAC and CRAC). In addition, the reactivity of aggregate is commonly evaluated through accelerated mortar bar test (AMBT) or concrete prism test (CPT) on standard mix design and aggregate grading based on the measured expansion at specific accelerated conditions and durations (AS-1141.60.1 2014; AS-1141.60.2 2014). However, for experimental studies in the literature, the utilisation of reactive aggregate for investigation of mechanical properties of ASR-affected concrete subjected to expansion measurements did not follow the same testing standard (Sirivivatnanon, Mohammadi & South 2016).

Alkali content

Alkali in concrete is the other reactant for ASR together with the reactive non-crystalline silica from reactive aggregates. Experimental results from previous studies indicate that of increasing alkali content in concrete can harm concrete properties (Shayan & Ivanusec 1989; Smaoui, Bérubé, et al. 2005). By investigating the effect of NaOH in concrete

containing reactive aggregate, Shayan & Ivanusec (1989) concluded that microstructure of concrete with higher alkali content was less dense compared to low alkali content concrete (Shayan & Ivanusec 1989). Through experimental study, Smaoui, Bérubé, et al. (2005) observed that the high alkali concrete presents more reticular and porous microtexture, caused a reduction in strength. In the proposed model, the proportion of sodium oxide equivalent as an input (ALKALI) is the total alkali content of concrete mixes, which is from both cement and amount added to mixing water.

Exposure condition

In addition to the reactive aggregate and alkali content, exposure condition, herein including temperature and moisture, creates an environment for initiating and developing of the alkali silica chemical reaction as well as for curing concrete. They thus strongly affect the ASR mechanism (Lindgård et al. 2012) and change in material properties of concrete (Kim, Han & Song 2002). For the entire experimental data in this study, the relative humidity remains at very high levels, and therefore it is not selected as a variable for exposure condition. The other factor, temperature (T), is considered as an input for the developed model.

Compressive strength of concrete

In current practice, the modulus of elasticity is commonly estimated through compressive strength due to their strong relationship (Kim, Han & Song 2002). From the dataset in this study, the compressive strength is not available for ASR damaged concrete but undamaged specimens at very low levels of expansion. The compressive strength of the undamaged concrete (CS) is selected as an input for the predictive model. It has to be noted that different testing standards were used to determine the compressive strength,

which can be from cube or cylinder specimens. In this study, CS is referred to as cylinder compressive strength. The relationship between the cylinder and cube strength proposed in Eurocode 2 (De Normalisation 2004) was adopted to convert cube compressive strength to the CS.

ASR-induced expansion level

As mentioned previously, expansion level is a key parameter to evaluate the ASR-induced damage in concrete and is the only variable that has been considered to estimate modulus of elasticity of ASR affected concrete as empirical models in current practice (Esposito et al. 2016; Kawabata et al. 2017; Martin et al. 2017). In this study, the expansion level (EXP) is considered together with the other influencing factors as input variables in the developed model.

Output variable

The ASR-induced degradation on modulus of elasticity has been commonly presented by normalising damaged modulus of elasticity to the undamaged modulus of elasticity, described by the following formula:

$$\beta_{Ec} = \frac{E_c}{E_{co}} \qquad (3.\ 5)$$

where, E_c is the modulus of elasticity of ASR damaged concrete, and E_{c0} is the undamaged modulus of elasticity which is referred to as negligible damage level of "control" specimens. The undamaged modulus of elasticity is commonly measured after 7, 14 or 28 days of curing at very low levels of ASR expansions of less than 0.03% (Sanchez et al. 2017). In this study, the normalised modulus of elasticity was adopted as the output variable in developing the ANN model. It is worth to note that effect of the influencing

factors to the change in modulus of elasticity of concrete due to ASR are different from one to another. Therefore, an evaluation of the contribution of each input variable to the output is a necessity in developing a high-performance predictive model.

3.1.4. ANN model development

3.1.4.1. Artificial Neural Network

Overview: Artificial neural network (ANN) is a computational system which simulates the human biological neural system with the ability of reasonably learning and tackling the practical problems. Generally, the ANN is made up of a set of inter-connected artificial elements via a layer-by-layer configuration and employs the transfer function to transform the information between arbitrary two layers. Through the network training, the ANN is able to adaptively change its configuration according to internal and external information, and the trained ANN is used to characterize the complicated relationship between the input and output. In a standard ANN model, there are three types of network layer: input layer, hidden layer, and output layer. The schematic layout of an artificial neural network developed in this study is illustrated in Figure 3.1. The neurons at different layers are connected with each other via the connection weight, the value of which is optimized through an objective function of the network during a learning process. The signals are sent from the input neurons to the hidden neurons, then processed by linear calculation with weights and bias, before passed through a transfer function to obtain signals for the output layer. The tangent sigmoid functions, which is one of the most commonly used transfer function (Altarazi, Ammouri & Hijazi 2018), is employed in the hidden layer to develop the networks in this study. One of the most important tasks in developing ANN is the learning process. In this study, two training algorithms,

Levenberg-Marquardt and Bayesian regularization, are used for this process for a comparative study. The details of these algorithms are presented in the following part.

In the ANN, the numbers of input and output neurons are determined by the practical problem, and the number of the hidden layers and hidden neuron number are determined according to the trial method. According to Heaton (2008), the number of hidden neurons should not be higher than twice the number of input neuron. In this study, various neural network structures with the numbers of hidden neurons up to 17 were tested to determine the optimal network configuration.

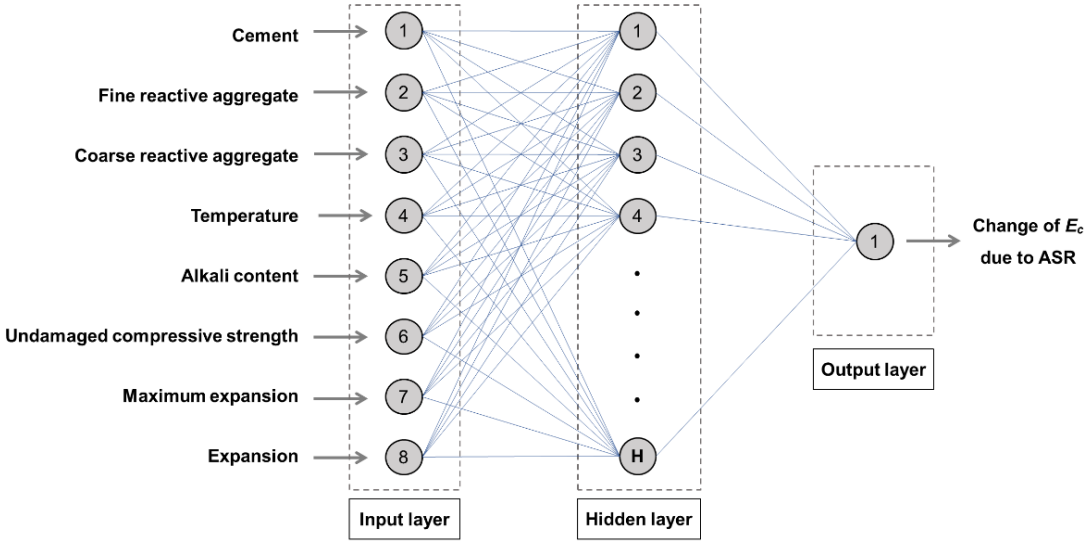

Figure 3.1: General architecture of the neural network for estimating the residual modulus of elasticity.

Among 8 factors considered, their impacts on the change of the elastic modulus are different from one to another. Therefore, it is necessary to provide an explanatory insight into the influence of each factor as an input on the output based on the developed neural networks. In this study, after achieving an optimal network of 8 input variables, different methods such as connection weights approach and partial derivatives are utilised to assess the relative contribution of model inputs to the output through the network weights. More

details of the connection weights approach and partial derivatives are presented in the next sections. Based on the analysis results, the less important input variables can be eliminated from the input set to reduce the required information for prediction models without reducing its accuracy.

Network training algorithm: Levenberg-Marquardt and Bayesian regularization

Backpropagation (BP) is a common supervised learning strategy for the ANN training process. In order to get the expected outputs, a number of training samples are used to adjust the connection weights between neurons and biases. The differences between the real results and predicted results are back-propagated from the output layer to the input layer to dynamically adjust the network parameters. There are several BP training algorithms that have been successfully utilised in predicting materials properties (Altarazi, Ammouri & Hijazi 2018). Among the backpropagation training algorithms, Levenberg-Marquardt (LM) algorithm is most commonly used, which is based on nonlinear least-square optimisation. Test results of LM algorithm on several approximation problems have validated its superiority over other training algorithms in terms of convergence and generalisation capacity (Altarazi, Ammouri & Hijazi 2018; Bal & Buyle-Bodin 2013). In this analysis, the error function E_D, which is the mean square error (MSE), is used as the objective function to optimize the network. Its mathematical expression is shown in Eq. (3.6). The learning process aims at minimizing this error function by adjusting the network weights and bias. In LM training algorithm, the *early stopping* technique is commonly utilised to improve network generalization and prevent overfitting (Altarazi, Ammouri & Hijazi 2018). In this technique, the data is divided into three subsets for training, validating and testing, where the validation error is used to monitor and control the overfitting.

$$E_D = \frac{1}{p}\sum_{i=1}^{p}(t_i - o_i)^2 \quad (3.6)$$

Here, t_i and o_i denote real value and ANN prediction of i^{th} sample and p denotes the sample number.

Along with early stopping, Bayesian regularization, which is an automated regularization procedure, is implemented in the Bayesian regularization (BR) training algorithm to overcome overfitting and improve the generalization ability. One of the key characteristics of this regularization technique is that no validation dataset is required like *early stopping* technique (Burden & Winkler 2008). Therefore, more data is added to training subset from the validation, which could be an advantage of BR over the LM with early stopping technique if there is limited available data for the learning process. Due to a small available data of 177 samples in this study, it is reasonable to utilise BR learning algorithm for developing the neural network predictive model.

In the BR algorithm, the objective function is modified from the mean square error function of LM (as shown in Eq. (3.6)) by adding a term quantifying the network weights E_w, as described in the following equations (MacKay 1992):

$$F = \alpha E_w + \beta E_D, \text{ with } \alpha + \beta = 1 \quad (3.7)$$

$$E_w = \frac{1}{n}\sum_{j=1}^{n} w_j^2 \quad (3.8)$$

where α and β are regularization parameters varying between 0 and 1, E_w is the sum of squares of the network weights, and n is total number of the weights. The training algorithm is aimed at optimizing regularization parameters and network weights to minimize the error of the model output and measured values. It has to be noted that the values of regularization parameters emphasize the significances in training process

whether it drives the network error smaller ($if\ \alpha \ll \beta$) or reduces the weights at specific expense of the errors ($if\ \alpha \gg \beta$) (Foresee & Hagan 1997). By constraining size of the network weights, the objective function $\boldsymbol{F}$ is able to reduce the number of effective weights to an optimized number, produce a smoother network response and improve generalization ability of the network. Therefore, in addition to optimal network weights, the optimization of the regularization parameters is an important task in Bayesian regularization training algorithm. In this training algorithm, the network weights, as well as regularization parameters, are considered as random variables and its density function is updated and optimized in the learning process using the Bayesian framework:

$$P(\boldsymbol{w}|D,\alpha,\beta,M) = \frac{P(D|\boldsymbol{w},\beta,M)P(\boldsymbol{w}|\alpha,M)}{P(D|\alpha,\beta,M)} \tag{3. 9}$$

where, $\boldsymbol{w}$ is the network weight vector; D is the training dataset; M represents the particular neural network structures developed; $P(\boldsymbol{w}|\alpha,M)$ is the prior density; $P(D|\boldsymbol{w},\beta,M)$ is the likelihood function, which is the probability of the data occurring; and, $P(D|\alpha,\beta,M)$ is the normalisation factor. The important task next is searching for optimal network weights to maximize the posterior probability $P(\boldsymbol{w}|D,\alpha,\beta,M)$, which leads to a minimized objective function. Foresee & Hagan (1997) proposed following iterative procedure to optimize the network weights and regularization parameters: (1) generate initial set of weights, α and β; (2) take one step of the LM algorithm to minimize the objective function F by finding the optimal weights; (3) a process to compute new estimates for the regularization parameters; (3) Iterate the above step until convergence. Details of the Bayesian optimization of the network weights and regularization parameters were obtained from Foresee & Hagan (1997).

In this study, both LM and BR training algorithms were adopted for training the neural networks, named as LMNN and BRNN, to determine a better performance prediction model. In addition to the mean square error (MSE) calculated as the error function E_D, the performance of the network with different training algorithms is also evaluated by the coefficient of determination (R^2), as shown in Eq. (3.10). The training algorithm that generates better performance is selected for further evaluation and development.

$$R^2 = \frac{\left[p\sum_{i=1}^{p} t_i \cdot o_i - (\sum_{i=1}^{p} t_i)(\sum_{i=1}^{p} o_i)\right]^2}{[p\sum_{i=1}^{p} t_i^2 - (\sum_{i=1}^{p} t_i)^2][p\sum_{i=1}^{p} o_i^2 - (\sum_{i=1}^{p} o_i)^2]} \quad (3.10)$$

In the ANN model, training data set is utilised to establish the predictive model, while its performance is evaluated based on validation samples that are distinct from those used for model training. It is important to note that there is no precise rule to partition the database, so various combinations for model training and testing data sets are taken into consideration. In the Levenberg-Marquardt neural network, the available dataset (177 samples) was randomly divided into three subsets for training, validation and testing with the ratio of 70%, 15% and 15%, respectively. Without requirements of a separate validation dataset, 85% of the available data was used for training in Bayesian regularization neural network (BRNN). Implementation of Levenberg-Marquardt and Bayesian regularization was performed in Matlab (R2016b).

3.1.4.2.Interpretation of the network weights for relative contribution of input variables

The effects of different influencing factors as input variables on the change in modulus of elasticity due to ASR can be understood based on the network weights by a visual approach such as the neural interpretation map (NID) (Özesmi & Özesmi 1999), or quantitative approaches (Gevrey, Dimopoulos & Lek 2003; Olden, Joy & Death 2004).

In NID, width of lines connecting nodes represents the absolute value of weight factors while the colour represents whether weight values are positive or negative. In an ANN model, a higher absolute value of connection weight represents a higher interaction between two neurons, while its sign represents the positive or negative effect of a neuron on another. The map is thus able to present the insight of network and the contribution of input variables to the elastic modulus reduction due to ASR.

There are several quantitative methods for assessing the contribution of model inputs to outputs in ANN based prediction models, such as sensitivity analysis, connection weights approach, Garson's algorithm, partial derivatives, input perturbation and forward stepwise addition (Gevrey, Dimopoulos & Lek 2003; Olden & Jackson 2002; Olden, Joy & Death 2004). By testing different methods for quantifying the importance of input variables, Olden, Joy & Death (2004) indicated that the connection weights approach is the most accurate method, while results from Gevrey, Dimopoulos & Lek (2003) shows that the partial derivatives gave the most stable results. Therefore, this study used both methods to evaluate the importance of input variables. The connection weights approach determines the relative contribution of ANN model inputs as a function of the neural network connection weights, presented as the following expression (Olden & Jackson 2002):

$$R_{ij} = \sum_{k=1}^{H} w_{ik} \cdot w_{kj} \qquad (3.\ 11)$$

Where, R_i denotes the relative contribution of the input variable x_i with regard to the output; H denotes the number of the hidden neurons; w_{ik} is the connection weight between the input variable x_i and the hidden neuron h_k; w_k is the connection weight between the hidden neuron h_k and the output neuron y_j.

By using all the training data, partial derivatives method considers the first-order effects of model inputs on outputs. The relative contribution index SSD_e of input variables to an ANN output regarding the data set is calculated as follows (Dimopoulos, Bourret & Lek 1995):

$$d_{mi} = s_m \sum_{k=0}^{H} w_{kj} \, . \, I_{km} . (1 - I_{km}) \, . w_{ik} \tag{3. 12}$$

$$SSD_i = \frac{1}{M} \sum_{m=1}^{M} (d_{mi})^2 \tag{3. 13}$$

in which, d_{mi} is the partial derivatives of the output y_m corresponding to input x_m, with m = 1 to M and M is the total number of training samples; s_m is the derivative of the output with respect to its inputs; I_{km} denotes the value of the k^{th} hidden neuron.

The relative contribution of input variables is then determined based on their relative contribution index. More details of connection weights approach and partial derivatives are obtained in Olden & Jackson (2002) and Dimopoulos, Bourret & Lek (1995), respectively. It has to be noted that the observation in this section is based on the proposed ANN approach with respect to the knowledge from the readily available experimental data in the literature.

3.1.5. Results and discussion

3.1.5.1. Optimization of ANN models

Due to differences in generating initial network weights, each neural network with specific number of hidden neurons and training algorithm was run 10 times to provide a generalization in comparison of different training algorithms. The best performance of different ANN models with different numbers of hidden neurons and two training

algorithms are shown in Figure 3.2. As mentioned previously, the performance of the ANN model in this study is determined in term of MSE and R^2. It has to be noted that a lower value of MSE and greater R^2 present a better fit between the measured and predicted values. Obviously, increasing number of hidden neurons improves the performance of ANN models by significantly reducing MSE and increasing R^2. For example, in both training algorithms, R^2 increases from around 0.75 in the models of 1 hidden neuron to roughly 0.94 in the 5 hidden neurons models. Subsequently, there are significant fluctuations in the performance of LMNNs when increasing number of hidden neurons. In addition, it is clear to see that the models of BR training algorithm produce better performance compared to the LM training algorithm models. Indeed, for all tested ANN models, the R^2 of LM algorithm is just roughly 0.93, while this value of BR algorithm is up to more than 0.97. For the BRNN, its performance becomes stable when the number of hidden neurons increase to 8 or higher. This is due to the advantages of BR training algorithm as presented in previous sections. The BR training algorithm, therefore, was chosen to further develop the prediction model for modulus of elasticity of ASR affected concrete.

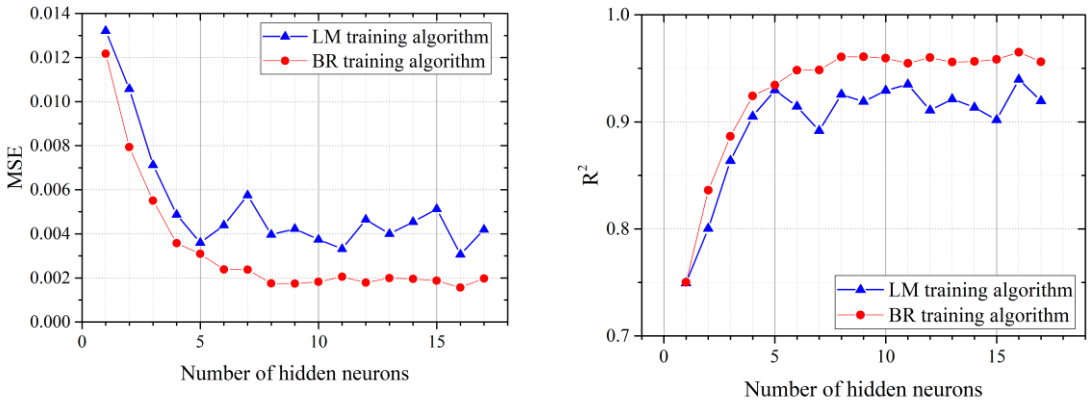

Figure 3.2: Training performance of LMNN and BRNN in term of MSE and R^2.

One important feature of the Bayesian regularization is that convergence of the optimization process to find optimal network weights and the regularization parameters are evaluated through *the effective number of parameters* (Foresee & Hagan 1997). This number also represents how effectively the networks are using network parameters (weights and biases). When the network is converged, it remains approximately the same even increasing number of network parameters. This is one of the advantages of the BRNN where the number of neurons in hidden layers is objectively optimized. Therefore, it is important to consider the effective number of parameters in optimizing the number of hidden neurons in BRNNs. Figure 3.3 presents the effective number of parameters of various BRNN models with different numbers of hidden neurons. While MSE and R^2 become stable at 8 hidden neurons, the BRNN models reach convergence at ten hidden neurons. This suggests that the optimal number of hidden neurons was determined to be 10. The ANN-based prediction model is then named as ANN 8-10-1 hereafter.

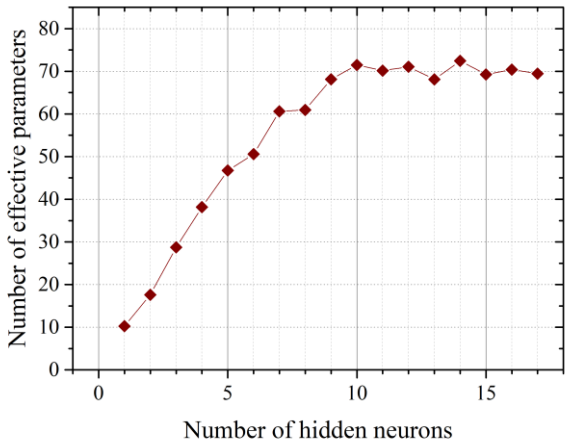

Figure 3.3: Number of effective parameters in BRNN.

Figure 3.4 shows the historical comparison between measured and predicted modulus of elasticity values from ANN 8-10-1 model for all the data samples. It is clearly seen that based on 8 input variables, the developed ANN model is able to accurately estimate the

residual modulus of elasticity. Especially, the ANN 8-10-1 model can track the change tendency of the normalised modulus of elasticity with high modelling accuracy. Figure 3.5 illustrates the correlation analysis results of the ANN 8-10-1 model for both training and testing data. If all the data points are located at the equality line, the coefficient of determination (R^2) is 1, corresponding to the best result of the prediction model. It can be seen from the figure that all the training and testing samples are uniformly distributed around the equality line, which indicates good prediction performance. The main reason contributing to this result is that the connection weights and bias of the developed ANN model are optimised during the training procedure. Consequently, the model with the best parameter values can achieve high performance in terms of predicting the modulus of elasticity of ASR-affected concrete.

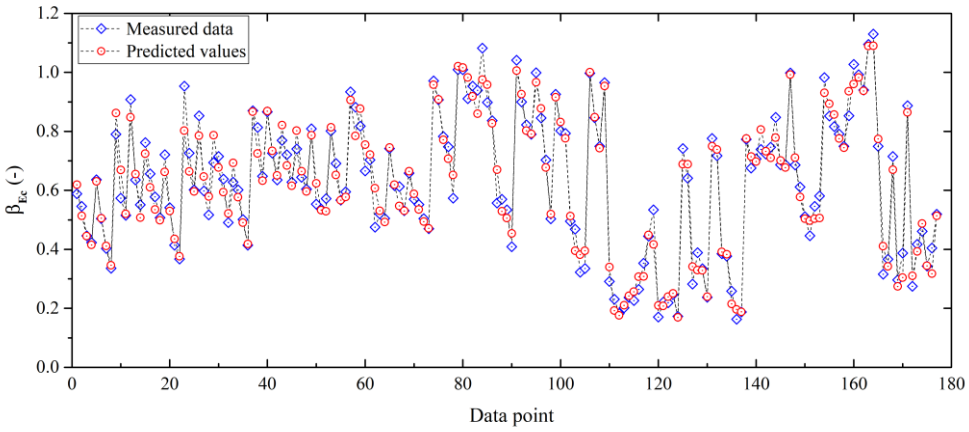

Figure 3.4: Historical comparisons of the modulus of elasticity between the measurements and predictions.

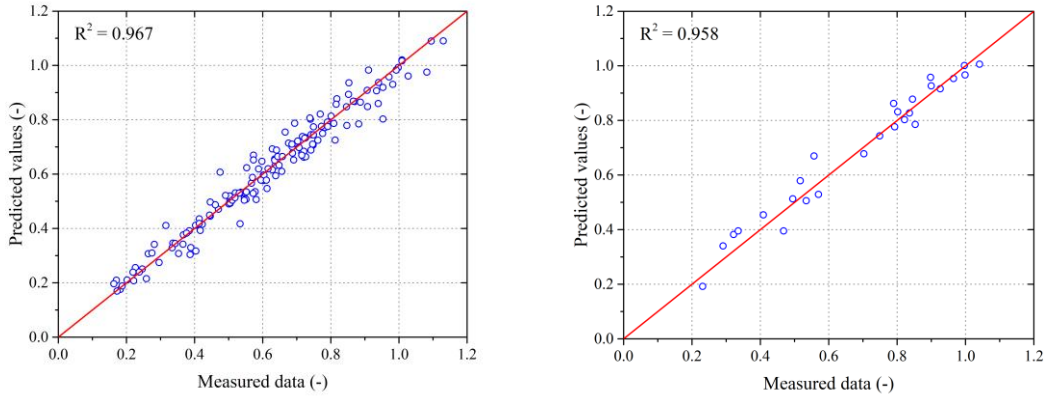

(a) Training phase (b) Testing phase

Figure 3.5: Regression analysis results of the ANN 8-10-1 model.

3.1.5.2. Comparison to empirical degradation laws

In this section, the existing empirical models (Esposito et al. 2016; Kawabata et al. 2017; Martin et al. 2017) were applied to estimate the modulus of elasticity according to the available collected experimental database. The ratio between predicted and measured modulus of elasticity change of all 177 experimental ASR affected concrete samples mentioned above are plotted with the expansion level in Figure 3.6.

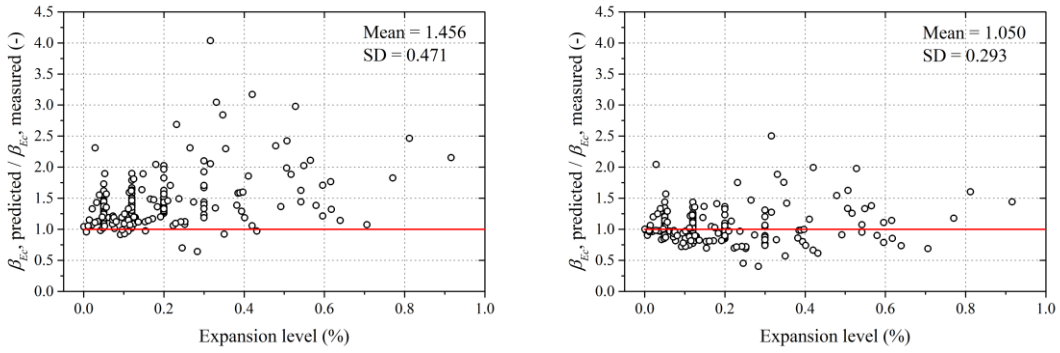

(a) Esposito et al. model (2016) (b) Kawabata et al. model (2017)

Figure 3.6: The relationship between the ratio β_{Ec}, predicted/β_{Ec}, measured and the expansion level of existing empirical models and the proposed model (SD: standard deviation).

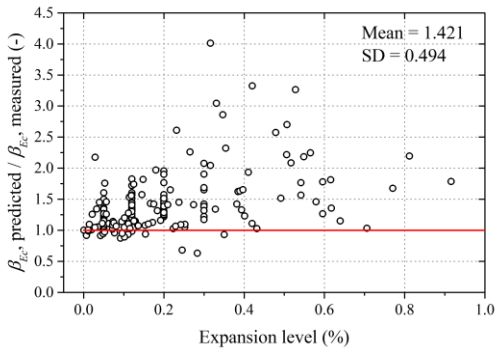

(c) Martin et al. model (2017)

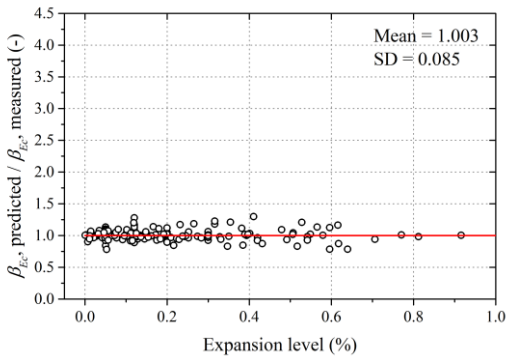

(d) The proposed model: ANN 8-10-1

Figure 3.6: Continued.

It is observed that three empirical models provide a better estimation of the modulus of elasticity reduction at low expansion level of less than 0.2%, and then increase estimation error as the expansion level increases. Furthermore, the ratio of predicted to the measured residual modulus of elasticity obtained from three empirical models vary in a wide range, as shown in Table 3.2. The proposed ANN model, however, achieves high accuracy in a large range of the expansion level where the mean and standard deviation of the ratio is just 1.003 and 0.085, respectively. In addition, the data points below the equality line in this figure mean that the predicted normalised modulus of elasticity is lower than the measured one, indicates the underestimation of the elastic modulus reduction due to ASR. In this context, it is apparent that the estimations based on regression parameters from Martin et al. (2017) and Esposito et al. (2016) are strongly conservative, where the estimated modulus of elasticity is higher than the measured values for most of the data groups, as shown in Figure 3.6 (a-b). These two empirical models give the reduction level of approximately more than 40% higher than the measured value.

In term of the mean square error (MSE) and coefficient of determination (R^2), the performances of the existing empirical models and the ANN model are shown in Figure 3.7 and Table 3.2. Lower and upper bounds, which cover 95% of all the data points, are

also plotted in Figure 3.7 to present the variation of predictive values. Among the three empirical models, the fitting curve from Kawabata et al. (2017) presents the highest accuracy, while the curve of Martin et al. (2017) is the lowest accuracy. More importantly, it is clear that the prediction performances of these empirical models are much lower than the proposed ANN model. For instance, the MSE (R^2) calculated based on the formulas from Esposito et al. (2016), Kawabata et al. (2017) and Martin et al. (2017) are $6.01e^{-2}$ (0.616), $2.04e^{-2}$ (0.617) and $5.05e^{-2}$ (0.613), respectively; while the MSE (R^2) of the model ANN 8-10-1 is $1.90e^{-3}$ (0.965**)**. It is clearly seen from Figure 3.6Error! Reference source not found. and Figure 3.7 that the estimated results from the three fitting curves are markedly scattered from the equality line. Moreover, the 95% confidence intervals of their predictive results are significantly wider than the results from the model ANN 8-10-1.

These observations prove the advantage and excellent capacity of neural networks techniques in optimisation and prediction problems. The fitting curves that are proposed to fit a certain set of data and just consider the effect of only the expansion level, thus, could not represent the reduction in modulus of elasticity due to ASR from different studies with differences in mix proportions, reactive aggregate, exposure condition and compressive strength. By taking into account the effect of different factors on the ASR in concrete, the proposed ANN approach shows excellent performance for the prediction of the reduction in concrete stiffness.

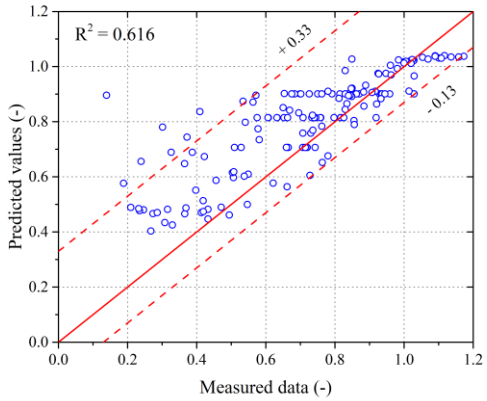

(a) Esposito et al. model (2016)

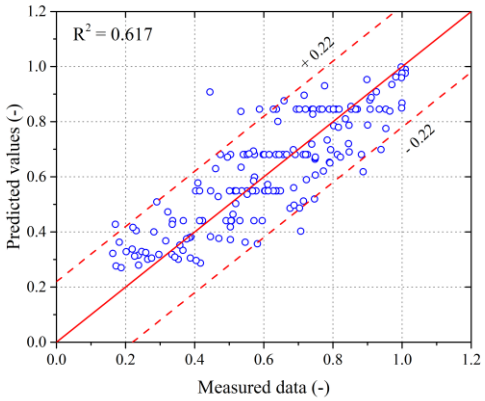

(b) Kawabata et al. model (2017)

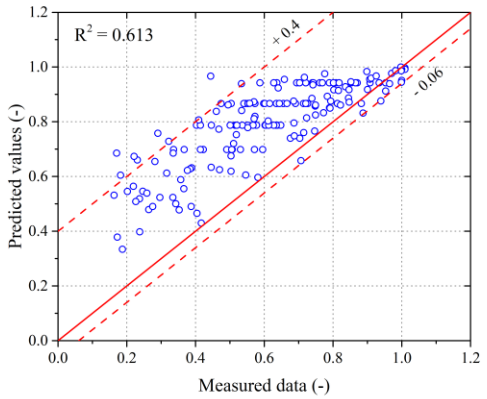

(c) Martin et al. model (2017)

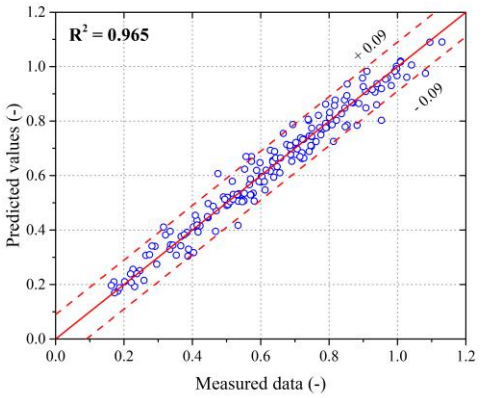

(d) The proposed model: ANN 8-10-1

Figure 3.7: Comparison of measured and predicted results of existing empirical models and the proposed model.

Table 3.2: Comparison of experimental data and calculated normalised modulus of elasticity according to different empirical models and the proposed ANN model

Model	Fitting constants	β_{Ec}, predicted/β_{Ec}, measured		Prediction performance	
		Min	Max	MSE	R^2
Esposito et al. (2016)	q_l = 1.04 m_l = -0.46 m_m = -1.89 m_h = -1.08 m_e = -0.21	0.641	4.035	0.0601	0.616

Table 3.2: Continued

Model	Fitting constants	β_{Ec}, predicted/β_{Ec}, measured		Prediction performance	
		Min	Max	MSE	R^2
Kawabata et al. (2017)	d_{max} = 0.740 ω = 470 ε_0 = 0	0.403	2.503	0.0204	0.617
Martin et al. (2017)	d_{max} = 1 ω = 120 ε_0 = 0	0.630	4.012	0.0505	0.613
ANN 8-10-1		0.781	1.297	1.90E-03	0.965

3.1.5.3. Interpretation of input variables contribution

Figure 3.8 shows the neural interpretation diagram (NID) of the model ANN 8-10-1, which represents the connection weights from input neurons to hidden neurons and hidden neurons to the output. The width of lines connecting nodes represent the absolute value of weight factors, and the colour represents polarity with red indicates the highest positive value and cyan corresponds to the highest negative value. At a glance, the NID provides a visual assessment of individual as well as the interacting impact of the model inputs. It is evident in Figure 3.8 that weights of connection between the expansion level (EXP) and the output are the most considerable, followed by MAXEXP. Other input variables also contribute at a certain level to the output; however, their relative contribution levels are difficult to be identified using the NID. Therefore, the use of connection weights approach and partial derivatives method is necessary for a quantitative quantification.

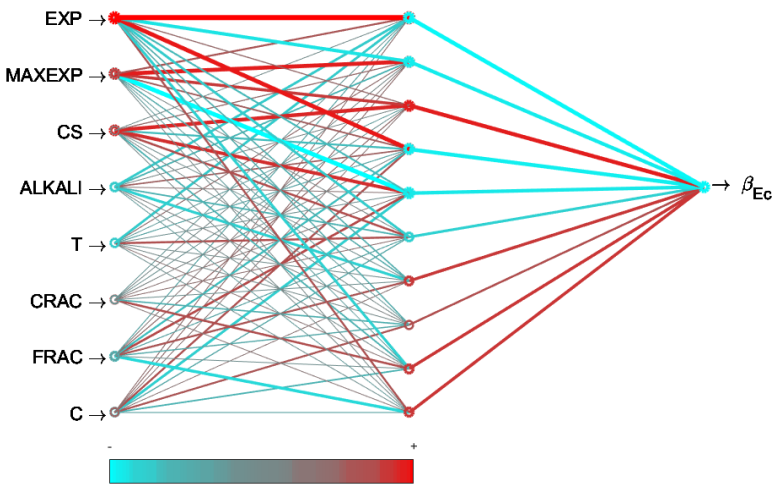

Figure 3.8: Neural interpretation diagram of the model ANN 8-10-1.

Figure 3.9 shows the results from the connection weights approach and partial derivatives method for calculating relative contributions of input variables. There is an obvious similarity in the relative importance levels between connection weights approach and partial derivatives. It is clearly seen that the impact of the expansion and maximum measured expansion on the modulus change are dominant compared to the rest. This represents the strong correlation between the expansion and modulus of elasticity change due to ASR as the common conclusion from the literature. Therefore, expansion is the only variable that has been used to estimate modulus of elasticity reduction in various empirical models in current practice. Nevertheless, it is not a comprehensive evaluation if the effects of other influencing factors are neglected. For instance, the contributions of T, ALKALI, and FRAC to the output are also significant based on the results from both the connection weights approach and partial derivatives. Other model inputs such as C, CRAC and CS also have certain impacts on the reduction in modulus of elasticity but at lower levels. Their relative important levels are different depending on the evaluation methods.

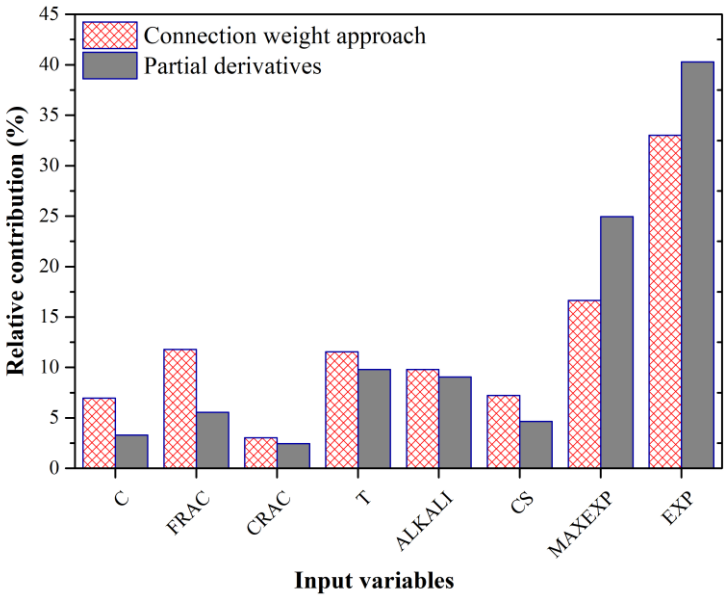

Figure 3.9: Relative contribution of input variables to the output.

3.1.6. Concluding remarks

The mechanism of ASR and its consequent effects on the modulus of elasticity are extremely complicated, yet the change in the modulus of elasticity hugely influence the structural behaviour of ASR-affected concrete structures. This poses a great challenge on the accurate determination of the residual modulus of elasticity of the ASR-affected concrete, even in the laboratory testings. Based on readily available experimental data published in the literature, this study developed an innovative approach to evaluate the modulus of elasticity of concrete affected by ASR, utilising artificial neural network (ANN). This approach takes into account not only ASR-induced expansion but also other influencing factors including the cement content, proportion of reactive fine and coarse aggregate, exposure condition, total proportion of alkali content, initial compressive strength at the undamaged condition, and maximum measured expansion. Two training algorithms, Levenberg-Marquardt (LM) and Bayesian regularization (BR), were utilised

in the learning process for a comparison and optimization study of the ANN structures. The following conclusions can be drawn:

- The prediction results from both LMNN and BRNN for the elastic modulus change due to ASR in this study agree quite well with the measured values. However, the BRNN presents a substantially better performance compared to LMNN in term of MSE and R^2 for the currently available dataset, which shows the advantages of the regularization procedure.

- The optimized ANN model has the ability to accurately evaluate the change of concrete elastic modulus due to ASR by including and weighting the contributions of various influential factors.

- In comparison to current empirical models, the ANN approach demonstrates superior performance with significantly lower mean square error and higher coefficient of determination in the prediction of the change in modulus of elasticity of concrete due to ASR. This approach thus provided a better estimation of modulus of elasticity for evaluation of ASR-damaged concrete as well as numerical modelling to assess structural behaviour. Once again, this result shows that contributions of the influencing factors have to be considered in the evaluation of elastic modulus change on ASR-affected concrete.

- Based on results from the connection weights approach and partial derivatives method, the expansion level has a major impact on the modulus of elasticity of ASR-affected concrete among the eight input variables. In addition, the maximum measured expansion, temperature, amount of alkali content and fine reactive aggregate also have significant contributions, while cement content and

proportion of reactive aggregate have less impact on the modulus of elasticity of ASR affected concrete.

The proposed approach is able to gain insight into ASR effects on the change in modulus of elasticity. However, additional experimental data on the modulus of elasticity of ASR-affected concrete is desirable to improve the model accuracy as well as to enhance the evaluation of influencing factors effects. This approach is potential for evaluation of concrete in the field, yet, it is still very challenging due to requirement of a comprehensive database have to be collected either from field testing or from actual structures suffering from ASR.

3.2. Computational homogenization approach for modulus of elasticity of ASR affected concrete

ASR is known to significantly reduce concrete stiffness, and it requires a model to quantify the stiffness loss of ASR-affected concrete. This work aims at developing a meso-scale model to provide a thorough understanding of stiffness reduction as a function of ASR-induced crack development. The crack pattern and extent based on experimental observations were explicitly and efficiently introduced into the meso-scale model using the Extended Finite Element Method. A first-order computational homogenization procedure is devised to determine the effective stiffness. The outcomes of the proposed model were compared with experimental results; its accuracy in describing ASR-distress development was evaluated.

3.2.1. Introduction

Several approaches, recommendations, and test procedures, have been developed to assess the potential alkali-reactivity of concrete aggregates and the efficiency of

preventive measures (e.g. control of the cement & concrete alkali content, use of supplementary cementing materials (SCMs), use of lithium based admixtures, etc.) before their use in the field (Fournier & Bérubé 2000; Sanchez 2014; Thomas, Fournier & Folliard 2008). Despite a few issues with some of these test procedures and the constant need of improvement in the different standards/protocols, the majority of experts agree that in general, it is now possible to build new concrete infrastructure with limited risk of ASR. However, there is currently no consensus about the most efficient method(s) that should be implemented, and when, for the rehabilitation of ASR-affected concrete infrastructure (Folliard et al. 2006; Fournier & Bérubé 2000; HB79 2015). In this context, numerical models might be necessary, enabling further analysis of ASR structural implications and ensuring a better decision making. Winnicki & Pietruszczak (2008), Saouma (2014), Erkmen, Gowripalan & Sirivivatnanon (2017) and Gorga, Sanchez & Martín-Pérez (2018) employed phenomenological elasto-plastic and damage models to consider ASR effect on structural behaviour by degrading concrete properties. However, to fully understand ASR-induced expansion and damage development, its distress mechanism needs to be identified. Reinhardt & Mielich (2011) proposed two different mechanisms for ASR damage in concrete: (1) ASR gel formation at the aggregate particles/interfacial transition zone (ITZ), thus inducing swelling and cracking in the cement paste; and (2) cracks generation within the aggregate particles due to gel pockets formation, which propagates to the cement paste as the expansion level increases. The former mechanism has been adopted in several ASR numerical models such as in Multon, Sellier & Cyr (2009), Poyet et al. (2007), Puatatsananon & Saouma (2013); yet, other researchers, such as Dunant & Scrivener (2010) claimed the former approach to be incomplete and adopted the latter mechanism for numerical simulations.

The development of cracks within the aggregate particles at the early stages of the chemical reaction has been confirmed by a series of microscopic analyses from Sanchez et al. (2016) and Sanchez et al. (2015). Sanchez et al. (2016) evaluated a wide number of concrete mixtures incorporating over ten distinct reactive aggregate particles through the *Damage Rating Index (DRI)* method. The DRI is a petrographic protocol performed with the use of a stereomicroscope (approximately 15-16x magnification) where damage features generally associated with ASR are counted through a 1 cm^2 (0.155 in^2) grid drawn on the surface of polished concrete sections (Sanchez et al. 2016).

Several studies developed meso-scale models to capture the distress and damage development mechanisms due to ASR, i.e., Dunant & Scrivener (2010), Comby-Peyrot et al. (2009), Iskhakov, Timothy & Meschke (2019), and Rezakhani, Alnaggar & Cusatis (2019). Meso-scale models generally introduce the aggregates and the cement paste explicitly; thus, concrete is modelled as a heterogeneous material with the aim of better understanding the effects of composite interactions and local damage mechanisms. Based on experimental observations, Sanchez et al. (2015) proposed a qualitative description of ASR induced crack generation and propagation as a function of its induced expansion development. A meso-scale computational model is required for the concrete material to adopt the model developed by Sanchez et al. (2015).

3.2.2. Computational homogenization approach

3.2.2.1. Equilibrium of a deformable body

The stress field is assumed continuous (before discretization), however, the displacement field is discontinuous between the interfaces. Let σ_{ij} denote the stress tensor and u_i be

the displacement vector field, $\{u_i\} = \langle u_1\ u_2\rangle^T = \boldsymbol{u}$. The stress tensor is related to the displacement gradient through the constitutive relation, i.e.,

$$\sigma_{ij} = D_{ijkl}\frac{\partial u_k}{\partial x_l} \tag{3. 14}$$

where components of the stiffness matrix D_{ijkl} , in general, are functions of the location vector $\{u_i\} = \langle u_1\ u_2\rangle^T = \boldsymbol{u}$ in a heterogeneous continuum. We limit our analysis to 2D problems, therefore, all indices *i*, *j*, *k* and *l* vary between 1 and 2 throughout the manuscript and thus, the stiffness matrix for the bulk of the continuum generally has six independent components considering the symmetry of the shear stresses $\sigma_{12} = \sigma_{21}$, i.e.,

$$D = [D_{ij}] = \begin{bmatrix} D_{1111} & D_{1122} & D_{1112} \\ D_{1122} & D_{2222} & D_{2212} \\ D_{1112} & D_{2212} & D_{1212} \end{bmatrix} \tag{3. 15}$$

The equilibrium equations can be written as

$$\frac{\partial \sigma_{ij}}{\partial x_j} + p_i = 0 \qquad \text{in} \qquad \Omega \tag{3. 16}$$

$$u_i = r_i \qquad \text{in} \qquad \Gamma_D \tag{3. 17}$$

$$\sigma_{ji} n_i = -s_j \qquad \text{in} \qquad \Gamma_N \tag{3. 18}$$

where Ω, Γ and Γ_N are the analysis domain, Dirichlet and Neumann boundaries respectively, and n_i is the normal vector component to the boundary surface. Dirichlet and Neumann boundaries are non-overlapping and decompose the whole external boundary, i.e., $\partial\Omega = \Gamma$ where $\Gamma = \Gamma_D \cup \Gamma_N$ and $\Gamma_D \cap \Gamma_N = \emptyset$. The body force per unit volume in the analysis domain is denoted with p_i, the specified displacement at the Dirichlet boundary is r_i and the specified traction at the Neumann boundary is s_i. The

Galerkin weak form of the above governing equations from Eqs. (3.16) to (3.18) can be expressed after integration by parts as

$$\int_{\Omega} \delta \frac{\partial u_j}{\partial x_i} \sigma_{ij} d\Omega + \int_{\Omega} \partial u_i p_i d\Omega + \int_{\Gamma_N} \partial u_i s_i d\Gamma = 0 \qquad (3.19)$$

where the admissible displacement field u_i is prescribed at the boundary Γ_D as in Eq. (3.17) and therefore, its variation vanishes, i.e., $\partial u_i = 0$ in Γ_D.

3.2.2.2. Homogenization

Separation of scales and first-order homogenization: In the description of our problem, the assumption is that the heterogeneous medium has rapidly oscillating properties and the sizes of the heterogeneities are small compared to the overall size of the medium. Our aim is to compute the macro stiffness properties from the known meso-scale properties which represent an average and thus, the small-scale variations will not be present in the homogenized problem, i.e.,

$$\widehat{D}_{ijkl} \frac{\partial^2 \bar{u}_i}{\partial x_j \partial x_k} = -p_l \qquad \text{in} \qquad \Omega \qquad (3.20)$$

where $\widehat{D}_{ijkl}$ are the components effective stiffness matrix after homogenization. In order to capture the meso-scale influence on the effective stiffness, a scaling parameter $\eta \to 1$ is introduced which represents the ratio between the size of the meso-scale structure and the macro-structure and thus, the stiffness is assumed to be varying based on this small parameter (Holmes 2013). Analytically, the homogenized stiffness $\widehat{D}_{ijkl}$ is defined as the case when $\eta \to 0$. Therefore, the size of the heterogeneity is introduced as a variable to be able to describe the homogenous case as a special case, as shown in Figure 3.10.

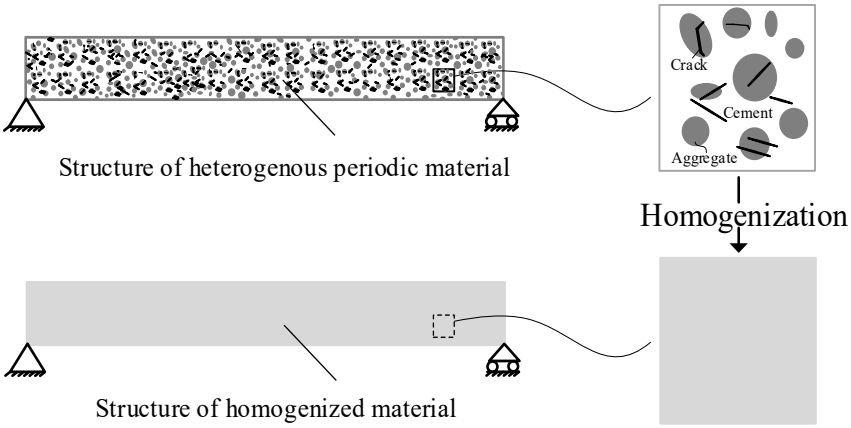

Figure 3.10: Schematic description of two-scale modelling based on homogenized material.

The displacement field $\bar{u}_i$ in Eq. (3.20) is called the first approximate solution. The idea is to approximate the solution of the heterogeneous problem by using the solution of a simpler problem, which is the homogenous problem. Thus, $\bar{u}_i$ refers to the solution of a simpler homogenized problem and the complete displacement field $\bar{u}_i$ is represented in the form of asymptotic expansion as

$$u_i(\mathbf{x},\mathbf{y}) = \bar{u}_i(\mathbf{x},\mathbf{y}) + \eta\bar{\bar{u}}_i(\mathbf{x},\mathbf{y}) + \eta^2\bar{\bar{\bar{u}}}_i(\mathbf{x},\mathbf{y}) + \cdots \quad (3.21)$$

The oscillatory behaviour is due to heterogeneity and therefore, meso-scale oscillations are due to the higher-order contributions, i.e., $\bar{\bar{u}}_i$, $\bar{\bar{\bar{u}}}_i$,…. Due to different orders of η, that form of approximation in Eq. (3.21) introduces a hierarchy between the contributions of each term in the series. In order to make the position vector x_i independent of the scaling parameter η and thus, to construct globally valid solutions for a variable η, two spatial scales are incorporated into the problem. This allows x_i always refer to the same material point as η changes and the position vector x_i now has the meaning of the slow scale or the macro-scale coordinate, measuring variations within the global region of interest only.

Therefore, in Eq. (3.21) there is another vector $y_i = x_i/\eta$ which is the fast coordinate, measuring variations within one period cell. As a result, the derivative operations transform into (Nielsen, Gottfredsen & Thøgersen 1993)

$$\frac{\partial}{\partial x_i} \to \frac{\partial}{\partial x_i} + \frac{1}{\eta}\frac{\partial}{\partial y_i} \tag{3. 22}$$

Thus, the analysis domain of the problem is extended as $\Omega^\eta = \Omega \times \eta \mathrm{Y}$, where Y denotes the domain of one cell that periodically repeats. In this case, Eq. (3.16) takes the form

$$\frac{\partial \sigma_{ij}(\mathbf{x},\mathbf{y})}{\partial x_j} + \frac{1}{\eta}\frac{\partial \sigma_{ij}(\mathbf{x},\mathbf{y})}{\partial y_j} = -p_i(\mathbf{x}) \tag{3. 23}$$

Where the asymptotic expansion of the stress tensor can be written as

$$\sigma_{ij}(\mathbf{x},\mathbf{y}) = \breve{\sigma}_{ij}(\mathbf{x},\mathbf{y}) + \eta\tilde{\tilde{\sigma}}_{ij}(\mathbf{x},\mathbf{y}) + \eta^2\tilde{\tilde{\tilde{\sigma}}}_{ij}(\mathbf{x},\mathbf{y}) + \ldots \tag{3. 24}$$

By substituting Eq. (3.21) into Eq. (3.14) and using derivative transform in Eq. (3.22), one obtains

$$\breve{\sigma}_{ij}(\mathbf{x},\mathbf{y}) = D_{ijkl}(\mathbf{x},\mathbf{y})\left(\frac{\partial \bar{u}_k(\mathbf{x})}{\partial y_l}\right) \tag{3. 25}$$

$$\tilde{\sigma}_{ij}(\mathbf{x},\mathbf{y}) = D_{ijkl}(\mathbf{x},\mathbf{y})\left(\frac{\partial \bar{u}_k(\mathbf{x})}{\partial x_l} + \frac{\partial \bar{\bar{u}}_k(\mathbf{x},\mathbf{y})}{\partial y_l}\right) = \bar{\sigma}_{ij}(\mathbf{x},\mathbf{y}) + \bar{\bar{\sigma}}_{ij}(\mathbf{x},\mathbf{y}) \tag{3. 26}$$

$$\tilde{\tilde{\sigma}}_{ij}(\mathbf{x},\mathbf{y}) = D_{ijkl}(\mathbf{x},\mathbf{y})\left(\frac{\partial \bar{\bar{u}}_k(\mathbf{x},\mathbf{y})}{\partial x_l} + \frac{\partial \bar{\bar{\bar{u}}}_k(\mathbf{x},\mathbf{y})}{\partial y_l}\right) \tag{3. 27}$$

Because of the fact that the series in Eq. (3.24) does not contain the term $\eta^{-1}\bar{\sigma}_{ij}(\mathbf{x},\mathbf{y})$, Eq. (3.25) should vanish. This is because η^{-1} is not bounded as $\eta \to 0$ which is contrary to the periodicity assumption for $\sigma_{ij}(\mathbf{x},\mathbf{y})$. Thus, from Eq. (3.25) it can be concluded that

$\bar{u}_i$ cannot depend on the fast coordinate **y**, i.e., $\bar{u}_i = \bar{u}_i(\mathbf{x})$. In the following analysis, only the first non-vanishing stress term is used, i.e., $\sigma_{ij}(\mathbf{x},\mathbf{y}) = \tilde{\sigma}_{ij}(\mathbf{x},\mathbf{y})$ and consequently, the terms higher than first order in the displacement ansatz are neglected, i.e., $\tilde{\tilde{\sigma}}_{ij}(\mathbf{x},\mathbf{y}) = 0$ and $u_i(\mathbf{x},\mathbf{y}) = \bar{u}_i(\mathbf{x}) + \eta\bar{\bar{u}}_i(\mathbf{x},\mathbf{y})$. Note that $\bar{\bar{u}}_i(\mathbf{x},\mathbf{y})$ is a periodic function in Y, i.e. $\bar{\bar{u}}_i(\mathbf{x},\mathbf{y}) = \bar{\bar{u}}_i(\mathbf{x},\mathbf{y}+\mathbf{Y})$, where **Y** is the period in fast coordinate. By substituting Eq. (3.26) into Eq. (3.23) and grouping the terms according to their order, i.e., $O(1)$ and $O(1/\eta)$ one obtains

$$\frac{\partial \tilde{\sigma}_{ij}(\mathbf{x},\mathbf{y})}{\partial x_j} + p_i(\mathbf{x}) = 0 \qquad \text{in} \qquad \Omega \qquad (3.28)$$

$$\frac{\partial \tilde{\sigma}_{ij}(\mathbf{x},\mathbf{y})}{\partial y_j} = 0 \qquad \text{in} \qquad \mathrm{Y} \qquad (3.29)$$

Variational setting for homogenization: By integrating the balance in Eq. (3.28) over a domain of one cell and using the variation of the first approximate displacement field $\delta\bar{u}_i$, after integration by parts the weak form of the equilibrium equation can be obtained as

$$\int_\Omega \delta\frac{\partial \bar{u}_j}{\partial x_i}\hat{\sigma}_{ij}\,\mathrm{d}\Omega + \int_\Omega \delta\bar{u}_i\, p_i\,\mathrm{d}\Omega + \int_{\Gamma_N} \delta\bar{u}_i\, s_i\,\mathrm{d}\Gamma = 0 \qquad (3.30)$$

where $\hat{\sigma}_{ij}$ is the effective stress tensor and determined by averaging the stress tensor over one cell, i.e.

$$\hat{\sigma}_{ij} = |\mathrm{Y}|^{-1}\int_{\mathrm{Y}} \sigma_{ij}(\mathbf{x},\mathbf{y})\mathrm{dY} = |\mathrm{Y}|^{-1}\int_{\mathrm{Y}} \left[\bar{\sigma}_{ij}(\mathbf{x},\mathbf{y}) + \bar{\bar{\sigma}}_{ij}(\mathbf{x},\mathbf{y})\right]\mathrm{dY} \qquad (3.31)$$

where $|\mathrm{Y}| = \int_{\mathrm{Y}} \mathrm{dY}$ is the area of the cell (i.e. volume for unit thickness). In obtaining Eq. (3.30), it has been assumed that the source terms p_i and s_i are independent of the fast

coordinate y_i . For the solution of the global equilibrium problem in Eq. (3.30), the whole stress tensor σ_{ij} needs to be expressed in terms of the average displacement gradient $\partial \overline{u}_i / \partial x_j$. For that purpose, Eq. (3.29) is used in the weak form by multiplying with the virtual displacement fluctuations $\delta \overline{\overline{u}}_i$ and integrating over a domain of one cell **Y**. After integration by parts with respect to fast coordinate y_i , one obtains

$$\int_{\mathrm{Y}} \delta \frac{\partial \overline{\overline{u}}_j}{\partial y_i} \sigma_{ij} \mathrm{dY} - \int_{\Psi} \delta \overline{\overline{u}}_j \sigma_{ji} n_i \mathrm{d}\Psi = 0 \qquad (3.32)$$

where $\Psi = \partial \mathrm{Y}$ is the boundary of the cell and Ψ represents the fast coordinate on the cell boundary. Eq. (3.32) is the Hill-Mandel condition for scale separation, which allows decoupling of the analysis of a heterogeneous material into analyses at the local and global levels. Thus, the solution of Eq. (3.32) builds the relationship between the gradients of the average displacement and the stress in one cell Y. Under the assumption of $\eta \to 0$, by using Eq. (3.32), the weak form over the whole domain in Eq. (3.19) can be replaced with Eq. (3.30) for the global analysis. Thus, the heterogeneous domain can be replaced by the equivalent homogenous material having calculated the effective properties at the local level. Despite the fact that $\overline{\overline{u}}_i(\mathbf{x},\mathbf{y})$ is a periodic function, i.e., $\int_{\mathrm{Y}} \frac{\partial \overline{\overline{u}}_i(\mathbf{x},\mathbf{y})}{\partial y_j} \mathrm{dY} = \mathbf{0}$, the integral of the stress component $\overline{\overline{\sigma}}_{ij}$ generally does not vanish in Y, i.e., $\int_{\mathrm{Y}} \overline{\overline{\sigma}}_{ij}(\mathbf{x},\mathbf{y}) \mathrm{dY} = \int_{\mathrm{Y}} D_{ijkl}(\mathbf{x},\mathbf{y}) \frac{\partial \overline{\overline{u}}_k(\mathbf{x},\mathbf{y})}{\partial y_l} \mathrm{dY} \neq \mathbf{0}$ thus, the two-scale analysis introduces the effect of fluctuations due to heterogeneity in the global analysis.

RVE Boundary Value Problem: In order to solve the cell problem in Eq. (3.32), a Representative Volume Element (RVE) needs to be introduced. The RVE is defined as the smallest micro-structural volume that sufficiently accurately represents the overall

macroscopic stiffness properties of interest. Thus, the size of the RVE should be selected large enough to be statistically representative of the distributions of the inclusions. Because of the finite size of the RVE, i.e., $\eta \neq 0$, homogenization is approximate unless exact RVE boundary conditions are imposed. Since exact boundary conditions are not known *a-priori* a chosen RVE is generally analysed using either uniform gradient, uniform traction or periodic boundary conditions. Therefore, the information on the cell boundary is lost due to Hill-Mandel condition for scale separation as there might be many candidates for $\eta\bar{\bar{u}}_i$ that satisfy Eq. (3.32). In other words, there is a micro-scale effect due to micro-fluctuations at the boundary of a finite size RVE that is not resolved in the two-scale analysis. The assumed micro-scale field existing at the RVE boundary influences the effective modulus by influencing the effective stress field, e.g. in Kanit et al. (2003). We assume that the aggregate and ASR induced crack distributions are such that the whole structure consists of spatially repeated cells as indicated in Figure 3.10. Therefore, Periodic Boundary Conditions are assumed herein and its implementation is discussed in the next section. Finite size RVE volume and boundary surface are denoted as V_{RVE} and S_{RVE}, respectively and thus, $\lim_{|V_{RVE}|\to 0} V_{RVE} = \mathrm{Y}$ and $\lim_{|V_{RVE}|\to 0} S_{RVE} = \Psi$. In first-order homogenization, the displacement at the RVE boundary i.e., at $\boldsymbol{\psi} \in S_{RVE}$ can be imposed as

$$\mathbf{u}(\boldsymbol{\psi}) = \bar{\mathbf{u}}(\bar{\mathbf{y}}) + \left(\boldsymbol{\psi} - \bar{\mathbf{y}}\right)\cdot\mathbf{g} + \mathbf{u}'(\boldsymbol{\psi}) \tag{3. 33}$$

where $\bar{\mathbf{y}} = \left|V_{RVE}\right|^{-1} \int_{V_{RVE}} \mathbf{y}\,\mathrm{dY}$ refers to the centre of the RVE, $\mathbf{g}$ is the specified average displacement gradient field obtained from the global problem in Eq. (3.30) i.e., $\mathbf{g}=\nabla_{\mathbf{x}}\otimes\bar{\mathbf{u}}$, and $\lim_{|V_{RVE}|\to 0} \mathbf{u}'\left(\boldsymbol{\psi}\right) = \eta\bar{\bar{\mathbf{u}}}\left(\boldsymbol{\psi}\right)$ is the contribution of the meso-scale fluctuations at the

boundary which is generally unknown. It should be noted that for convenience and without losing generality, for the purpose of determining the local stress field, the origin of the RVE coordinates can be taken at $\bar{\mathbf{y}}$, i.e., $\bar{\mathbf{y}}=0$ and the average displacement can be assumed zero, i.e., $\bar{\mathbf{u}}(\bar{\mathbf{y}})=0$.

By considering that the forcing term for the deformation of the RVE is the constant average displacement gradient one obtains

$$\int_{S_{RVE}} \mathbf{u} \otimes \mathbf{n} \mathrm{d}\Psi = \mathbf{g} \int_{V_{RVE}} \mathrm{dY} \tag{3. 34}$$

By introducing $\delta\boldsymbol{\sigma}$ as the weighting function in the weak form of Eq. (3.34), one obtains the RVE problem similar to the general form introduced in Miehe & Koch (2002) based on the Lagrange multiplier technique Belytschko et al. (2014), i.e.

$$\int_{V_{RVE}} \nabla_{\mathrm{y}} \otimes \delta\bar{\bar{\mathbf{u}}} : \boldsymbol{\sigma} \, \mathrm{dY} - \int_{S_{RVE}} \delta\bar{\bar{\mathbf{u}}} \cdot \boldsymbol{\lambda} \mathrm{d}\Psi - \int_{S_{RVE}} \delta\boldsymbol{\lambda} \cdot (\mathbf{u} - \boldsymbol{\psi} \cdot \mathbf{g}) \mathrm{d}\Psi = 0 \tag{3. 35}$$

where $\int_{V_{RVE}} \mathrm{dY} = \int_{S_{RVE}} \boldsymbol{\psi} \cdot \mathbf{n} \mathrm{d}\Psi$ has been used and $\boldsymbol{\lambda} = \mathbf{n} \cdot \boldsymbol{\sigma}$ is the Lagrange multiplier vector which constraints the average displacement in the RVE based on the specified average displacement gradient field $\mathbf{g}$. Thus, each of the two components of $\boldsymbol{\lambda}$ can be identified as the total tractions at the boundary points $\boldsymbol{\psi} \in S_{RVE}$. Eq. (3.35) can be solved to determine the whole stress field $\boldsymbol{\sigma}$ in terms of the average displacement gradient $\mathbf{g}$. From the solution of Eq. (3.35) and by using Eq. (3.31), one obtains the relationship

$$\hat{\boldsymbol{\sigma}} = \hat{\mathbf{D}} : \mathbf{g} \tag{3. 36}$$

where $\hat{\mathbf{D}}$ is the effective stiffness matrix to be used for the global solution in Eq. (3.30).

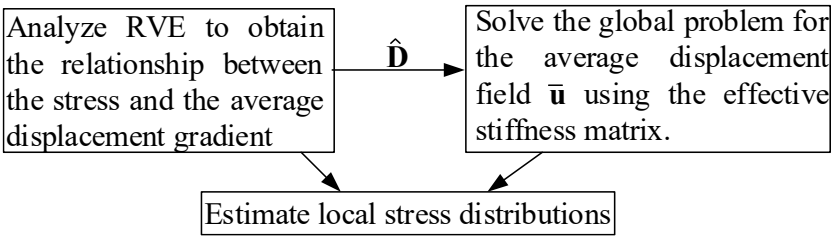

Figure 3.11: Schematic outline for the two-scale analysis procedure.

The schematic outline in Figure 3.11 describes the multi-scale analysis procedure based on the idea of separation of scales. Once the boundary conditions are chosen, equations can be solved to calculate the local RVE stress tensor σ_{ij} . Accordingly, the effective stress tensor $\hat{\sigma}_{ij}$ can be calculated by using the local stress tensor σ_{ij} in Eq. (3.31). Three cases of displacement gradient need to be introduced to determine all components of the stiffness matrix through the displacement gradient and stress relationship, i.e.

$$\begin{bmatrix} \hat{\sigma}_{11}^{1} & \hat{\sigma}_{11}^{2} & \hat{\sigma}_{11}^{3} \\ \hat{\sigma}_{22} & \hat{\sigma}_{22}^{2} & \hat{\sigma}_{22}^{3} \\ \hat{\sigma}_{12} & \hat{\sigma}_{12}^{2} & \hat{\sigma}_{12}^{3} \end{bmatrix} = \begin{bmatrix} \hat{D}_{1111} & \hat{D}_{1122} & \hat{D}_{1112} \\ \hat{D}_{1122} & \hat{D}_{2222} & \hat{D}_{2212} \\ \hat{D}_{1112} & \hat{D}_{2212} & \hat{D}_{1212} \end{bmatrix} \begin{bmatrix} \overset{\text{Case1}}{1} & \overset{\text{Case2}}{0} & \overset{\text{Case3}}{0} \\ 0 & 1 & 0 \\ 0 & 0 & 1 \end{bmatrix} \tag{3.37}$$

It should be noted that the resulting stiffness matrix is symmetrical.

3.2.2.3. Numerical implementation

Implementation of the RVE boundary conditions: The numerical solution procedure can be developed by selecting the displacement field $\mathbf{u}$ in the form of

$$\mathbf{u} = \mathbf{A}\mathbf{a} \tag{3.38}$$

and the Lagrange multiplier field $\boldsymbol{\lambda}$ in the form of

$$\boldsymbol{\lambda} = \mathbf{G}\mathbf{h} \tag{3.39}$$

where $\mathbf{A}$ and $\mathbf{G}$ are the matrices of selected approximation functions for $\mathbf{u}$ and $\boldsymbol{\lambda}$, respectively. In Eqs. (3.38) and (3.39), $\mathbf{a}$ and $\mathbf{h}$ are the vectors of unknown parameters after discretization. It should be noted that for numerical implementation the rest of the equations refer to the algebraic forms after discretisation, thus matrices and vectors appear side by side are multiplied by dot product. By substituting Eqs. (3.38) and (3.39) into Eq. (3.35) one obtains the algebraic form of the RVE problem as

$$\begin{bmatrix} \mathbf{K} & \mathbf{S}^{\mathrm{T}} \\ \mathbf{S} & 0 \end{bmatrix} \begin{Bmatrix} \mathbf{a} \\ \mathbf{h} \end{Bmatrix} = \begin{Bmatrix} \mathbf{0} \\ \boldsymbol{\Theta}\mathbf{g} \end{Bmatrix} \tag{3. 40}$$

where $\mathbf{K}$, $\mathbf{L}$ and $\boldsymbol{\Theta}$ can be identified as $\mathbf{K} = \int_{V_{RVE}} \frac{\partial \mathbf{A}}{\partial \mathbf{y}}^{\mathrm{T}} \mathbf{D} \frac{\partial \mathbf{A}}{\partial \mathbf{y}} \mathrm{dY}$, $\mathbf{S} = \int_{S_{RVE}} \mathbf{G}^{\mathrm{T}} \mathbf{A} \mathrm{d}\Psi$ and $\boldsymbol{\Theta} = \int_{S_{RVE}} \mathbf{G}^{\mathrm{T}} \boldsymbol{\psi}^{\mathrm{T}} \mathrm{d}\Psi$. In Eq. (3.40), the stress for the heterogeneous RVE domain is obtained according to Eq. (3.14), i.e., $\boldsymbol{\sigma} = -\mathbf{D} \frac{\partial \mathbf{A}}{\partial \mathbf{y}} \mathbf{a}$ and it was considered that in the RVE problem $\bar{\mathbf{u}}$ is specified, i.e., $\delta \mathbf{u} = \eta \delta \bar{\bar{\mathbf{u}}}$. From the general algebraic form of the RVE problem in Eq. (3.40) one obtains the following cases by imposing constraints on the Lagrange multiplier $\boldsymbol{\lambda}$ and/or the displacement $\mathbf{u}$ at the boundary S_{RVE}. The interior points of the RVE are located at $\mathbf{y} \in \overline{V}_{RVE} - S_{RVE}$, i.e., $\left\{ \mathbf{y} : \mathbf{y} \in \overline{V}_{RVE} \text{ and } \mathbf{y} \notin S_{RVE} \right\}$, where $\overline{V}_{RVE}$ is the closure of the RVE domain. On the other hand, for the purpose of imposing constraints, the boundary is decomposed into two parts, i.e., $S_{RVE} = S_{RVE}^{+} \cup S_{RVE}^{-}$ with outward normal $\mathbf{n}^{+} = -\mathbf{n}^{-}$ at associated points $\boldsymbol{\psi}^{+} \in S_{RVE}^{+}$ and $\boldsymbol{\psi}^{-} \in S_{RVE}^{-}$, respectively (see Figure 3.12(a)). Every point on the boundary is paired with its image on the other side of the boundary. This pairing is done in a standard manner, e.g. in Larsson et al. (2011). Thus, a point $\boldsymbol{\psi}^{+} \in S_{RVE}^{+}$ on the right boundary finds its image $\boldsymbol{\psi}^{-} \in S_{RVE}^{-}$ at the left boundary

with the same y_2 coordinate. Similarly, a point $\boldsymbol{\psi}^+ \in S_{RVE}{}^+$ on the top boundary finds its image $\boldsymbol{\psi}^- \in S_{RVE}{}^-$ at the bottom boundary with the same y_1 coordinate as shown in Figure 3.12(a). Note that corner points have two images, i.e., in both horizontal and vertical directions.

The **K** and **S** matrices and the vector of nodal displacements **a** can be partitioned considering the interior and boundary nodes, as a result of which from Eq. (3.40) one obtains

$$\mathbf{Ka} = \begin{bmatrix} \mathbf{K}_{II} & \mathbf{K}_{IB} \\ \mathbf{K}_{IB}{}^{\mathrm{T}} & \mathbf{K}_{BB} \end{bmatrix} \begin{Bmatrix} \mathbf{a}_I \\ \mathbf{a}_B \end{Bmatrix} \tag{3. 41}$$

and

$$\mathbf{Sa} = \begin{bmatrix} \mathbf{S}_I & \mathbf{S}_B \end{bmatrix} \begin{Bmatrix} \mathbf{a}_I \\ \mathbf{a}_B \end{Bmatrix} \tag{3. 42}$$

where subscript *B* refers to the boundary nodes and *I* refers to the internal nodes. Figure 3.12(b) shows the boundary nodes and the interior nodes separately in order to explain the implementation of the boundary constraint conditions explicitly. Note that as $\mathbf{S}$ is only defined through the boundary integral, $\mathbf{S}_I$ naturally vanishes at the internal nodes since $\mathbf{G} = \mathbf{0}$ at $\mathbf{y} \in \overline{V}_{RVE} - S_{RVE}$.

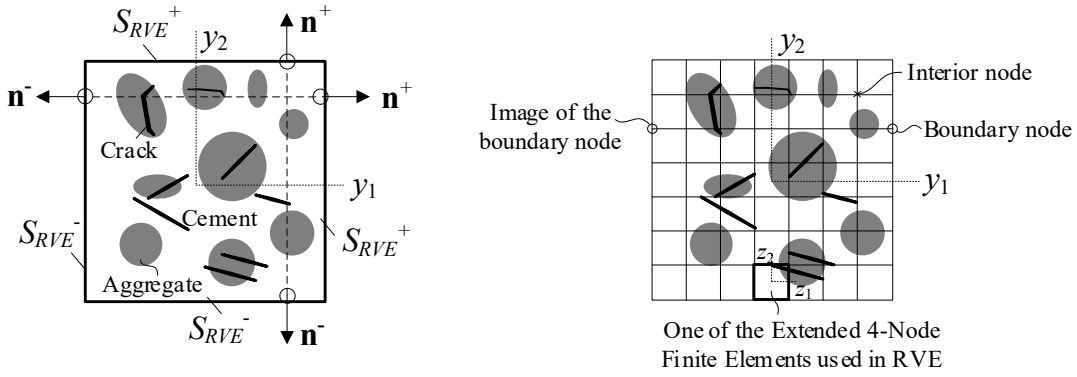

a) Schematic picture b) Mesh for the numerical solution

Figure 3.12: RVE of cracked concrete

Periodic displacement RVE boundary conditions: The fine scale fluctuations of the displacement field at the boundary does not vanish, i.e., $\mathbf{u}'(\boldsymbol{\psi}) \neq 0$, however, it is assumed that due to periodicity the boundary fluctuations on $\boldsymbol{\psi}^{+} \in S_{RVE}^{+}$ are same on the opposite side $\boldsymbol{\psi}^{-} \in S_{RVE}^{-}$. Thus, considering that $\mathbf{u}'(\boldsymbol{\psi}^{+}) - \mathbf{u}'(\boldsymbol{\psi}^{-}) = 0$, the constraint for the periodicity condition can be introduced in the form of

$$\mathbf{u}(\boldsymbol{\psi}_k^{+}) - \mathbf{u}(\boldsymbol{\psi}_k^{-}) = \left(\boldsymbol{\psi}_k^{+} - \boldsymbol{\psi}_k^{-}\right)^{\mathrm{T}} \mathbf{g}, \tag{3. 43}$$

where subscript *k* refers to the node number on the boundary. Note that the total boundary traction is anti-period i.e.

$$\boldsymbol{\lambda}^{+} = -\boldsymbol{\lambda}^{-} \tag{3. 44}$$

where $\boldsymbol{\lambda}^{+}$ and $\boldsymbol{\lambda}^{-}$ act on the nodes at $\boldsymbol{\psi}^{+} \in S_{RVE}^{+}$ and $\boldsymbol{\psi}^{-} \in S_{RVE}^{-}$, respectively. Using anti-periodicity of the traction, at the boundary nodes the stress can be expressed with reduced number of degrees of freedom using the **w** vector as

$$\mathbf{h} = \mathbf{P}^{\mathrm{T}} \mathbf{w}, \tag{3. 45}$$

where

$$\mathbf{P}=\begin{bmatrix} 1 & 0 & \cdots & 0 & \cdots & -1 & 0 & 0 & \cdots & 0 \\ 0 & 1 & \cdots & 0 & \cdots & 0 & -1 & 0 & \cdots & 0 \\ \vdots & \vdots & \ddots & & \ddots & \vdots & \vdots & \vdots & \ddots & \\ 0 & 0 & \cdots & 1 & \cdots & 0 & 0 & 0 & \cdots & -1 \end{bmatrix} \quad \text{(image)} \tag{3.46}$$

Note that in each row of **P** there are only two non-zero values which correspond to nodes that are images of each other. By substituting Eqs. (3.43) and (3.45) into Eq. (3.40) and using Eqs. (3.41) and (3.42) one obtains the solution of the RVE problem from the below algebraic equations as

$$\begin{bmatrix} \mathbf{K}_{II} & \mathbf{K}_{IB} & \mathbf{0} \\ \mathbf{K}_{IB}^{\mathrm{T}} & \mathbf{K}_{BB} & \mathbf{S}_B^{\mathrm{T}}\mathbf{P}^{\mathrm{T}} \\ \mathbf{0} & \mathbf{P}\mathbf{S}_B & \mathbf{0} \end{bmatrix} \begin{Bmatrix} \mathbf{a}_I \\ \mathbf{a}_B \\ \mathbf{w} \end{Bmatrix} = \begin{Bmatrix} \mathbf{0} \\ \mathbf{0} \\ \mathbf{P}\Theta\mathbf{g} \end{Bmatrix} \tag{3.47}$$

Note that the last row in Eq. (3.47) can be interpreted as the imposition of the constraint in Eq. (30), i.e., $\mathbf{u}(\boldsymbol{\psi}_k^{+})-\mathbf{u}(\boldsymbol{\psi}_k^{-})=\mathbf{A}_{half}\left(\mathbf{a}_B^{+}-\mathbf{a}_B^{-}\right)=\left(\boldsymbol{\psi}^{+}-\boldsymbol{\psi}^{-}\right)^{\mathrm{T}}\mathbf{g}=\mathbf{A}_{half}\mathbf{P}\mathbf{a}_B=\mathbf{P}\boldsymbol{\psi}^{\mathrm{T}}\mathbf{g}$ as

$$\begin{aligned} &\int_{S_{RVE}} \delta\boldsymbol{\lambda}\left(\mathbf{u}-\boldsymbol{\psi}^{\mathrm{T}}\mathbf{g}\right)\mathrm{d}\Psi=\delta\mathbf{w}^{\mathrm{T}}\mathbf{P}\int_{S_{RVE}}\mathbf{G}^{\mathrm{T}}\left(\mathbf{A}\mathbf{a}_B-\boldsymbol{\psi}^{\mathrm{T}}\mathbf{g}\right)\mathrm{d}\Psi \\ &=\delta\mathbf{h}^{\mathrm{T}}\left[\int_{S_{RVE}^{+}}\mathbf{G}^{\mathrm{T}}\left(\mathbf{A}\mathbf{a}_B^{+}-\boldsymbol{\psi}^{+\mathrm{T}}\mathbf{g}\right)\mathrm{d}\Psi+\int_{S_{RVE}^{-}}\mathbf{G}^{\mathrm{T}}\left(\mathbf{A}\mathbf{a}_B^{-}-\boldsymbol{\psi}^{-\mathrm{T}}\mathbf{g}\right)\mathrm{d}\Psi\right] \\ &=\delta\mathbf{h}^{\mathrm{T}}\int_{S_{RVE}^{+}}\mathbf{G}^{\mathrm{T}}\underbrace{\left(\mathbf{A}_{half}\mathbf{P}\mathbf{a}_B-\mathbf{P}\boldsymbol{\psi}^{\mathrm{T}}\mathbf{g}\right)}_{\text{Strong condition}}\mathrm{d}\Psi \end{aligned} \tag{3.48}$$

where $\mathbf{a}_b^{+}$ and $\mathbf{a}_b^{-}$ refer to the nodes at $\boldsymbol{\psi}^{+}\in S_{RVE}^{+}$ and $\boldsymbol{\psi}^{-}\in S_{RVE}^{-}$, respectively, and $\mathbf{A}_{half}$ is obtained after partitioning **A** as $\mathbf{A}^{\mathrm{T}}=\begin{bmatrix}\mathbf{A}^{+\mathrm{T}} & \mathbf{A}^{-\mathrm{T}}\end{bmatrix}$ where $\mathbf{A}^{+}$ and $\mathbf{A}^{-}$ are related to the nodes at the relevant half of the boundary at S_{RVE}^{+} and S_{RVE}^{-}, respectively and $\mathbf{A}_{half}=\mathbf{A}^{+}=\mathbf{A}^{-}$.

Interpolation of the displacement and Lagrange multiplier fields: Following Melenk & Babuška (1996) and Belytschko & Black (1999), the displacement field in terms of a continuous and a discontinuous component are expressed as

$$\mathbf{u} = \mathbf{N}\mathbf{d} + \mathbf{H}\big|_{\Gamma_{DI}}\,\mathbf{N}\boldsymbol{\beta} \tag{3. 49}$$

At the element level $\mathbf{N}=\begin{bmatrix} N_1 & 0 & N_2 & 0 & N_3 & 0 & N_4 & 0 \\ 0 & N_1 & 0 & N_2 & 0 & N_3 & 0 & N_4 \end{bmatrix}$ is the matrix of the standard finite-element shape functions, $\mathbf{d}=\langle d_{11} \quad d_{12} \quad d_{21} \quad d_{22} \quad d_{31} \quad d_{32} \quad d_{41} \quad d_{42} \rangle^{\mathrm{T}}$ is the column vector of nodal displacement values, $\mathbf{H}\big|_{\Gamma_{DI}}$ is the vector of Heaviside function at the discontinuity interface Γ_{DI}, and,

$\boldsymbol{\beta}=\langle \beta_{11} \quad \beta_{12} \quad \beta_{21} \quad \beta_{22} \quad \beta_{31} \quad \beta_{32} \quad \beta_{41} \quad \beta_{42} \rangle^{\mathrm{T}}$ is the vector of enriched degrees of freedom. Thus, **A** in Eq. (3.38) for one element can be written as $\mathbf{A}=\begin{bmatrix} \mathbf{N} & \mathbf{H}\big|_{\Gamma_{DI}}\mathbf{N} \end{bmatrix}$ and **a** consist of both standard and enriched degrees of freedom, i.e., $\mathbf{a}^{\mathrm{T}}=\langle \mathbf{d}^{\mathrm{T}} \quad \boldsymbol{\beta}^{\mathrm{T}} \rangle$. It should be noted that in the previous section the constraints related to boundary conditions are applied on the standard nodal displacements, i.e., $\mathbf{d}$ only and not on those of the enriched degrees of freedom due to displacement discontinuity at the interface. For the standard rectangular elements of the size $2a$ x $2b$ as shown in Figure 3.13(a) below, the shape function components can be explicitly given below for convenience as $N_1=(a-z_1)(b-z_2)/(4ab)$, $N_2=(a+z_1)(b-z_2)/(4ab)$, $N_3=(a+z_1)(b+z_2)/(4ab)$ and $N_4=(a-z_1)(b+z_2)/(4ab)$. Note that for each element local coordinates z_1 and z_2 are used within the RVE coordinate system $\mathbf{y} \in \overline{V}_{RVE}$ in Figure 3.12.

The displacement jump at the discontinuity interface Γ_{DI} can be written as

$$\left[\!\left[\mathbf{u}\right]\!\right] = \mathbf{N}\big|_{\Gamma_{DI}}\,\boldsymbol{\beta} \tag{3. 50}$$

where $\mathbf{N}\big|_{\Gamma_{DI}}$ is a partition of unity at the discontinuity interface Γ_{DI} and vanishes everywhere else. In general, the stress field at the bulk of the heterogeneous continuum can be expressed in term of the nodal displacements as

$$\boldsymbol{\sigma} = \mathbf{D}\left(\mathbf{B}\mathbf{d} + \mathbf{H}\big|_{\Gamma_{DI}}\mathbf{B}\boldsymbol{\beta}\right) \tag{3. 51}$$

where $\boldsymbol{\sigma}$ is the column vector of stress components, i.e., $\boldsymbol{\sigma} = \langle \sigma_{11} \quad \sigma_{22} \quad \sigma_{12} \rangle^{\mathrm{T}}$, $\mathbf{B}$ is a matrix of the derivatives of the shape functions. The traction vector at the discontinuity interface $\mathbf{t}$ can be written as

$$\mathbf{t} = \mathbf{c}\,\mathbf{N}\big|_{\Gamma_{DI}}\,\boldsymbol{\beta} \tag{3. 52}$$

where $\mathbf{c}$ is a matrix of interface cohesive stiffness. Note that in Eq. (3.19), stress $\boldsymbol{\sigma}$ is conjugate to displacement gradient while, $\mathbf{t}$ is conjugate to displacement jump at the discontinuity interface, therefore $\mathbf{t}$ is a vector of two components in two directions. On the other hand, for the interpolation of the Lagrange multiplier field $\boldsymbol{\lambda}$ in Eq. (3.39) $\mathbf{G}$ is selected based on linear functions. Thus, for one element it can be written as $\mathbf{G} = \begin{bmatrix} L_1 & 0 & L_2 & 0 \\ 0 & L_1 & 0 & L_2 \end{bmatrix}$, in which $L_1 = \left(0.5l - z_b\right)/l$ and $L_2 = \left(0.5l + z_b\right)/l$. As shown in Figure 3.13(b), z_b refers to the one dimensional edge coordinate and l is the corresponding edge span (e.g. either $l = 2a$ or $l = 2b$ in Figure 3.13(a)). For one element, $\mathbf{h}$ in Eq. (3.39) can be written as $\mathbf{h} = \langle h_1 \quad h_2 \rangle^{\mathrm{T}}$.

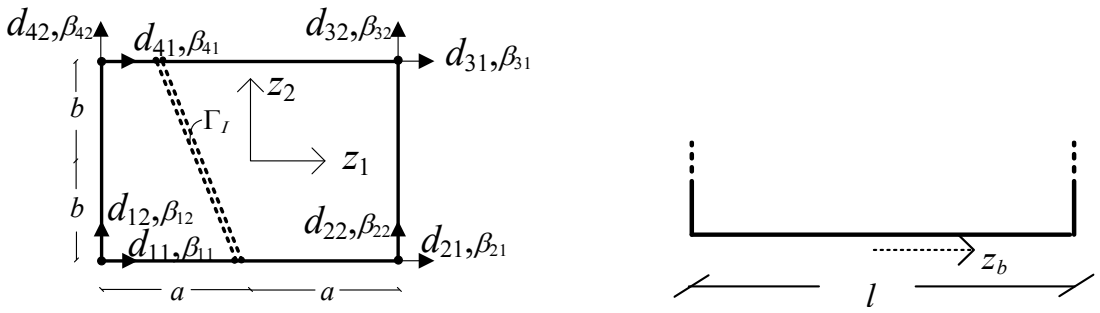

(a) (b)

Figure 3.13: (a) Standard bilinear rectangular element enriched to introduce discontinuity, and (b) Edge of the element

3.2.3. Modelling concrete stiffness reduction due to ASR

3.2.3.1. ASR distress development and its effect on concrete stiffness properties

ASR in concrete generates a secondary product (i.e. ASR gel) that induces pressure and leads to crack formation within the aggregate particles and surrounding cement paste (see Figure 3.14(a)). Sanchez et al. (2015) proposed a qualitative meso-scale model to describe ASR cracks generation and propagation as a function of its induced expansion development. According to the author, ASR cracks are initially developed within aggregate particles at low expansion levels (i.e. up to 0.05%). At moderate levels of expansion (i.e. 0.12%), although some additional cracks are still generated within the aggregates, the existing cracks previously formed at low expansion levels keep propagating and may reach the boundaries of the aggregate particles. Once the expansion increases to higher levels (i.e. > 0.2%), the overall damage is mostly dominated by the propagation of pre-existing cracks to the surrounding cement paste (see Figure 3.14(b)). It is worth noting that two types of cracks may be induced by ASR in concrete: (1) cracks "cutting" the aggregate particles, namely "sharp cracks" (type A), and (2) cracks outlining

the aggregate particle boundaries, namely “onion skin cracks” (type B). The proportion of onion cracks (type B) is about 20-30 % of the total cracks, yet it may vary according to the aggregate lithotype (i.e. mineralogy). In addition to the extension of cracks from reactive aggregate particles as shown in Figure 3.14(b), several cracks develop in the surrounding cement paste due to swelling pressures from the particles, yet, do not penetrate into the particle.

In the research conducted by Sanchez et al. (2015), crack density (number and length of cracks per area) has been related to the reduction of stiffness of affected concrete. Figure 3.15 illustrates test results from Sanchez et al. (2017), include the changes in the measured elasticity moduli (Figure 3.15(a)) and crack densities (Figure 3.15(b)) corresponding to different levels of expansion reached by 35 MPa concrete specimens incorporating distinct reactive coarse aggregates. The figure shows that as the expansion level increases, the elasticity modulus reduces while the crack density increases. According to Sanchez et al. (2015), the proportion of open cracks in aggregate and cement paste are different for different concrete mixtures and levels of expansion. However, in all tested specimens, the majority of open cracks are found in the aggregate particles, being around 70% to 85% of the total number of cracks. More details on the experimental setup and measurements can be found in Sanchez et al. (2015) and Sanchez et al. (2017). Note that the legends used in Figure 3.15 (as well as Figure 3.18) refer to the type of reactive aggregate, the type of non-reactive aggregate and the concrete grade, respectively, (e.g. for "NM + Lav 35", NM is reactive coarse aggregate, Lav is non-reactive fine aggregate and 35 is the concrete grade i.e. 35 MPa). The notation is adopted from Sanchez et al. (2017).

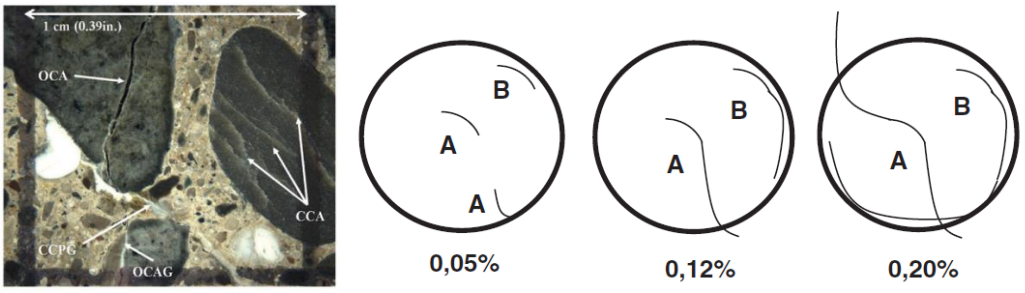

(a) (b)

Figure 3.14: Crack development in concrete due to ASR: (a) Open cracked in aggregate and cement paste; (b) Qualitative crack development model at different levels of expansion [based on Sanchez et al. (2015)].

(a)

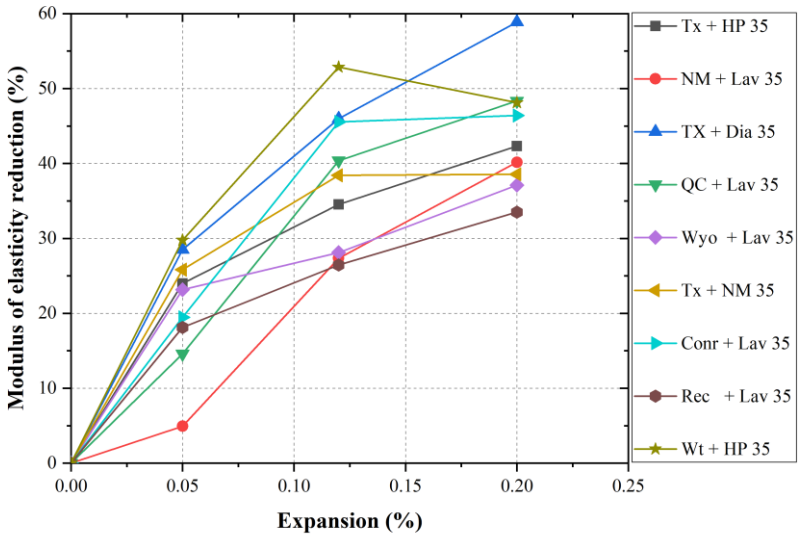

(b)

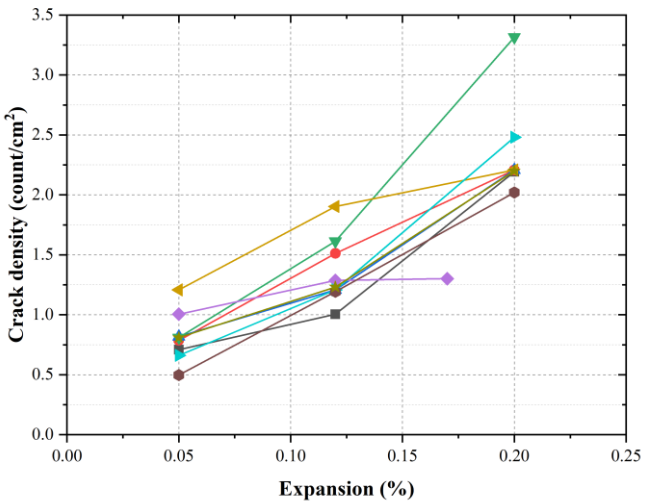

Figure 3.15: Test results from Sanchez et al. (2017): (a) modulus of elasticity reduction and (b) crack density with respect to expansion degree.

3.2.3.2. Development of RVE with ASR induced cracks

RVE of concrete as heterogeneous material: Elastic properties of ASR affected concrete is numerically modelled using the proposed computational homogenization approach. Concrete at the mesoscale level consists of aggregates and cement paste. Before ASR occurrence, the volume fraction and properties of aggregates and cement paste determine the stiffness of the RVE (Wriggers & Moftah 2006). Literature shows that the shape of aggregates has little effect on the elastic behavior (Kim & Abu Al-Rub 2011). In the RVE model, the aggregates are considered to be circular and their diameters vary between 9.5mm and 19.5mm. The aggregate distribution curve shown in Figure 3.16(a) is based on Sanchez (2014). In the RVE model shown in Figure 3.16(b), we have used maximum possible aggregate sizes passing through the sieve opening, i.e., the number of aggregates corresponding to diameters of 9.5mm, 12.7mm, 16.0mm and 19.5mm are 4, 5, 5 and 2, respectively. The aggregate distribution curve in Figure 3.16(a) is somewhat standard and the use of similar dimensions and volume fractions can be found in the literature, e.g. Wriggers & Moftah (2006) and Kim & Abu Al-Rub (2011). Properties of the aggregate and cement and the corresponding volume fraction used in the RVE model are shown in Table 3.3**.**

Table 3.3: Material properties used in the RVE

Parameter	Value
Young's modulus of cement	20 GPa
Poisson's ratio of cement	0.2
Young's modulus of aggregates	60 GPa
Poisson's ratio of aggregates	0.2
Aggregate sizes	9.5-19.5 mm
Volume fraction of aggregates	45 %

As discussed by Mirkhalaf, Andrade Pires & Simoes (2016) and Rezakhani, Zhou & Cusatis (2017), the size of RVE is selected based on the maximum aggregate size, where 75 x 75 mm^2 RVE size is deemed accurate. The number of 4-node square elements used is 3600, which is small enough to keep the computational cost reasonably low. Lines of discontinuity due to phase changes (from aggregate to cement paste) are introduced using the Extended Finite Element Method, while keeping the underlying mesh regular (Sukumar et al. 2001). As the bond between aggregate particles and cement paste is assumed to be perfect, very large interface cohesive stiffness values are used to represent the bond in Eq. (3.52).

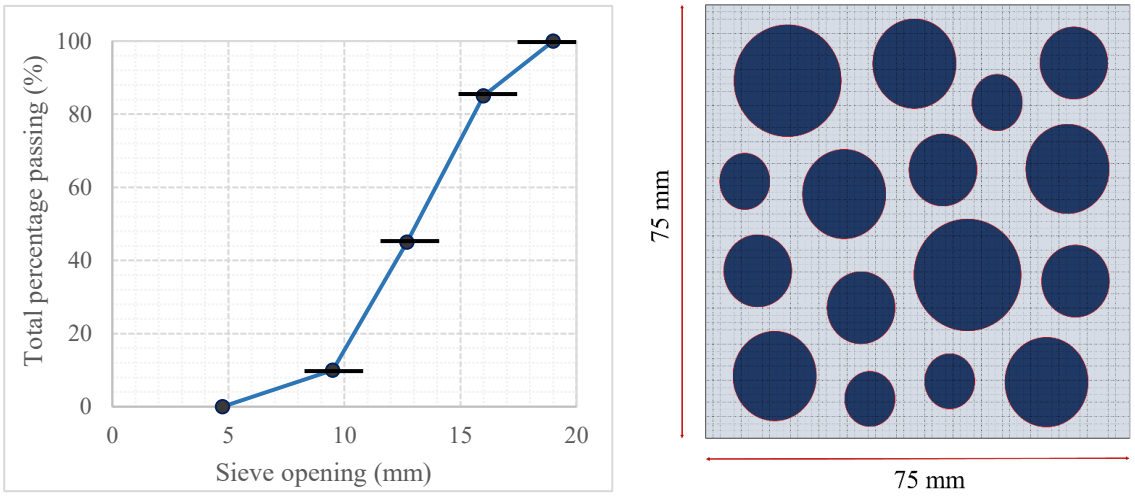

(a) (b)

Figure 3.16: (a) Aggregate size distribution curve considered in this study (b) geometry of the RVE.

Procedure of introducing cracks into RVE: The RVE of ASR affected concrete is modelled for three levels of expansion (i.e., 0.05%, 0.12% and 0.2%). The locations and sizes of ASR induced open cracks follow the qualitative damage model proposed by Sanchez et al. (2015). Crack densities corresponding to expansion levels given in Figure

3.15(b) for different concrete mixtures have been averaged and used to calculate the crack lengths and numbers in the RVE.

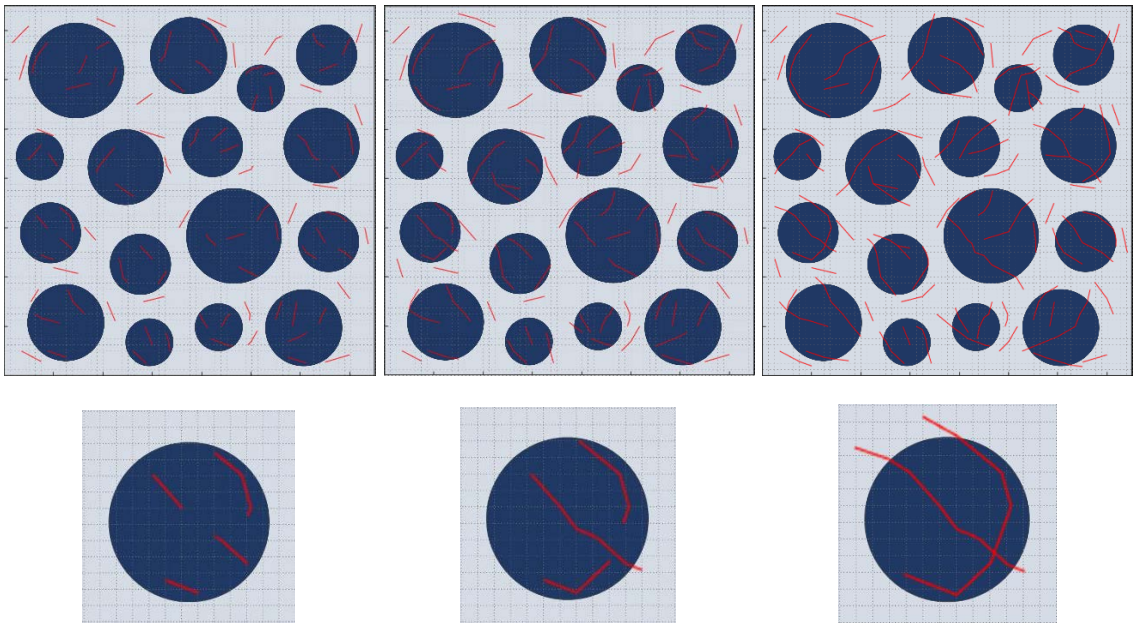

(a) 0.05 % (b) 0.12 % (c) 0.2 %

Figure 3.17: RVE of concrete at different levels of expansion and typical development of cracks in a single aggregate in the RVE.

By taking the average length of an open crack in a 1 cm^2 cell as 0.707 cm, the crack density data from Figure 3.15(b) is converted to total crack length in the RVE. Based on the quantitative information for a given level of expansion, the shapes and locations of the cracks in the RVE are determined. These calculations are displayed in Table 3.4, which were used as the input data for the RVE model as shown in Figure 3.17**.** Typical cracked aggregate particles at different expansion levels are also presented in Figure 3.17**.** It is worth noting herein that cracks networks observed in experimental testing are far more connected as both close and open cracks are measured, while in the numerical model, only open cracks were considered. Since the majority of the ASR induced cracks occur within the aggregate (Sanchez et al. 2015), 75% of the open cracks are placed in

the aggregate particles present in the RVE model. Open cracks are again introduced into the RVE model by using the Extended Finite Element Method (Belytschko & Black 1999). ASR induced cracks are assumed completely open and therefore, the interface cohesive stiffness in Eq. (3.52) is assumed as zero. The crack pattern used in the model meets both the qualitative and quantitative criteria of the ASR induced crack development as per Sanchez et al. (2015). It should be noted that the stiffness of the aggregates and cement paste are assumed to remain the same at different levels of expansion and thus, the change in the effective properties of the macro-scale concrete is only due to development of open cracks at the meso-scale.

Table 3.4: Information on open cracks in the RVE of ASR affected concrete

Expansion level	Crack density (counts/cm^2)	Total number of cracks per RVE (75x75 mm^2)	Total length (mm)	Total length of crack in aggregate (mm)	Total length of crack in cement (mm)
0.05%	0.9	50.6	358.0	268.5	89.5
0.12%	1.4	78.8	556.8	417.6	139.2
0.20%	2.2	123.8	875.0	656.3	218.8

3.2.4. Results and discussion

The results of the RVE modelling are shown in Table 3 and plotted against the experimental data in Figure 3.19, from which one can verify that the stiffness properties are close in both directions, i.e., $\hat{D}_{1111} \approx \hat{D}_{2222}$. Numerical predictions of $\hat{D}_{1111}$ and $\hat{D}_{2222}$

based on the RVE always fall in between upper and lower bounds based on the experimental data of Sanchez et al. (2017). This outcome encourages the use of crack development patterns and density information proposed by Sanchez et al. (2015). It is worth noting that the experimental data averaged in Table 3.5 is collected from five 35 MPa concrete mixtures whose modulus of elasticity vary between 30 GPa and 38 GPa. Figure 3.18 shows that the stiffness reduction based on RVE remains in between the experimental results based on those 5 mixtures and thus, the RVE results are fully within the range of the experimental data. The aggregate distribution and material properties were assumed within a reasonable range because of the lack of detailed information. However, it is shown in Figure 3.19-Figure 3.24 that variations from the assumed values cause insignificant differences in terms of the predicted stiffness reductions in elastic modulus due ASR. Figure 3.19 and Figure 3.20 show the reductions in $\hat{D}_{1111}$ and $\hat{D}_{2222}$, respectively of the RVE model for different expansion levels when the elasticity modulus of the concrete is varied between 18 GPa and 22 GPa. Figure 3.21 shows that the reduction percentage is not affected by the concrete grade. Similarly, Figure 3.22 and Figure 3.23 show the reductions in $\hat{D}_{1111}$ and $\hat{D}_{2222}$ when the elasticity modulus of the aggregate is varied between 54 GPa and 67 GPa. Again, the reduction percentages in the stiffness corresponding to different expansion values are not affected as shown in Figure 3.24. On the other hand, in predicting the stiffness values, current study assumes stationary cracks and does not consider the friction between rough surfaces of slightly open cracks. Consideration of friction and contact could be particularly important in predicting the strength and progressing crack propagations. In such a progressive failure analysis assumption of Periodic RVE boundary conditions may become less accurate especially when the cracks hit the boundaries. Several strategies have been proposed to

predict the RVE boundary conditions when periodicity assumption due to crack propagation needs to be abandoned e.g., in Larsson et al. (2011).

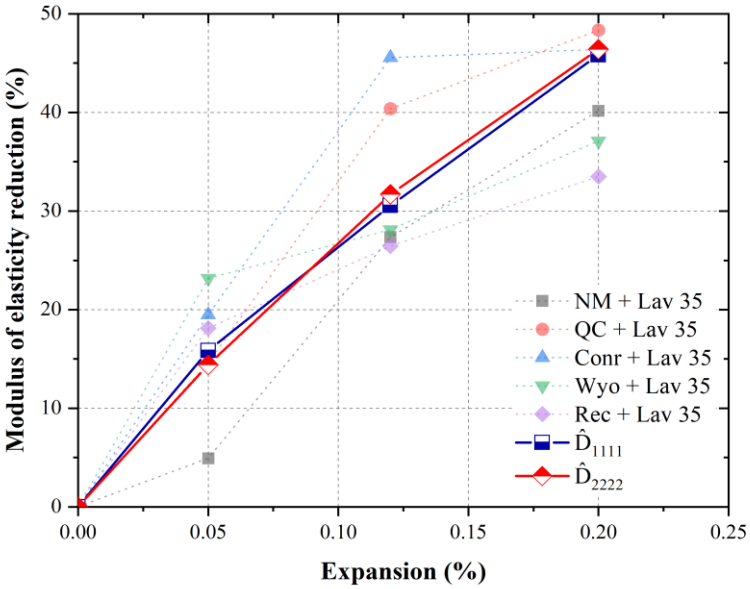

Figure 3.18: Reduction of concrete stiffness vs. expansion based on the homogenized RVE.

Table 3.5: Effective stiffness properties of ASR affected concrete in GPa

Expansion level	RVE $\hat{D}_{1111}$ (**reduction**)	RVE $\hat{D}_{1122}$	RVE $\hat{D}_{1112}$	RVE $\hat{D}_{2222}$ (**reduction**)	RVE $\hat{D}_{2212}$	RVE $\hat{D}_{1212}$	Experiment [Sanchez[35]] (**reduction**)
0.00%	33.6 (**0.00%**)	8.3	0.05	33.8 (**0.00%**)	-0.12	12.3	30 – 38
0.05%	29.2 (**13.1%**)	6.52	-0.04	29.7 (**12.1%**)	-0.2	11.3	(**16.1%**)
0.12%	24.1 (**28.3%**)	4.69	0.03	24.8 (**26.6%**)	-0.01	9.93	(**33.6%**)
0.20%	18.8 (**44.0%**)	2.65	0.13	18.6 (**45.0%**)	0.28	8.13	(**41.1%**)

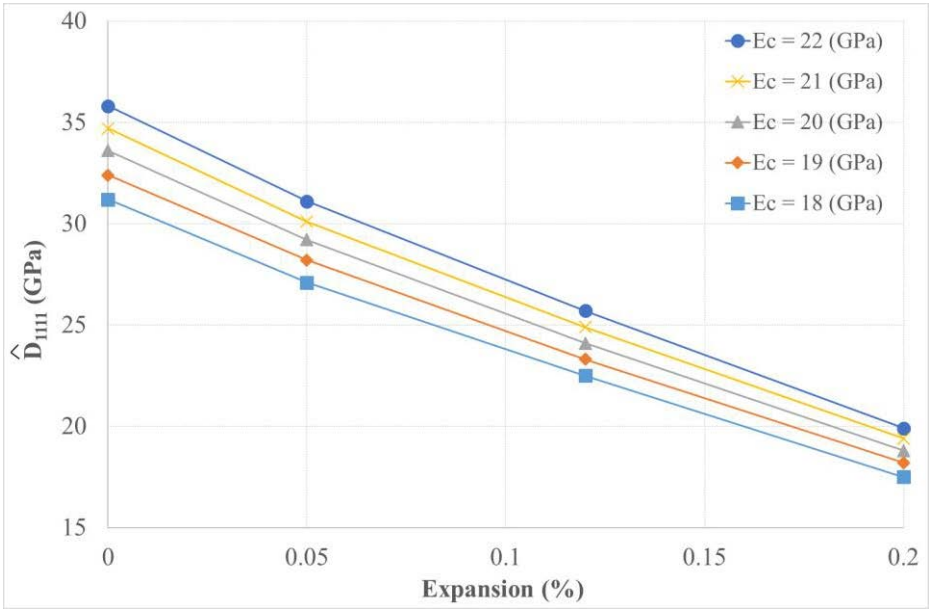

Figure 3.19: Reduction in $\hat{D}_{1111}$ vs. expansion for different cement elastic moduli.

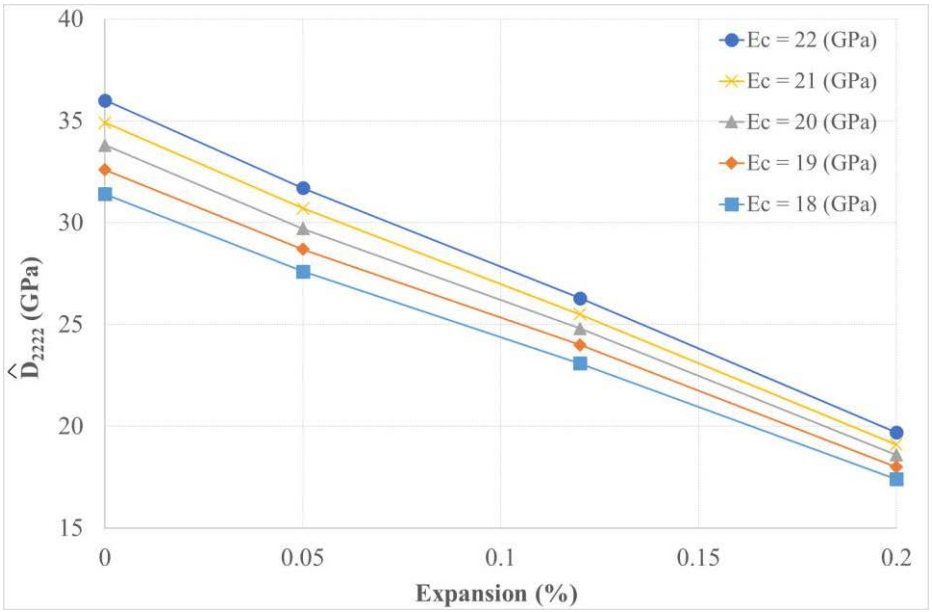

Figure 3.20: Reduction in $\hat{D}_{2222}$ vs. expansion for different cement elastic moduli.

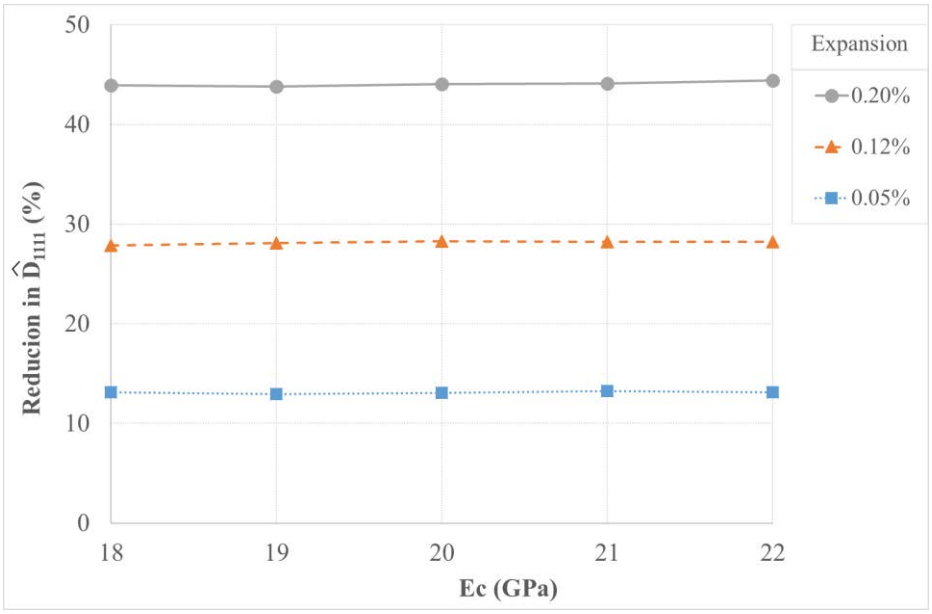

Figure 3.21: Effect of cement elastic modulus on ASR related reduction of concrete stiffness.

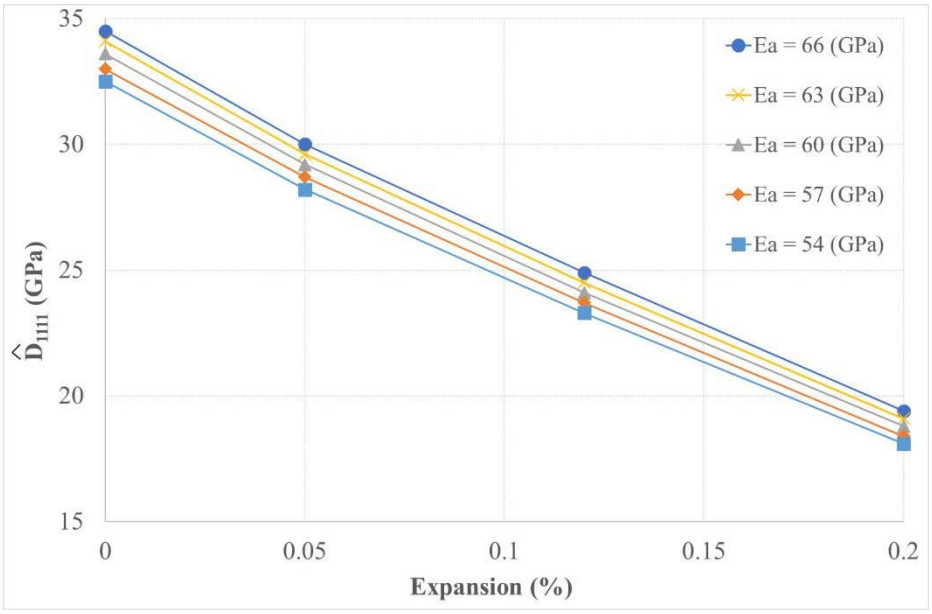

Figure 3.22: Reduction in $\hat{D}_{1111}$ vs. expansion for different aggregate elastic moduli.

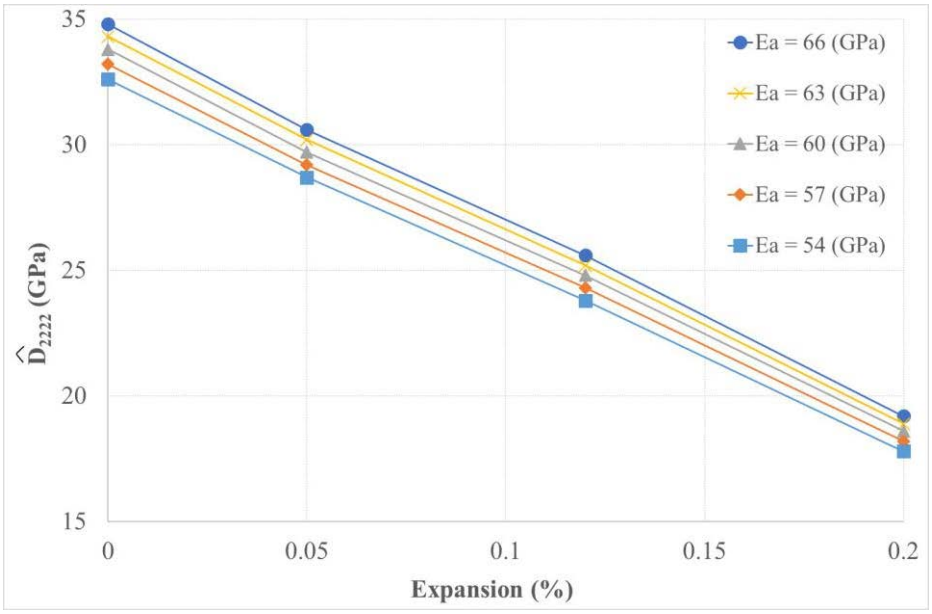

Figure 3.23: Reduction in $\hat{D}_{2222}$ vs. expansion for different aggregate elastic moduli.

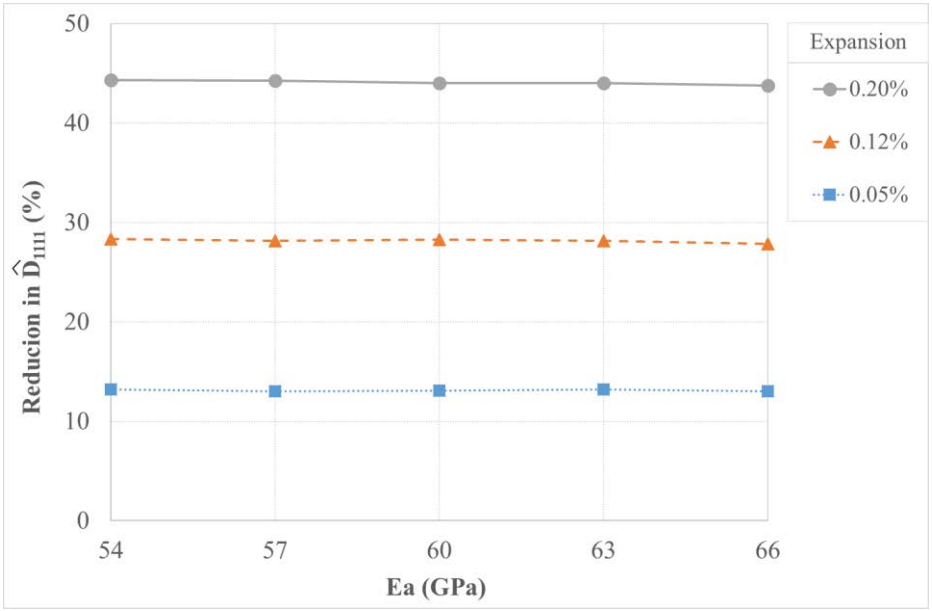

Figure 3.24: Effect of aggregate elastic modulus on ASR related reduction of concrete stiffness.

3.2.5. Concluding remarks

A computational homogenization procedure was developed to determine the effective stiffness of ASR-affected concrete mixtures. The meso-scale RVE model was continuum-based in which circular aggregates and cement matrix were assumed fully bonded in the concrete mix. ASR induced cracks were considered fully open, i.e., cohesionless and frictionless. Discontinuities (due to phase changes and/or crack openings) were efficiently introduced into the regularly meshed RVE model by using the Extended Finite Element Method. For 35 MPa concrete mixtures containing reactive coarse aggregates, the results suggest that up to 0.2% ASR induced expansion levels, about 75% of the cracks develop within the aggregate particles. While the experimental results used for benchmarking purposes showed variations, in all cases considered in the current study they provided upper and lower bounds to the proposed meso-scale RVE model results. In this intricate problem of solid mechanics with inherent uncertainties, and considering the lack of accurate predictive tools, the outcomes encourage the use of proposed crack development patterns and density information for modelling purposes up to 0.2% ASR induced expansion levels.

Based on the insight gained in this study, the meso-scale RVE based computational homogenization procedure can be extended to a wider range of concrete mixtures presenting distinct aggregate natures and reactivities (i.e., potential to reach different and higher expansion levels). In practice, the model thus can be used to determine the modulus of elasticity based on crack data observed from core samples. This is important to get the best out of core samples, which are limited in field investigations.

To improve the reliability of the model, uncertainties in the stiffness properties, aggregate volume fractions and the crack pattern can be accounted for by utilizing stochastic

approaches. The proposed crack development scheme can be used as a basis in model updating strategies for damage detection purposes. For residual load capacity predictions of ASR affected structures, meso-scale RVE modelling approach can be adopted within a two-scale structural analysis frame-work.

3.3. Summary

In this chapter, critical reviews on factors affecting the reduction in modulus of elasticity as well as empirical models currently used in practice for estimation of the reduction were provided. Due to significant effects of ASR to the modulus of elasticity, different methods were implemented to provide better evaluation of the reduction in the modulus of elasticity. The proposed artificial neural network model was capable of evaluating impact of different factors such as reactive aggregates, alkali content and concrete strength in addition to the expansion to the modulus of elasticity, and provides better estimation of the reduction in modulus of elasticity due to ASR. In addition, the developed computational homogenization was able to link the measurement of cracking in concrete to the reduction of modulus of elasticity. Based on the insight gained in this study, the meso-scale RVE based computational homogenization procedure can be extended to a wider range of concrete mixtures presenting distinct aggregate natures and reactivity (i.e., potential to reach different and higher expansion levels).

Chapter 4: A semi-empirical model for forecasting ASR-induced expansion of concrete in the field

In this chapter, a novel semi-empirical approach was proposed for forecasting ASR-induced expansion of unrestrained concrete in the field using laboratory measurements data. The model accounts for effects of reactive aggregate type and nature, alkali leaching, alkali contribution from aggregates and environmental conditions (i.e., temperature and relative humidity). First, laboratory test data of ASR-affected concrete containing a wide range of reactive aggregates and alkali content/leaching, and exposed to various conditions were gathered to develop and calibrate the model parameters for an ideal expansion curve without leaching. This ideal expansion curve without leaching is necessary to predict the expansion of field concrete blocks/members without or with minimal leaching. Then, the model was utilised to forecast ASR-induced expansion of concrete blocks containing different reactive aggregates and alkali contents, which were exposed to three different outdoor conditions in Canada and the USA. Agreeing reasonably well with the measured data, the proposed model is promising for forecasting expansion of unrestrained concrete in the field. Analysing the modelling results also highlights the importance of alkali leaching and environmental conditions on the correlation of laboratory and field performance.

4.1. Introduction

Alkali-silica reaction (ASR), one of the most harmful distress mechanisms affecting concrete material and structures, which causes deleterious expansion, important crack formation followed by reductions in concrete mechanical properties as well as in long-term performance (i.e., durability and serviceability) of concrete structures (Fournier et

al. 2010; ISE 1992; Sanchez et al. 2017). The best solution for ASR is preventing its occurrence in new construction, yet prevention is no longer feasible for current ASR-affected infrastructure worldwide. These affected structures require comprehensive diagnosis and prognosis protocols for evaluating the current damage degree and forecasting the potential of further deterioration. Such information is essential to specify efficient method(s) for remedial/rehabilitation strategies and management procedures for the affected structures. In this regard, several techniques for diagnosis and prognosis have been developed and improved over the last decades. Nowadays, state-of-the-art diagnosis techniques have been achieved to successfully identify and assess the current cause and extent of ASR-induced damage; however, there are still limited numbers of effective techniques for the prognosis of the physicochemical mechanism to forecast how ASR will progress in the coming months or years. To accomplish this requirement, several mathematical models (i.e., empirical, semi-empirical, analytical and numerical) have been developed to provide insightful information on the potential of future deterioration. All these models, however, are either oversimplified, and thus are inaccurate for assessing the distress mechanism properly, being mostly applied to laboratory-made specimens (Capra & Bournazel 1998; Grimal et al. 2010; Larive 1997; Multon & Sellier 2016), or very overcomplicated, being most of the times impractical, and requiring heavy computer processing (Comi, Kirchmayr & Pignatelli 2012; Hariri-Ardebili, Saouma & Merz 2018; Saouma & Perotti 2006a; Sellier et al. 2009). In this context, it is necessary to develop a practical, yet effective empirical/analytical model for forecasting the field expansion based on laboratory testing results.

4.2. Background

4.2.1. ASR-induced expansion: laboratory versus field performance

Several laboratory test procedures such as the accelerated mortar bar test (AMBT) and concrete prism test (CPT), i.e., from ASTM International, Canadian Standards Association CSA, European RILEM and Australian Standard test methods, have been developed to assess the potential alkali-reactivity of concrete aggregates and the efficiency of preventive measures before their use in the field. In addition, several comparative field exposure studies have been developed to establish reliable benchmarking and examine the reliability of the laboratory standard tests for the above-mentioned applications (Fournier et al. 2018). Despite the robustness and applicability of these standards/protocols in identifying potential reactivity of a large number of aggregates, the majority of experts agree that some limitations still exist in classifying borderline reactive aggregates while the use of the above tests along with determining the level of preventive measures required (i.e., control of the concrete alkali content, use of supplementary cementing materials (SCMs) and lithium-based admixtures) to suppress ASR (Doug Hooton et al. 2013; Fournier et al. 2019; Ideker et al. 2012; Thomas et al. 2006). In addition, observations from comparative laboratory-field studies show that the behaviour of concrete mixtures incorporating similar reactive aggregates vary greatly in the laboratory and in the field; it is often reported that field specimens such as exposed concrete clocks display significantly higher expansion than laboratory specimens (Doug Hooton et al. 2013; Fournier et al. 2019; Ideker et al. 2012), especially while the use of preventive measures. An example from Thomas et al. (2006) is shown in Figure 4.1 (Thomas et al. 2006), where the authors tested for expansion of concrete containing different proportions of a high-alkali cement (1.15% $Na2O_e$ per cement mass) and a reactive flint sand (25% of the total aggregate)

from both laboratory testings (i.e., CPT and AMBT) and field blocks test. The concrete blocks display two times greater ASR-induced expansions than laboratory specimens at 2-years. The lack of a proper laboratory-field correlation brings important concerns on the use of laboratory testing protocols to forecast the long-term performance of ASR affected concrete structures in the field. Moreover, it raises an important question in the ASR community: what is the reason for the currently poor laboratory to field performance correlation? Thomas et al. (2006), who after conducted several comparative laboratory-field performance studies, concluded that the main reason of this difference is the significant leaching of alkalis from the laboratory specimens, which is often much smaller in size and exposed a more "leaching-preferable" condition when compared to the field members. The same conclusion was found in Ideker et al. (2012) and Fournier et al. (2009). Indeed, Lindgard and co-workers when measuring ASR-induced expansion and alkali leaching over the concrete prism test (CPT), verified that concrete specimens might lose between 3 to 20% of alkalis in the first 4 weeks and up to 50% after one year (Lindgård, Thomas, et al. 2013). Recently, Sinno & Shehata (2019) measured ASR-induced expansion and leaching of concrete specimens made of the reactive Spratt limestone and Sudbury greywacke-argillite aggregates using different sample sizes (i.e., 75 mm-standard prisms and 100 x 300 mm cylinders). The results showed up to more than 25% and 40% of alkali leaching at 1.5 years of the Spratt and Sudbury samples, respectively. In addition, for both reactive aggregates, the smaller cross-section samples (i.e., the prisms) showed prominent leaching and consequently lower ultimate expansion when compared to the larger samples (i.e., the cylinders). In this context, it is very likely that alkali leaching of large samples (e.g., blocks exposed to weathering presenting 400 x 400 mm cross-sections) in the field conditions could be significantly lower than the small

laboratory samples. Furthermore, Bérubé et al. (2002) observed that the amount of alkali contribution from aggregates in the long-term exposed field members could be significant for some specific aggregates, thus could seriously affect ASR-induced expansion in the field. For instance, the test results from Bérubé et al. (2002) show that some aggregates may release up to 3.4 kg/m^3 to the pore solution of concrete; such significant alkali contribution could be the reason why several dam structures built with concrete mixtures displaying less than 2 kg/m3 Na_2O equivalent (Na_2O_e) display important induced expansion in the field while presenting negligible expansion in the laboratory testing (Bérubé et al. 2002; M.-A. Bérubé 1992).

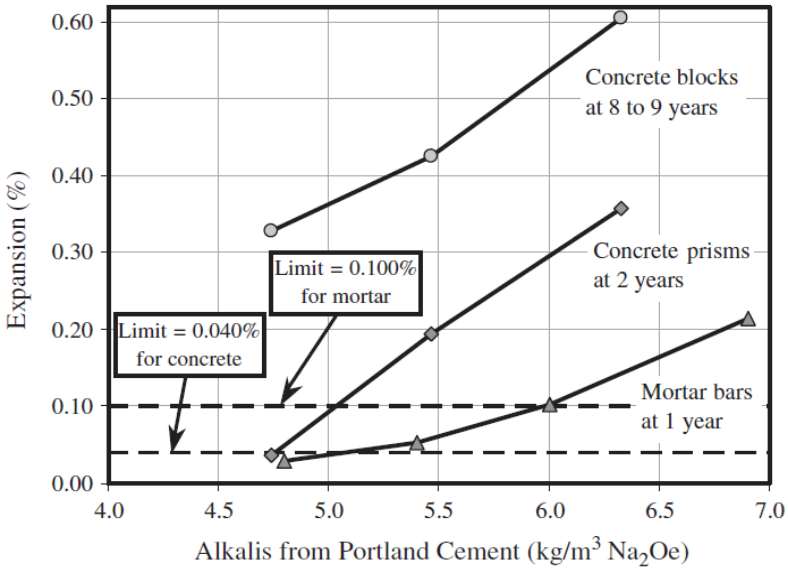

Figure 4.1: Differences between lab and field test results in term of ultimate expansion (Thomas et al. 2006).

The aforementioned limitations of laboratory test procedures still require intensive and extensive studies to improve laboratory-field correlations and thus provide better predictions of ASR prognosis in field structures. Likewise, ongoing research has been focusing on developing alternative tests and improving the current test methods to limit or eliminate the leaching of alkalis in concrete, such as the miniature concrete prism test

(MCPT) (AASHTO 2019) and the concrete cylinder test (CCT) (Chopperla 2019). On the other hand, with the current understanding of the laboratory-field expansion correlation and relatively large database available, mathematical modelling of ASR-induced expansion of field structures/structural members based on laboratory observations is necessary to enable further analysis of ASR structural implications and ensure a better decision making in the rehabilitation of ASR-affected concrete infrastructure. Therefore, several empirical, analytical and numerical approaches have been proposed to provide predictive information on ASR-induced expansion of affected structures in the field, such as thermo-chemo-mechanical models (Saouma & Perotti 2006a; Ulm et al. 2000), finite element inverse analyses (Sellier et al. 2009), multi-scale chemical analyses (Multon & Sellier 2016), analytical models (Kawabata et al. 2016), etc. Yet, to the best knowledge of the authors' understanding, the applicability of the vast majority of the proposed models is still limited in current practice due to either the complexity of the models or even the lack of their validation with experimental database comprised of a wide range of concrete mixtures and reactive aggregates.

4.2.2. Larive's semi-empirical model for ASR-induced expansion

A number of empirical and analytical models has been developed to estimate ASR kinetics and induced expansion in the laboratory (Capra & Bournazel 1998; Larive 1997), which combined with numerical analyses were intended to predict the structural implications (i.e., deformation, stability) of structures, structural members (Comi, Kirchmayr & Pignatelli 2012; Saouma & Perotti 2006a; Ulm et al. 2000). Among these models, the semi-empirical model proposed by Larive (1997) is one of the most accepted and widely used by the ASR community (see Figure 4.2) (Gorga, Sanchez & Martín-Pérez 2018; Goshayeshi 2019; Kawabata et al. 2016; Saouma & Perotti 2006a; Ulm et al. 2000). The

model for the stress-free expansion evolution was developed based on an extensive experimental database of more than 600 concrete specimens incorporating various reactive aggregates and exposed to different laboratory conditions. In this model, ASR kinetics and induced expansion were constructed as a function of three main model parameters: ultimate expansion (ε^{∞}), latency (τ_L) and characteristic (τ_C) times (Larive 1997), given by

$$\varepsilon(t,\theta) = \frac{1 - e^{-\frac{t}{\tau_c(\theta)}}}{1 + e^{-\frac{t-\tau_L(\theta)}{\tau_c(\theta)}}} \times \varepsilon^{\infty} \tag{4.1}$$

Typical expansion curves formed by the model are shown in Figure 4.2. There is not a clear physical meaning for the latency and characteristic times, however, one could agree that the latency time represents for the initiation period of ASR-induced expansion while the characteristic time define the expansion rate after the initiation. The time constants τ_L and τ_C were derived as temperature-dependent parameters, as shown in Eq. (4.2 – 4.3) after Ulm et al. (2000).

$$\tau_c(\theta) = \tau_c(\theta_0)\left[U_C\left(\frac{1}{\theta} - \frac{1}{\theta_0}\right)\right] \tag{4.2}$$

$$\tau_L(\theta) = \tau_L(\theta_0)\left[U_L\left(\frac{1}{\theta} - \frac{1}{\theta_0}\right)\right] \tag{4.3}$$

where, θ is the absolute temperature ($\theta\ K = 273 + T\ °C$); θ_0 is reference absolute temperature, which is typically referred to exposure temperature in laboratory testing; U_C and U_L are thermal activation constants, derived from the Arrhenius physical chemistry concept (Larive 1997; Ulm et al. 2000):

$$U_C = 5400 \pm 500K \tag{4.4}$$

$$U_L = 9400 \pm 500K \tag{4.5}$$

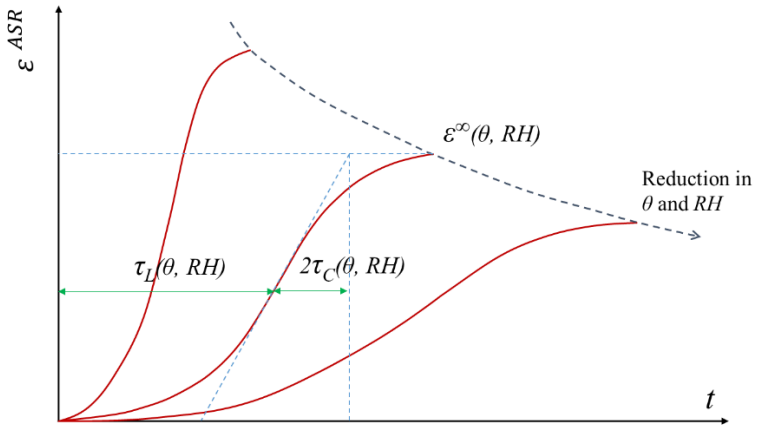

Figure 4.2: ASR-induced expansion curves obtained from Larive's model with considering temperature and relative humidity effects after Saouma & Perotti (2006a).

In addition to the temperature dependency of the time constants, Saouma & Perotti (2006a) further developed the model by introducing the effect of relative humidity and stress state (i.e., for structural modelling) to the expansion behaviour of concrete structures. The authors adopted the relative humidity-dependent coefficient of the *ASR swelling* proposed by Capra & Bournazel (1998) into the Larive's model, which directly reduces the ultimate expansion ε^{∞}:

$$f(h) = RH^{8} \tag{4.6}$$

where, *RH* is the internal relative humidity or relative humidity in the material pores. This coefficient is normally set to be zero when the relative humidity within the material is lower than 80% (Capra & Bournazel 1998; Kagimoto & Kawamura 2011; Saouma & Perotti 2006a). This updated form of the Larive's model with both temperature and humidity considerations have been thereby utilised in several numerical studies for ASR-induced expansion and structural implications (Comi, Kirchmayr & Pignatelli 2012; Hariri-Ardebili, Saouma & Merz 2018; Saouma & Perotti 2006a). Yet, it is important to notice that the current form of the relative humidity dependency displays extremely high sensitivity and impact on ASR-induced expansion. For instance, if the internal RH reduce

from 100% as normally expected in the laboratory testing to 95%, ASR-induced expansion reduces down to almost 45%. In this regard, although various sophisticated ASR numerical models adopted this humidity-dependent coefficient to account for the humidity effect (Hariri-Ardebili, Saouma & Merz 2018; Saouma & Perotti 2006a), relative humidity values as high as 100% have been frequently used in practice, which yields a *f(h)* equals to 1 (i.e., for dam structures). Elsewhere, Comi, Kirchmayr & Pignatelli (2012) proposed an analytical approach to account for the effects of concrete saturation degree on ASR-induced expansion through new parameters coupled to Larive's conventional model (i.e., τ_C, τ_L and ε^{∞}). The model was well calibrated using experimental data from Larive (1997) and yielded efficient results in chemo-mechanical or chemo-thermo-damage models for evaluation of ASR-induced expansion and deformation in structures (Comi, Kirchmayr & Pignatelli 2012). It is worth mentioning that measuring the degree of saturation in practical applications for field structures is difficult (and not convenient) for long-term measurements due to its destructive nature.

Finally, although the concrete alkali content is one of the most crucial factors affecting ASR-induced expansion (Lindgård, Sellevold, et al. 2013), its effect has not been taken into consideration in the updated Larive's model by Saouma & Perotti (2006a), and thus the model is not applicable for estimating the potential of induced expansion of concrete mixtures displaying distinct alkali loadings. Therefore, Goshayeshi (2019) proposed a modification of the Larive's model to account for the alkali content and other important parameters such as aggregate's reactivity (i.e., type and nature/reactivity), temperature and relative humidity, aiming for fully describing AAR-kinetics and -induced expansion. However, this study has only focused on laboratory-made specimens under free expansion conditions, and further analyses are still required to assess the suitability of the

proposed approach for structures in the field. Furthermore, the model proposed in Goshayeshi (2019) did not account for alkali leaching, and as aforementioned, this parameters is critical for assessing field structures.

4.3. Scope of work

As discussed in the previous sections, there is currently a lack of efficient models for forecasting ASR-induced expansion in the field; the likely reasons of the current situation is the complexity of ASR physicochemical process itself along with the poor laboratory-field correlations often obtained. The ultimate aim of this study is to provide a robust and engineering-friendly tool to estimate ASR-induced expansion of unrestrained field concrete members based on experimental observations and laboratory testing data. To accomplish this goal, a semi-empirical model was developed by adopting the Larive's model with additional considerations to account for the most important factors affecting ASR-induced expansion such as aggregate type and nature, concrete alkali content, leaching and releasing of alkalis, temperature, and RH. The model was validated using laboratory test data available in the literature. The proposed model was then used to estimate ASR-induced expansion of concrete members containing reactive aggregates manufactured for three important and distinct experimental campaigns: Ontario Ministry of Transportation (MTO) project at Kingston (Ontario, Canada) (Doug Hooton et al. 2013), CANMET project (Ottawa, Ontario, Canada) (Fournier et al. 2019; Fournier et al. 2009), and the University of Texas project (Texas, Austin, USA) (Ideker et al. 2012). Finally, further analyses on effects of the key factors (i.e., concrete alkali content, alkali leaching, alkali contribution from aggregates and environmental conditions) on ASR-induced expansion of affected concrete members in the field were then performed.

4.4. Model development and calibration on laboratory testing data

This section presents development of the semi-empirical model based on Larive's model and its validation on different reliable sets of laboratory test data. The dependency of the model parameters (i.e., ε^{∞}, τ_L and τ_C) to temperature and relative humidity is adopted from (Hariri-Ardebili & Saouma 2018; Larive 1997; Ulm et al. 2000) as presented in Section 4.2.2 to account for the effects of environmental conditions; i.e., differences between accelerated laboratory and field exposure conditions or between different field conditions. The dependency on alkali content and leaching are developed in this study and validated using the reliable experimental data available in the literature such as from Fournier & Bérubé (2000), Lindgård, Thomas, et al. (2013) and Sinno & Shehata (2019). To model expansion of concrete blocks/structural members in the field (i.e., with an assumption that no leaching of alkalis occurs) from laboratory tests' data, it is necessary to compensate the reduction in expansion due to leaching to replicate ASR expansion level in the field. In this regard, this section aims at developing and validating the semi-empirical model for estimation of an ideal expansion curves for the "*no leaching*" scenario, which is to use in ***Section 4.5*** along with the consideration of field climatic conditions to model the long-term expansion of concrete in the field.

4.4.1. Overview of the semi-empirical model

In order to account for the effect of temperature, relative humidity, and concrete alkali content and leaching, a semi-empirical model was proposed based on the Larive's model by incorporating those effects into the three model parameters, ε^{∞}, τ_c, and τ_L. The value of the ultimate expansion ε^{∞} depends on reactive aggregate used, relative humidity in concrete and alkali content, while characteristic time and latency time (τ_c, and τ_L) are

dependent on the reactive aggregate, temperature, relative humidity. In addition, amount of alkalis leaching (i.e., from laboratory tests, depending on the reactive aggregate, specimen size, and exposed condition) could change the characteristic time and latency time of the expansion. As such, the three model parameters could be defined as:

$$\varepsilon^{\infty} = \varepsilon^{\infty}(AG, RH, A) = \varepsilon^{\infty,o}(AG, RH_0, A_0) \times k_{\varepsilon,RH} \times k_{\varepsilon,A} \quad (4.7)$$

$$\tau_c = \tau_c(AG, T, RH, LA) = \tau_c^o(AG, T_0, RH_0, A_0) \times k_{c,T} \times k_{c,RH} \times k_{c,LA} \quad (4.8)$$

$$\tau_L = \tau_L(AG, T, RH, LA) = \tau_l^o(AG, T_0, RH_0) \times k_{L,T} \times k_{L,RH} \times k_{L,LA} \quad (4.9)$$

where, *AG, RH, T, A* and *LA* denote the reactive aggregate type/nature, relative humidity (%), temperature (°C), concrete alkali content (kg/m^3), and alkali leaching at 1-year (%), respectively. Dependent coefficients are introduced to account for the effects of these factors as mentioned above. The model parameters and dependent coefficients are explained in detail as follows:

- $\varepsilon^{\infty,o}(AG, RH_0, A_0)$, $\tau_c^o(AG, T_0, RH_0, A_0)$ *and* $\tau_l^o(AG, T_0, RH_0)$ are ultimate expansion and ASR time constants at a reference boundary condition, i.e., *T = 38°C*, *100% RH* and alkali loading $A = A_o$;
- $k_{\varepsilon,\ RH}$: *RH*-dependent coefficient of the ultimate expansion, where $k_{\varepsilon,\ RH}$ = 1 at *R.H* = 100%;
- $k_{\varepsilon,\ A}$ and $k_{\varepsilon,\ Ao}$: alkali content-dependent coefficient of the ultimate expansion, where $k_{\varepsilon,\ A}$ = 1 at *A = 5.25* kg/m^3;
- $k_{c,\ T}$ and $k_{L,\ T}$: temperature-dependent coefficient of the time constants (τ_c and τ_L), where $k_{c,\ LA}$ & $k_{L,\ LA} = 1$ at *T = 38°C*;
- $k_{c,\ LA}$ and $k_{L,\ LA}$: alkali leaching-dependent coefficient of the time constants (τ_c and τ_L) ($k_{c,\ LA}$ & $k_{L,\ LA} = 1$ if no leaching occurs, *LA = 0%).*

Details of all these dependent coefficients are presented in the following sections.

4.4.2. Consideration of reactive aggregate used in concrete

This section discusses the attainment of the ultimate expansion and ASR time constants ($\varepsilon^{\infty,o}$, $\tau_L{}^o$ and $\tau_C{}^o$) at any alkali loading $A = A_o$ exposed to 38^oC and $100\%\ RH$ condition. These model parameters mainly depend on the aggregate type (fine/coarse) and nature (lithotype) of the reactive aggregate used in concrete along with the alkali content of the mix. The quantification of the alkali content effect is presented in the next sections, while this section mainly focuses on the effect of the reactive aggregate type and nature on ASR-induced expansion development.

The effect of the reactive aggregate's type (fine/coarse) and nature (lithotype) on both ASR kinetics and ultimate expansion has been demonstrated in numerous experimental campaigns over the last decades, e.g., in (Fournier et al. 2009; Ideker et al. 2012; Sanchez 2014). It has been verified that not only the amount of reactive mineral phases within the aggregate particles but also the particles size (i.e., specific surface area) play an important role on ASR-induced development.

According to ASTM C1778 (C1778 2016) and AASHTO PP65 (2011), reactive aggregates can be classified into three main classes, i.e., moderately reactive, highly reactive, and very highly reactive depending on the expansion level obtained from either the 1-year concrete prism test (CPT) or the 14-day accelerated mortar bar test (AMBT). For instance, Sanchez et al. (2017) conducted an extensive laboratory experimental study on the expansion of 12 concrete mixtures incorporating ten different reactive aggregates varying in types and natures (Sanchez et al. 2017). Details on the characteristics of the

aggregates (both reactive and non-reactive) may be found in (Sanchez 2014; Sanchez et al. 2017). Figure 4.3(a) shows the expansion data over time of the tested concrete mixtures.

(a)

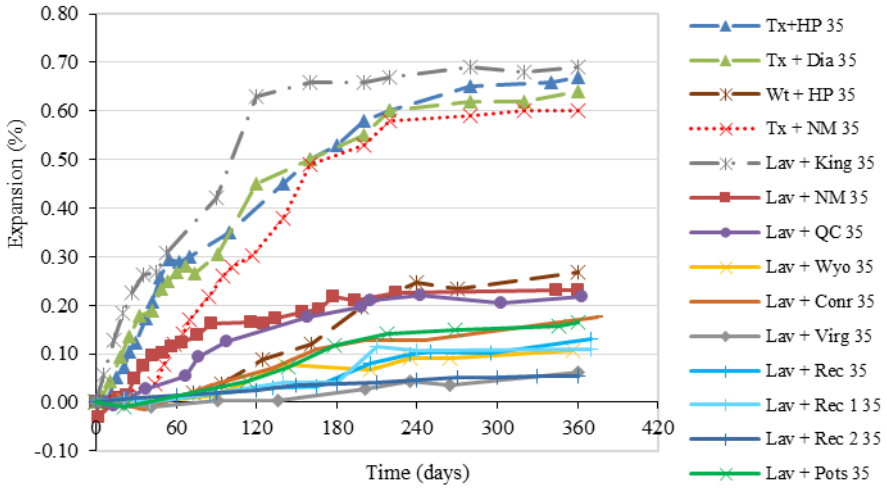

(b)

	Damage degree	Expansion levels at one year (%)	τ_C^o (day)	τ_L^o (day)	$\varepsilon^{\infty,o}$ (%)
ASR - Fine and Coarse	Ultra High	≥ 0.50	42	103	0.60
ASR - Fine	Ultra High	≥ 0.50	71	0	0.65
	High	0.20 to 0.499	38	157	0.26
ASR Coarse	High	0.20 to 0.499	50	44	0.23
	Moderate	0.10 to 0.199	45	165	0.15
	Marginal	0.06 to 0.099	43	168	0.08
	Negligible/Marginal	0.04 to 0.059	57	89	0.05

Figure 4.3: Effect of aggregate type/nature on expansion: (a) test data from Sanchez et al. (2017), and (b) model parameters proposed by Goshayeshi (2019).

It can be seen from Figure 4.3(a) that significant induced expansion (i.e., higher than 0.30%) is attained from mixtures incorporating aggregates with very highly reactivity (e.g., Tx sand) within an exposure period of less than 100 days, while mixtures incorporating moderately reactive aggregates (e.g., Rec and Wyo coarse reactive aggregates) have taken almost 1 year to reach 0.10% of expansion. Moreover and interestingly, very distinct kinetics (i.e., expansion rate) were obtained for different

concrete mixtures; e.g., although the same expansion has been reached at 1 year for the mixtures incorporating NM and Wt coarse aggregates, different expansion rates were gathered from both mixtures, since a significant latency time (i.e., time required to trigger the induced expansion) is observed for the Wt mixture. In this regard, Goshayeshi (2019) identified two main kinetics trends of ASR-induced expansion: 1) a very fast ascending curve with little to no latency time and no levelling off trend up until the ultimate expansion is reached and, 2) a slower ascending curve, presenting some latency time and a significant levelling off trend close to the ultimate expansion. These trends were found to be mainly dependent on the type and nature of the reactive aggregate.

It is worth noting that a large number of reactive aggregates have been used around the world displaying distinct minerology and reactivity degree. The latter poses difficulties in quantifying the influence of the aggregate's type and nature into the model; in this respect, based on the extensive test database from (Sanchez et al. 2017) and the use of the least-square method for curve-fitting, Goshayeshi (2019) proposed seven different sets of parameters for Larive's model ($\tau_L{}^o$, $\tau_C{}^o$ and $\varepsilon^{\infty,o}$) according to the aggregates type and nature for "control mixtures" displaying 4.6 kg/m^3 of alkalis (see Figure 4.3(b)). The proposed model parameters have been successfully applied for expansion and deformation modelling of *Robert-Bourassa Charest overpass* in Quebec City, Canada (Gorga, Sanchez & Martín-Pérez 2018) and *Paulo Afonso IV Dam* structure in Paulo Afonso, Brazil (Gorga et al. 2020). Nevertheless, due to the large variety of aggregates bearing very distinct physicochemical parameters and thus reactivity degrees, there are still many challenges to adopt one set of model parameters to different aggregates. In addition, it is important to notice that even though laboratory test procedures are conducted in well-controlled conditions while assessing the expansion behaviour of concrete mixtures incorporating

reactive aggregates, the test outcomes (i.e., expansions as a function of time) often display remarkable variations between different laboratories (Fournier & Malhotra 1996; Fournier & Rogers 2008). For instance, Fournier and Malhotra (1996) (Fournier & Malhotra 1996) conducted an inter-laboratory study on ASR, where 24 laboratories across Canada, the USA France and Brazil assessed the potential reactivity of two reactive coarse aggregates with known behaviour (provided by CANMET); yet the different laboratories used their local non-reactive fine aggregates and general Portland cement (PC) that met the requirements of the CPT as per CSA A23.2-14A. The results showed that expansion measurements at 1-year and 2-years of exposure can be up to 39.6% and 48.5% different, respectively, regardless of the use of the same reactive aggregate and test procedure. The authors explained that the main reason of this high variability in the test outcomes could be attributed to the differences in mixture proportioning parameters such as the cement composition, physicochemical features of the non-reactive aggregates used from the local sources as well as the permissible range in the water-to-cement ratio (i.e., 0.42-0.45). Due to this huge variation, the use of a single laboratory expansion curve in the estimation of different field concrete members that used the same reactive aggregate source could provide misleading information. Therefore, in order to calculate the three Larive's model parameters (i.e., $\varepsilon^{\infty,o}$, $\tau_L{}^o$ and $\tau_C{}^o$), a priority list for obtaining laboratory expansion curves is suggested as follows: *(1) laboratory concrete specimens should be manufactured using the same raw materials (i.e., reactive and non-reactive aggregates and Portland cement) than field concrete members and*, *(2) laboratory concrete specimens should display the same mix-proportions than field concrete members*. For the first source, the best curve fitting using the least squares regression could be used to obtain the model parameters at the reference condition as tested in the laboratory. Yet, this information is not always

available in assessing existing structures. The information provided in (Goshayeshi 2019), as shown in Figure 4.3(b) thus could be used as the second priority.

Finally, it is important to mention that along with the model parameters ($\varepsilon^{\infty,o}$, $\tau_L{}^o$ and $\tau_C{}^o$), the information of alkali leaching is also required from laboratory expansion testing to establish the laboratory-field correlation as presented previously. Therefore, a more comprehensive database on the reactive aggregates, which consists of information about the aggregate type (i.e., fine or coarse; gravel, crushed or natural), petrography, 14-day AMBT, 1-year CPT, reactivity level, model parameters ($\varepsilon^{\infty,o}$, $\tau_L{}^o$ and $\tau_C{}^o$) and alkali content/leaching, is extremely helpful and will be addressed in future work.

4.4.3. Consideration of environmental conditions: temperature and relative humidity effect

4.4.3.1. Temperature

As presented previously, the temperature dependence of the time constants τ_C and τ_L of unrestrained concrete specimens are adopted from Ulm et al. (2000) (Ulm et al. 2000). These dependent coefficients were developed based on physicochemical parameters and were thoroughly calibrated using a significant experimental database from Larive (1997):

$$k_{C,T} = exp\left[U_C\left(\frac{1}{\theta} - \frac{1}{\theta_0}\right)\right] \tag{4.10}$$

$$k_{L,T} = exp\left[U_L\left(\frac{1}{\theta} - \frac{1}{\theta_0}\right)\right] \tag{4.11}$$

where, θ_0 is reference absolute temperature ($\theta\, K = 273 + T\, °C$, $T_0 = 38^0C$); U_C and U_L are thermal activation constants. This temperature dependence model of the τ_C and τ_L has been widely accepted and successfully implemented in forecasting expansion of not only

samples manufactured in the laboratory but also field structures such as dams and bridges (Hariri-Ardebili, Saouma & Merz 2018; Saouma & Perotti 2006b; Ulm et al. 2000).

4.4.3.2. Relative humidity

A wide range of experimental studies have been conducted to investigate the effect of RH on the ASR-induced expansion. By controlling/measuring RH and the corresponding induced expansion on concrete specimens at 21ºC, Stark (1991) (Stark 1991) and Bérubé et al. (2002) (Bérubé et al. 2002) stated that *an internal-RH of 80 % was required for ASR to occur in concrete*. It is also well established from laboratory testing on ASR-affected concrete that the higher the internal and external relative humidity, the higher the expansion in concrete (Kagimoto & Kawamura 2011; Poyet 2006). In addition, Steffens et al. (2003) suggested that the internal humidity affect ion transport in the porous network for both topochemical and through-solution reactions, and thus contribute to the overall kinetics of the ASR in concrete (Steffens 2003).

In terms of the modelling, the relative humidity-dependent model proposed by Capra and Bournazel (1998) (Capra & Bournazel 1998) as aforementioned is adopted in this study. This internal RH dependency is written in form of the dependent coefficient $k_{\varepsilon,\ RH}$:

$$k_{\varepsilon,\ RH} = RH^{8} \tag{4.12}$$

where, RH herein is the internal relative humidity or relative humidity in the material pores. The model was utilised for developing a constitutive model for ASR in Saouma and Perotti (2006) and is widely accepted and used in modelling ASR-induced expansion (Hariri-Ardebili, Saouma & Merz 2018; Saouma & Perotti 2006a).

4.4.4. Consideration of alkali content and alkali leaching

As presented in ***Section 2.1***, the laboratory test specimens (normally 75 by 75 by 285 mm prisms or 100 by 200 mm cylinders) evaluated through the concrete prism test (CPT) at 38^{o}C or at 60^{o}C leach out remarkable amounts of alkalis, and thus observe significantly lower induced expansions than those measured in field members (Doug Hooton et al. 2013; Fournier et al. 2009; Ideker et al. 2012; Lindgård, Thomas, et al. 2013; Sinno & Shehata 2019; Thomas et al. 2006). Therefore, in order to establish laboratory-field correlations, leaching on ASR-affected samples developing induced expansion in the laboratory has to be accounted for. In terms of expansion modelling, it certainly requires a model for an ideal expansion curve without leaching to simulate the "*no leaching*" scenario of the field exposed members. Inputs for this model should be measurable from the laboratory expansion testing, such as expansion over time, initial alkali content along with amount of leaching over time.

This study proposes a novel semi-empirical model to take into consideration of both alkali content and leaching into the model of expansion over time for the ideal "*no leaching*" scenario. The validation of this particular model on alkali content/leaching dependency were then conducted on experimental data available in the literature from both laboratory testing (Lindgård, Thomas, et al. 2013; Sinno & Shehata 2019) and long-term field studies (Doug Hooton et al. 2013; Fournier et al. 2009). It is worth noting that the idea "*no leaching*" expansion curve is not available from any laboratory testing since there is always a certain extent of leaching occurring. Therefore, the validation of the model using field data becomes extremely important.

4.4.4.1. Alkali content and leaching model development

The amount of alkali leaching over time of a concrete mixture incorporating reactive aggregate is herein considered proportional to the initial alkali content of the mixture, and this proportional value remains the same for any initial alkali content. This means that the higher the alkali content, the higher the alkali leaching (in mass) at a given time period. The same observation is obtained from the experimental work of Costa et all. (2017) (Costa 2017). According to Lingard et al. (2013), the majority of leaching occurs within the first 52 weeks of exposure at 38ºC and 100% RH (Lindgård, Thomas, et al. 2013). Since the standard laboratory test procedures are normally conducted within a 1-year period, and there is little expansion gained after 1 year, the amount of leaching at 1-year is found to be the most meaningful to consider and to evaluate its effects. In this semi-empirical model, both the initial alkali content in concrete and the alkali leaching at 1-year are considered for calculation of the alkali content-dependent coefficient of ultimate expansion ($k_{\varepsilon,A}$), while the amount of alkali leaching at 1-year is also used for determination of dependent coefficients for the time constants ($k_{C,AL}$ *and* $k_{L,AL}$). More details on this calculation procedure are presented in the next sections.

In addition, there are many other factors affecting ASR-induced expansion in the laboratory; thus, some assumptions have to be made for developing and simplifying the proposed semi-empirical model: (1) the effects of the specimen size and casting direction are ignored in this study except for the amount of alkali leaching, and (2) no alkali release from the aggregates in the short-term (i.e., within 1-year testing period of the CPT) is accounted for. Regarding the second assumption, Bérubé et al. (2002) stated that the alkali contribution from aggregates in the long-term (i.e., several years) to ASR-induced development in field concrete is far more significant when compared to short-term

laboratory tests. Furthermore, because of significant leaching takes place in laboratory testing, the alkalinity of the concrete pore solution is reduced, which makes the potential contribution from the aggregates less significant (Drolet, Duchesne & Fournier 2017). The effect of the alkali contribution from aggregates therefore, is considered in this study only for long-term field exposed members.

Calculation of the alkali content-dependent coefficient for the ultimate expansion ($k_{\varepsilon,A}$)

For the alkali content-dependent coefficient $k_{\varepsilon,A}$, experimental data from the literature (Costa 2017; Fournier & Bérubé 2000; Sinno & Shehata 2019) are collected for a comparison of alkali content from 1.5 kg/m^3 to 12.4 kg/m^3, as shown in Figure 4.4, in which 5.25 kg/m^3 is assumed to be the control alkali content ($k_{\varepsilon,A} = 1.00$). Most of these works were conducted with alkali contents lower than 5.25 kg/m^3 to evaluate the alkali threshold for reactivity testing. Only Fournier et al. (2000) tested alkali contents up to 12.4 kg/m^3, where the results show a huge variation of the coefficient $k_{\varepsilon,A}$ for alkali contents higher than 5.25 kg/m^3. Apparently, the higher alkali content, the higher the $k_{\varepsilon,A}$, yet, the induced expansion start increasing significantly from alkali contents of about 4 kg/m^3 before start decreasing back again after 9 kg/m^3. It is worth mentioning that $k_{\varepsilon,A}$ could vary as per the reactive aggregate type and nature, along with the concrete mix-proportion; yet, there is limited results on this in the literature. In this study, $k_{\varepsilon,A}$ is obtained by averaging these available experimental data to take into account the impact of alkali content on the ultimate expansion, as shown in Figure 4.4. In the next sections, the proposed coefficient $k_{e,A}$ is calibrated and validated using the experimental data from (Lindgård, Thomas, et al. 2013; Sinno & Shehata 2019), as well as the field exposure data from (Doug Hooton et al. 2013; Fournier et al. 2019; Fournier et al. 2009; Fournier et al. 2018).

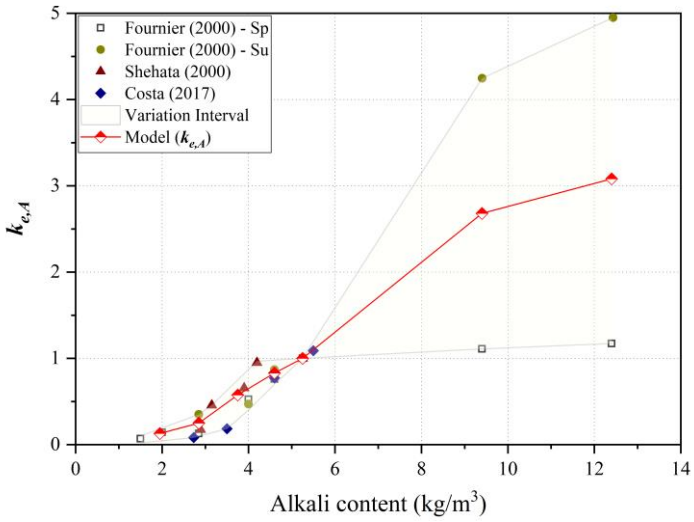

alkali content (kg/m3)	$k_{\varepsilon,A}$
1.50	0.08
1.95	0.15
2.85	0.25
3.75	0.58
4.60	0.82
5.25	1.00
9.40	2.68
12.40	3.08

Figure 4.4: Dependency of the ultimate expansion (ε^{∞}) to the alkali content.

Simulation of the "no leaching" expansion curve

Considering a concrete mixture containing reactive aggregate fabricated in the laboratory containing an initial alkali content of A_o (kg/m^3), due to the leaching over time, a higher alkali loading (namely updated alkali content, *A, kg/m*^{3}) should be required to compensate for the leaching amount in order to simulate the ideal "*no leaching*" scenario of the original A_o alkali loading. As such, the updated alkali loading A could be calculated from the original alkalis A_o and the leaching amount measured at 1-year (*LA, %*):

$$A = \frac{A_o}{1 - LA} \tag{4.13}$$

$$\text{or, } A_o = A \times (1 - LA) \tag{4.14}$$

As shown in Eq. (4.13 – 4.14), the use of this updated alkali content *A* keeps at 1 year the same initial amount of alkali A_o of the tested concrete mixture. For instance, for a concrete containing 5.25 kg/m^3 alkalis with 1-year alkali leaching of 20% (i.e., 80% remaining) in the concrete prism test (CPT), an updated alkali content of 6.56 kg/m^3 is adopted for the ideal "no leaching" expansion calculation, which secures 5.25 kg/m^3 (i.e., *80% of* 6.56

kg/m^3) alkalis after a 1-year test. Next, the alkali content-dependent coefficients $k_{\varepsilon,A}$ and $k_{\varepsilon,Ao}$ are derived from the alkali loading of A and A_o, respectively, based on the proposed relationship illustrated in Figure 4.4. The fractional difference between $k_{\varepsilon,A}$ and $k_{\varepsilon,Ao}$ is utilised to increase the induced expansion measured in the laboratory on small samples to represent its ideal expansion curve without leaching:

$$\varepsilon^{\infty}_{no\ leaching} = \varepsilon^{\infty}_{test} \times \frac{k_{\varepsilon,A}}{k_{\varepsilon,Ao}} \quad (4.15)$$

in which, $\varepsilon^{\infty}_{no\ leaching}$ is the ideal ultimate expansion of the "no leaching" scenario; $\varepsilon^{\infty}_{test}$ is the ultimate expansion obtained from the best curve-fitting of the expansion curve measured in the laboratory (i.e., CPT). In the case that the original concrete in the laboratory contains 5.25 kg/m^3 of alkalis, the coefficient $k_{\varepsilon,Ao}$ is equal to 1 and thus the formula in Eq. (4.15) is as same as in Eq. (4.7).

Calculation of alkali leaching-dependent coefficient to the characteristic time and latency time ($k_{C,LA}$ and $k_{L,LA}$):

According to Lindgård et al. (2013) and Sinno & Shehata (2019), the more the alkalis leach out, the earlier the expansion levels off. Lindgård et al. (2013) reported that the expansion of small concrete prisms (70 × 70 × 280 mm) with 33 % alkali leaching at 1 year is likely to level off after 1.5 years of exposure, while larger Norwegian prisms (100 × 100 × 450 mm, 16.5 % leaching at 1 year) continue to expand throughout two years of exposure to about *40% higher than the* ASTM/CSA prisms' expansion (Lindgård, Thomas, et al. 2013). In terms of the Larive's expansion model parameters, this observation means that an increase in the leaching amount results in a decrease of the characteristic and latency times, as shown in Figure 4.5. The same experimental observation was also reported in Sinno & Shehata (2019). This phenomenon could be

explained for the plateau of the expansion curve after the alkali content of the concrete mixture drops to below the alkali threshold required to maintain ASR.

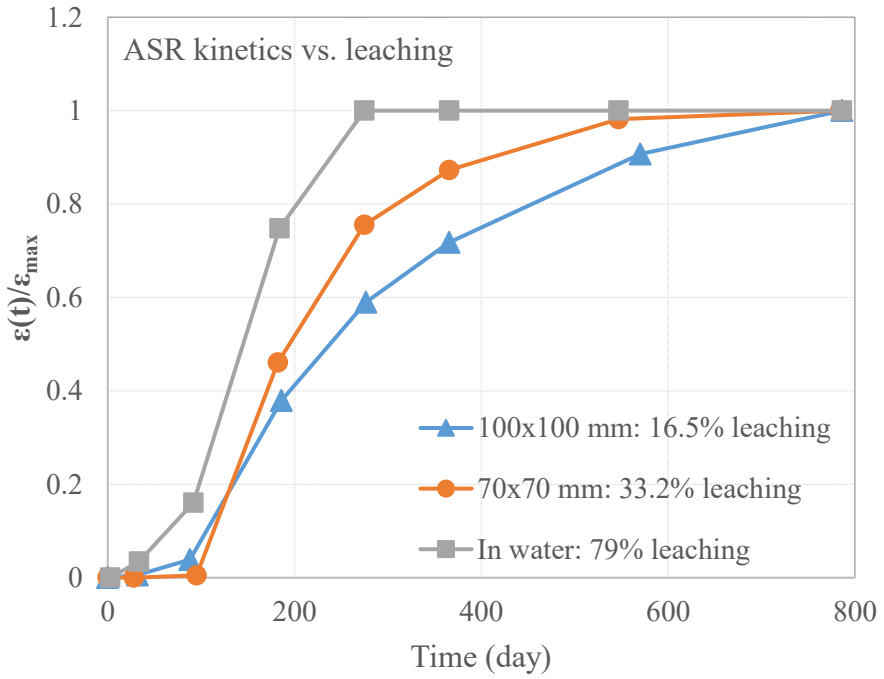

Figure 4.5: Effect of alkali leaching on the ASR kinetic (Lindgård et al. 2013).

Figure 4.6 illustrates the reduction of τ_C *and* τ_L with respect to 1-year alkali leaching, which is obtained from experimental data of both Lindgård et al. (2013) and Sinno & Shehata (2019). It is worth noting that in these figures the value of 0% alkali leaching is linearly projected from different leaching values from the experimental data. Analysing the above figures, one observes that the characteristic time displays a higher reduction rate due to leaching than the latency time. Linear functions obtained from the best curve-fitting on the experimental data are calculated and adopted for the determination of two alkali leaching-dependent coefficients of the time constants, $k_{C,LA}$ and $k_{L,\,LA}$.

$$\tau_{C,no\ leaching} = \frac{\tau_{C,test}}{k_{C,LA}} \tag{4.16}$$

$$\tau_{L,no\ leaching} = \frac{\tau_{L,test}}{k_{L,LA}} \tag{4.17}$$

$$k_{C,LA} = -1.05 \times LA + 1 \quad (4.18)$$

$$k_{L,LA} = -0.7 \times LA + 1 \quad (4.19)$$

in which, $\tau_{C,no\ leaching}$ and $\tau_{L,no\ leaching}$ are the ideal characteristic and latency times of the "no leaching" scenario, respectively; $\tau_{C,test}$ and $\tau_{L,test}$ is the characteristic and latency times obtained from the best curve-fitting of the expansion curve measured from the laboratory test (i.e., the CPT). It should be also noted that these two alkali leaching-dependent coefficients on the time constants (i.e., $k_{C,LA}$, $k_{L,LA}$) are to take into consideration of leaching only and thus are independent to the concrete alkali content. The influence of the initial alkali content on the time constants is not considered in this study due to lacking of available experimental data.

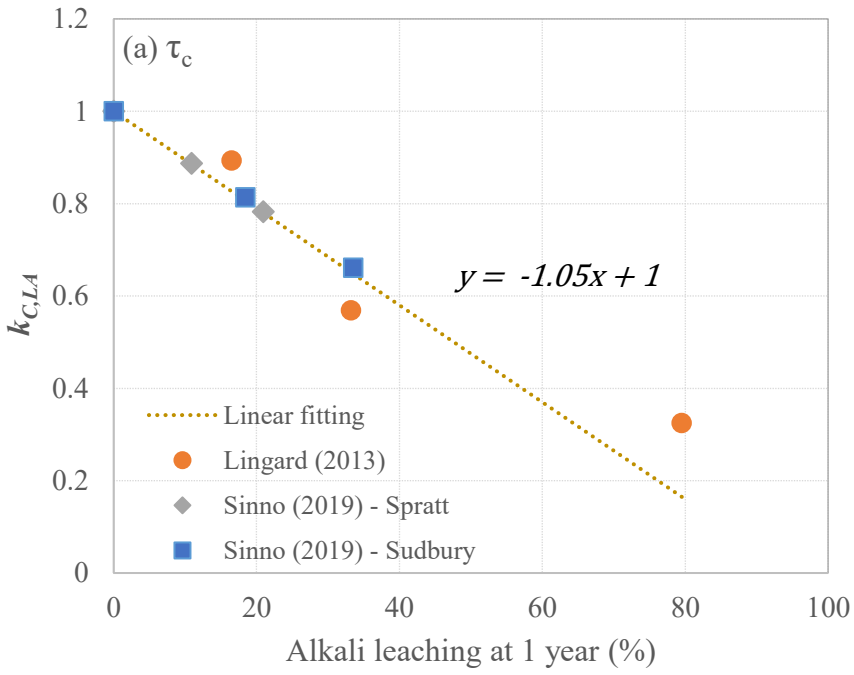

Figure 4.6: ASR kinetics parameters with respect to alkali leaching at 1 year.

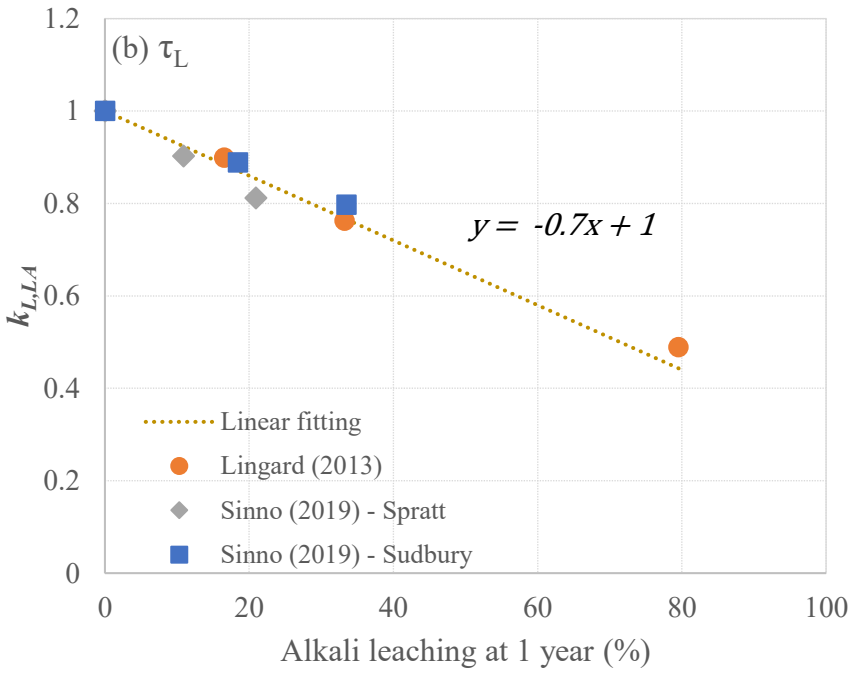

Figure 4.6: Continued.

4.4.4.2. Model validation of the idea "no leaching" expansion curve using Lingard's experimental data (Lindgård, Thomas, et al. 2013)

Lindgård and co-workers conducted three series of CPTs varying specimen dimensions and exposure conditions: (1) 100 × 100 × 450 mm prisms exposed to 38ºC and 100% RH, (2) 70 × 70 × 280 mm prisms exposed to 38ºC and 100% RH, and (3) 70 × 70 × 280 mm prisms submerged in de-ionised water at 38ºC to promote leaching of alkalis (Lindgård, Thomas, et al. 2013). An identical concrete mixture incorporating reactive aggregate and 3.75 kg/m^3 alkalis was used in the study for all the three series. Total alkali leaching was measured over time from both water in the bottom of storage containers and in the lining inside the containers. The leaching amounts at 1 year for those three series were about 16.5 %, 33.2 % and 79.5 %, respectively. Analysing expansion results in Figure 4.7(a) together with the leaching amounts, once again one verifies that on the same concrete mixture, the higher the alkalis leached out, the lower the induced expansion observed. In an idealised scenario however, there should be an identical expansion curve for this

particular concrete mixture regardless of the specimen dimensions and exposure conditions if there was no alkali leaching.

The experimental data (i.e., expansion, leaching of alkalis) of these three series were collected and utilised for calculation of an ideal "*no leaching*" expansion curve for the concrete mixture using the proposed model for alkali content and leaching considerations, namely approach 1, approach 2 and approach 3, respectively, as shown in Table 4.1. As aforementioned, these three approaches are expected to provide an identical expansion curve for the ideal "*no leaching*" scenario. Details of the experimental data and model parameters are showed in Table 4.1 and Figure 4.7. The model outcomes from approach 1 and 2 (i.e., based on test results of 70x70 mm and 100x100 mm prism kept in 100% RH) show very good agreement with the ideal expansion curves. Calculated ultimate expansions from these two approaches are closely matched; i.e., 0.603 and 0.599 for approach 1 and approach 2, respectively, while only the characteristic time τ_C is slightly different. The approach 3 (based on samples soaked in de-ionised water) provides a divergent ideal expansion curve compared to the first two approaches. The extremely high leaching of alkalis due to the harsh exposure condition, (i.e., about 45 % and 80% alkali leached out at 8 weeks and 1 year, respectively) led to an updated alkali content of 18.5 kg/m^3 after the compensation, which is out of the alkali range proposed to build this model (i.e., 12.4 kg/m^3). This observation also indicates that the test results from the samples in 100% RH should be preferable for the calculation of the ideal expansion curve.

Multon & Sellier (2016) developed a multi-scale analysis on the same set of experimental data from Lindgård's work to obtain a theoretical expansion curve of the concrete without leaching. The result is shown in Figure 4.7(b). It shows that the ideal expansion curves obtained from the first two approaches (i.e., approach 1 and 2) are comparable to results from the multi-scale model proposed in Multon & Sellier (2016). This agreement indicates

that different methods (i.e., semi-empirical versus multi-scale) could produce the same result for concrete expansion if no leaching occurs. In addition, it highlighted a great impact of leaching on ASR-induced expansion, which is important for evaluating the expansion of the field exposure members with minimal leaching.

Table 4.1: Experimental data and empirical model parameters for the concrete tested in Lindgård et al. (2013)

Lindgård et al. (2013)		Approach 1	Approach 2	Approach 3
	Test series	100x100 mm Prism (100% RH)	70x70 mm Prism (100% RH)	70x70 mm Prism (In de-ionised water)
Experimental and fitting data (leaching cases)	Initial alkali content (kg/m^3)	3.75		
	$k_{\varepsilon,A0}$	0.575		
	τ_C	130	85	40
	τ_L	205	185	145
	ε^{∞}	0.435	0.300	0.045
	1-year leaching (%)	**16.5**	**33.2**	**79.5**
Model parameters (non-leaching cases)	Updated alkali content (kg/m^3) (After compensated)	4.49	5.61	**18.29**
	$k_{C,LA}$	0.865	0.728	0.348
	$k_{L,LA}$	0.921	0.841	0.618
	$k_{\varepsilon,A}$	0.798	1.147	3.866
	$\frac{k_{\varepsilon,A}}{k_{\varepsilon,A}(3.75)}$	1.387	1.995	6.723
	τ_C	150.3	116.8	114.9
	τ_L	222.6	220.1	234.5
	ε^{∞}	0.603	0.599	0.303

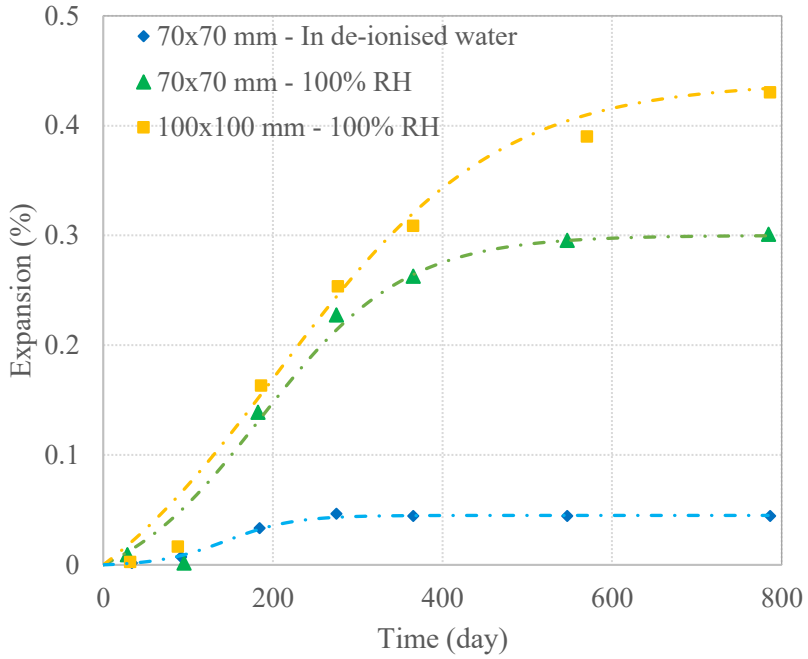

(a) ASR expansion results and the best curve-fitting Larive's model curves

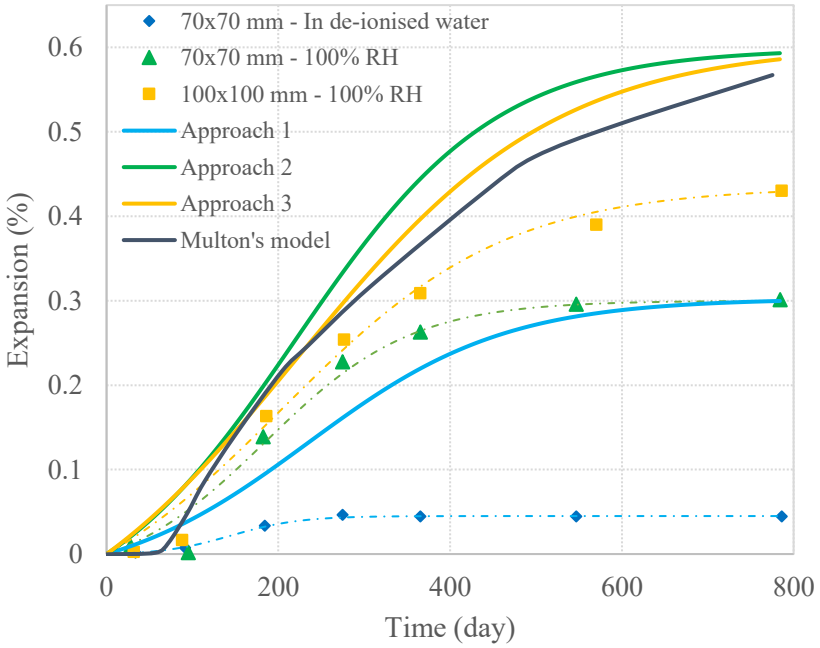

(b) model outcomes compared to multi-scale modelling results from Multon & Sellier (2016)

Figure 4.7: Model validation on Lindgård's data for the ideal expansion curve.

4.4.4.3.Model validation on Sino and Shehata's experimental data

Similar to the experiments in Lindgård et al. (2013), Sino & Shehata (2019) (Sinno & Shehata 2019) evaluated ASR-induced expansion of 75 × 75 × 280 mm prisms and 150 × 300 mm cylinders incorporating two reactive aggregates (i.e., Spratt limestone and Sudbury crushed gravel), displaying a concrete alkali content of 5.25 kg/m^3, and kept at 38ºC and 100% RH. The expansion was measured over two years, as shown in Figure 4.8(a), while the total alkali leaching was measured from the water in the bottom of the storage containers after 1.5 years of exposure. The alkali leaching obtained at 1.5 years of the prisms and cylinders were 25.8 % and 13.5 % respectively, for the mixture incorporating the Spratt limestone, and 41.3 % and 22.7 % for the mixture incorporating Sudbury gravel. One can see that the leaching of alkalis from prisms is almost twice of those from the cylinders for the mixtures incorporating both reactive aggregates. Thus, it is obvious that expansion obtained from the cylinders (as larger size specimens) is significantly higher than the prisms for both Spratt and Sudbury reactive aggregates (see Figure 4.8). Moreover, mixtures made of the Sudbury gravel presented significant higher leaching when compared to the Spratt. In this context, the expansion of specimens made of Sudbury could increase significantly further if no or minimal alkalis have leached out from the specimens. Assuming the effect of casting direction is negligible as previously discussed, the expansion curves measured from prism and cylinder specimens should be identical if no leaching occurs.

The proposed model in Section 4.4.1 was utilised to estimate the ideal expansion curves for both Spratt and Sudbury mixtures based on the expansion and alkali leaching data. Similar to the previous model validation on (Lindgård, Thomas, et al. 2013), the expected outcomes from the model is an identical ideal expansion curves obtained from prisms'

and cylinders' test data for the "no leaching" scenario for each of concrete mixtures incorporating Spratt and Sudbury. Details of the experimental data, the model parameters and dependent coefficients are shown in Table 4.2. The alkali leaching at 1-year is assumed to be 85 % of 1.5-year leaching as per leaching observations made over 2 years from the test series of Lindgård et al. (2013).

Table 4.2: Experimental data and empirical model parameters for the concrete tested in (Sinno & Shehata 2019)

Sino and Shehata (2019)		Sudbury		Spratt	
		Based on Prism's data	Based on Cylinder's	Based on Prism's	Based on Cylinder
Experimental and fitting data (leaching cases)	Initial alkali content (kg/m^3)	5.25			
	$k_{\varepsilon,A}$	1			
	τ_C	65	75	95	110
	τ_L	170	185	40	45
	ε^{∞}	0.183	0.245	0.220	0.290
	1-year leaching (%)	**33.5**	**18.5**	**20.9**	**10.9**
Model parameters (non-leaching cases)	Updated alkali content (A, kg/m^3) (After compensated)	7.895	6.442	6.64	5.89
	$k_{C,AL}$	0.725	0.848	0.829	0.911
	$k_{L,AL}$	0.839	0.911	0.900	0.948
	$k_{\varepsilon,A}$	2.071	1.482	1.562	1.260
	$\frac{k_{e,A}}{k_{e,A}(5.25)}$	2.071	1.482	1.562	1.260
	τ_C	89.6	88.4	114.6	120.8
	τ_L	202.6	203.0	44.5	47.5
	ε^{∞}	0.379	0.363	0.344	0.365

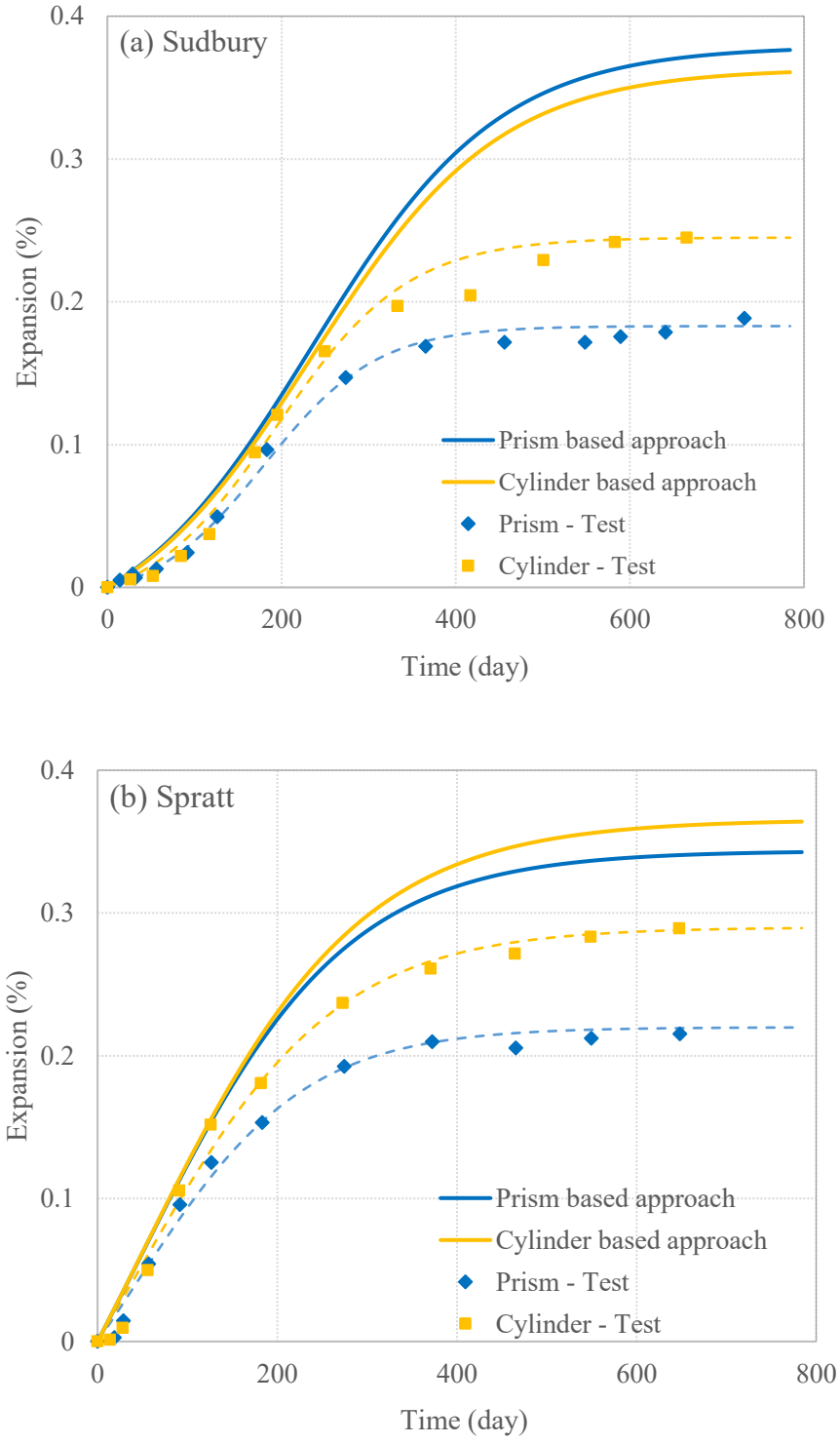

Figure 4.8: Model validation on Sino and Shehata's data for the ideal expansion curve.

For the concrete mixtures made of both Sudbury and Spratt reactive aggregates, only 6% difference of ultimate expansion between the two approaches is obtained, while both approaches provide almost the same time constants (τ_C and τ_L). This very good agreement between the two approaches for both reactive aggregates on determining the ideal expansion curve for the "no leaching" scenario, together with the previous calibration and varlidation on Lindgård's experimental work, proves the capability of the proposed semi-empirical model to account for the alkali content and leaching. Furthermore, it is noticed that the ideal ultimate expansion of the concrete mixture made of Sudbury gravel could reasonably be higher than the Spratt's, which could be explained by the higher leaching occurred from the Sudbury specimens as previously discussed.

4.5. Forecasting ASR-induced expansion in the field

In this section, the proposed semi-empirical model is utilised for the modelling of ASR-induced expansion of field blocks incorporating different reactive aggregates, alkali contents, and exposed to outdoor conditions to appraise its applicability for field members.

4.5.1. Implementing the semi-empirical model for forecasting expansion of field exposed concrete blocks

For the field exposed concrete members, it is worth noting that ASR-induced development is far more complicated than the controlled laboratory conditions due to many factors, such as continuously change in the ambient temperature and RH, effect of rainfall, solar radiation and other damage mechanisms (i.e., shrinkage, creep, freezing and thawing) (Courtier 1990; Deschenes Jr et al. 2018; Gorga, Sanchez & Martín-Pérez 2018). For simplification for forecasting expansion of field-exposed members using the proposed semi-empirical model, some important assumptions need to be made, as follows:

(1) *There is no alkali leaching from the field blocks/members*: Leaching of alkalis of small cross-section specimens (i.e., 75x75 mm) has been reported from many experimental studies; i.e., in (Lindgård, Thomas, et al. 2013; Sinno & Shehata 2019). However, in concrete blocks or real concrete members, due to their larger dimensions, leaching usually takes place only in locations near to the concrete surface (i.e., about 20 mm – thick layer) as shown in Figure 4.9 (Courtier 1990), while the inner part remains with the same initial alkali content. The same observation is also found in Hooton et al. (2013) while conducting petrographic examination of concrete beam in the field, in which the authors suggested leaching occurred within the first 25 mm of the beam (Doug Hooton et al. 2013). Therefore, the minimal alkali might leach out from large concrete samples in the field and thus it is reasonable to assume no alkali leaching from the field blocks. Moreover, except for the effect of larger block dimensions on reducing alkali leaching, it is also assumed that there is no other effect of specimen size or casting direction while utilising laboratory small sample data for the calculation of ASR-induced expansion in field blocks/members;

(2) *The effects of other mechanisms such as shrinkage, freezing and thawing, sulphate attack, etc., on ASR-induced expansion are not accounted for in this model*: Knowing that the concrete members containing reactive aggregate in the field are affected by not only ASR but rather a combination of mechanisms (Deschenes Jr et al. 2018), the ASR-induced expansion is considered to be dominant in the investigated concrete blocks. A combination effect of all these deterioration mechanisms will be investigated in a future study.

(3) *Internal temperature is similar to the ambient temperature*. According to (Doug Hooton et al. 2013; Gorga, Sanchez & Martín-Pérez 2018), the temperature inside

concrete members could be affected by solar radiation and snow coverage (if any). Yet, the effect is normally limited to the surface portion of the concrete member. The internal temperature therefore, is assumed to be the same as the ambient temperature and uniformly distributed throughout the depth of concrete block for simplification. Moreover, there is no alkali-silica reaction, and thus no expansion occurs at ambient temperatures below 0^{o}C.

(4) *The internal RH is assumed to be uniformly distributed throughout the concrete samples*. On the relative humidity consideration, the internal RH is affected by several factors such as the ambient RH, precipitation, concrete permeability and temperature. According to Kagimoto & Kawamura (2011), the ambient RH affects only the cover of concrete members, and it takes years to balance the internal RH in the concrete cover and the ambient RH, while the concrete core most likely remains saturated. Moreover, external water supplying (i.e., from raining) could significantly increase the internal RH in concrete members (Gorga, Sanchez & Martín-Pérez 2018; Kawabata et al. 2016). Yet, the internal RH could rapidly reduce when severe cracking on the surface occurs at high expansion levels (due to faster moisture evaporation), and thus increase the thickness of the lower RH cover layers. The variation of the internal RH throughout concrete members and its change over time has to be extensively considered, i.e., through finite element analysis or multi-scale modelling. In the context of the proposed semi-empirical model, the internal RH of field exposed concrete large specimens is first assumed to be 100% and applied uniformly in the specimen and remains the same throughout its exposure duration for a simplification of the ASR-induced expansion calculations. The sensitivity of RH to the field exposed blocks expansion is considered as a parametric study.

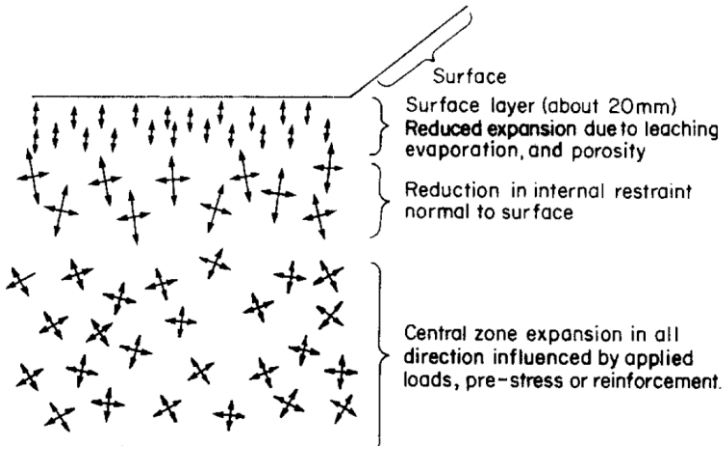

Figure 4.9: Development of expansion at different zones in a concrete member (Courtier 1990).

In general, inputs for the estimation of field exposed blocks expansion are: (1) observations from laboratory testing (i.e., ASR-induced expansion and alkali leaching over time) and, (2) environmental conditions in the field (i.e., ambient temperature and humidity, precipitation, snow and solar radiation). A two-step calculation procedure shown in Figure 4.10 was proposed to account for these two input groups for the calculation of field-exposed blocks expansion. The expansion curve and 1-year alkali leaching are utilised for the calculation of the model parameters of the semi-empirical model for the ideal "*no leaching*" scenario in the controlled environmental conditions (*Section 4.4*), while environmental conditions are taken into consideration of the differences between laboratory and field conditions as well as possible changes of field conditions over time.

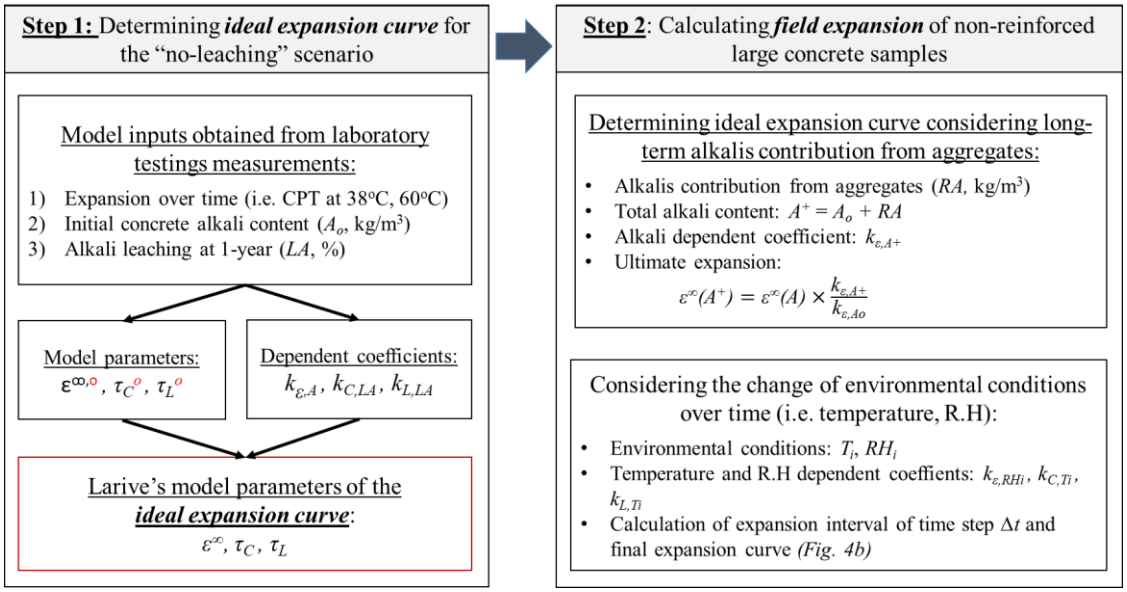

Figure 4.10: Overall procedure for modelling expansion of concrete in the field.

In the first step, by assuming that no leaching of alkalis occurs from the field blocks, the ultimate expansion and time constants (ε^{∞} and τ_C, τ_L) of the ideal "*no-leaching*" scenario are calculated from the expansion over time and the alkali leaching amount at 1 year measured from laboratory samples. The inputs obtained from the laboratory tests include expansion over time, initial concrete alkali content and leaching of alkalis at 1 year. The implementation procedure of this step is proposed and presented in Section 4.4.

In the second step, factors affecting the field expansion, such as long-term alkali contribution from aggregates and environmental conditions (i.e., temperature, humidity) are taken into account. For the alkali contribution from the aggregates (whether occurs), alkalis are normally released over time during long-term exposure in the field. Yet, there is currently no experimental data available for this time-dependent alkali release in field concrete. Therefore, the contribution of alkalis from aggregates (RA, kg/m^3) is considered in this study as an additional amount to the total concrete alkali content. As such, after calculating the ideal "no leaching" expansion curve for the concrete mixture with the

original alkali content of A_o (kg/m^3), the alkali content-dependent coefficients of A_o and A_o + RA alkalis are adopted to update the ideal ultimate expansion (i.e., considering the alkali contribution from the aggregates). It is important to note herein that the test procedure for long-term alkali release is still limited, thus the amount of releasing is commonly approximately estimated from the aggregates testing in alkaline solutions.

After finalising the ideal expansion curve at the reference laboratory exposure conditions (i.e., 38^{o}C and 100% RH), the effect of field environmental conditions is considered through temperature- and RH-dependent coefficients presented in Section 4.4.3. Figure 4.11 illustrates the calculation procedure to capture the effect of the environmental conditions in the field, which is adopted from (Kawabata et al. 2016). As the temperature and RH in the field and thus in concrete changes over time, their effects on ASR-induced expansion have to be continuously considered. Each environmental condition produces an expansion curve of the concrete, namely a master curve. Expansion calculation is implemented through the determination of the incremental expansion of every single time step Δt. The incremental expansion at the time t_i is calculated based on the master curve of the corresponding environmental conditions (i.e., T_i, RH_i). The monthly average ambient temperature was utilised for the expansion calculation of the concrete blocks; thus the time step of 1 month was adopted in this work.

The validation of the proposed semi-empirical model has been then conducted using three important experimental campaigns: : (1) Kingston exposure site, ON, Canada (Doug Hooton et al. 2013; MTO 2018); (2) CANMET exposure site, ON, Canada (Fournier et al. 2019; Fournier et al. 2009; Fournier et al. 2018); and (3) The University of Texas at Austin, USA (UT) (Fournier et al. 2009; Ideker et al. 2012).

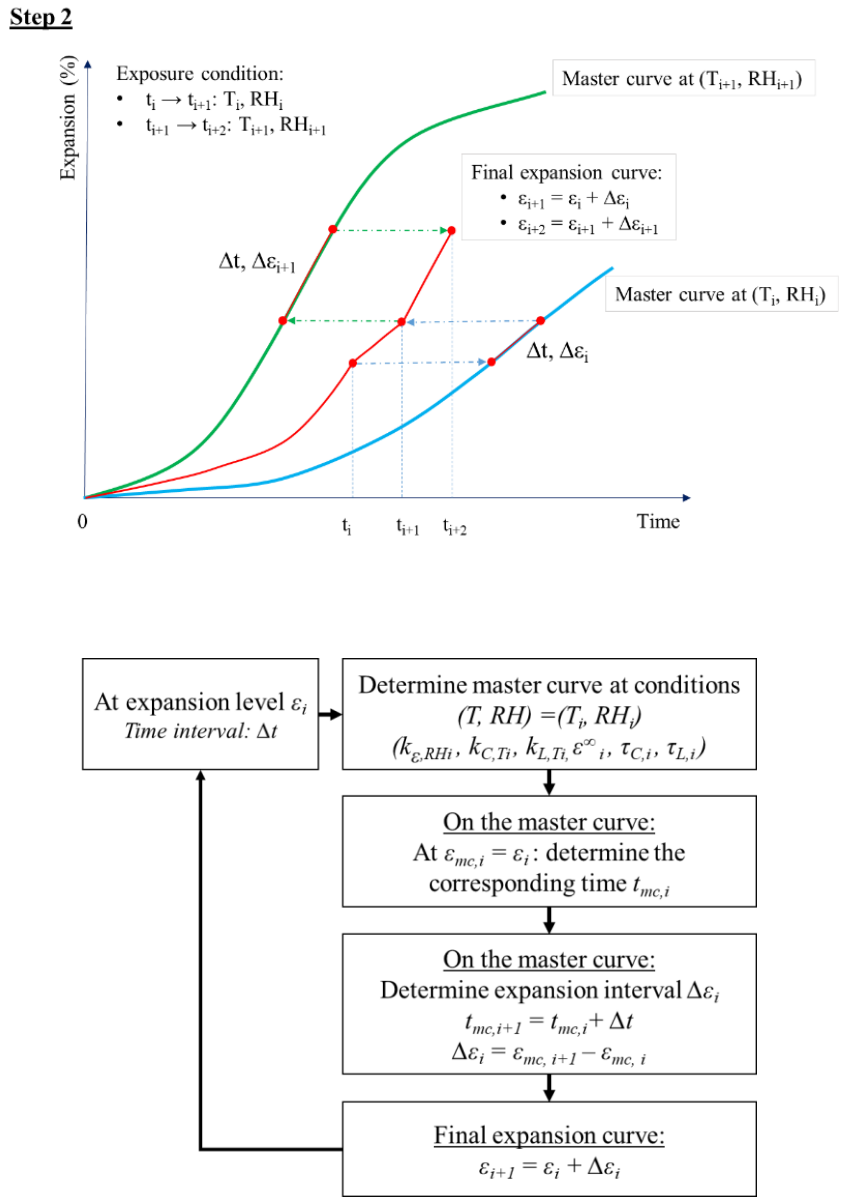

Figure 4.11: Schematic procedure for the consideration of environmental conditions.

4.5.2. Overview of exposure sites/samples and climatic conditions

4.5.2.1. Kingston exposure site

This outdoor exposure site was established by the Ontario Ministry of Transportation (MTO) in Kingston, Ontario, Canada in 1991, which aimed at providing correlation between short-term laboratory tests and long-term performance, as well as evaluating the efficiency of SCMs in mitigating ASR development (Doug Hooton et al. 2013; MTO

2018). Different concrete mixtures incorporating the Spratt reactive aggregate, both high- and low-alkali content cements, and several types and proportions of SCM have been used in this experimental campaign. The low- and high-alkali cements (LAPC and HAPC) contained 0.79% and 0.46% Na_2O equivalent per cement mass, respectively, which consists of 3.33 kg/m^3 and 1.91 kg/m^3 of alkalis in the concrete, respectively. The field study was conducted on both pavement slabs (0.2 x 1.2 x 4 m) and beams (0.6 x 0.6 x 2 m) both reinforced and non-reinforced, while three prisms (75 x 75 x 400 mm) were manufactured from the same concrete mixtures for laboratory testing. In (Doug Hooton et al. 2013), the authors reported for up to 20-year data of all these field-exposed elements and CPT samples. A recent report from the MTO in 2018 reported the updated 27-year data of this field exposure site (MTO 2018). In this study, only the data from the CPT samples and non-reinforced field beam elements (with both low- and high- cement contents) were utilised for the purpose of validation of the proposed model.

4.5.2.2. CANMET and UT exposure sites

The CANMET and UT exposure sites were established as a part of a comparative study on the laboratory versus field performance using a wide variety of reactive aggregate types and natures across North America to study the efficiency of laboratory testing in representing field performance in different climatic conditions as well as to investigate the effectiveness of numerous preventive measures (Fournier et al. 2009; Ideker et al. 2012). Concrete mixtures incorporating several reactive aggregates and different concrete alkali contents were tested for expansion in both the laboratory (i.e., CPT) and in the field (i.e., 0.40 × 0.40 × 0.70 m blocks manufactured in Ottawa - CANMET and Texas -UT). There are two main series of concrete blocks tested in these two sites: (1) an “exchange series” where concrete blocks were made at CANMET to be tested at both CANMET and UT sites, and (2) blocks with almost identical mixtures both made and tested at CANMET

and UT. The CPT expansion test results and corresponding field data of the second series were reported in (Fournier et al. 2019; Fournier et al. 2009; Fournier et al. 2018) up to 20-year exposure, while tested data of the exchange series is available only up to 3 years. In this study, the data of two concrete mixtures (i.e., containing Spratt limestone, Sudbury gravel) are collected for the model validation. The mix proportioning used for the concrete mixtures incorporating these two reactive aggregates are almost identical from the two sites; therefore, the results are preferable to evaluate the effect of environmental conditions. Figure 4.12 shows information on weather conditions including yearly average temperature, relative humidity and precipitation. The environmental conditions in Kingston are almost the same as in Ottawa (CANMET); therefore, the same temperature was used for the calculation of both sites.

(a)

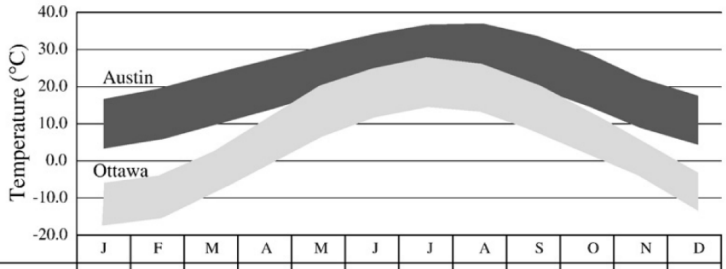

		J	F	M	A	M	J	J	A	S	O	N	D
Ottawa	Average	-10.8	-8.7	-2.5	5.7	13.4	18.3	20.9	19.5	14.3	7.8	1.0	-7.1
	High	-6.1	-4.1	2.2	10.8	19.1	23.8	26.5	24.9	19.5	12.5	4.8	-3.0
	Low	-15.3	-13.3	-7.1	0.6	7.7	12.7	15.4	14.1	9.1	3.0	-2.8	-11.1
Austin	Average	10.1	12.5	16.5	20.1	23.9	27.2	29.0	29.1	26.4	21.4	15.4	11.2
	High	15.7	18.4	22.5	26.1	29.3	32.7	35.0	35.3	32.3	27.4	21.2	16.8
	Low	4.4	6.7	10.5	14.2	18.6	21.7	23.0	22.9	20.4	15.4	9.6	5.5

(b)

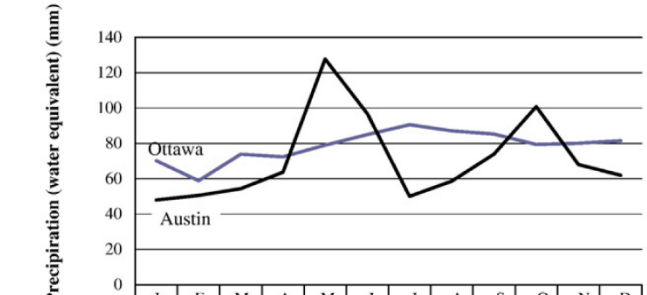

	J	F	M	A	M	J	J	A	S	O	N	D
Ottawa	70.2	58.9	73.9	72.4	79	85	90.6	87.1	85.3	79.4	80.1	81.5
Austin (mm)	48.0	50.5	54.4	63.8	127.8	96.8	50.0	58.7	73.9	100.8	68.1	62.0

Figure 4.12: Average yearly temperatures (a) and precipitation (b) at Austin and Ottawa & Kingston (Fournier et al. 2009).

In this study, the leaching of alkalis at 1-year required for the calculation of the ideal "no leaching" expansion curve of concrete with Spratt and Sudbury are assumed to be 21.9 % and 35.1% of the total concrete alkali content, respectively, which is 85% of the 1.5-year leaching amount measured from the CPT in Sino & Shehata (2019) (Sinno & Shehata 2019). In addition, the alkali release from these two reactive aggregates may also be important in the estimation of the field expansion. As such, Bérubé et al. (2002) tested the alkali release of the Spratt and Sudbury aggregates through crushing (i.e., 1.25 - 5 mm particles in size) and immersion of the aggregates particles in different solutions (i.e., distilled water, saturated lime and 0.7 N NaOH (or KOH) solutions) for 578 days at 38^{o}C; the 0.7 M alkaline solution was the most similar to the concrete pore solution bearing a high alkali Portland cement. The amount of alkali release in 0.7 M alkaline solution after 578 days of the Sudbury aggregate was more than 0.166% per aggregate mass with high potential of further increasing when compared to only 0.009% of the Spratt aggregate. This result is reasonable since the total $Na2O_e$ content in the Sudbury and Spratt aggregates measured in the same study were 4.35% and only 0.09% per aggregate mass, respectively. Moreover, the authors stated that the amount of alkali release from long-term exposed concrete incorporating coarse aggregate particles in the field could be as high as from the crushed particles measured after 578 days in this aggressive condition. With the significant amount of alkalis possibly contributing to ASR-induced development from the Sudbury aggregate, the expansion calculation of the Sudbury blocks without and with the alkali contribution of 0.166% per aggregate mass (i.e., 1.75 kg/m^3 of concrete) were conducted for comparison purposes. Conversely, the alkalis release from the Spratt aggregate is assumed negligible.

4.5.3. Modelling expansion of Kingston non-reinforced concrete beams

The CPT results were utilised for calculating the ASR-induced expansion of 27-year field-exposed beams incorporating low and high-alkali cement (LAPC and HAPC), as shown in Figure 4.13. Apparently, the ultimate expansion obtained from the CPT is significantly lower than the expansion of the field beam at 27-year exposure. This difference is considered in the proposed model by considering the alkali leaching from the CPT. Furthermore, the concrete beams exposed to lower temperatures (i.e., the maximum temperature of 26.5ºC) show significantly lower expansion rates when compared to prisms at 38ºC. The temperature-dependent model is adopted to account for this environmental condition difference.

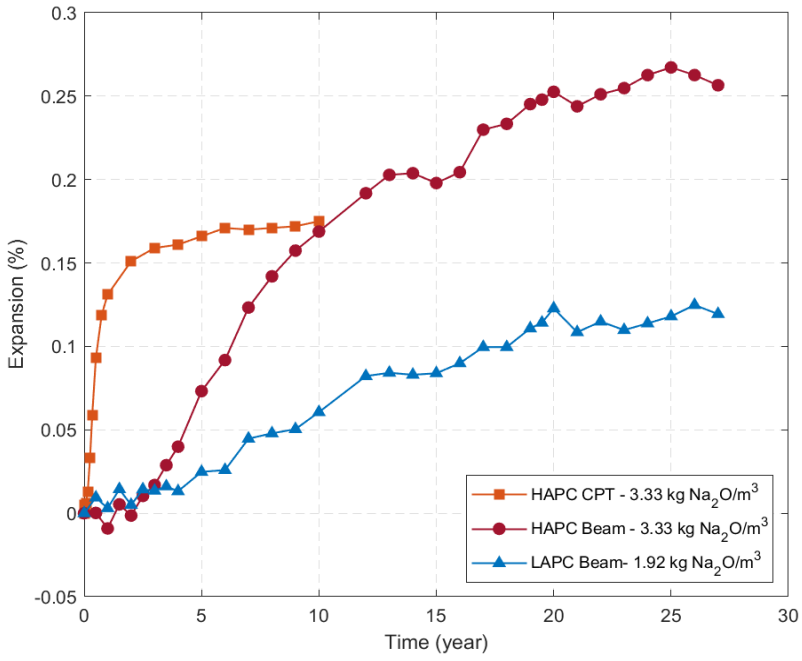

Figure 4.13: Experimental results of field beams exposed in Kingston exposure site and the corresponding CPT.

As stated previously, inputs for the proposed semi-empirical model are the initial concrete alkali content, the expansion over time and leaching of alkalis from the CPT test. The total Na_2O equivalent of the LAPC and HAPC concrete mixtures were 1.92 kg/m^3 and 3.33 kg/m^3 (i.e., 0.46% and 0.79% per cement mass), respectively, which were all from the cement. The alkali leaching at 1 year for the concrete mixture containing Spratt aggregate was assumed to be 21.9 % of the total concrete alkali content, which is 85% of the 1.5-year leaching amount measured from the CPT in (Sinno & Shehata 2019). Calculation of model parameters for the ideal "no leaching" expansion curve of HAPC concrete is shown in Table 4.3. In this table, τ_C, τ_L and ε^{∞} are firstly derived from the expansion curve measured in laboratory testing through curve fitting. The alkali content-dependent coefficients, $k_{\varepsilon,Ao}$ and $k_{\varepsilon,A}$, are calculated using the relationship provided in Figure 4.4 for original and updated alkali content for the no leaching scenario, respectively. Alkali leaching-dependent coefficients for time constants, $k_{C,LA}$ and $k_{L,LA}$, are determined from Eq. 4.18 and 4.19, respectively, using the data of alkali leaching at 1 year provided.

The ideal expansion curve of LAPC is derived from the HAPC's using the proposed relationship in Figure 4.4. Temperature and relative humidity effects are considered through Eqs. 4.10 – 4.12 and their time-dependent consideration are implemented using the procedure proposed in Figure 4.11. Since the internal RH was assumed to be 100%, only the monthly average temperatures (see Figure 4.12) were used to consider the field environmental conditions in Kingston, Ontario.

Table 4.3: Model parameters for ideal expansion curve of LAPC and HAPC concrete

Test data and model parameters derived from test data		Model parameters for the ideal "no-leaching" expansion curve	
Initial concrete alkali content (kg/m^3)	3.33	Updated alkali content (kg/m^3) (After compensated the leaching)	4.27
$k_{\varepsilon,Ao}$	0.423	$k_{C,LA}$	0.781
τ_C	120	$k_{L,LA}$	0.846
τ_L	120	$k_{\varepsilon,A}$	0.721
ε^{∞}	0.165	$k_{\varepsilon,A}/k_{\varepsilon,Ao}$	1.702
1-year leaching (%)	21.9	τ_C	**153.7**
		τ_L	**141.8**
		ε^{∞}	**0.281**

Results

For both concrete mixtures HAPC and LAPC, the calculation for field beams were calculated with and without considering the alkali leaching from the CPT test for comparison purposes. Figure 4.14 shows the predicted results of both mixtures with and without considering the alkali leaching effect in comparison to the measured data. Apparently, without considering alkali leaching (i.e., directly used the experimental results from the CPT), the estimated expansions are significantly smaller than the measured ones for both HAPC and LAPC concrete mixtures. Such finding is consistent with the experimental observations from many other studies when comparing laboratory

and field expansion (Doug Hooton et al. 2013; Fournier et al. 2019; Ideker et al. 2012; Thomas et al. 2006). By taking the leaching of the CPT into consideration, the calculation provided very good agreement with the measured data. For the HAPC, the ultimate expansion of the modelled expansion curve is slightly higher than the maximum expansion measured from the blocks, while the calculated ultimate expansion of the LAPC is slightly smaller than the measured one. However, there is no sign of flattening the expansion curve of the LAPC beam; therefore, the estimated expansion could significantly underestimate the expansion of the LAPC beam after 27 years. These differences could come from the difference in 1-year alkali leaching amount of HAPC and LAPC, which is assumed the same for concrete mixtures of different alkali contents. Furthermore, the proposed unique relationship between alkali content and ultimate expansion may also contribute to the differences.

In general, the proposed model which considering the effects of alkali content and alkali leaching significantly improve the correlation between laboratory testing and long-term field performance of ASR-affected concrete. This outcome also highlights the importance of measuring alkali leaching from expansion tests in the laboratory.

(a)

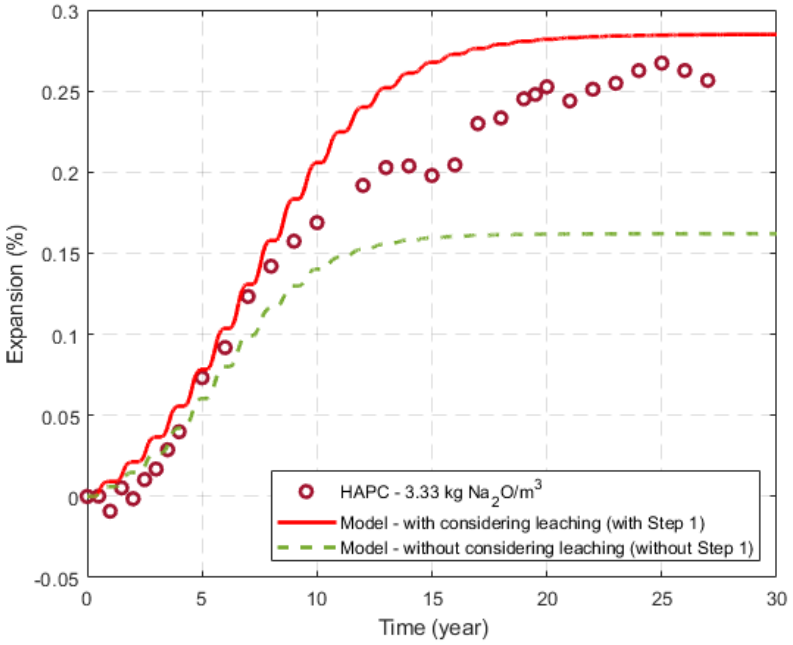

(b)

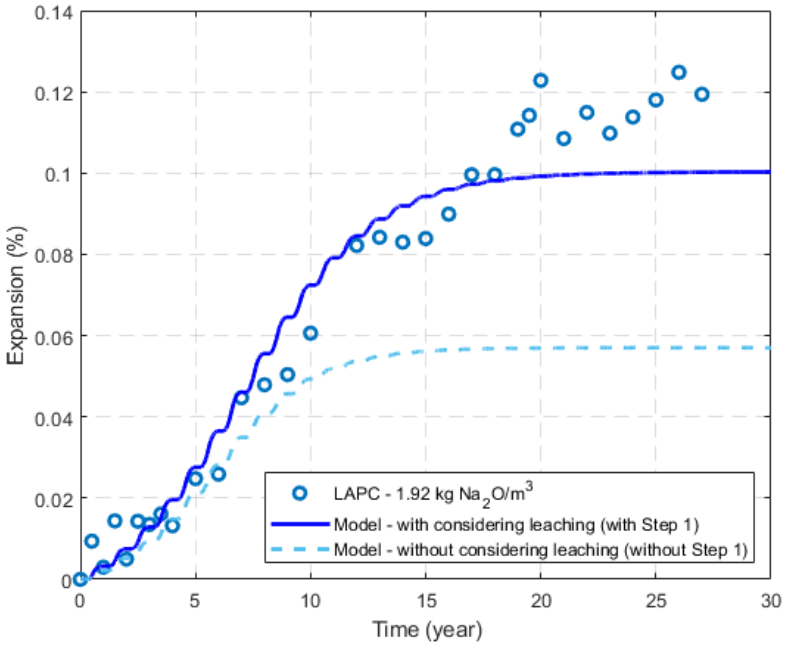

Figure 4.14: Model outcomes in comparison to the experimental data: (a) HAPC and (b) LAPC non-reinforced beams.

4.5.4. Modelling expansion of CANMET non-reinforced concrete blocks

Test data of concrete incorporating Spratt and Sudbury reactive aggregates and various concrete alkali content investigated in CANMET and UT sites were collected for validation purposes. Three typical amounts of Na_2O_e were used in this experimental campaign: 0.4%, 0.9% and 1.25% (boosted with additional reagent grade NaOH) per cement mass, equivalent to approximately 1.7, 3.8 and 5.25 kg/m^3, respectively. Table 4.4 presents the calculation of model parameters for the ideal "no leaching" expansion curve for mixtures made of Spratt and Sudbury aggregates bearing 5.25 kg/m^3 alkalis. The Sudbury concrete shows lower ultimate expansion from the measurements but higher ultimate expansion for the ideal expansion curve when compared to the Spratt. This observation could be explained by the significant alkalis leaching from Sudbury concrete in the laboratory.

Table 4.5 shows the ultimate expansion calculated for other mixtures varying in concrete alkali content. Figure 4.15 shows the predicted results of the mixtures containing Spratt and Sudbury aggregates bearing 5.25 kg/m^3 of alkalis with and without considering the alkalis leaching. Similar to the observation from Kingston's beams, it is obvious that without considering the leaching effect, the model underestimates field expansions of blocks made of both Spratt and Sudbury aggregates. Accounting for the leaching of alkalis, the model provides a good estimation of Spratt blocks' induced expansion. Similar to the observation from the Kingston's beams, the model results are closely matched with experimental observations for induced expansion up until 0.1%; however, at higher expansion levels (i.e., above and beyond 0.15%), the calculated expansion rate is noticeably higher than the measured expansion.

Table 4.4: Model parameters for ideal expansion curves of Spratt and Sudbury blocks tested in CANMET

CANMET and UT sites		**Spratt**	**Sudbury**
Test data and model parameters derived from test data	Initial alkali content (kg/m^3)	5.25	
	$k_{\varepsilon,Ao}$	1	
	τ_C	100	85
	τ_L	130	215
	ε^{∞}	0.250	0.200
	1-year leaching (%)	21.9	35.1
Model parameters for the ideal "no-leaching" expansion curve	Updated alkali content (A, kg/m^3) (After compensated)	**6.72**	**8.09**
	$k_{C,LA}$	0.781	0.649
	$k_{L,LA}$	0.846	0.754
	$k_{\varepsilon,A}$	1.597	2.150
	$k_{\varepsilon,A}/k_{\varepsilon,Ao}$	1.597	2.150
	$\boldsymbol{\tau_C}$	**128.1**	**131.0**
	$\boldsymbol{\tau_L}$	**153.6**	**285.0**
	$\boldsymbol{\varepsilon^{\infty}}$	**0.399**	**0.430**

Table 4.5: Calculation of the ultimate expansion of mixtures varying in concrete alkali content

	Spratt			**Sudbury**			
A *(kg/m^3)*	5.25	3.78	1.68	5.25	3.78	5.25 + **1.75** (***RA***)$^{(*)}$	3.8 + **1.75** (***RA***)$^{(*)}$
$\boldsymbol{k_{\varepsilon,A}}$	1	0.588	0.108	1	0.588	1.708	1.113
$\boldsymbol{\varepsilon^{\infty}}$ *(%)*	0.399	0.235	0.043	0.430	0.253	0.735	0.479
$^{(*)}$ considering additional long-term alkali contribution from the aggregate							

For the Sudbury blocks, despite improving the expansion estimation by considering only the leaching of alkalis in the laboratory, the predicted expansion is still remarkably lower than the measurements, i.e., 0.408% from the model compared to 0.651% from the measurement at 20 years of exposure (see Figure 4.15(c)). Conversely, the model with additional consideration of alkali release provides, as shown in Figure 4.15(d), significantly better expansion estimation when compared to the previous one. By raising the total alkalis from 5.25 kg/m^3 to 7.0 kg/m^3, the ultimate expansion increases by about 70% compared to the model outcome ignoring the releasing effect. This result highlights the significant effect of alkali contribution from aggregates to the long-term field expansion for some particular aggregates, as well as emphasises the validity of the alkali release results reported in (Bérubé et al. 2002), which are negligible for the Spratt aggregate and significant for the Sudbury aggregate.

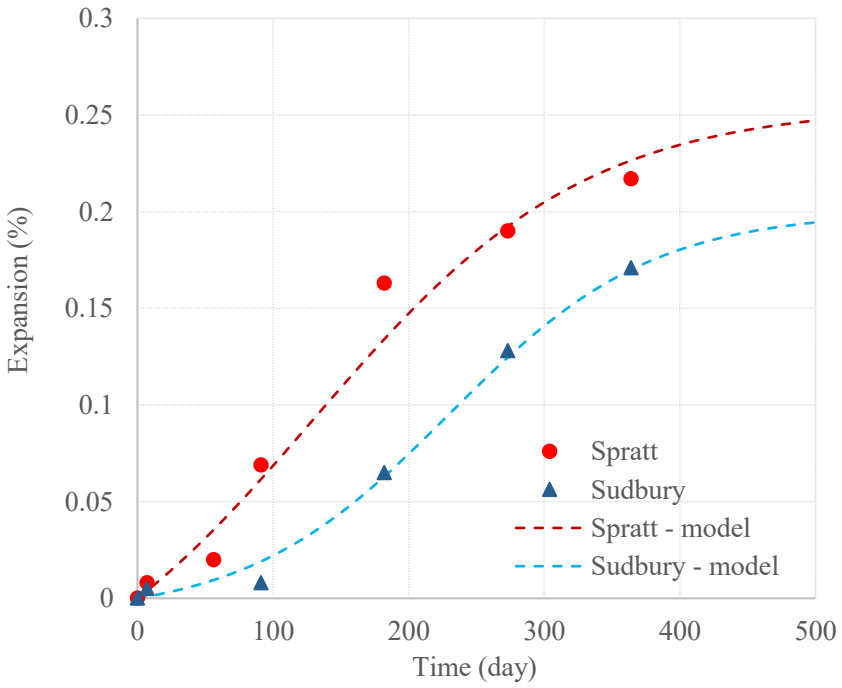

(a) Expansion curves derived from CPT test results

Figure 4.15: Model outcomes in comparison to the experimental data of specimens in CANMET

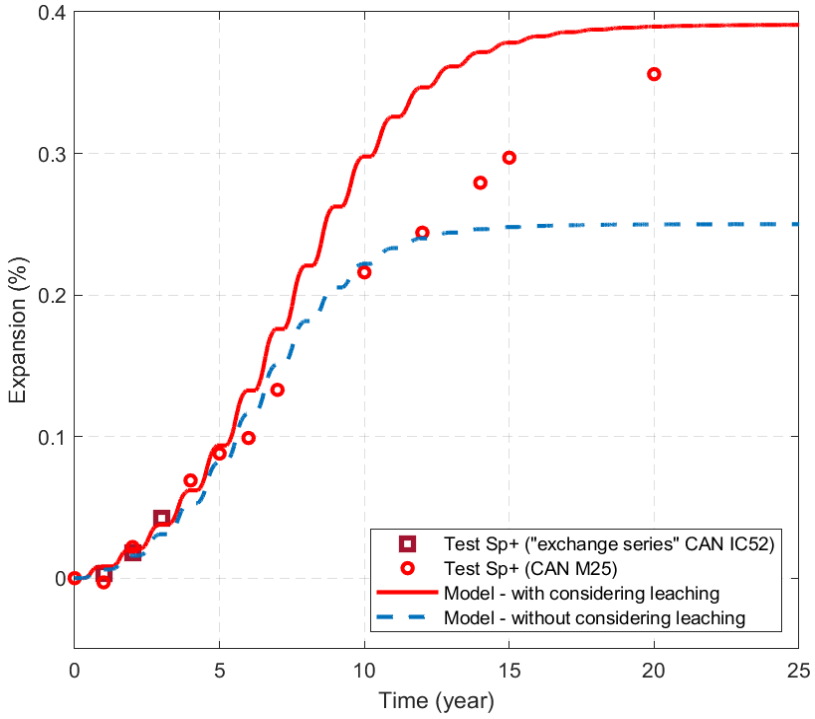

(b) Spratt concrete blocks

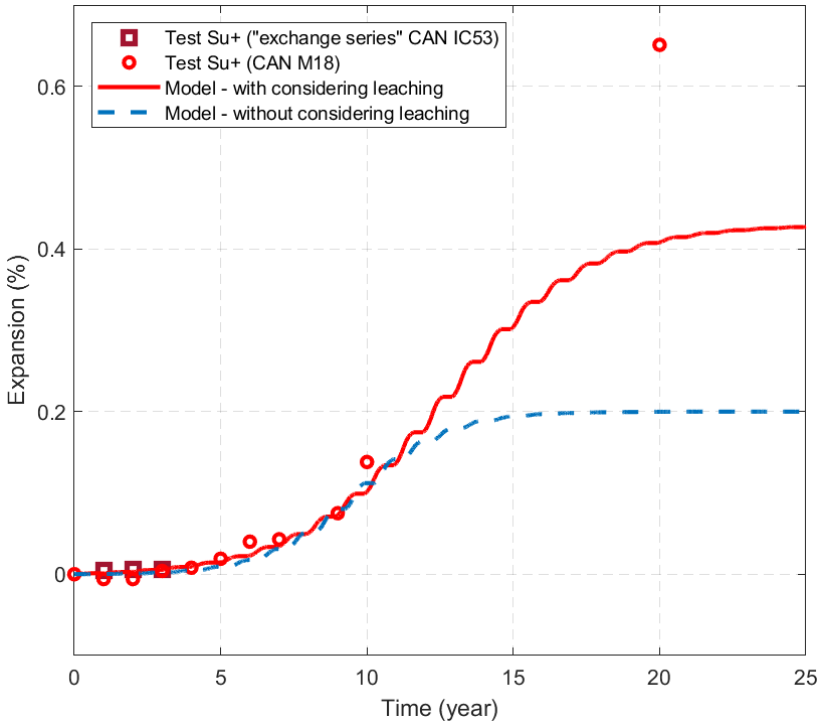

(c) Sudbury concrete blocks without considering alkali release

Figure 4.15: Continued.

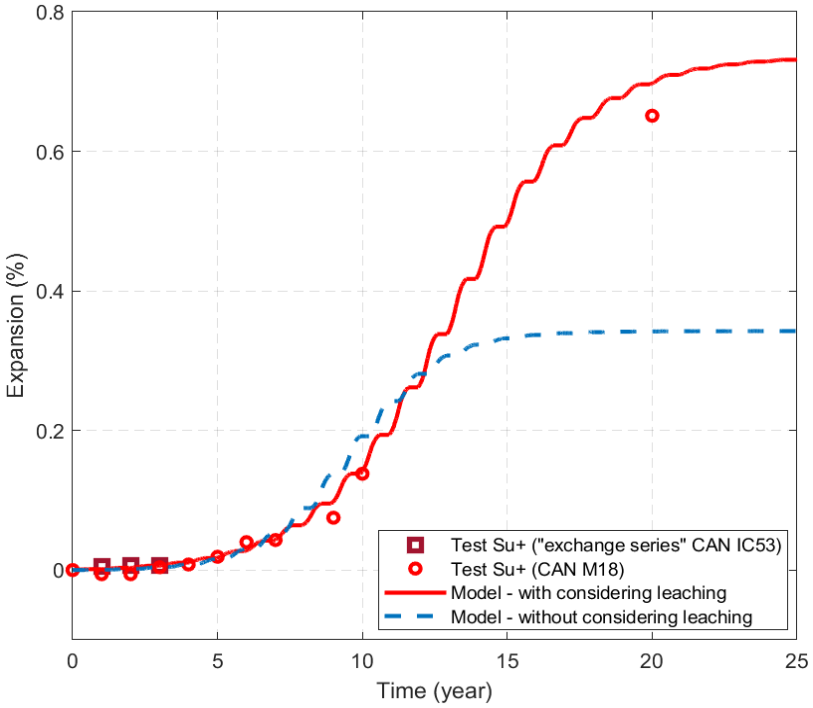

(d) Sudbury concrete blocks with considering alkali release

Figure 4.15: Continued.

Figure 4.16 illustrates the model outcomes for the mixtures made of Spratt and Sudbury aggregates varying in concrete alkali level in comparison to the measured data. For the Spratt concrete blocks, the model captures very well the expansion of the block with 0.9% alkali content but underestimates the expansion of blocks with 0.4% of alkali. As suggested in (Deschenes Jr et al. 2018), the combination of ASR and freezing and thawing cycles could increase the expansion of concrete mixtures made of borderline-reactive aggregates. Therefore, the consideration of this combination is required in future works to avoid the misleading in estimating and evaluating the risk of using borderline-reactive aggregates in practice. For the Sudbury concrete blocks, by accounting for the alkali contribution by the aggregate, the model also provides excellent results for the concrete made of cement with 0.9% of alkalis (i.e., 3.78 kg/m^3). This result again shows the reasonability of considering the alkali contribution by aggregate along with the applicability of alkalis – expansion relationship proposed in ***Section 4.4.4***.

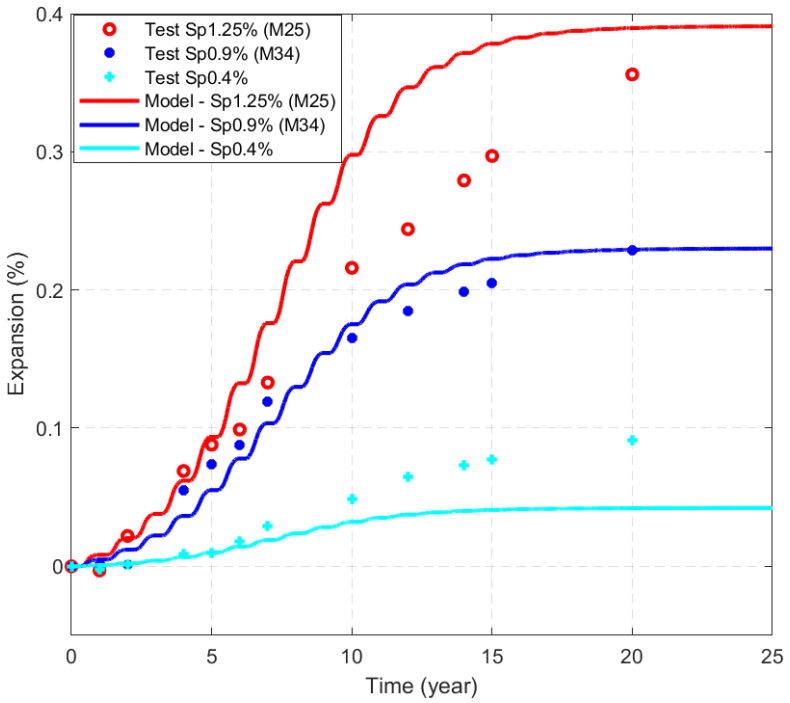

(a) Spratt concrete blocks

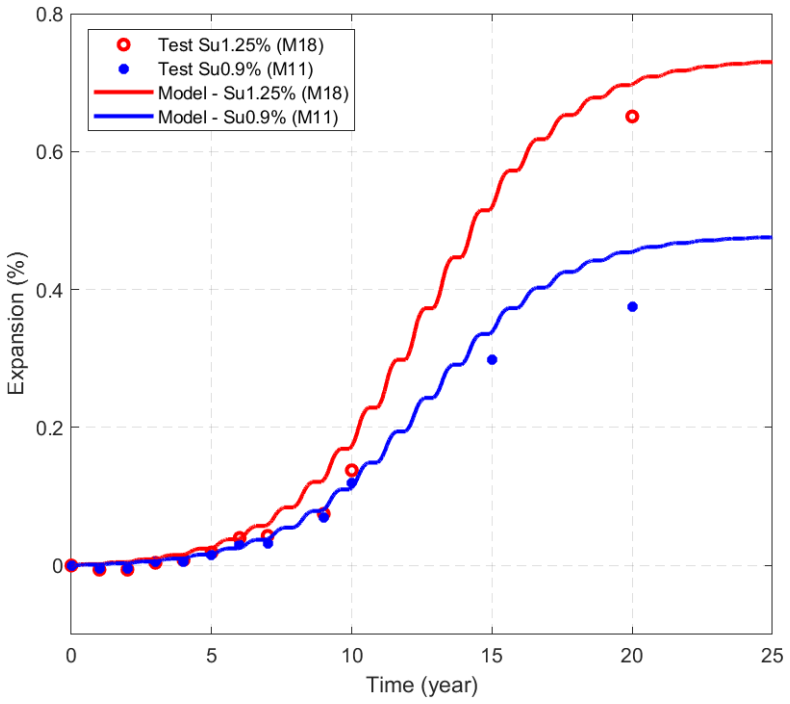

(b) Sudbury concrete blocks

Figure 4.16: Model outcomes in comparison to the experimental data of specimens incorporating different alkali contents in CANMET.

4.5.5. Modelling expansion of UT non-reinforced blocks

Thanks to the field data from the Kingston and CANMET exposure sites, the proposed model proved its efficiency in correlating laboratory and field performance of ASR-affected concrete by accounting for the alkali leaching in the laboratory along with climatic conditions in Ontario, Canada. This section aims at further validate the proposed model at different environmental conditions, i.e., warmer climate conditions in Texas (UT site), and cooler climate conditions in Ottawa (CANMET site). The climatic conditions in Texas, as shown in Figure 4.12, indicate almost the same high level of precipitation but significantly higher temperature when compared to the Ontario climate conditions. The field expansion of concrete blocks in the UT site was thus about 4-5 time faster than the blocks with the same concrete mixtures in CANMET (Fournier et al. 2009).

The model parameters established for the ideal “no leaching” expansion curves of the mixtures made of Spratt and Sudbury reactive aggregates at CANMET were utilised for determining the expansion of the corresponding concrete blocks stored in Texas, by adopting the temperature-dependent model presented in Section 4.4.3. Figure 4.17 shows the model outcomes of concrete blocks made of Spratt and Sudbury at CANMET and UT sites in comparison to the field observations. Similar to the experimental observations of (Fournier et al. 2009), the ASR-induced expansion calculated for blocks kept at the UT was obviously faster than CANMET’s, i.e., about 4-5 times. For mixtures made of Spratt and Sudbury reactive aggregates, the model outcomes are relatively close to the block measurements made and kept at the UT. For the exchange series, the measured ones are notably smaller than the calculated ones. This difference could be from a delay of expansion due to transportation of the blocks in the first year. In general, the proposed model provides a reasonably good estimation of ASR-induced expansion from the two

sites with different environmental conditions using only a single set of the laboratory testing data.

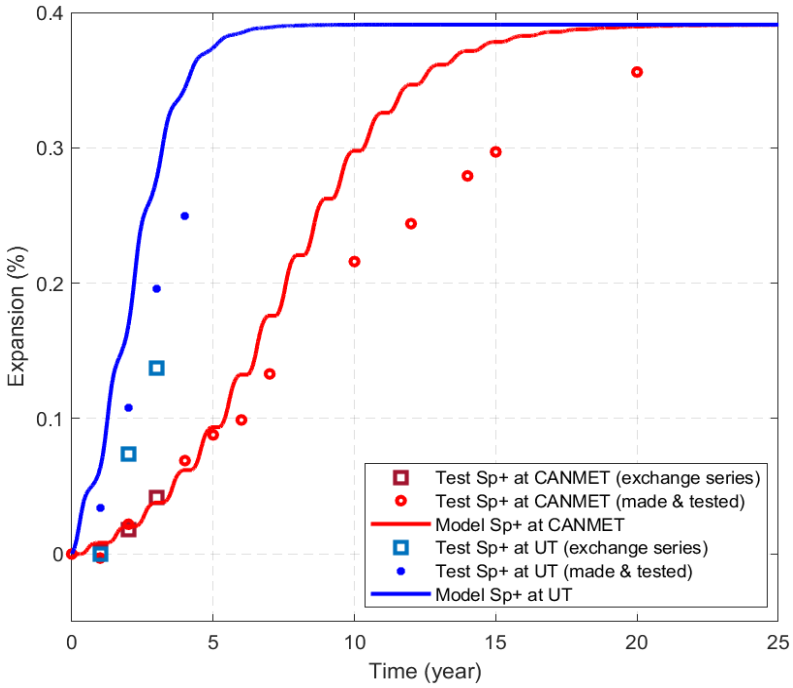

(a) Spratt concrete blocks

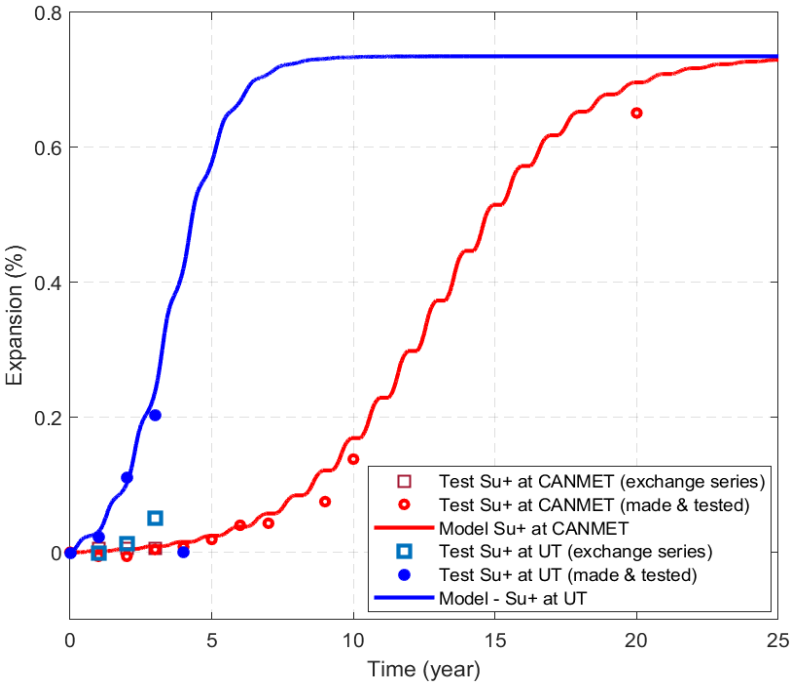

(b) Sudbury concrete blocks

Figure 4.17: Model outcomes in comparison to the experimental data of concrete blocks kept at CANMET and UT sites.

4.6. Discussion

4.6.1. Consideration of alkali leaching from test samples and alkali releasing from aggregate: their importance and limitation

It is well established that the concrete prism test (CPT) is likely the most reliable standard test method for assessing the reactivity of aggregates in the laboratory; yet it has been found that its reliability is inadequate to predict ASR-ultimate induced expansion (i.e., maximum expansion) in the field (Fournier et al. 2009; Thomas et al. 2006). Specifically, the CPT expansion results normally underestimate the long-term expansion of field concrete members. As mentioned earlier, the main reason for this lack of laboratory-field correlation is the alkalis leaching of concrete, which is significantly higher from laboratory test specimens (and minimal in field members). Therefore, consideration of the alkalis leaching is crucial in forecasting ASR-induced expansion in field concrete members based on laboratory observations.

The procedure presented in ***Section 4.5.1*** showed the capability to account for the effects of the alkali content and leaching to predict ASR-induced expansion in field concrete. The validity of the proposed procedure is shown by the good agreement between modelling and field results for concrete mixtures made of Spratt reactive aggregate and stored in three different exosure sites (i.e., Kingston, CANMET and UT); whereas, the model without considering the leaching of alkalis obviously underestimates ASR-induced expansion of affected concrete in all these three exposure sites. This observation, again, highlights the importance of the alkali content on ASR-induced expansion as well the need of considering the leaching of alkalis in the estimation of field concrete based on laboratory test results (i.e., CPT). On the effect of alkali leaching, it is important to notice that the proposed reationship between the ultimate expansion (ε^{∞}) and alkali content was

based on laboratory data of 1-year CPT from various studies, which was basically from concrete samples with different leaching levels. Hence, the ultimate expansion measured at different alkali contents, either from the field exposed blocks or from laboratory testing with limited leaching such as the MCPT and CCT (Chopperla 2019), are very useful to improve the relationship. Moreover, current practice of using CPT is mainly for assessing the potential reactivity of aggregates; therefore, attention is normally not paid to measuring the alkalis leaching. The susscessful outcome obtained from the proposed semi-empirical model emphasized the great significance of alkali leaching measurements of mixtures incorporating different reactive aggregates for predicting the potential of fufure ASR-induced expansion and deterioration (i.e., prognosis) of ASRaffected concrete in the field. Furthermore, the alkali contribution from aggregates of long-term exposure concrete in the field was reported to be significant for some particular aggregates such as the reactive Sudbury aggregate (Bérubé et al. 2002; Sinno & Shehata 2019), which notably contributes to the expansion of the field concrete as previously observed by (Fournier et al. 2018). Despite of appraising the leaching of alkalis, the proposed model still underestimates the expansion of Sudbury field concrete blocks. By additionally considering the alkali contribution from the Sudbury aggregate using data from (Bérubé et al. 2002), the proposed model (see ***Section 4.5.1***) provides a better estimation of the field blocks expansion. However, it is worth noting that the reliability of test methods for assessing the alkali release from aggregates is still limited, and therefore, more attention should be paid to obtain better measurements of the potential alkali contribution from aggregates (Drolet, Duchesne & Fournier 2017).

4.6.2. Effect of environmental conditions: RH and temperature

In the previous sections, the average monthly concrete temperature and 100% internal RH were reasonably assumed for the forecasting of expansion. The temperature in concrete, however, could vary due to the continuous change of the ambient temperature and effects of solar radiation and snow coverage. For instance, the concrete temperature in the skin portions could significantly increase under solar radiation (Gorga, Sanchez & Martín-Pérez 2018; Sanchez LF 2020).

On the relative humidity, as discussed in the previous sections, the relative humidity in concrete normally remains very high (i.e., saturated) in high-humidity climates plus the frequent water supplying from rain as the conditions in Ottawa and Texas. Yet, it must be noted that the RH in the skin portions of concrete blocks could reduce over time to balance with the ambient RH, especially when cracking occurs. Therefore, it is important to evaluate the effect of these temperature and RH change on the concrete expansion in the field. As such, a parametric study is conducted on the concrete mixtures made of Spratt and Sudbury reactive aggregates from the CANMET site to appraise the sensitivity of the temperature and RH on the field concrete expansion. Minimum and maximum temperature given in Figure 4.12 were adopted in the semi-empirical model to assess the sensitivity of concrete temperature. The variation of temperature herein is about ± 5ºC of the average temperature. Moreover, a lower RH of 95% is adopted in the model with a simplification of the same RH throughout the exposure period. It is worth noting that herein the assumption of uniform temperature and RH throughout the concrete member is still kept.

Figure 4.18 illustrates the field expansion calculated at the minimum, maximum and average temperatures. It is obvious that the temperature significantly influences the rate

of ASR-induced expansion. For example, for both Spratt and Sudbury concrete blocks, the expansion rate could be two times lower if the temperature reduces, for instance, 5ºC. The field expansion at the minimum and maximum temperatures thus completely cover all the experimental data points for both mixtures. This great sensitivity, however, requires a more comprehensive analysis of internal temperature in the long-term exposed concrete members to provide a better estimation of ASR-induced expansion.

The model results of the field expansion for the internal RH of 95% are shown in Figure 4.19. Analysing the plots, one can verify a strong effect of the RH on ASR-induced ultimate expansion. For example, on Spratt blocks, the ultimate expansion reduces from 0.391% to only 0.26% when reducing the internal RH from 100% to 95%. It is interesting to notice that the field expansion calculated for both Spratt and Sudbury blocks at 100% and 95% RH cover very well the measured ones. This emphasises the possibility of the reduction in the relative humidity during the long-term exposure of field concrete.

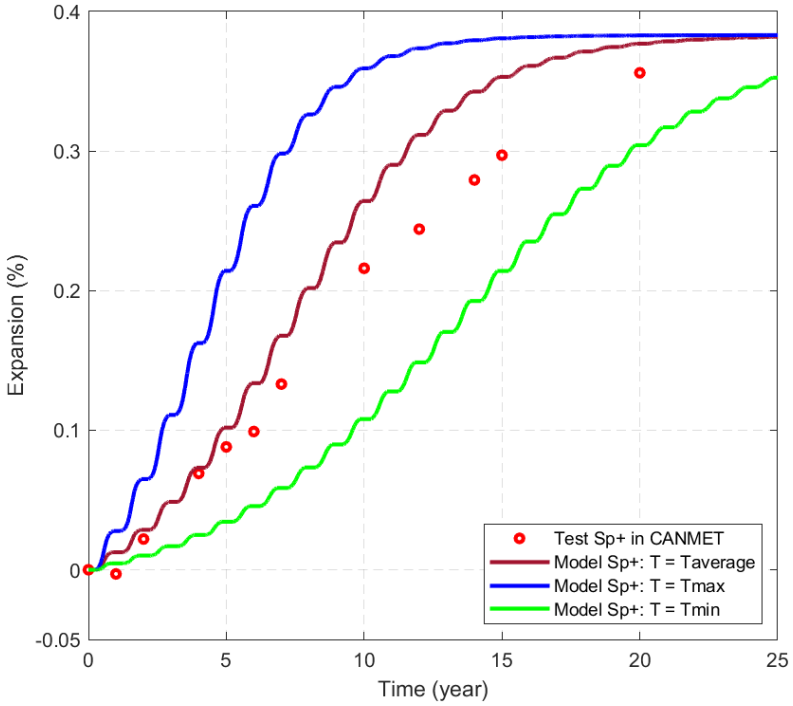

(a) Spratt concrete blocks

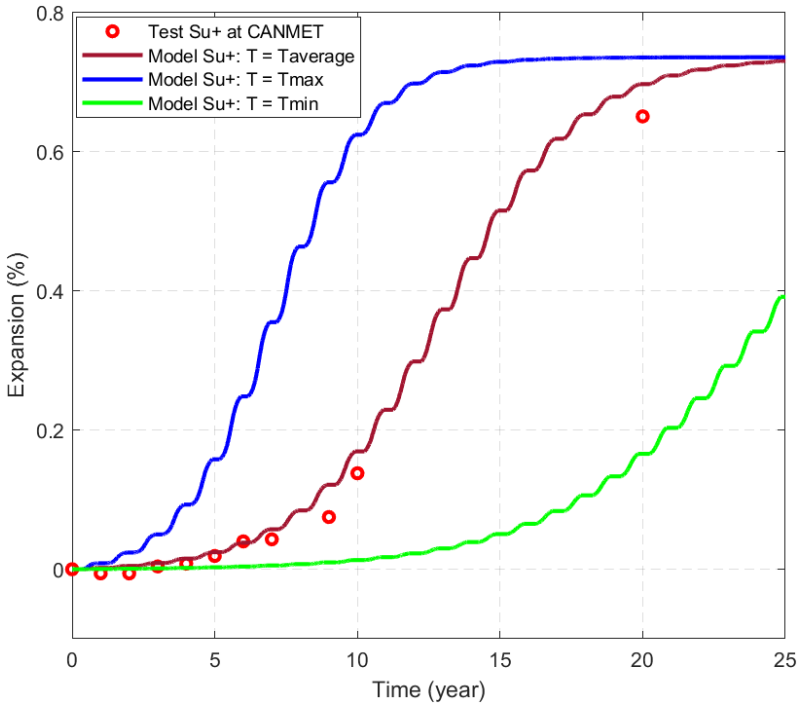

(b) Sudbury concrete blocks

Figure 4.18: Field expansion of concrete blocks at CAMENT at various temperatures.

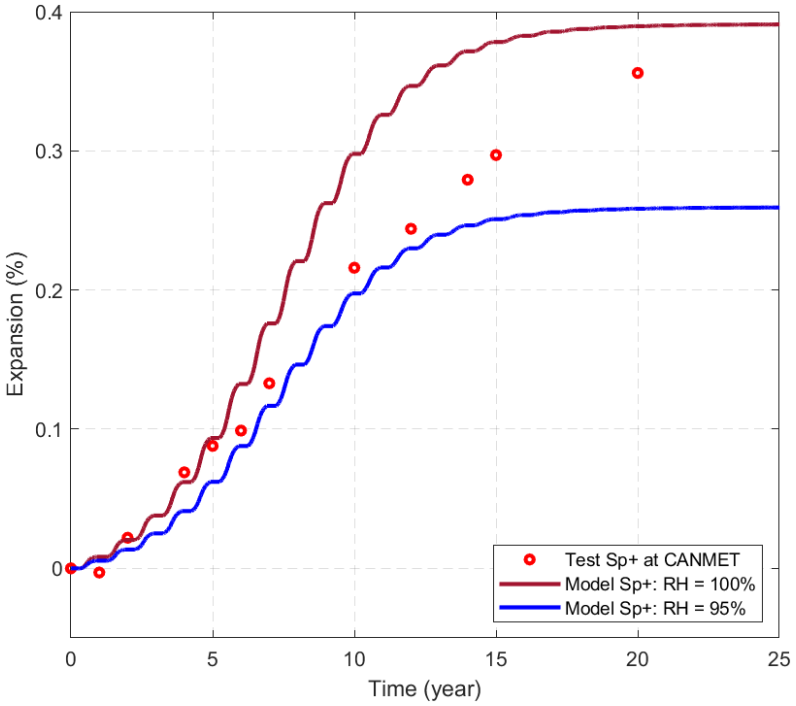

(a) Spratt concrete blocks

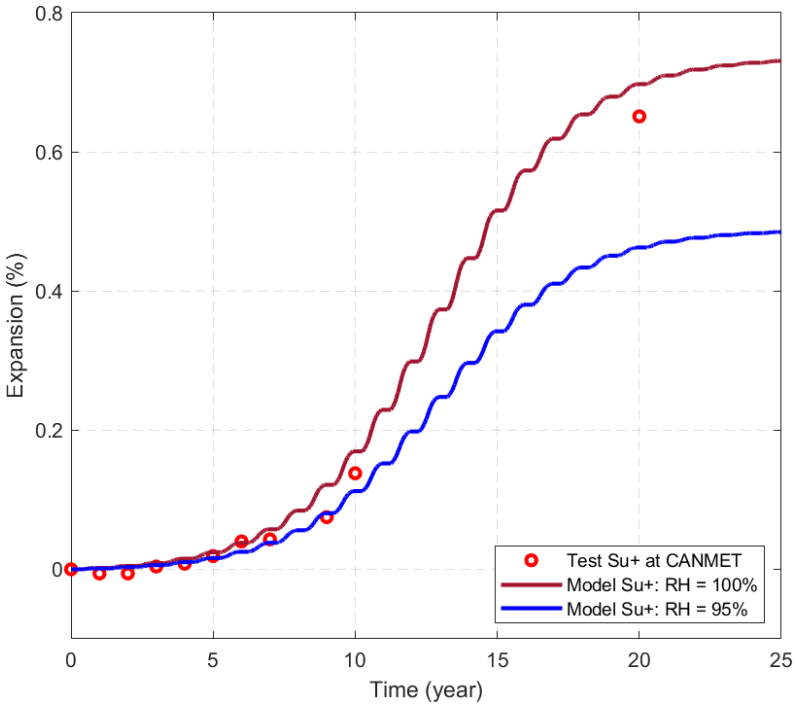

(b) Sudbury concrete blocks

Figure 4.19: Field expansion of concrete blocks at CAMENT at various RH inputs.

4.7. Concluding remarks

In this chapter, a semi-empirical model was proposed to correlate the laboratory testing to field concrete expansion, which is essential for the prognosis of ASR affected concrete structures. In addition to the laboratory expansion data, the model took into consideration of key factors affecting the expansion behaviour both from laboratory testing (i.e., concrete alkali content, alkali leaching from laboratory samples) and from the field (i.e., the temperature and relative humidity of field concrete and alkali contribution from the aggregates) in the form of Larive's model. The proposed model was able to reproduce expansion behaviour of concrete blocks exposed to different fields such as Kingston site (Ontario, Canada), CANMET site at Ottawa (Ontario, Canada) and UT site at Texas (Austin, USA). Based on the model development and results, the following conclusions can be drawn:

- The leaching of alkalis is significant in the laboratory testing on small samples affecting not only the ultimate expansion but also the time constants (i.e., characteristic and latency times) of the concrete, whereas, it is minimal in the field concrete blocks/members. By using the expansion curve and leaching at 1 year measured from laboratory testings, the proposed model is capable to estimate an ideal expansion curve without leaching to reproduce the field concrete expansion, which was well-calibrated using the different reliable laboratory testing results. In comparison to the prediction without considering the leaching, forecasting of the field expansion using the proposed model shows significant improvement in forecasting expansion of non-reinforced concrete beam exposed at the Kingston for 27 years and concrete blocks kept at CANMET for 20 years. Especially, the model results of Spratt concrete are closely matched the field observations from both

Kingston and CANMET specimens. In this regards, measurement of the alkali leaching is suggested to be very important to increase the reliability of the CPT in appraising maximum potential expansion and damage degree of the field concrete.

- For the long-term exposed concrete, the total alkali content of the concrete is contributed not only from the cement but also possibly from the aggregates. Remarkable amount of alkali released from Sudbury reactive aggregate measured in (Bérubé et al. 2002) was adopted to raise the total alkali content of this concrete mixture for the long-term expansion estimation. The good agreement between the model outcomes and measurement results of the 20-year exposed concrete blocks containing Sudbury reactive aggregate at CANMET site highlighted the significance of alkali contribution from aggregates to the long-term expansion of concrete in the field.

- The effect of environmental conditions (i.e., ambient temperature and relative humidity, precipitation) in this study are considered indirectly through concrete temperature and relative humidity. The model was successful in reproducing the expansion of both Spratt and Sudbury concrete blocks at CANMET and UT sites (i.e., the same mixture composition) using the same set of laboratory test results and their environmental condition. This outcome is crucially important in using the same the same reactive aggregates and mixture for forecasting and correlating the expansion of concrete members exposed to different locations in a country, which vary in the environmental conditions. In this regard, it is important to note that the concrete temperature highly influences the expansion rate, whereas the relative humidity has a great impact on the ultimate expansion. In addition, the modelling results also shows that the assumption of high internal RH such as 95-100 % is

reasonable for the concrete blocks kept in relatively high ambient RH and precipitation environmental condition such as at CANMET-Ottawa and UT-Texas.

The proposed simplified empirical model provides a practical, yet effective tool for forecasting ASR expansion of non-reinforced concrete in the field based on laboratory testing results. Yet, to be able to use for the prognosis of ASR affected concrete structures, the model development for reinforced and prestressed concrete member is necessary and currently in progress of development. In addition, concrete with supplementary cementing materials (SCM), which is normally used to prevent ASR, has not been investigated in this study. Therefore, it is necessary to conduct modelling for the concrete with SCM to help assess the efficiency of using SCM in preventing ASR in the field concrete. Finally, additional reliable experimental data on ASR expansion, alkali leaching and alkali releasing from aggregates from both the laboratory and the field are essential to enhance the proposed model.

Chapter 5: Numerical modelling framework for expansion and capacity of reinforced concrete affected by ASR

In Chapter 4, the proposed semi-empirical model showed its ability to forecast ASR expansion of unrestrained concrete exposed to the field conditions. For actual applications to reinforced concrete structures, effects of reinforcement and other restraints to the expansion have to be taken into consideration. As a continuation of the semi-empirical model, this chapter presents the development of a numerical modelling framework for the ASR expansion of reinforced concrete. The numerical model is a finite element-based one, which was developed in the commercial FEA package ABAQUS using the concrete damaged plasticity model. The effect of reinforcement constraints on expansion was considered in expansion modelling via two widely accepted empirical stress-dependent anisotropic expansion models. In the model, different user subroutines were developed for implementation of both the expansion-stress and expansion-mechanical properties reduction relationships. Validation of the developed numerical model was conducted using different reliable experimental datasets derived from the literature. Finally, the model was extended to modelling for the structural capacity, in which the spatial stress and residual mechanical properties were transferred from the expansion modelling.

5.1. Background

This section presents the background on impacts of stress and reinforcement restraint on the ASR expansion progress. The information is useful to specify an appropriate for modelling expansion of reinforced concrete members in numerical analyses. A review on different numerical modelling approaches for the ASR expansion and different factors required special attention in the modelling is also provided.

5.1.1. Stress-dependency of ASR expansion

Unlike unrestrained specimens in laboratory testing, concrete in actual reinforced structures is usually subjected to restraints from applied loading/prestressing, reinforcement or surrounding non-expansive boundaries, which changes the ASR expansion behaviour in reinforced concrete structures compared to the free expansion (Saouma & Perotti 2006b). Several experimental studies have examined the effects of restraints on ASR expansions (Berra et al. 2010; Dunant & Scrivener 2012; Gautam et al. 2017b; Gorga, Sanchez & Martín-Pérez 2018; Kagimoto, Yasuda & Kawamura 2014; Liaudat et al. 2018; Multon & Toutlemonde 2006). For instance, Dunant & Scrivener (2012) tested for ASR expansion of concrete under various uniaxial stress levels, i.e., 5 MPa, 10 MPa and 15 MPa. Their results show more than 80% reduction in AR expansion along the applied stress direction (i.e., the longitudinal direction) at 5 MPa stress level, while the longitudinal expansions of concrete samples under 10 MPa and 15 MPa are almost negligible. In addition, concrete under restraints such as applied stresses and steel rings in multiple directions showed anisotropic expansion behaviour in the work by Multon & Toutlemonde (2006), namely stress-dependent anisotropic expansion behaviour, in which expansions were transferred from more compressed directions to less or non-compressed ones. The authors observed that ASR volumetric expansion remained virtually constant at whatever the stress state. The volumetric expansion here is total expansions measured in three principal directions. This study, however, failed to provide a model to quantify the stress-dependent anisotropic expansion behaviour at different stress levels in three dimensions. On this issue, several studies have recently conducted expansion tests under multiaxial stress states, such as in Gautam et al. (2017b) and Liaudat et al. (2018). In addition to the expansion transferring from stressed to unstressed

directions, both studies, however, reported reductions in ASR volumetric expansion as hydrostatic stress increases, i.e., as shown in Figure 5.1 from observations in Liaudat et al. (2018). Based on the experimental results, Gautam et al. (2018) and Liaudat et al. (2018) proposed different empirical models for 3D stress-dependent anisotropic expansion in 3D numerical modelling applications such as finite element analyses. Both models have been widely used for numerical modelling of structures damaged by ASR (Gautam et al. 2017b; Gorga, Sanchez & Martín-Pérez 2018; Pourbehi, van Zijl & Strasheim 2019; Roth 2020). More details of these two models are presented in the next sections.

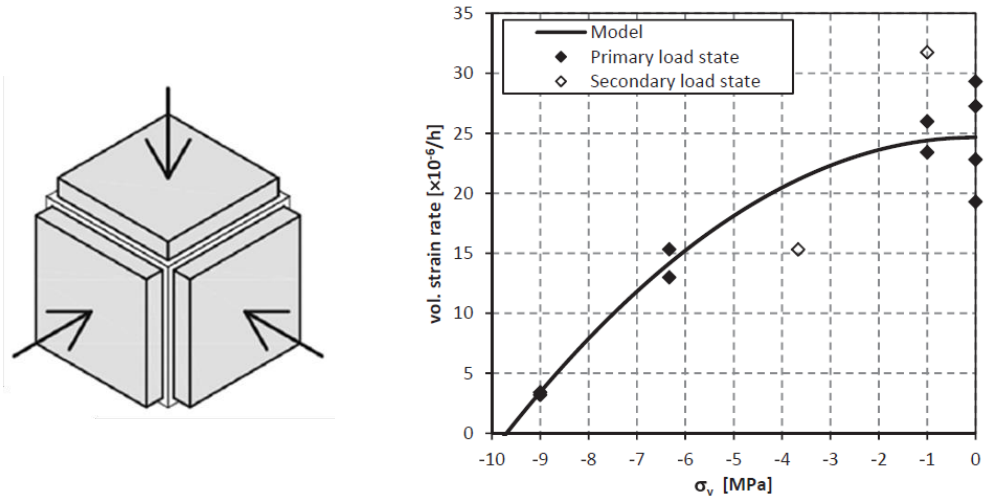

(a) Multiaxial stress test setup *(b) Volumetric expansion with respect to volumetric stress*

Figure 5.1: Multiaxial stress test setup and results in Liaudat et al. (2018).

5.1.2. Effect of reinforcement restraint to ASR-induced expansion

For reinforced concrete structures affected by ASR, the presence of reinforcement could change the expansion behaviour of concrete in comparison to the free expansion (Doug Hooton et al. 2013; ISE 1992). It is often observed that the expansion is commonly

inhibited in the direction along the steel reinforcement and increasingly occurs in other less restrained directions, which leads to cracking along the main reinforcement. An example is exhibited in Figure 5.2(a) from ISE (1992), which was obtained from different experimental testings, and it shows a significant reduction in expansions of reinforced concrete compared to those of non-reinforced concrete (i.e., free expansion) as the reinforcement ratio increases. For instance, using 1% of steel reinforcement in concrete could reduce expansion in the reinforcement direction up to 80% of the free expansion according to test data from Hanshin. Moreover, the same expansion transferring behaviour was observed due to multiaxial reinforcement layout and ratios in the experimental tests of Allford (2016) and Giannini (2012). For instance, Giannini (2012) tested for expansion of non-reinforced and reinforced concrete blocks in the field, where main reinforcement was arranged only in the longitudinal direction of the blocks. The author observed almost the same total expansion from three orthogonal directions from the non-reinforced and reinforced concrete blocks, yet, expansion in the longitudinal direction dropped from 85% to less than 40% of those measured in transverse directions.

Due to this significant effect of reinforcement restraints, several studies have been conducted on reinforced concrete specimens to establish empirical expansion-reinforcement ratios for estimating ASR expansion in reinforced concrete members (Aryan et al. 2020; Doug Hooton et al. 2013; Graff 2017). The impact of reinforcement restraint on ASR expansion, however, varies from one to another. The expansion rate may also contribute to the variation as shown in Figure 5.2(b), in which a high expansion rate tends to induce a higher reduction of the expansion due to reinforcement confinement. In this regard, the confinement effect of reinforcement could be different for concrete in the field, where expansion rate is commonly significantly lower than what laboratory-

accelerated tests report. More importantly, it is difficult to apply the restrained expansion-reinforcement ratio relationships in actual structures due to: firstly, more complicated arrangements of reinforcement in different directions; and secondly, the applied stress and boundary conditions. This is after taking into account that confinement in one direction could affect expansion in other directions.

It is also worth noting that as ASR expansions in reinforced concrete occur, compressive stresses in concrete also increase as shown in Figure 5.2(b) due to steel reinforcement restraint. In terms of the numerical modelling of reinforced concrete expansions, the effects of reinforcement restraints could be considered via compressive stress confinement by taking advantage of well-established expansion-multiaxial stress relationship (i.e., stress-dependent anisotropic expansion models) mentioned above. The higher reinforcement ratio used in one direction, the higher compressive stress is generated in concrete in this direction to restrained concrete expanding. Using the expansion-stress relationship also provides flexibility in modelling anisotropic expansion behaviour under both applied and generated multiaxial confinements of actual RC structures. Another important aspect of ASR expansion in reinforced concrete is yielding of reinforcement at high expansion levels, which may consequently affect serviceability and capacity of the structures. The numerical modelling should be able to assess deformation of the reinforcement so that the structural condition is accurately understood.

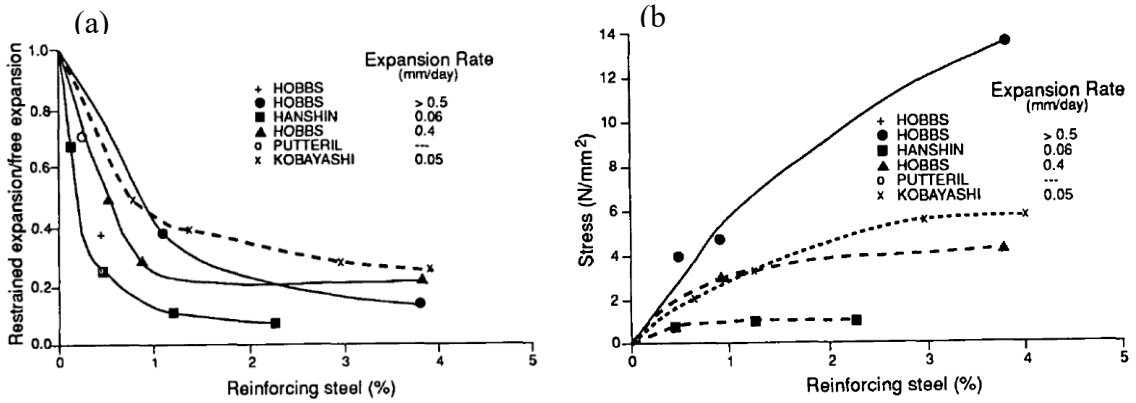

Figure 5.2: Effect of reinforcement on ASR expansion (ISE 1992): (a) restrained expansion with respect to reinforcement ratio; and (b) stress development in concrete.

5.1.3. Numerical modelling of ASR expansion in reinforced concrete

Over the years, several modelling approaches have been proposed to model ASR expansion in concrete from the micro-, meso-, macro- to structural scales. The models at micro-scale often focus on the ion diffusion-reaction mechanisms at the chemical reaction products level such as in Puatatsananon & Saouma (2013), while a typical meso-scale model simulates gel swelling in a representative elementary volume (REV) consisting of matrix (cement paste) and aggregates as a heterogeneous material, as reported in Esposito & Hendriks (2016). Taking into account the complexities of ASR characteristics, a link from the formation of gel product and its swelling behaviour in concrete micro- and meso-structures to their consequent expansion was established thanks to these models. However, they are highly complex due to the requirements of several physicochemical and mechanical variables to describe reaction and swelling phenomena from either microscopic laboratory observations or mathematical assumptions. It is even more challenging to upscale these models to structural levels for condition assessment of complex structures such as dams and bridges. As a more practical approach for

engineering applications, the macro-scale model is commonly conducted for expansion modelling at the structural level by simply imposing ASR-free expansion by considering the effects of confinements such as applied stresses and reinforcement, as noted by Saouma & Perotti (2006b) and Comi, Fedele & Perego (2009). Note that free expansion herein is the expansion observed from unrestrained concrete. These macroscale models can extend to simulations of cracking, failure and serviceability aspects of affected structures. Therefore, the macro model is the most suitable compared to others to be conducted in this study since its main focus is on condition assessment and capacity evaluation of reinforced concrete structures damaged by ASR. In the last decade, several macro-models have been proposed for expansion and damage assessment modelling, such as Saouma & Perotti (2006b), Comi, Fedele & Perego (2009), Morenon et al. (2017); Roth (2020). However, the majority focused on modelling of dam structures and only a few models addressed the expansion behaviour of reinforced concrete members. As such, modelling practices to assess expansion and damage progression of reinforced concrete members are currently lacking.

The model at the structural level requires the free expansion advancement of concrete as the most important input. The most reliable source of free expansion of concrete should be from unrestrained concrete components exposed to the same environmental conditions, yet this data is unlikely to be available for existing structures. Another approach to obtain the free expansion curve is from modelling. The semi-empirical model for free expansion of concrete presented in the previous chapter highlighted the necessity to recognise several factors affecting concrete expansion such as types/nature of reactive aggregates, exposure conditions (i.e., temperature, humidity) as well as concrete alkali content. The numerical modelling of the ASR expansion in concrete structures in current

practice, however, usually assumes the free expansion curve to obtain expected measurable parameters such as deformation at particular locations of the structure. These measurable parameters yet may not be accurate for actual structures due to lacking suitable references. In this context, the semi-empirical model developed in Chapter 4 becomes crucial to provide accurate input to the expansion modelling of reinforced concrete structures in the field.

Another important consideration in modelling ASR expansion of reinforced concrete is the effects of restraints on three-dimensional (3D) expansion advancement. As highlighted previously, the restraints (i.e., from applied stresses, reinforcement, or surrounding non-expansive materials) constitute a crucial factor affecting expansion of restrained concrete, i.e., actual structures or structural members (Gautam et al. 2017b; Saouma & Perotti 2006b). For instance, increasing compressive stress in a direction confines expansion in this direction, but it may increase expansions in other orthogonal directions and lead to anisotropic development of the expansion (Multon & Toutlemonde 2006). This expansion transfer behaviour requires a consideration of the multiaxial expansion-stress relationship in the modelling of ASR expansion under various types of confinement. Due to the complexity of the reaction and consequent deleterious expansion, this relationship should be derived from experimental testings and extensive numerical modelling validation. To the best of the author's knowledge, two empirical models proposed by (Saouma & Perotti 2006b) and Liaudat et al. (2018) for one, and Gautam et al. (2017b) for the other. They are the most widely used because they take into account the expansion-stress dependence and confinement-induced anisotropic expansion behaviour (Gorga, Sanchez & Martín-Pérez 2018; Pourbehi, van Zijl & Strasheim 2019). Yet, their application to the modelling effects of reinforcement restraint on ASR

expansion have not been thoroughly investigated with reference to actual structures. In addition, these two empirical models differ in terms of expansion-stress relationship. A comprehensive study on modelling ASR expansion of reinforced concrete is thus necessary for better understanding and selection of a suitable constitutive model.

Lastly, mechanical properties of concrete are important in numerical modelling for the ASR expansion development in reinforced concrete, and especially for evaluating the capacity afterwards. As highlighted in Chapter 3, mechanical properties of concrete (i.e., compressive and tensile strength, modulus of elasticity) have been reported to decline as expansion increases (ISE 1992, Sanchez 2014). Alternatively, deformation/strain of concrete in general under applied stresses and generated stress from restraints is affected by concrete stiffness. Therefore, it is important to have either sufficient measurements or accurate estimation of the residual material properties of the ASR-affected concrete for accurate modelling of ASR-induced expansion in concrete structures. Measurements of mechanical properties of concrete, i.e., from accompanied specimens or core samples are yet not always available; as such, estimating the residual mechanical properties becomes necessary. On this theme, it is important to note that experimental data from the literature presented in Chapter 3 shows great variations in mechanical properties deterioration at any given expansion level. Therefore, either accurate modelling concrete mechanical properties in structures must be developed, or any uncertainty in the estimation of concrete mechanical properties has to be taken into account when modelling the expansion of concrete structures.

5.2. Stress-dependent anisotropic expansion model

As mentioned previously, the ASR-induced expansion behaviour of concrete under restraints/confinements is significantly different and far more complicated in comparison to the free expansion of unrestrained concrete. As such, a constitutive model is required to simulate the restrained ASR expansion. The constitutive model enables considerations of: (i) reaction kinetics (or, reaction advancement) in relation to affecting factors such as temperature and relative humidity in concrete; and (ii) effects of multi-axial stresses and restraints to the ASR-induced expansion. The former is normally referred to as the expansion of un-restrained concrete, namely free expansion of concrete, while the latter is required to simulate the relationship between the free expansion and restrained expansion of concrete. The former was covered by the thermodynamically-based semi-empirical model proposed in Chapter 4. In this chapter, the confinement effect is addressed to accomplish the constitutive model for the ASR expansion and be implemented in the numerical model, i.e., finite element analyses.

Some assumptions were made in implementing the ASR expansion model in FE analyses. First, reaction advancement is considered through volumetric expansion and redistribution weights derived from stress tensor of concrete elements. It is supported by a strong relationship between the volumetric expansion and 3D stress state of concrete due to the transferring behaviour of expansions observed from many experimental studies, such as Gautam et al. (2017b), Giannini (2012), Liaudat et al. (2018) and Multon & Toutlemonde (2006). In terms of numerical modelling, all sorts of restraints and confinements can be considered through the expansion-stress relationship, namely stress-dependent anisotropic expansion model (Saouma 2014). Here, experimental testings in the literature show significant effects of compressive stresses on ASR expansion (Gautam

et al. 2017b; Liaudat et al. 2018), while the effects of tensile cracking are very limited (Jones & Clark 1996). A general form of the incremental ASR strain tensor to be implemented in the FE analysis could be expressed as:

$$\dot{\boldsymbol{\varepsilon}}^{\boldsymbol{ASR}} = \boldsymbol{EWE}^{T} f(\boldsymbol{\sigma}) \dot{\varepsilon}_{V}^{ASR,free} \tag{5.1}$$

where $\dot{\varepsilon}_{V}^{ASR,free}$ is the free volumetric expansion of concrete, $f(\boldsymbol{\sigma})$ is expansion-stress dependent function accounting for the impact of stress state on ASR expansion, $\boldsymbol{E}$ is the eigenvectors derived from the stress tensor, and $\boldsymbol{W}$ is the weight tensor that distributes the volumetric expansion to each of three principal directions, given by:

$$\boldsymbol{W} = \begin{bmatrix} W_1 & 0 & 0 \\ 0 & W_2 & 0 \\ 0 & 0 & W_3 \end{bmatrix} \tag{5.2}$$

Several models have been proposed for the expansion-stress dependence, yet, not all of these models are derived from multi-axial testing schemes and able to determine the expansion distribution weights. As discussed previously, two empirical models were devised based on the tri-axial stress testing data and widely used in the numerical modelling at the structural level, and these were derived from Gautam et al. (2017b) and Liaudat et al. (2018). The latter was a refinement of the constitutive model proposed in Saouma & Perotti (2006b), which is one of the most widely accepted for numerical modelling of ASR expansion in mass concrete structures. Both can account for the expansion-stress dependence and confinement-induced anisotropy of the ASR expansion to determine the volumetric expansion and distributed weights. These two models were adopted in this study as the stress-dependent anisotropic expansion model for simulating ASR-induced expansion of reinforced concrete for comparing and selecting the most suitable model. The following section presents in detail these two models, i.e., from

Saouma & Perotti (2006b) - Liaudat et al. (2018) (hereafter Saouma's model) and from Gautam et al. (2017b) (hereafter Gautam's model).

5.2.1. Saouma's model

This model considered reaction advancement through volumetric expansion and redistribution weights derived from the stress tensor. Two important considerations made in this model can be listed as: (i) increasing hydrostatic compressive stress may reduce ASR volumetric expansion; and (ii) the redistribution of expansion was done by allocating weights to principal stress directions based on the associated principal stress. The volumetric expansion of concrete under stresses is defined as:

$$\dot{\varepsilon}_V^{ASR} = \Gamma_c(\sigma_v)\dot{\varepsilon}_V^{ASR,free} \tag{5.3}$$

in which, $\dot{\varepsilon}_V^{ASR,free}$ is the free volumetric ASR expansion as defined previously; Γ_c represents ASR volumetric expansion reduction under compressive stresses, given by:

$$\Gamma_c(\sigma_v) = \begin{cases} 1 & if\ \sigma_v \geq 0 \\ 1 - (\sigma_v/\bar{\sigma}_v)^2 & if\ 0 > \sigma_v \geq \bar{\sigma}_v \\ 0 & if\ \sigma_v < \bar{\sigma}_v \end{cases} \tag{5.4}$$

where σ_v is the volumetric stress determined from the first invariant I_σ of the stress tensor $\sigma_v = I_\sigma/3$; $\bar{\sigma}_v = -9.7$ MPa according to Laudiat et al. (2018), is the volumetric stress limit below which ASR expansion is completely prevented.

It is noted herein that the free volumetric expansion is the ASR expansion of unrestrained concrete. In Saouma and Perotti (2006), the free volumetric expansion evolution was adopted from Larive (1998) with additional consideration of relative humidity effect based on Capra and Bournazel (1998). More details concerning Larive's model and the modified version are presented in Section 4.2.1 in Chapter 4. The most reliable source for

the free volumetric expansion curve is from fitting Larive's model to expansion of accompanied unrestrained members/samples in the same environmental conditions. This data is available only from some experimental testings but not from actual structures. Hence, in most cases when modelling for expansion of concrete structures in the field, the free volumetric expansion curve is usually assumed and validated using measured and monitoring data on the investigated structures, such as in Pourbehi, van Zijl & Strasheim (2019) and Hariri-Ardebili, Saouma & Merz (2018). The monitoring data is either not always available, or missing a reference to the undamaged state. In this regard, the improved version of the free expansion model based upon Larive's model (see ***Chapter 4***) could help to overcome this challenging issue, in which free expansion of concrete in the field can be predicted using laboratory tests' data.

The volumetric expansion is then distributed to three principal stress directions by assigning their associated weights W_i. The expansion in each principal direction is defined as:

$$\dot{\varepsilon}_i^{ASR} = W_i \dot{\varepsilon}_V^{ASR},\ i = k, l, m \tag{5.5}$$

The weight in a principal direction was defined based on not only the stress value in this direction but also from stresses in other directions. Specifically, the weight in the principal direction k (i.e., W_k) is calculated based on three principal stresses σ_k, σ_l and σ_m as follows:

1. Given σ_k, identify the quadrant encompassing σ_l and σ_m, which consist of nine interpolation regions and sixteen nodes, as shown in Figure 5.3(a). σ_u is the stress limit where the ASR expansion is totally suppressed, taken as σ_u = 9.7 MPa. Four neighbouring nodes of each region will be used for determining the weight;

2. Determine the weights of the neighbouring nodes $\widetilde{W}_i(\sigma_k)$ from the table in Figure 5.3(b) through proper linear interpolation of σ_k;

3. Calculate the weight W_k as:

$$W_k(\sigma_k, \sigma_l, \sigma_m) = \sum_{i=1}^{4} N_i(\sigma_l, \sigma_m)\widetilde{W}_i(\sigma_k) \tag{5.6}$$

$$\widetilde{W}_i(\sigma_k) = \left[\widetilde{W}_1(\sigma_k) \;\; \widetilde{W}_2(\sigma_k) \;\; \widetilde{W}_3(\sigma_k) \;\; \widetilde{W}_4(\sigma_k)\right] \tag{5.7}$$

where, $N_i(\sigma_l, \sigma_m)$ is commonly used bilinear shape functions in FEA used for the interpolation, given by:

$$N_1(\sigma_l, \sigma_m) = \frac{1}{ab}[(a - \sigma_l)(b - \sigma_m)] \tag{5.8}$$

$$N_2(\sigma_l, \sigma_m) = \frac{1}{ab}[\sigma_l(b - \sigma_m)] \tag{5.9}$$

$$N_3(\sigma_l, \sigma_m) = \frac{1}{ab}[\sigma_l \sigma_m] \tag{5.10}$$

$$N_4(\sigma_l, \sigma_m) = \frac{1}{ab}[(a - \sigma_l)\sigma_m] \tag{5.11}$$

in which, a and b constitute the dimensions of the quadrant, i.e., (a_1, b_1), (a_2, b_2).

An example of determining the neighbouring nodes $\widetilde{W}_i(\sigma_k)$ where $0 \leq \sigma_l, \sigma_m \leq \sigma_u$ is given by:

$$W_1(\sigma_k) = \frac{1}{3}\frac{(a - \sigma_k)}{a} \tag{5.12}$$

$$W_2(\sigma_k) = \frac{1}{2}\frac{(a - \sigma_k)}{a} \tag{5.13}$$

$$W_3(\sigma_k) = \frac{1}{3} + \left(1 - \frac{1}{3}\right)\frac{a - \sigma_k}{a} \tag{5.14}$$

$$W_4(\sigma_k) = \frac{1}{2}\frac{(a - \sigma_k)}{a} \tag{5.15}$$

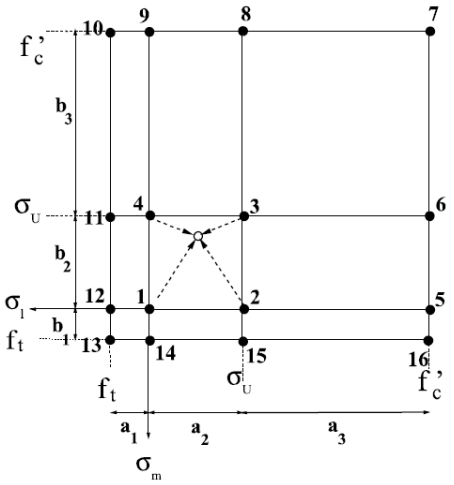

(a) Interpolation regions

Node	σ_l	σ_m	$\sigma_k \geq 0$	$\sigma_k = \sigma_u$	$\sigma_k = f_c'$
1	0.	0.	1/3	0.	0.
2	σ_u	0.	1/2	0.	0.
3	σ_u	σ_u	1.	1/3	0.
4	0.	σ_u	1/2	0.	0.
5	f_c'	0.	1/2	0.	0.
6	f_c'	σ_u	1.	1/2	0.
7	f_c'	f_c'	1.	1	1/3
8	σ_u	f_c'	1.	1/2	0.
9	0.	f_c'	1/2	0.	0.
10	f_t'	f_c'	1/2	0.	0.
11	f_t'	σ_u	1/2	0.	0.
12	f_t'	0.	1/3	0.	0.
13	f_t'	f_t'	1/3	0.	0.
14	0.	f_t'	1/3	0.	0.
15	σ_u	f_t'	1/2	0.	0.
16	f_c'	f_t'	1/2	0.	0.

(b) Weights at interpolation points

Figure 5.3: Weights distribution (Saouma & Perotti 2006b).

5.2.2. Gautam's model

In Gautam et al. (2018), a series of multiaxial-stress expansion tests under different stress levels was conducted to investigate the stress-dependent anisotropy. The same observations on stress-induced anisotropy of ASR expansion under confinement were observed, in which an increase of confinement in one direction reduced expansion in this direction but promoted higher expansion in the other orthogonal directions. The total volumetric expansion, therefore, remained almost unchanged regardless of whether an increase in the confinement occurred. Based on the experimental observations, the authors proposed a new empirical model to account for effects of the stress confinement on the ASR expansion.

In contrast to Saouma's model, the effect of stress on the volumetric expansion in Gautam's model was coupled to the weight of all three principal directions. The model consists of two primary expansion-stress relationships, i.e., uncoupled axial expansion (pe_{un}) and maximum possible axial expansion (pu_{max}), which represent the ratio between the restrained expansion in each principal direction to the free volumetric expansion. The former represents the axial expansion in a given direction that is calculated from the normal stress acting in this direction and decoupled from effects of stresses in the other directions. The axial expansion level is 33.3% at the no-stress state and this declines as the stress in this direction increases. Based on the test data and modelling results, the authors concluded that if the compressive stress in a given direction is less than 1.7 MPa, then expansion in this direction could be affected by stresses in the other directions. As such, the latter was proposed to estimate maximum possible expansion in a given direction to indirectly consider the effect of stresses in the other directions. The expansion of less confined or non-confined direction could be as high as 77.2% of the free volumetric expansion, which is transferred from the other heavily confined directions. The expansion in a given direction therefore varies from the uncoupled axial expansion to the maximum possible axial expansion.

The uncoupled axial expansion and maximum possible axial expansion are given by:

$$pe_{un,i} = a + \frac{b-a}{1+\left(\frac{\sigma_i}{c}\right)^d} \tag{5.16}$$

$$pu_{max,i} = A + \frac{B-A}{1+\left(\frac{\sigma_i}{C}\right)^D} \tag{5.17}$$

where model constants (*a, b, c, d*) and (*A, B, C, D*) were obtained from curve-fitting from the experimental observations; the constants *a*, *b*, *c*, and *d* are 11.4%, 33.3%, 1.8, and 6.5,

respectively, while A, B, C, and D are 11.4%, 77.2%, 1.3, and 5.4, respectively. Figure 5.4 illustrates these two expansion-stress dependent curves.

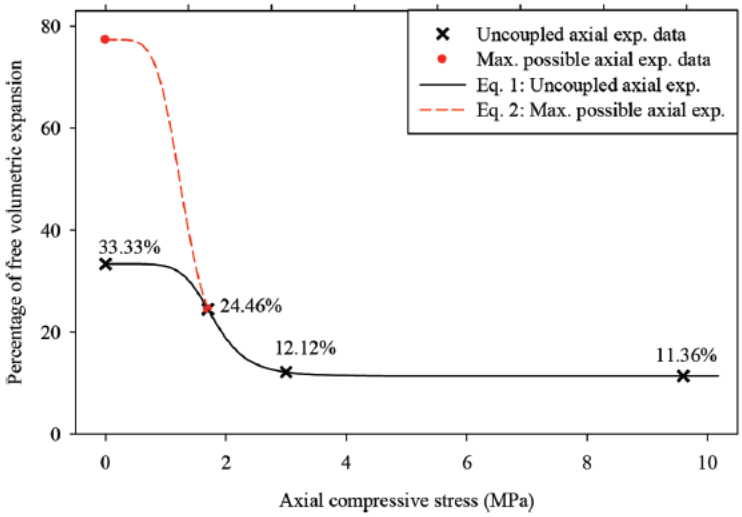

Figure 5.4: Uncoupled and maximum axial expansion with respect to axial compressive stress (Gautam et al. 2017b).

Expansion in each of the three primary directions is then determined using these two expansion-stress relationships. It is noted that the total expansion in three directions, in any case, is not greater than the free volumetric expansion, which means that total weight is not greater than 100%. If the sum of $pu_{max,i}$ in three directions is not greater than 100%, the weight in each direction is equal to the respective maximum possible axial expansion $pu_{max,i}$, such that:

$$W_i = pu_{max,i} \qquad if \sum_{i=1}^{3} pu_{max,i} \leq 100\% \tag{5.18}$$

If the sum of $pu_{max,i}$ in three principal directions is greater than 100%, the weight in each direction is recalculated based on both $pu_{max,i}$ and $pe_{un,i}$ to meet the constraint on total weights of 100%. The difference between 100% and total uncoupled axial expansions, if

available, is distributed to each direction which is proportional to the difference in $pu_{max,i}$ and $pu_{un,i}$, given by

$$W_i = pu_{un,i} + \frac{(pu_{max,i} - pu_{un,i})}{\sum_{i=1}^{3}(pu_{max,i} - pu_{un,i})}\left(100\% - \sum_{i=1}^{3} pu_{un,i}\right), if \sum_{i=1}^{3} pu_{max,i} > 100\% \quad (5.19)$$

In the test set up by Gautam et al. (2018), only normal stresses were applied in three primary directions, which could be considered as three principal directions. Therefore, the weights calculated above are equivalent to the weights in three principal directions, so that incremental ASR strain tensor is as same as in Eq. 5.1 to capture the ASR anisotropic behaviour. Added to this, the experimental observations revealed an insignificant effect of stress confinement on the reaction kinetic and thus decoupled the stress effect in the reaction kinetic in this proposed model. In Gautam et al. (2018), a numerical model for ASR expansion was then conducted using the proposed model compared to the constitutive model of Saouma & Perotti (2006b). The authors reported better prediction results obtained from this newly proposed model. This multiaxial expansion-stress dependent model was then adopted to model the Robert-Bourassa/Charest overpass (Quebec City, Canada), which had sustained ASR damage (Gorga, Sanchez & Martín-Pérez 2018).

Finally, it is worth noting that due to the need for recognising effects of stresses to the expansion, the weights are calculated to distribute the free volumetric expansion to three principal stress directions instead of the three principal strain directions. Knowing that the principal strain directions and principal stress direction are not co-aligned, the calculation may be slightly erroneous. Referring to the free volumetric expansion, it is commonly defined in experimental testing as the total expansions in three primary

directions, such as longitudinal, transversal and vertical directions for rectangular prism specimens or axial and radial directions for cylindrical specimens. The expansions measured in these directions may differ due to effects of casting directions, as reported in Smaoui et al. (2004) and Hayes (2020) on concrete blocks and large slabs, respectively. Inherent uncertainties in this casting direction-induced anisotropic expansions cause difficulties in modelling of the ASR expansion in concrete structures. In terms of numerical modelling, additional factors can be introduced into Eq. (5.1) to account for this casting-induced anisotropic behaviour. However, casting direction anisotropy significantly varies from one study to another. In this research, free expansions in three primary directions are assumed to be uniform as one-third of the free volumetric expansion. Note that the term "free expansion" hereafter (without volumetric) is defined as the value of free expansion in one direction instead of the free volumetric expansion.

5.3. Consideration of mechanical properties reduction due to ASR

It has been well established that the progress of ASR in concrete causes problems for mechanical properties to varying extents. Contrariwise, under applied stresses, changes in mechanical properties (i.e. concrete stiffness) of concrete affect its stress state, and consequently also the advancement of ASR due to the stress-dependency of the expansion. Therefore, considering expansion-dependent mechanical properties is necessary for simulation of ASR in reinforced concrete structures. Especially, it becomes crucial at the stage of assessing load-carrying capacity of the affected structures.

On investigating existing structures undergoing ASR, the most reliable method to achieve mechanical properties of concrete would be testing core samples extracted from the structures at different locations and directions (Fournier et al. 2010). Yet, extracting cores is limited regarding locations or number of investigations during service life of the

affected structures due to its cost and structural safety. Whenever this data is not available, it is necessary to estimate the concrete mechanical properties for condition assessment and capacity evaluation of the structures based on measurable or reliably estimable data. Here, the most obvious correlation is between mechanical properties and expansion, as shown in Chapter 3. Therefore, it is reasonable to estimate mechanical properties using a measured or estimated expansion level.

In terms of the expansion of the field concrete, the semi-empirical model presented in Chapter 4 could provide a reliable estimation based on laboratory measurements. On the expansion-mechanical properties relationship, however, experimental data from the literature showed a significant variation of the residual mechanical properties at any given expansion level. Note that the residual mechanical properties herein are defined as the ratio in mechanical properties of the ASR-affected concrete to those of undamaged concrete. It is noted that the undamaged strength and stiffness herein was measured at 28-day due to availability of the data. Additional consideration of maturity of concrete is necessary in future works for assessing long-term performance of concrete in the field.

To account for and quantify this uncertainty, mechanical properties of the ASR-affected concrete were defined as interval variables with respect to the expansion level. Upper and lower bounds were proposed for residual compressive strength, tensile strength and modulus of elasticity, which cover their variation from experimental data presented in ***Section 2.2***. Figure 5.5 shows the upper and lower bounds of the mechanical properties, together with the experimental data collected from the literature. As such, in addition to an FE analysis of mean values of the mechanical properties, two other analyses can be conducted to simulate the worst- and best-case possible scenarios of structural behaviour.

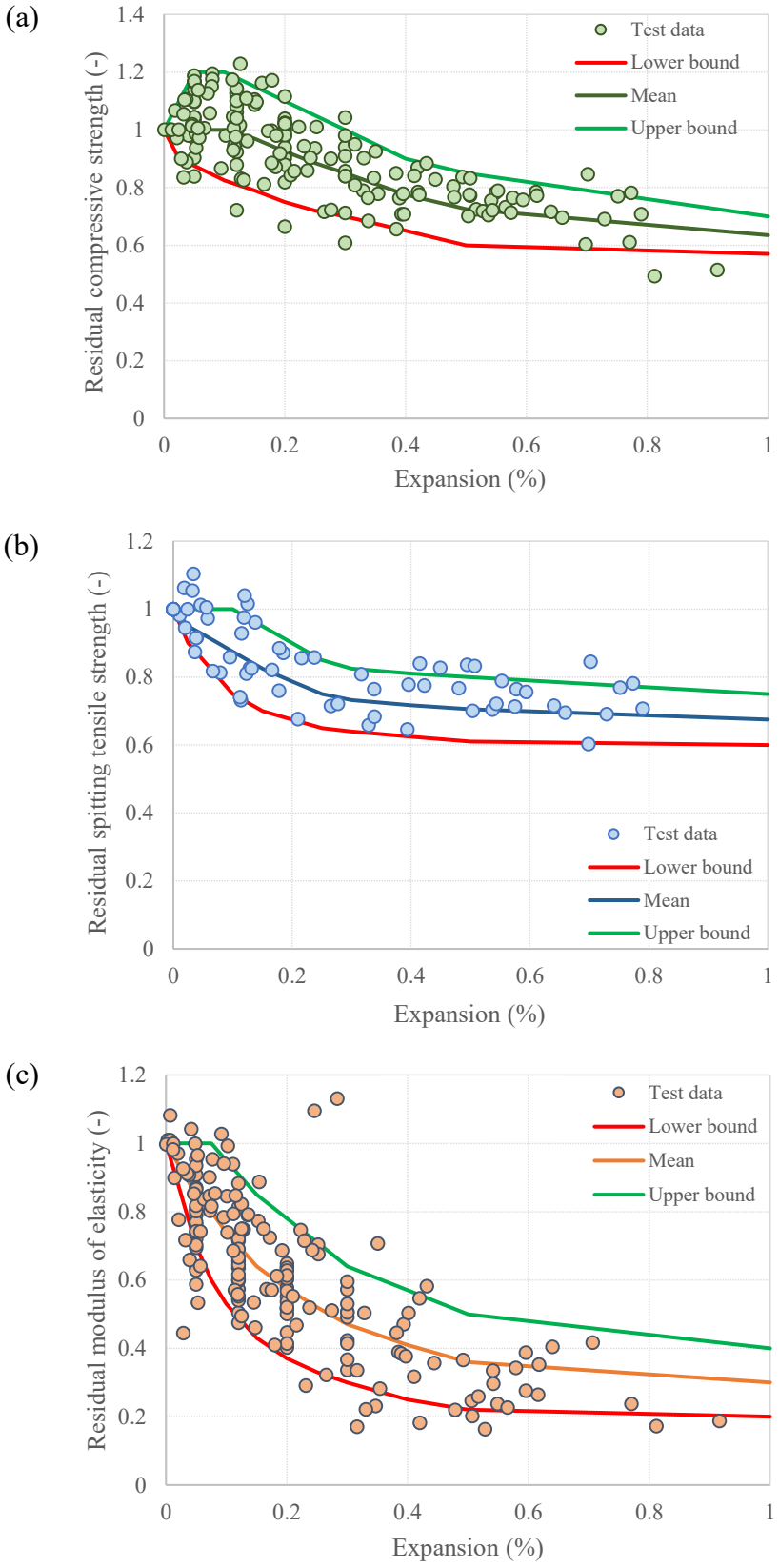

Figure 5.5: Proposed upper and lower bounds of (a) compressive strength, (b) tensile strength and (c) modulus of elasticity.

It is worth noting that the expansion in the expansion-mechanical properties relationship presented above is measured as the length change of the test sample. It is assumed that this measured expansion is as one-third of the volumetric expansion despite casting direction-induced anisotropy on the measured expansion. In numerical modelling in this study, the mechanical properties of concrete are subsequently correlated to one-third of the volumetric expansion of concrete elements using the relationships shown in Figure 5.5. An important assumption has to be made on the *isotropic behaviour of concrete* in concrete damage plasticity model in the FE analyses. Future investigations on anisotropic behaviour of concrete material due to anisotropic expansion are necessary.

In summary, the FE model for ASR expansion and consequently for load-carrying capacity evaluation requires taking into account the mechanical properties' changes with respect to the expansion level. Implementation of the ASR constitutive model and mechanical properties changes in a FE framework are presented in the next section.

5.4. FE modelling of ASR expansion in reinforced concrete

5.4.1. Constitutive modelling of reinforced concrete

This section briefly presents the constitutive model of reinforced concrete used in finite element modelling. The finite element analysis is implemented in the commercial FEA software ABAQUS using the concrete damage plasticity model (CDP), which is accessible to the engineering community (Systèmes 2014). The CDP model is a continuum and plasticity-based damage model, in which two main failure mechanisms of concrete material are either compressive crushing or tensile cracking. The model adopts the yield function proposed in Lee & Fenves (1998) to account for different evolutions of strength under tension and compression conditions. Definition of the yield function

requires information on the ratio of the initial compressive yield stress under biaxial loading by the initial compressive yield stress under uniaxial loading (f_{b0}/f_{c0}), ratio of the second stress invariant on the tensile meridian (K). Non-associated flow rule is adopted incorporating with the Drucker-Prager hyperbolic function as the flow potential function, which requires defining the dilation angle (ψ) and eccentricity of the plastic potential flow (ε). In this study, the model parameters are set as defaults as in the user's manual, shown in Table 1.

Table 5.1: Model parameters of the CDP

Parameter	ψ	ε	f_{b0}/f_{c0}	K
Value	36	0.1	1.16	0.667

Compressive behaviour

Other important inputs for the CDP are the concrete behaviour under uniaxial compression and uniaxial tension. In this study, a nonlinear uniaxial stress-strain behaviour of concrete under compression ($\sigma_c - \varepsilon_c$) was defined in accordance with the Hognestad parabola (Hognestad 1951). This model has been widely used for modelling of nonlinear behaviour of reinforced concrete structures under shear and flexural failure, for instance in Abu-Obeidah, Hawileh & Abdalla (2015) and Hawileh (2015). The model consists of a nonlinear ascending branch and a linear descending branch, given by:

$$\sigma_c = f_c' \left[2\frac{\varepsilon_c}{\varepsilon_{c0}} - \left(\frac{\varepsilon_c}{\varepsilon_{c0}}\right)^2 \right] \tag{5.20}$$

in which, σ_c is the concrete compressive stress, ε_c is the concrete compressive strain, f_c' is the compressive strength of concrete (in MP), $\varepsilon_{c0} = \frac{2f_c'}{E_c}$ is the concrete compressive strain at the peak stress, E_c is the modulus of elasticity of concrete (in MPa). The modulus

of elasticity of concrete of undamaged concrete can be calculated as $E_c = 21500\ (0.1f_c')^{1/3}$ (MPa) in accordance with the CEB-FIP Model code 1990 (Comit 1990).

Tensile behaviour

In tension, the tensile stress is linear elastic up to its tensile strength (f_t). The tensile strength, if not available, can be calculated either from splitting tensile strength ($f_{t,sp}$) by $f_t = 0.9f_{t,sp}$, or from compressive strength as $f_t = 1.4(0.1f_c)^{2/3}$ in accordance with the CEB-FIP Model code 1990 (Comit 1990). After cracking, the post-peak tension softening behaviour is adopted from Wang & Hsu (2001), which has been widely used in non-linear finite element analysis of reinforced concrete structures (see Dede & Ayvaz (2009) (Feng, Ren & Li 2018). An advantage of this model is its independence to the finite element mesh. The post-cracking tension behaviour is defined as:

$$\sigma_t = f_t \left(\frac{\varepsilon_{cr}}{\varepsilon_t}\right)^{0.4} \tag{5.21}$$

in which, f_t is the tensile strength of concrete, and ε_{cr} is the strain at concrete cracking, and ε_t is the tensile strain.

As discussed previously, ASR affects compressive strength, tensile strength and modulus of elasticity of concrete, thus altering the compressive and tensile behaviour of concrete. In order to account for these changes as the expansion increases, series of compressive and tensile stress-strain curves were designed at different representative expansion levels for the FE model inputs. An example of uniaxial compressive stress-strain curves at different expansion levels for 35 MPa concrete is shown in Figure 5.6, which are for the mean values of modulus of elasticity and compressive strength with respect to the expansion level. FE modelling in ABAQUS is capable of controlling the mechanical

properties change of each element with respect to its expansion level by using user-defined subroutines and field variables. More details of the FE model implementation are presented in the next section.

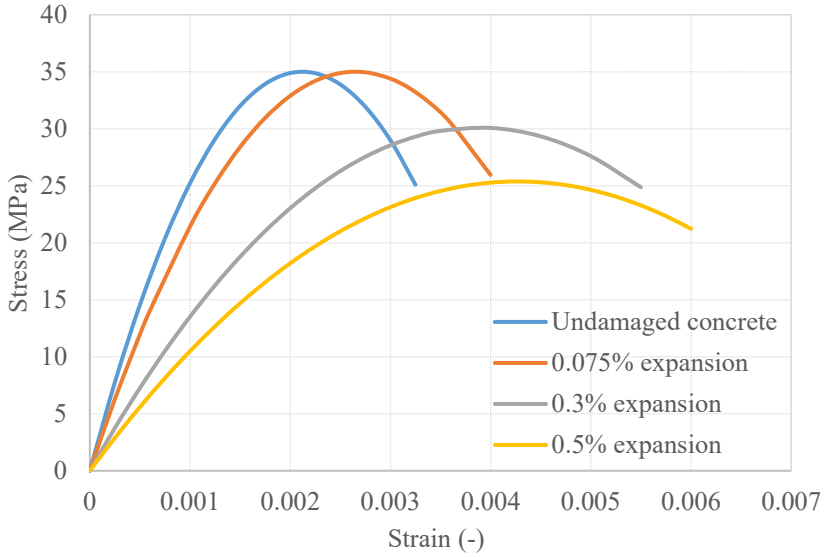

Figure 5.6: Compressive stress-strain behaviour of concrete at different expansion levels.

Reinforcement behaviour

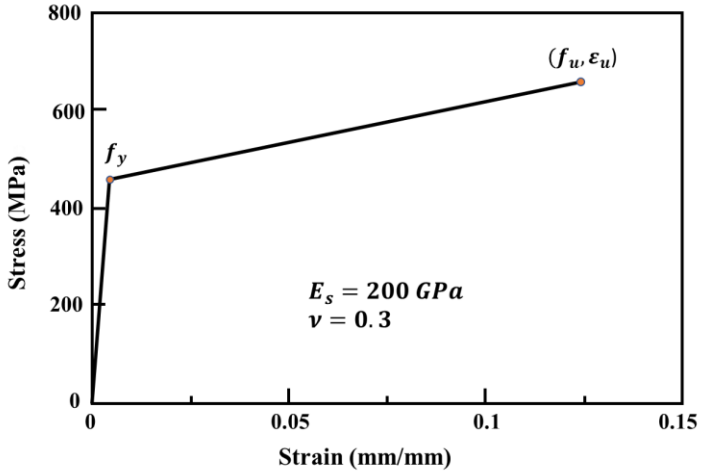

Figure 5.7: Stress-strain behaviour of the reinforcement.

The reinforcement is idealised as a bilinear strain hardening yield stress-strain behaviour as shown in Figure 5.7. A typical Young's modulus of 200 GPa and Poisson's ratio of 0.3

were adopted for all analyses. A perfect bond model between concrete and reinforcement was assumed for modelling the reinforcement embedded in concrete.

5.4.2. Implementation of the ASR constitutive model in ABAQUS/Standard

In the FE model, the reaction advancement is indirectly implemented by imposing equivalent ASR strains to concrete elements. The total strain is decomposed into the elastic strain $\boldsymbol{\varepsilon}^{el}$, plastic strain $\boldsymbol{\varepsilon}^{pl}$ and ASR strain $\boldsymbol{\varepsilon}^{ASR}$, given by:

$$\boldsymbol{\varepsilon} = \boldsymbol{\varepsilon}^{el} + \boldsymbol{\varepsilon}^{pl} + \boldsymbol{\varepsilon}^{ASR} \tag{5.22}$$

The elastic strain and plastic strain are mechanical strains calculated at each increment in concrete damage plasticity model by the ABAQUS Implicit solver. The plastic strain is determined when the strain on concrete element exceeds the elastic range, which can originate from the cracking strain (in tension) and inelastic strain (in compression). On this issue, the plastic strain can serve to qualitatively estimate cracking intensity and orientation in the concrete damaged plasticity model (Earij et al. 2017).

The ASR strain is defined as an anisotropic strain tensor, which is calculated as Eq. 5.1 at each increment and for each concrete element based on the current incremental free volumetric strain and stress state of the concrete element. In addition, as mentioned before, increasing the deleterious expansion causes degradation in concrete mechanical properties, and vice versa, a change in the mechanical properties under confinement would exert an impact on the stress state of concrete elements and thus expansion strain. Therefore, both the ASR strain tensor and material properties parameters (i.e., elastic modulus, tensile strength) have to be updated at every increment. The time increment in FE modelling has to be small enough to capture effects of the change in concrete's

properties. Note that creep and shrinkage in concrete were not considered for the current model.

Implementation of the ASR advancement requires four main tasks at each increment and for each concrete element:

(i) determining material properties at this current incremental step based on the level of expansion strain; and

(ii) determining principal stresses values and the eigenvectors (***E)*** at the current step;

(iii) calculating the weight tensor (***W***) and ASR strain tensor using the ASR constitutive model as presented in section 5.2;

(iv) imposing ASR strain tensor to concrete elements.

To implement these tasks in the FE model in ABAQUS, two user subroutines are adopted and developed using FORTRAN language, included USDFLD and UEXPAN. The purpose of USDFLD is to define field variables (FVs), in order to update the material properties of concrete with respect to the equivalent expansion strain, i.e., for task (i). In USDFLD, the utility routine GETVRM was used to access material point data such as element stress tensor, principal stresses and strains. With all these data available, the constitutive models presented in section 5.2 were conducted to calculate the weights and eigenvectors tensor to obtain the incremental ASR strain tensor for each element, per tasks (ii) and (iii). The incremental ASR strain tensor was stored as Solution Dependent Variables (SDVs) so that it could pass to the UEXPAN subroutine. In the UEXPAN, the incremental ASR strain was implemented to concrete elements as anisotropic expansion, per task (iv). Figure 5.8 shows the flowchart for the implementation of the chemo-mechanical modelling in ABAQUS with the user subroutines.

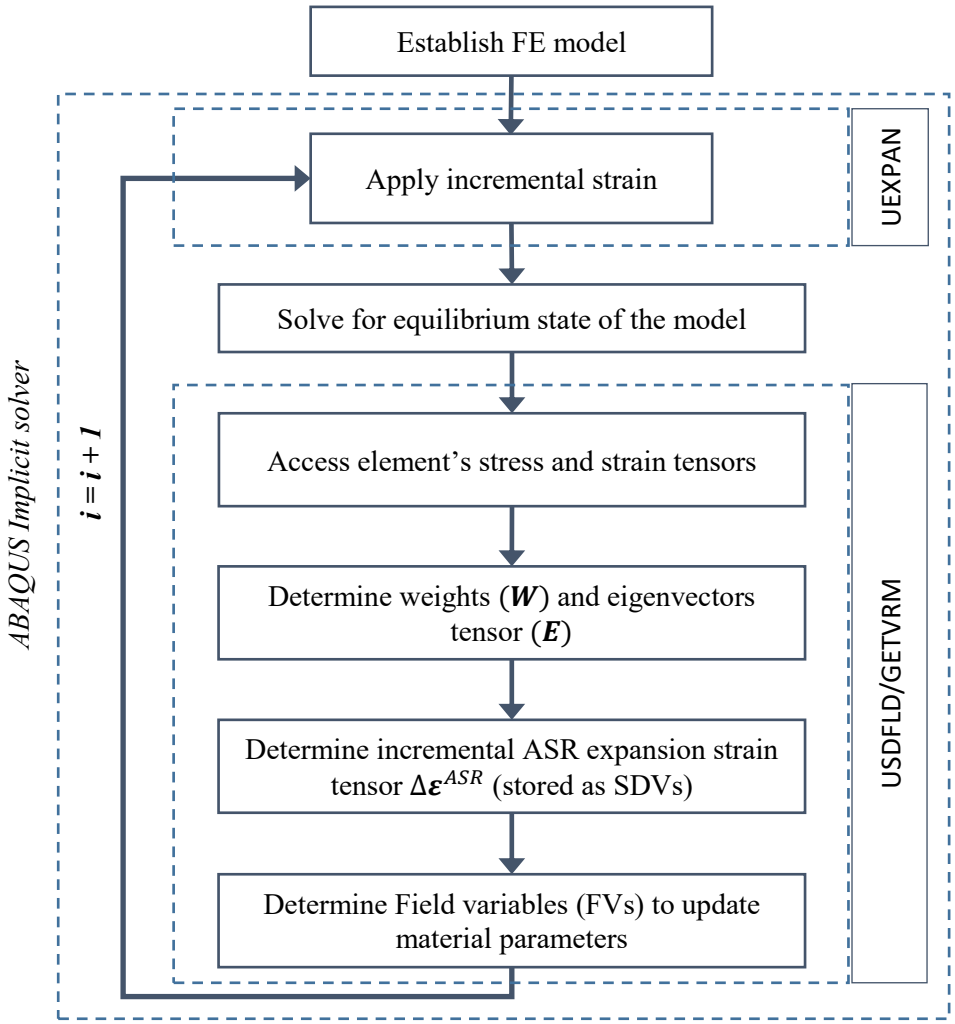

Figure 5.8: Flowchart for implementation of the ASR constitutive model in ABAQUS.

In the next sections, case studies were conducted to examine the ability of the proposed model to replicate ASR expansion of reinforced concrete at different reinforcement ratios. In both selected cases, the availability of data from both non-reinforced and reinforced samples at the same size, casting methods as well as exposure condition is extremely useful for modelling to reduce their associated uncertainties. Two numerical models, namely Model I and Model II, were developed using Saouma's and Gautam's constitutive models, respectively. All the results presented hereafter are referred to as Model I and Model II. The main focus of the FE analysis is, therefore to correlate the free expansion

as an input to the confined expansion of reinforced concrete samples. For a consideration of other chemical-related aspects of the reaction such as environmental conditions, reactive aggregate or alkali loading, see Chapter 4. Afterwards, the FE model was applied to estimate reinforced concrete beams in the field, which derive from the Kingston exposure site.

5.5. Model validation: ASR-induced expansion of concrete samples at different reinforcement ratios

To validate ASR expansion-stress dependent models in modelling ASR expansion of reinforced concrete members, as well as the CDP model and user subroutines in ABAQUS, the experimental data reported in Aryan et al. (2020) at different reinforcement ratios were adopted in the FE model. In Aryan et al. (2020), all the unreinforced and reinforced specimens were prepared via the same method and exposed to the same environmental conditions; therefore, uncertainties regarding those factors can be reduced in the FE modelling.

5.5.1. Test description

Aryan et al. (2020) conducted a series of expansion tests on concrete prism (150 x 150 x 525 mm) with and without reinforcement. Two concrete mixtures incorporating highly reactive sand El Paso-TX with different concrete alkalis levels were designed at different alkali content levels, namely Batch 2 and Batch 3. Batch 2 concrete was prepared with the alkali level of 0.6% per cement mass (i.e., mainly from cement), while in Batch 3 concrete, the alkalis was boosted by 1.25% per cement mass by adding external alkalis. Three levels of reinforcement ratio were tested, these being 1.23%, 2.18%, and 3.41% using four rebars of 9.525 mm, 12.7 mm, and 15.875 mm in diameters, respectively, with

a concrete cover of 25 mm (*note: from personal communications with Dr. Mohammad Hanifehzadeh who is co-author of this work*). Figure 5.9 shows the sketch of the specimens and reinforcement configuration.

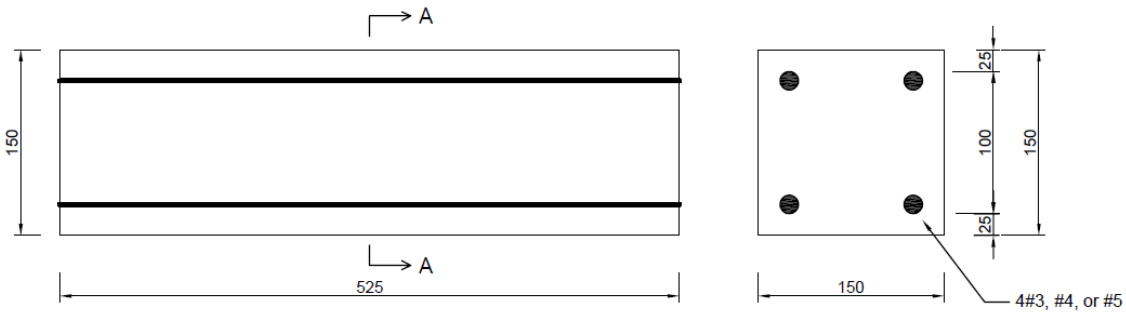

Figure 5.9: Dimensions and reinforcement configuration of the reinforced concrete prisms (unit: mm).

This set of specimens was exposed outside with water spray water twice a week to maintain high relative humidity in concrete. Expansion measurement was done every two weeks and up to two years of exposure. Yet, the expansion of both batches tended to level off after 1 year of exposure; therefore, a 1-year expansion period was extracted for the model's validation.

In addition, concrete cylinders were prepared along with the prisms for mechanical properties tests, in other words compressive strength, tensile strength and modulus of elasticity. The first measurement of compressive strength and splitting tensile strength was conducted at 28-day, where the modulus of elasticity was measured after 3-month exposure. Both Batch 2 and Batch 3 concrete revealed the same trend of material properties changing with respect to time and expansion levels, in which compressive strength slightly increased and splitting tensile strength declined in comparison to 28-day values. Interestingly, despite a high level of expansion of Batch 3 concrete, i.e., at about 0.6% expansion level measured from accompanied prisms, there is an insignificant

reduction in modulus of elasticity and splitting tensile strength compared to the value measured at the 3-month time, while the compressive strength still remains higher than 28-day strength. In this validation model, the concrete compressive strength was assumed to be the same as the 28-day value, while the modulus of elasticity and splitting tensile strength remained the same as the 3-month values.

5.5.2. FE model description

5.5.2.1. Geometry and mesh

Due to the symmetry of the prism geometry and boundary conditions, only a quarter of the full prism was simulated with the use of symmetric boundary conditions as shown in Figure 5.10. 3D 8–node hexahedral element with reduced integration (**C3D8R**), which is the most widely used in finite element modelling of reinforced concrete, was selected to model the concrete. For the reinforcement, the 3D 2-node linear beam element (B31) was utilised for modelling the reinforcement, which could simulate both axial and curvature change (bending) deformation. The reinforcement is embedded in concrete with the perfect bond model assumed, which implies full compatibility between concrete and reinforcement deformation. In order to extract the expansion of concrete from the model as the same derived from the measurement, the expansion strain extracted from relative displacement in the longitudinal direction of two nodes by a distance of 75 mm, as shown in Figure 5.10.

To investigate the FE mesh sensitivity, three mesh sizes were adopted to perform the analysis of RC prism of 1.23% of reinforcement, which are approximately 5 mm, 10 mm and 15 mm for both concrete and reinforcing bars elements. In this mesh sensitivity analysis, Saouma's model for the stress-dependent anisotropic expansion was considered.

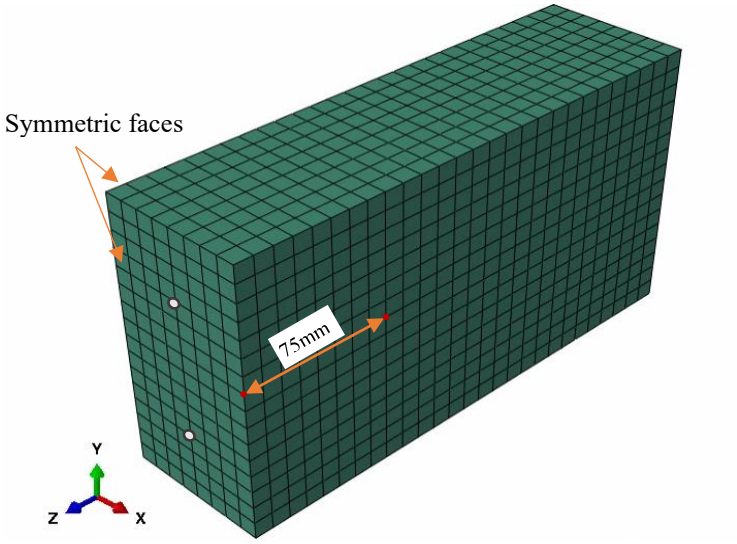

Figure 5.10: Geometry and boundary conditions of the reinforced concrete prism.

5.5.2.2.Material properties

The material properties used in the numerical modelling of reinforced prisms are shown in Table 5.2. Due to only insignificant change being observed from experimental testings of both Batch 2 and Batch 3, the mechanical properties were assumed to be constant in the numerical modelling.

Table 5.2: Material properties of the concrete and reinforcing steel

	Concrete	**Steel bars**
Compressive strength (MPa)	38	–
Tensile strength (MPa)	2.7	–
Young's modulus (GPa)	22	205
Poisson's ratio (-)	0.15	0.3
Yield stress (MPa)	–	415
Ultimate strength (MPa)	–	625
Ultimate stress (mm/mm)		0.1
Density (kg/m^3)	2400	7820

5.5.2.3. Consideration of stress-dependent anisotropic expansion model

For consideration of stress-dependency of the expansion, both Saouma's and Gautam's models were adopted for modelling expansion of the RC prisms for a comparison, namely Model I and Model II, respectively. The need to consider stress-dependent anisotropic expansion, instead of applying expansion strain uniformly in three principal directions, should be investigated. In this regard, a numerical model without accounting for the effect of stress state on the expansion rate, namely "*isotropic model*" was conducted to compare Model I and Model II that adopt Saouma's and Gautam's model for the expansion-stress relationship, respectively. In the "isotropic model", expansions are imposed uniformly in three principal directions without considering the effects of stress confinement of the expansion evolution.

5.5.3. Free expansion model

As stated beforehand, one of the important inputs for modelling expansion of reinforced concrete is the free volumetric expansion curve. With the availability of expansion data of non-reinforced prisms that are exposed to identical exposure conditions with the reinforced prisms, Larive's model can be directly used to obtain the free expansion curve for further modelling of the restrained expansion. Model parameters and free expansion curve (as one-third of the free volumetric expansion) of both Batch 2 and Batch 3 concrete mixtures are shown in Table 5.3 and Figure 5.11. It is assumed that the free expansions in three principal directions are initially identical as one-third of the free volumetric expansion. It is clearly seen that the expansion of Batch 3 where alkali content was boosted to 1.25% is significantly higher than the expansion of Batch 2 without additional alkalis. This remarkable impact of alkali content was highlighted and successfully modelled in Chapter 4. More importantly, it is important to note that the reinforced and

non-reinforced concrete prisms were made from the same reactive aggregate, non-reactive aggregate, mixture proportion, and casting and curing methods; thus the only primary difference is the reinforcement constraint.

Table 5.3: Larive's model parameters of free volumetric expansion curves

Larive's model parameters	**Batch 2**	**Batch 3**
Characteristic time, τ_c (day)	55	85
Latency time, τ_L (day)	10	40
Maximum free volumetric expansion, ε_v (%)	0.675	1.83

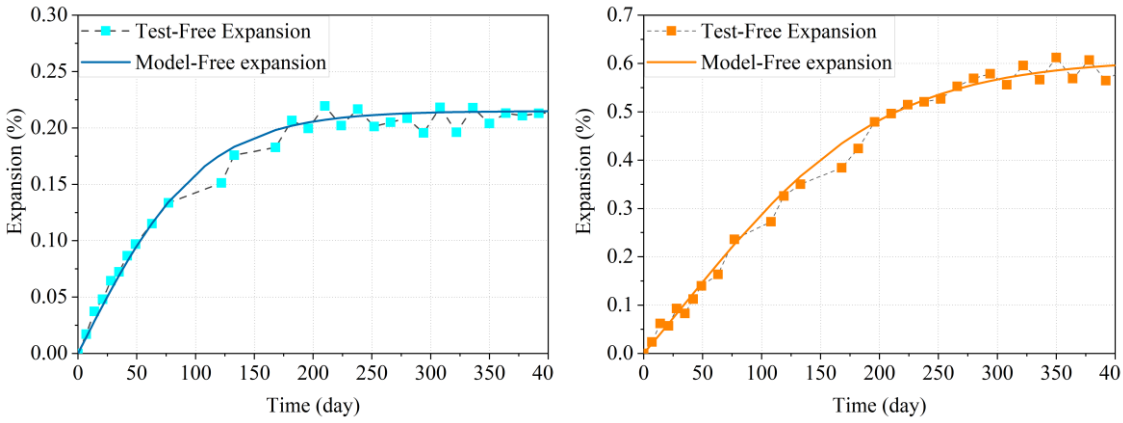

Figure 5.11: Model and measured free expansion curves of (a) Batch 2 and (b) Batch 3.

5.5.4. Results and discussion

5.5.1.1. *Effects of mesh size and reinforcement element*

A mesh sensitivity study was conducted on the concrete mixture Batch 3 with a reinforcement ratio of 1.23%. Expansion curves obtained from three FE models using three mesh sizes (i.e., approximately 5 mm, 10 mm and 15 mm) are illustrated in Figure 5.12. In general, the differences between these three expansion curves are insignificant.

Three expansion curves are almost identical in the first 100-day period of exposure, and then slightly diverge after 200 days. The divergence reduces as the mesh size reduces, in which the expansions of 7.5 mm and 10 mm models become almost identical. In this study, the mesh size of 10 mm was then selected for all other FE analyses of the RC prisms tested in Aryan et al. (2020).

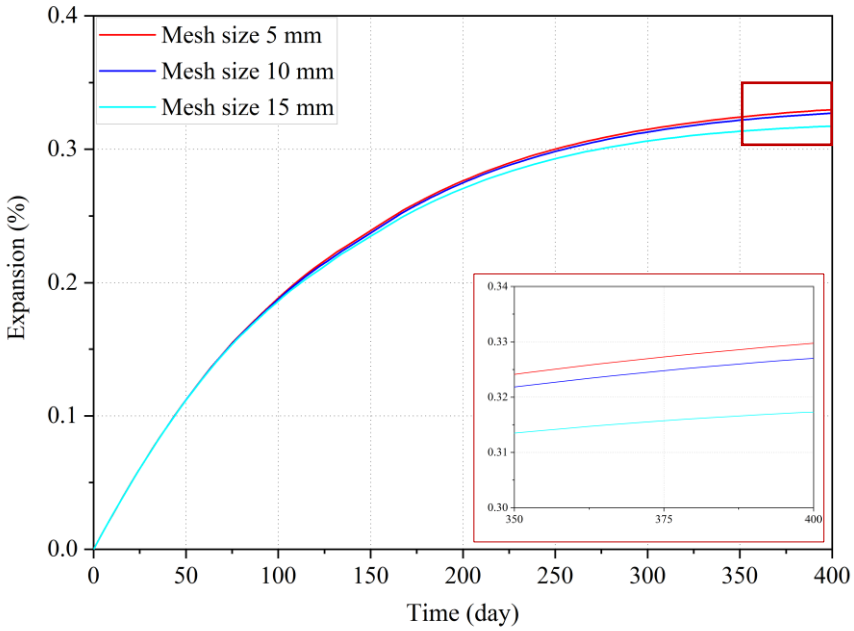

Figure 5.12: FE results on ASR expansion strain at different mesh sizes of the Batch 3 prism with 1.23% reinforcement ratio.

5.5.1.2. *Effects of isotropic versus anisotropic expansion model*

To emphasise the importance of accounting for the stress-dependent anisotropic expansion, an "isotropic model" without considering the 3D expansion-stress dependency was conducted on the reinforced concrete prisms of Batch 3. The model was to compare Model I as an "anisotropic model" using Saouma's model. In the isotropic model, the compressive stress in concrete induced by tension in reinforcement still restrains expansion in the longitudinal reinforcement direction in each time step; however, the

induced compressive stress in concrete does not influence the expansion rate of concrete for calculation of incremental expansion of the next time step. Therefore, the incremental expansion in each step of the isotropic model is as same as that value of the free expansion case. However, in the anisotropic models as presented previously, the stress state of the concrete at the current time step decides the extent of increase or decrease of incremental expansion in the next step.

Figure 5.13 shows computed results of Model I and the “isotropic model”, which is with and without considering the expansion-stress dependency effect, respectively, in comparison to measured data and free expansion curves. It is obvious that at all three reinforcement ratios, expansions of concrete obtained from the isotropic model are markedly higher than the measured data. The difference is greater as the time increases while conversely, the anisotropic model estimates the confined expansion better. Model I, which used Saouma's model to assess expansion-stress dependency, yields at slightly higher expansions in comparison to the measured expansions. In general, considering the expansion-stress dependency improved the estimation of expansion of RC prisms at all three reinforcement ratios.

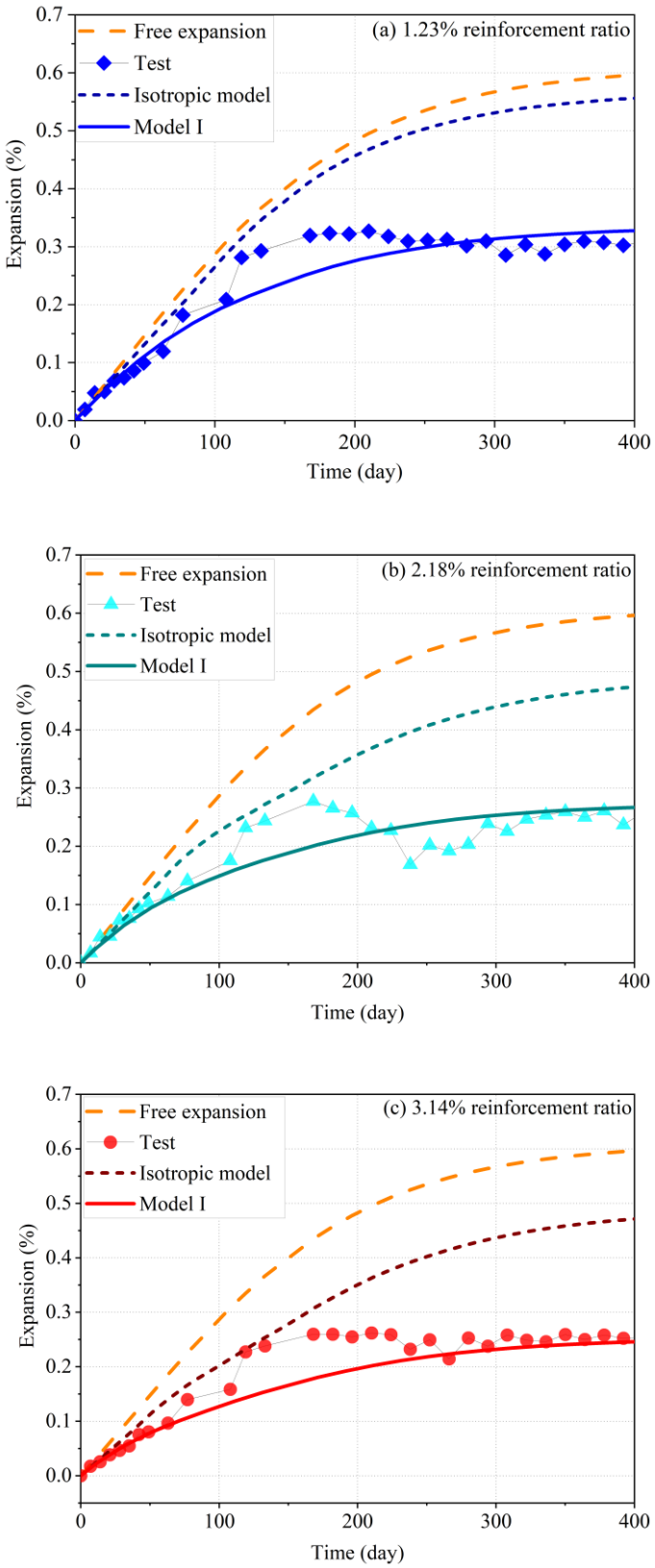

Figure 5.13: Comparison of modelling ASR expansion with and without considering expansion-stress dependency.

5.5.1.3. Comparison model outcomes to test data at different reinforcement ratios

Figure 5.14 and Figure 5.15 show the modelling results for expansions of Batch 2 and Batch 3 RC prisms of three reinforcement ratios in comparison to the experimental measurements. The results are from Model I and Model II, which used Saouma's and Gautam's models to consider the impacts of reinforcement on ASR expansion, respectively.

In general, there is a good agreement in expansions between experimental observations and numerical results for both Batch 2 and Batch 3 at all reinforcement ratios. Both the experimental data and modelling results show a significant reduction in expansions of prisms by using 1.23% of reinforcement, while increasing the reinforcement to 3.14% does not reduce expansions at the same rate. When comparing the two models, Model I using Saouma's model provided a slightly better estimation of the restrained expansion than Model II. Gautam's model seems to be "over-confined" to expansion in this case study.

Furthermore, reinforcement restraint affects the Batch 3 prism much more than the Batch 2 prism. For instance, expansions of the Batch 3 prism reduce up to 55% of the free expansion curve by using 1.23% of reinforcement, while this value of the Batch 2 prism is only about 30%. Table 5.4 presents the ratio of restrained expansion to free expansion obtained from the modelling of Batch 2 and Batch 3 mixtures after 1-year exposure. It is obvious that at the same reinforcement ratio, the higher the free expansion level, the lower restrained expansion/free expansion is observed, which means higher reduction in the restrained expansion. This observation can be explained by the rising compressive stress in concrete in the longitudinal direction (i.e., along the main reinforcement direction) due to generated compressive stress in concrete by reinforcing bars. For instance, Figure 5.16 shows the stress in concrete from Model I of the prism with 1.23% reinforcement ratio.

Results are extracted from the symmetric section of the prism. It shows that the compressive stress in concrete of Batch 3 prism is as high as 5.61 MPa, while this value of Batch 2 prism is about 3.75 MPa. It is noted here that the higher free expansion level, the higher compressive stress in concrete was generated in concrete, and then prevents expansion in the respective direction at a greater extent (see Figure 5.4). This observation can explain the significant variations in reduction levels at any given reinforcement ratio in ISE (1998) as shown in Figure 5.2, where the free expansion level of all the investigated concrete may vary from one to another. Therefore, instead of empirically considering only reinforcement ratio to estimate expansion of reinforced concrete, taking into account the free expansion level of concrete is also necessary. In this context, performing numerical modelling could provide more comprehensive and insightful information.

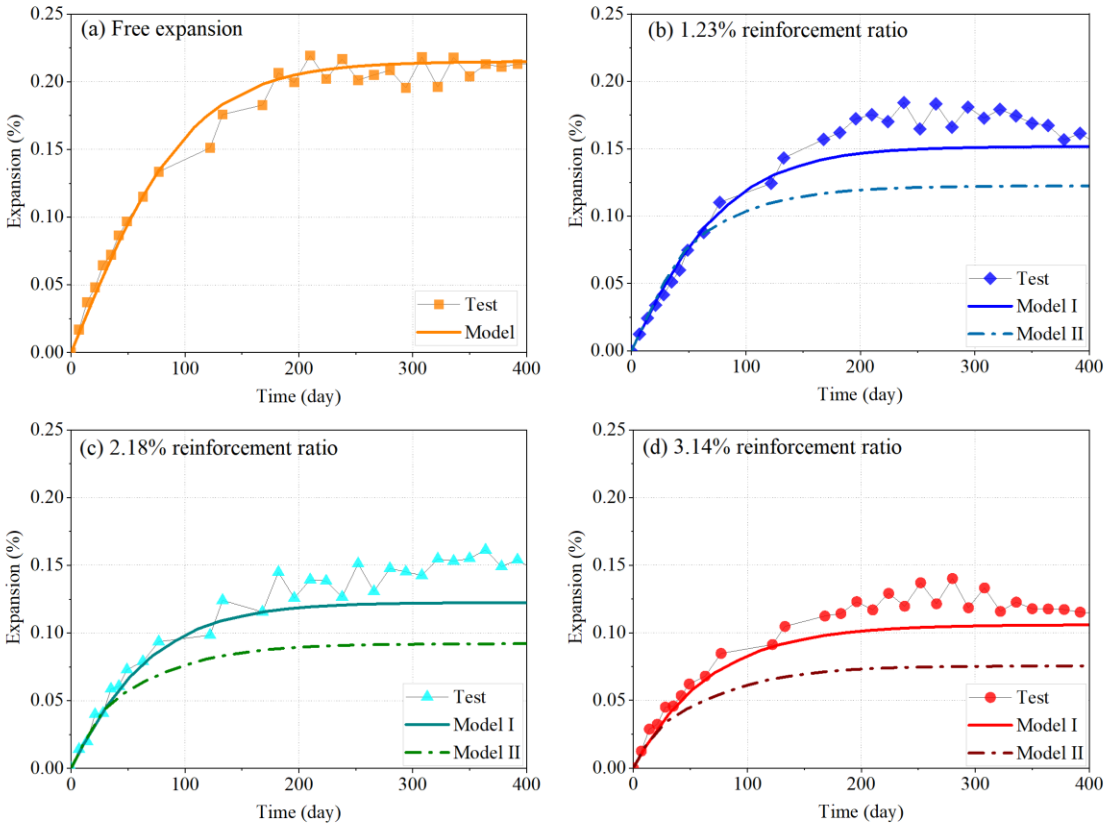

Figure 5.14: Modelling results versus measurement data of Batch 2 concrete prisms with: (a) non-reinforcement (free expansion), (b) 1.23%, (c) 2.18% and 3.14% reinforcement ratio.

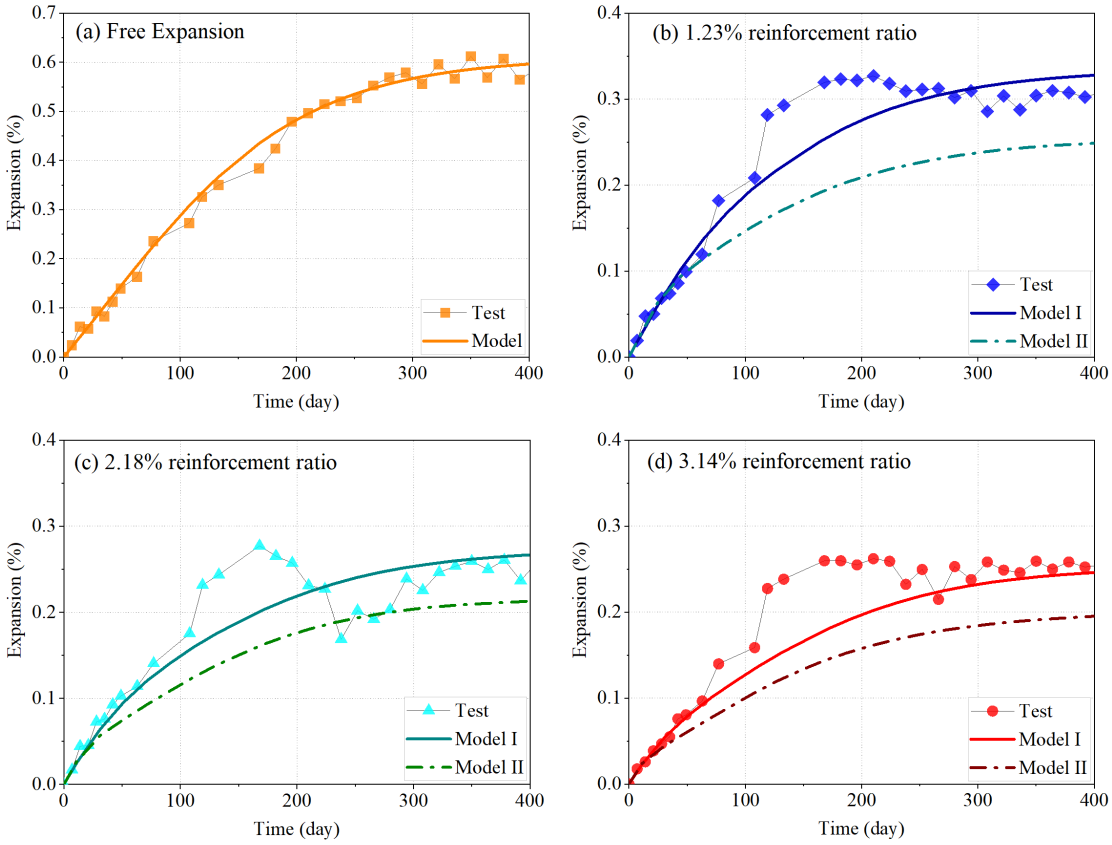

Figure 5.15: Modelling results versus measurement data of Batch 3 concrete prisms with: (a) non-reinforcement (free expansion), (b) 1.23%, (c) 2.18% and 3.14% reinforcement ratio.

Table 5.4: Confined reinforced expansion from Model I in comparison to free expansion

	Batch 2		**Batch 3**	
	1-year expansion (%)	Restrained expansion/ free expansion (%) (*)	1-year expansion (%)	Restrained expansion/ free expansion (%)(*)
Free expansion	0.2146	100	0.5893	100
1.23% reo	0.1515	70.6	0.3244	55.0
2.18% reo	0.1224	57.1	0.2632	44.7
3.41% reo	0.1057	49.2	0.2423	41.1
(*) These expansions are observed in the longitudinal reinforcement direction				

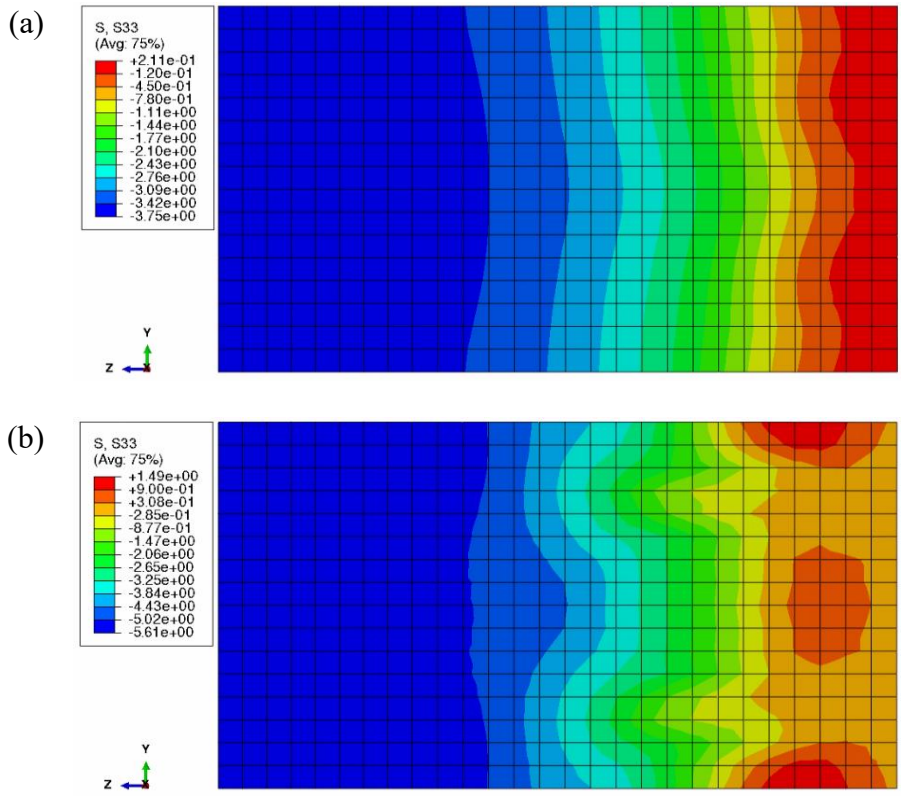

Figure 5.16: Stress distribution in the longitudinal direction (S33) of concrete prisms of 1.23% reinforcement ratio: (a) Batch 2 mixture and (b) Batch 3 mixture.

5.6. Application for modelling ASR-induced expansion of large-scale reinforced concrete beams in the field

In this section, the FE model was conducted to model expansion of reinforced concrete beams tested at the Kingston site, Ontario, Canada. An overview of this exposure site was presented in Chapter 4. In that chapter the proposed semi-empirical model served to predict the expansion of unreinforced beams based on laboratory testings data. The FE model implemented in this chapter is a continuation of the unrestrained expansion to modelling the expansion of the reinforced concrete beams.

5.6.1. Test description

Two main concrete mixtures incorporating the Spratt reactive aggregate and either low- or high-alkali content cement were tested for ASR-induced expansion in the field. The high- and low-alkali cement (HAPC and LAPC) contained 0.79% and 0.46% Na_2O equivalent per cement mass, respectively, which is 3.33 kg/m^3 and 1.91 kg/m^3 of mixtures, respectively. For each concrete mixture, reinforced and non-reinforced concrete beams (0.6 x 0.6 x 2 m) were prepared and exposed at the Kingston site for long-term measurements. A recent report from the MTO in 2018 provides 27-year data update of this field exposure site (MTO 2018). The measurement data of non-reinforced concrete beams were used in Chapter 3 for forecasting free expansions of the concrete in the field based on laboratory observations and provided very promising results. Note that the reinforced and non-reinforced concrete beams were made from the same reactive and non-reactive aggregates, mixture proportion and casting and curing method; thus, the only primary difference is the reinforcement restraint. On this point, the expansion measured from the non-reinforced concrete beams is an ideal free expansion input to the FE model. An additional consideration on the effect of reinforcement is then performed to estimate expansion of the reinforced concrete beam.

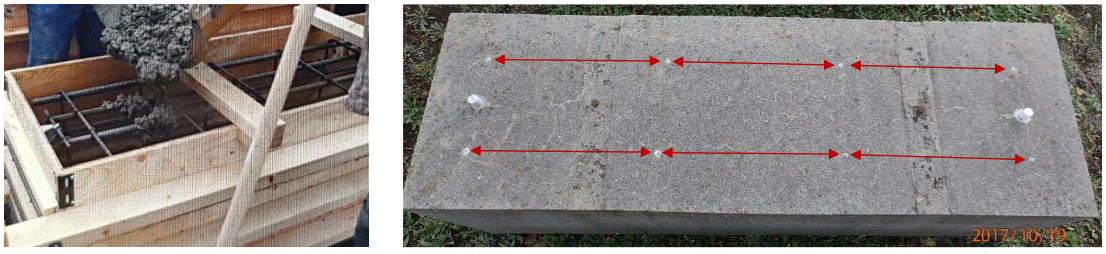

(b) Sample preparation (c) Expansion measurement stations

Figure 5.17: Kingston field test (MTO 2018).

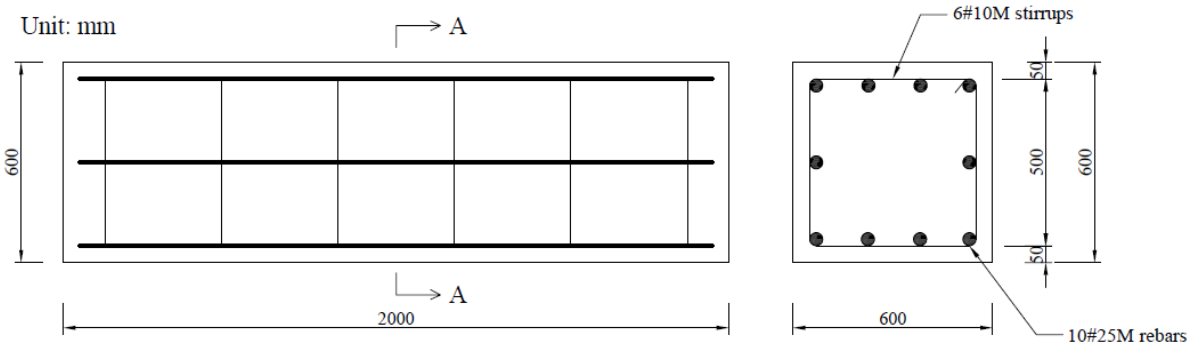

Figure 5.18: Dimensions and reinforcement configuration of RC beams.

The reinforced beams were made with the reinforcement ratio of 1.41% and concrete cover of 50 mm (see Figure 5.17(a)). In this test, expansions were measured from six stations on the top surface of the beams using a dial gauge device with a nominal length of 508 mm, as shown in Figure 5.17(b). Average expansions were calculated and reported in their final reports, i.e., in Doug Hooton et al. (2013) and MTO (2018). Figure 5.18 shows dimensions and reinforcement layout of the RC beams at the Kingston site. (*note: some of this information is based on personal communications with the main investigators of the Kingston site, Dr. Doug Hooton and Dr. Chris Rogers*).

Figure 5.19 presents the expansion data after 27-year exposure of non-reinforced and reinforced beams for both HAPC and LAPC mixtures (MTO 2018). It is obvious that ASR expansion reduced significantly due to the presence of reinforcement, i.e., up to 50% reduction when contrasted to expansions of the non-reinforced beams. Besides, the expansion rate of reinforced beams dropped noticeably after 15 years and this led to the plateau of the expansion curves, while non-reinforced beams kept expanding after 20 years' exposure. It is worth emphasising the uniqueness of this 27-year field data of reinforced concrete beams and its importance to the investigation of reinforcement effect.

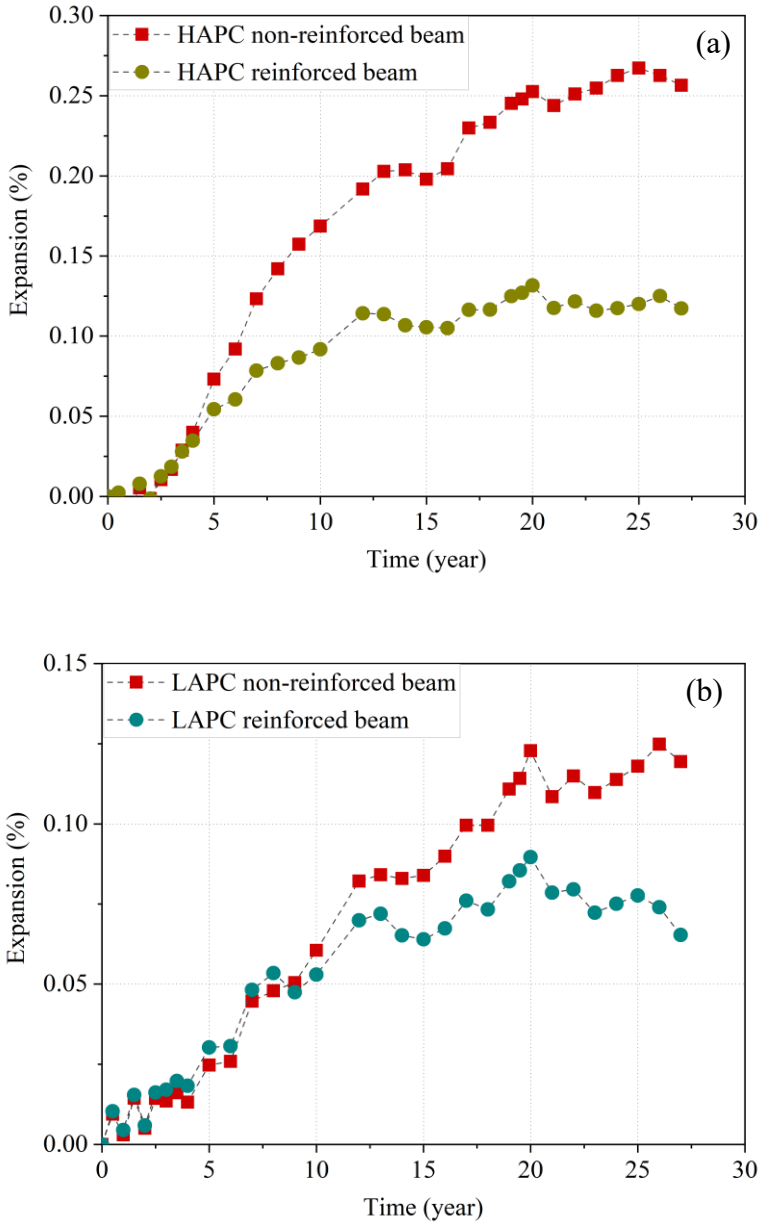

Figure 5.19: 27-year expansion data of non-reinforced and reinforced beams at Kingston site (MTO 2018): (a) HAPC mixture and (b) LAPC mixture.

5.6.2. Free expansion model

In this case study, two approaches were used to obtain the free expansion input to the FE model. Taking advantage of the available expansion data measured from non-reinforced beams, the first approach adopted Larive's model to obtain the free volumetric expansion

curve by fitting the expansion data measured from the non-reinforced beams. Model parameters of free volumetric expansion curve are shown in Table 5.5, while the free expansion as one-third of the free volumetric expansion was plotted together with measured data in Figure 5.20. These free expansion curves obtained from non-reinforced concrete beams with exactly the same mixture proportion and exposed to the same environmental conditions are ideal inputs for the expansion model of reinforced concrete beams. By using an "exact" free expansion curve for inputs, the FE model is expected to produce a good estimation for expansions of the reinforced concrete beams.

The information about free expansions of non-restrained members is usually not available for actual structures where all the members are under restraints/confinements. Therefore, the expansion model developed in Chapter 3 becomes crucial for estimating the free expansion of concrete in the field based upon laboratory measurements and environmental conditions in the field. In this regard, the second approach utilised results from the semi-empirical model as the free expansion input to the FE model to illustrate the continuity of modelling ASR expansion as a holistic approach. An interval of free expansion curves, which includes a lower and upper bound with considering a variation of relative humidity in concrete, i.e., from 95% to 100%, respectively, was used to model expansions of the reinforced concrete beams. Figure 5.21 shows these lower and upper bounds of the free expansion curves obtained from the proposed semi-empirical model in Chapter 3. As discussed previously in Chapter 3, the semi-empirical model underestimated expansions of the LAPC mixture; however, it was significantly improved from the model without considering leaching of alkalis in laboratory testings.

Table 5.5: Larive's model parameters of free volumetric expansion curves

Larive's model parameters	**HAPC**	**LAPC**
Charateristic time, τ_c (year)	3.70	5.00
Latency time, τ_L (year)	7.50	8.20
Maximum free volumetric expansion, ε_v (%)	0.789	0.369

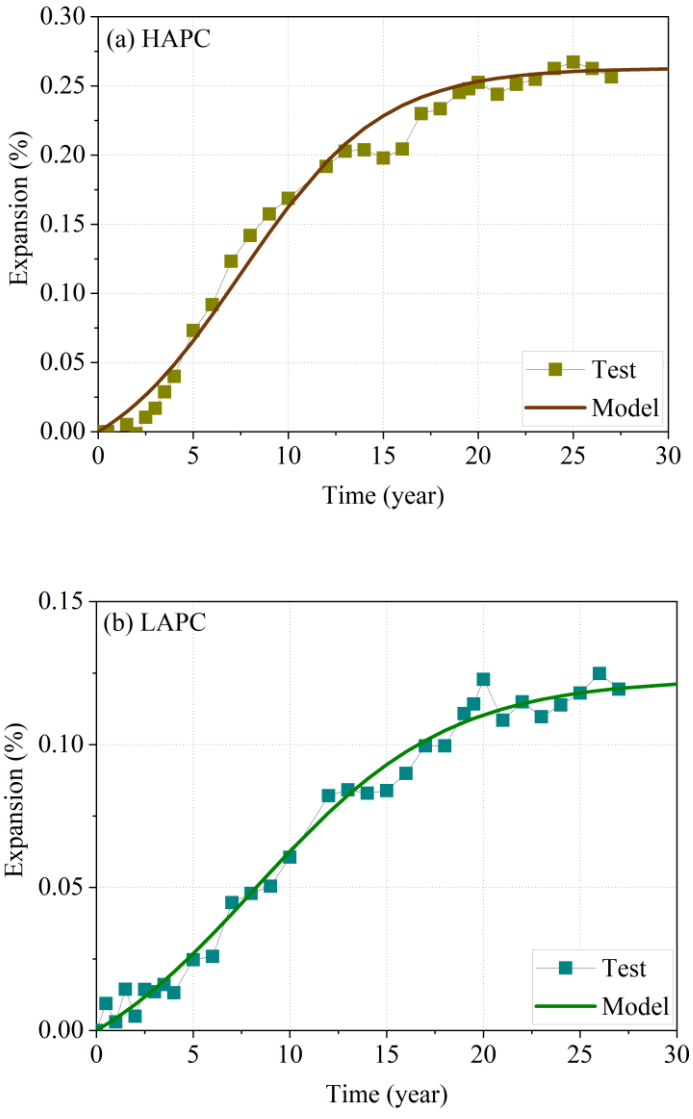

Figure 5.20: Measured and modelled free expansion curves of non-reinforced

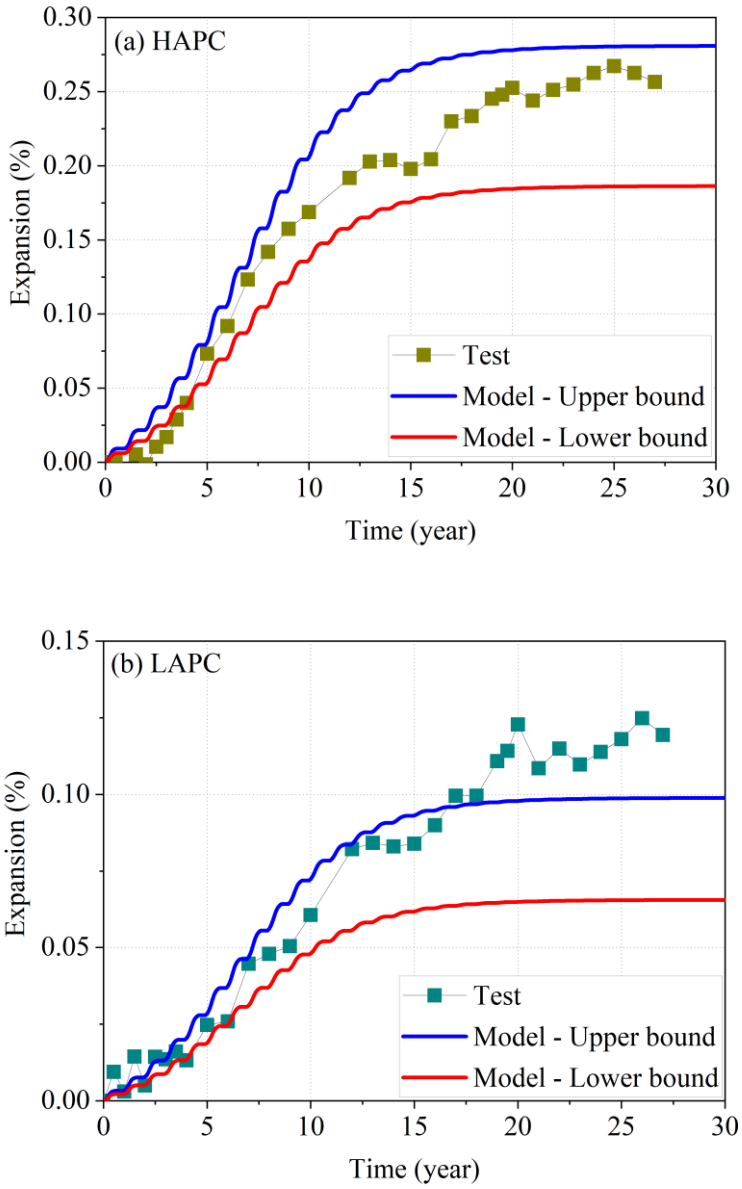

Figure 5.21: Measured and modelled free expansion curves of non-reinforced beams using the proposed semi-empirical model.

5.6.3. FE model description

Due to the symmetry of the prism geometry and boundary conditions, only a quarter of the full prism was simulated with the use of symmetric boundary conditions, as shown in Figure 5.22. 3D 8–node hexahedral element with reduced integration (C3D8R) and B31 three-node beam element were used for concrete and reinforcement respectively in finite

element modelling of RC beams. The reinforcement is embedded in concrete with the perfect bond model assumed, which means the concrete and reinforcement deformation are fully compatible. The models consist of 53600 C3D8R elements of concrete and 517 B31 elements of main reinforcements and stirrups, respectively, with an approximate size of 15 mm. Material properties of concrete (both HAPC and LAPC mixtures) measured at 28-day and steel reinforcement are shown in Table 5.6. The degradation of concrete mechanical properties was taken into account by using the mean residual mechanical properties–expansion relationship proposed in Section 5.3. Effects of the variations in residual mechanical properties were also investigated.

Both Saouma's and Gautam's models were implemented in Model I and Model II, respectively, to account for the effects of reinforced confinement. To reproduce the expansion measurement on the beams, expansion strain was determined from relative displacement of two nodes located at a distance of 800 mm, and their locations are detailed in Figure 5.22.

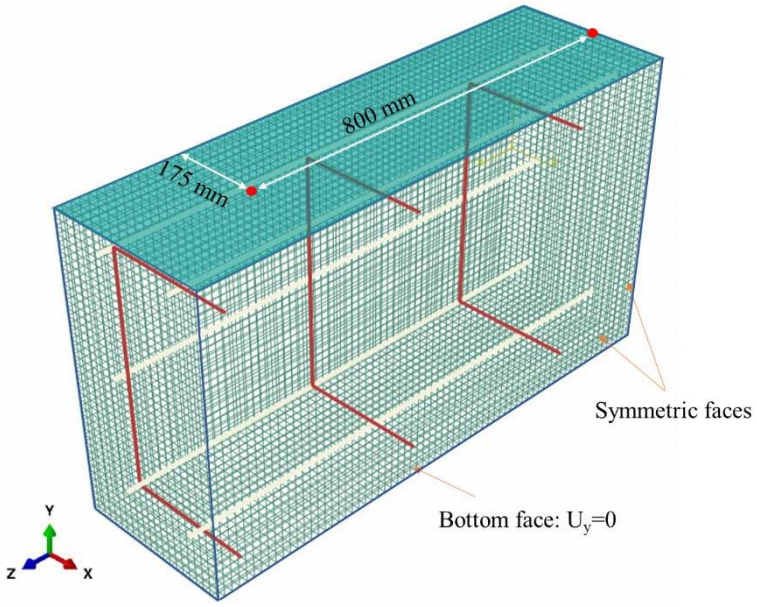

Figure 5.22: Geometry and boundary conditions of reinforced concrete prism.

Table 5.6: Material properties of the concrete and reinforcing steel

	HAPC concrete	**LAPC concrete**	**Steel bars**
Density (kg/m^3)	2400		7820
Poisson's ratio (-)	0.2		0.3
Young's modulus (GPa) (*)	32.8	34.0	205
Yield stress (MPa)	–		415
Ultimate strength (MPa)	–		625
Cubic compressive strength (MPa)	35.6	39.6	–
Tensile strength (MPa) (*)	3.15	3.42	–

(*) Calculated from measured compressive strength and splitting tensile strength in accordance with the CEB-FIP Model Code 1990

5.6.4. Results and discussion

5.6.4.1. FE modelling using "exact" free expansion input

Figure 5.23 shows the numerical results of HAPC and LAPC reinforced concrete beams from Model I and Model II using the "exact" input of free expansion curves. It is clear that both models provide estimate very well the expansion evolution of the reinforced beams. Model II using Gautam's expansion-stress dependent model is slightly better compared to Model I using Saoum's model. Similar to the experimental measurements, both models show that expansion of reinforced beams of HAPC and LAPC become relatively stable after 15 years and 20 years exposure, respectively, despite rising expansion in non-reinforced beams. This observation is very important for the prognosis

of ASR expansion in the actual structures, where potential expansion and damage in the future have to be identified.

It is also evident that the expansion results obtained from the two models are almost identical up to 0.075% expansion level, while at higher expansion levels, lower expansion rate are observed from Model II. This is because of the significant impact of compressive stress on ASR expansion in Gautam's model at the stress level of higher than 1.7 MPa (see Figure 5.4) (Gautam et al. 2017). However, it is worth noting herein that the more expansion is restrained in one direction, the higher expansion should be occurred in the other less restrained directions. This is shown in Figure 5.24 on expansions along the vertical direction of the reinforced beams. Vertical expansions obtained from Model II using Gautam's model is higher than the expansion in the results from Model I. Higher expansion in the vertical direction could explain the development of cracks along the main reinforcement's direction, as shown in Figure 5.25, which is commonly observed in field structures affected by ASR. It is noted that the plastic strain (PE) shown in Figure 5.25 is the strain values exceeding the elastic range, which can be used to represent the strain after concrete starts cracking. It can be seen that cracks start from the middle of the beam at the bar level and propagate along the beam toward the end of the beam.

The vertical expansions from both models are higher than the free expansions. This is again due to the transferring behaviour of expansion due to confinements, as discussed previously. Such observation is important for assessing expansion and deformation of actual structures, where expansion in the field needs to be measured in different directions to provide a comprehensive assessment. In this regard, more confirmation of 3D expansion due to reinforced confinement is necessary to refine the ASR constitutive model.

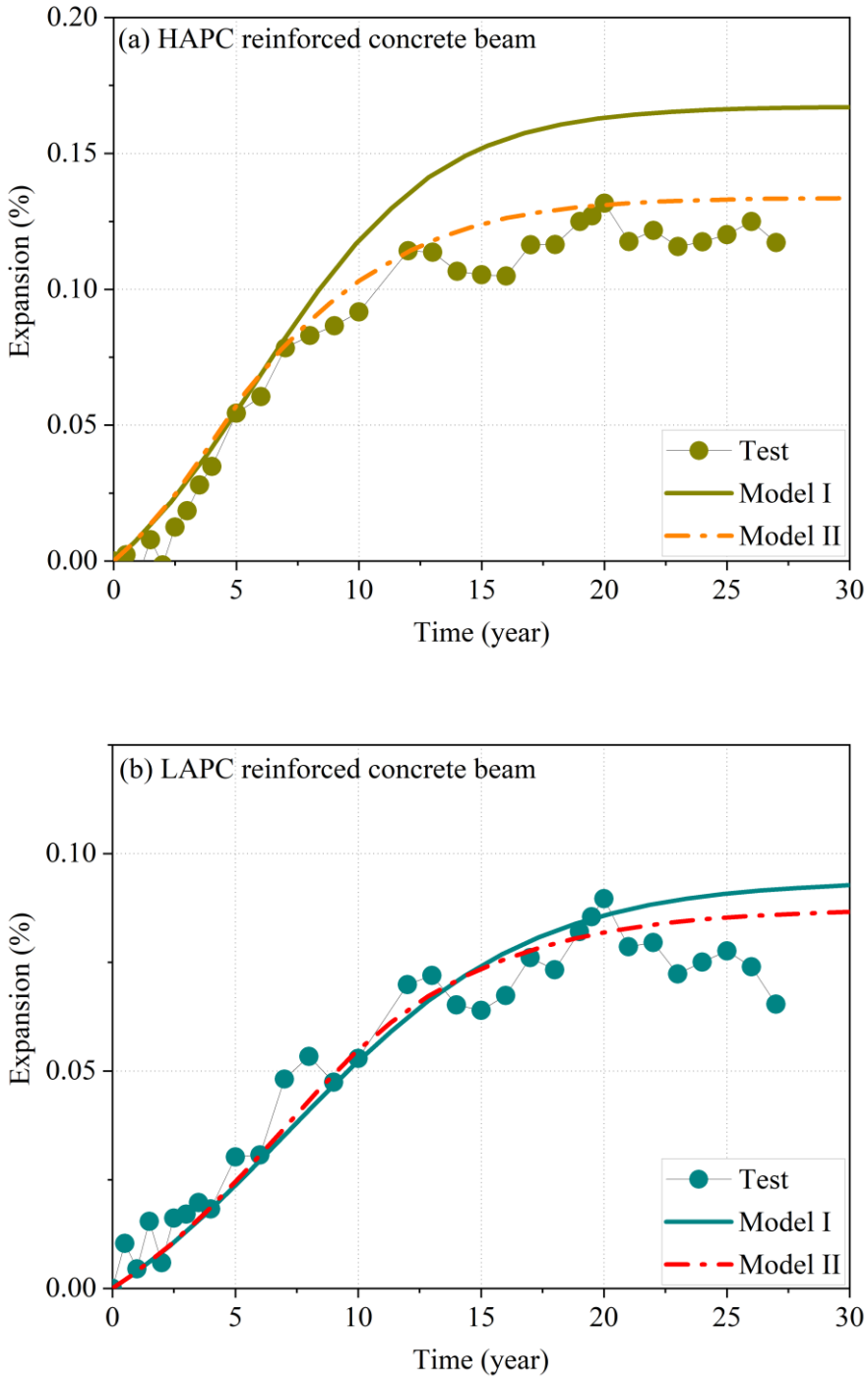

Figure 5.23: Numerical expansion curves of reinforced concrete beams of HAPC and LAPC mixtures.

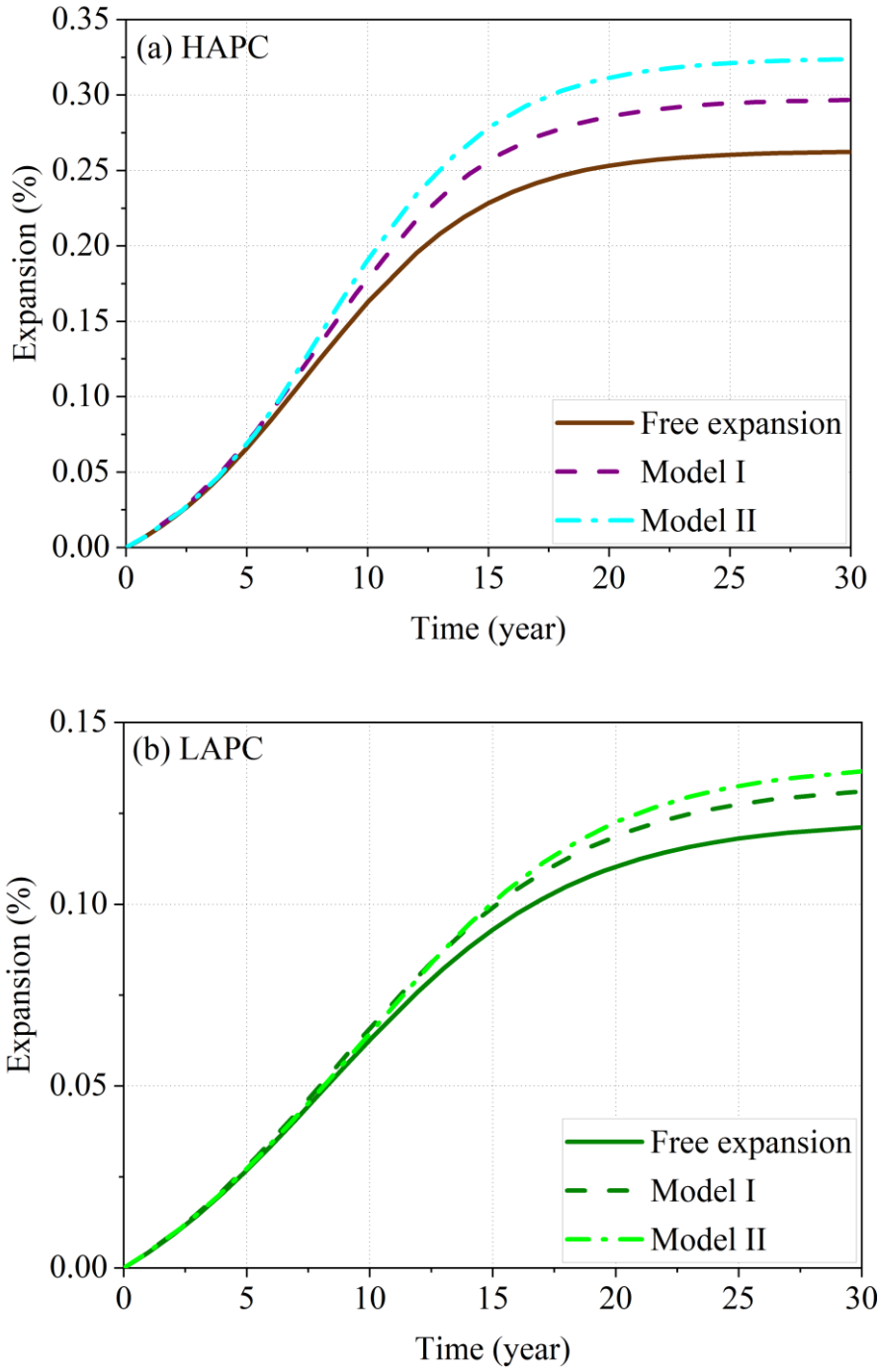

Figure 5.24: Numerical expansions in the vertical direction of the reinforced beams.

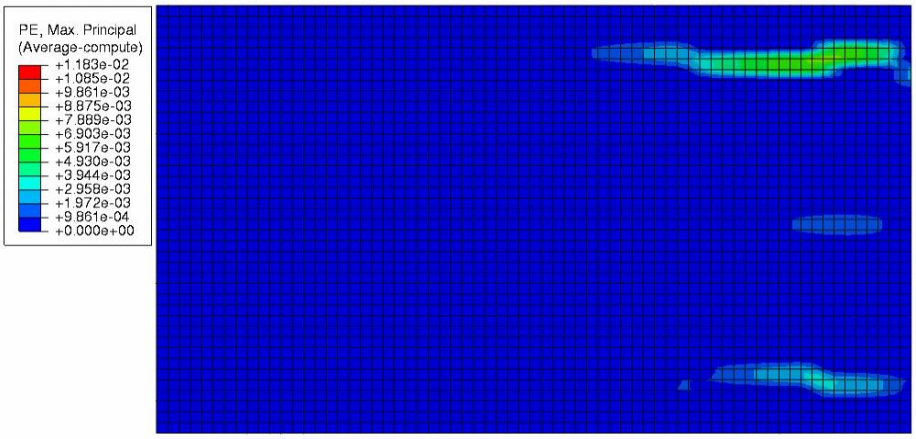

Figure 5.25: Development of cracks along the main reinforcing bars from the reinforced beam of HAPC.

5.6.4.2. Effect of the variation in residual mechanical properties to ASR expansion

The variations in residual mechanical properties as presented in Section 5.3 were considered in the numerical model to investigate their effects on the expansion of the reinforced concrete beams. Model II was selected for the investigation in this section due to its better expansion predictions for both HAPC and LAPC beams. The results of FE models using upper bound, lower bound and mean values of the residual mechanical properties. Overall, it can be seen that impacts of the variations in residual mechanical properties on expansion of the reinforced beams are insignificant. Furthermore, the higher expansion level, then the higher impact of the variations which was observed; thus, the impact on the reinforced beam of HAPC is more notable than on the LAPC one. This could be explained by the increase in mechanical deformation as the compressive stress in concrete increases (ISE 1992).

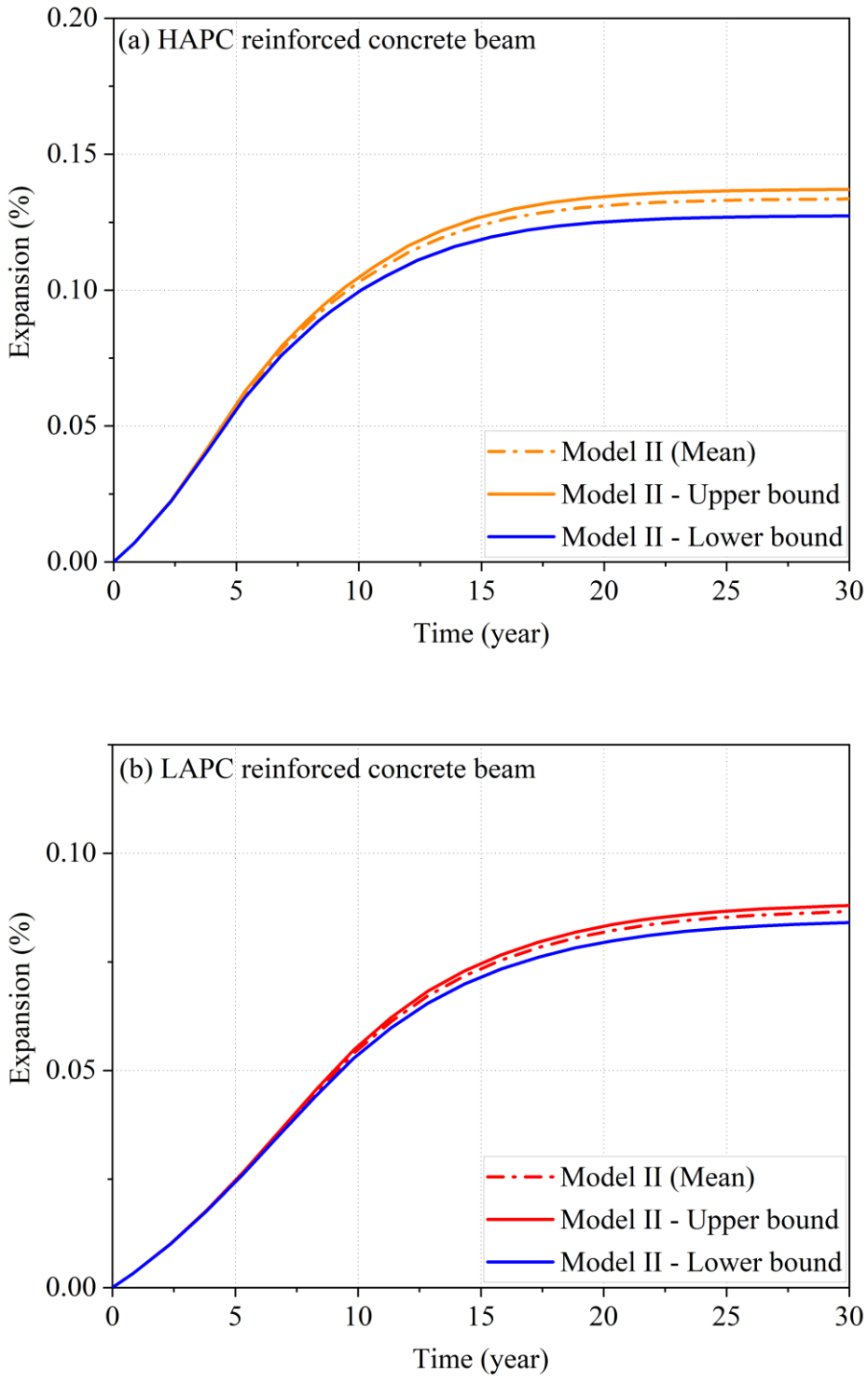

Figure 5.26: Predicted expansion curves of reinforced concrete beams of HAPC and LAPC using upper bound, lower bound and mean values of the residual mechanical properties.

5.6.4.3. FE modelling using free expansion from the semi-empirical model

Both Model I and Model II show their ability to account for reinforcement restraints in estimating expansions of reinforced concrete beams with the "exact" free expansions input. Therefore, the most important task in evaluating actual structures is providing an accurate estimation of free expansion of concrete in the environmental conditions in the field. The more accurate free expansion curve is, the better estimation of the restrained expansion could be obtained. Figure 5.27 and Figure 5.28 show, respectively, the numerical results of HAPC and LAPC reinforced beams using intervals of free expansion curves obtained from the semi-empirical model as the inputs to the FE model. With a better estimation of free expansions for the HAPC mixture from the semi-empirical model, the numerical models provide ranges of expansion which cover almost the whole measured expansion curve of the reinforced beam. Likewise, due to moderate underestimation of free expansion curves of the LAPC mixture, predicted expansions of the respective reinforced beam are slightly lower than the measured data, in which the measured curve is close to the upper bound of the modelled expansion. This again emphasises the importance of providing accurate forecasting of the free expansion of concrete prior to conducting a numerical analysis for any actual structures.

An integrated modelling approach consisting of the novel semi-empirical model and numerical model developed in this study was able to forecast expansion of actual reinforced concrete members in the field. The most important information that should be paid more attention is the construction documentation of structures. These records should provide both concrete mixture information (i.e., reactive aggregate, alkali content) enabling various laboratory tests to achieve the semi-empirical model's inputs, and reinforcement arrangement data enabling proper finite element analyses.

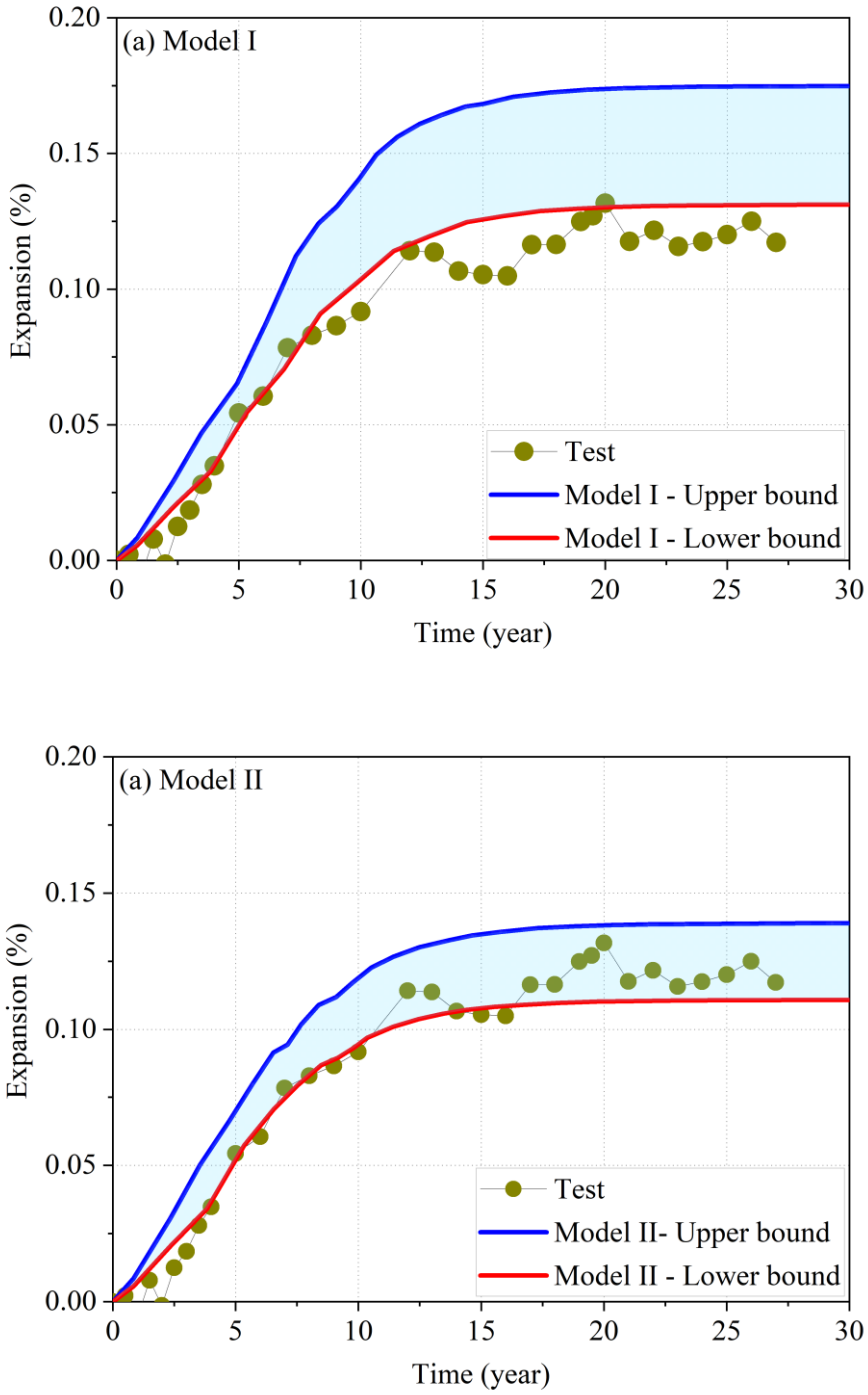

Figure 5.27: Numerical expansion curves of the HAPC reinforced beam from Model I and Model II using upper and lower bounds of free expansion curves from the semi-empirical model.

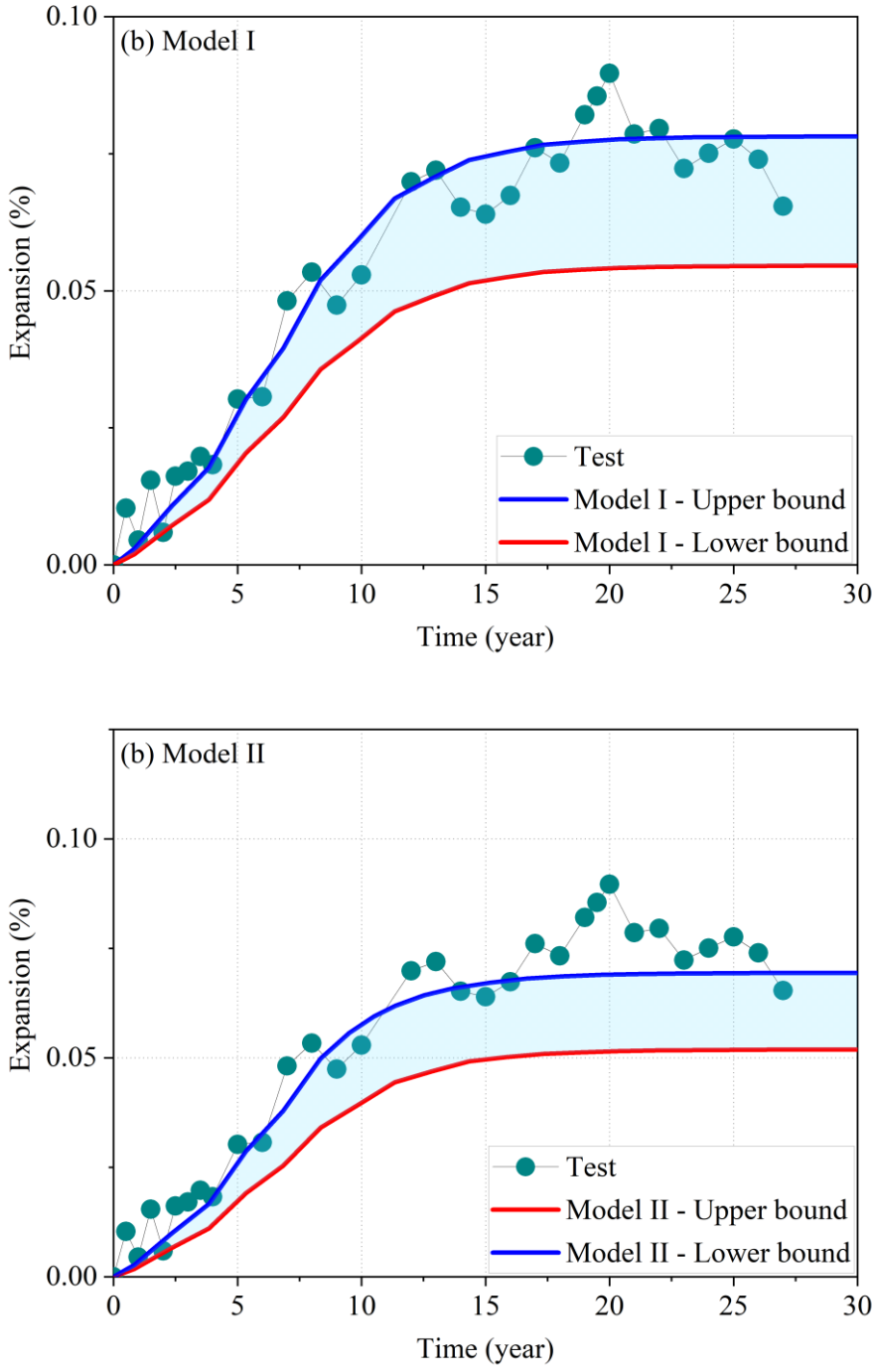

Figure 5.28: Numerical expansion curves of the LAPC reinforced beam from Model I and Model II using free expansion curves from the semi-empirical model.

5.7. An application for modelling ASR expansion and capacity of reinforced concrete beams

In this section, an application of the developed FE model was conducted for both expansion and load-carrying capacity modelling. The experimental data from the field concrete is an ideal dataset for this application of modelling both the expansion and capacity, yet, they are not available. Therefore, this study was conducted using an experimental dataset from laboratory testing, which aims to show the capacity of the developed FE model to transfer the expansion modelling results (i.e., concrete expansion, tension in reinforcements, residual mechanical properties and stress state of concrete and reinforcement elements with spatial variations) to the modelling for the load-carrying capacity of the reinforced concrete members. This integrated FE model is able to consider the effects of ASR-induced spatial variation of stress state and residual mechanical properties of concrete elements to the load-carrying capacity. In this regard, experimental data from Fan & Hanson (1998) on reinforced concrete beams tested in the laboratory were selected for this investigation as an example. The expansion model was performed in the same way as previous case studies prior to transferring to modelling for the load-carrying capacity.

5.7.1. Test description

Fan & Hanson (1998) conducted a series of test on reinforced concrete beams (150 x 250 x 1500 mm) for ASR expansion and capacity. Their tensile reinforcement ratio is 1% by using 2#5 bars (approximately 16 mm in diameter). The beam's dimensions and reinforcement configuration are shown in Figure 5.9(a). Two reinforced concrete beams were prepared, namely, 5R1 and 5N1 (or reactive beam and non-reactive beam), which used concrete mixtures containing reactive and non-reactive aggregates, respectively,

with the same mixture proportions. They were immersed in an alkali solution at 38ºC with periodic expansion measurements for 1 year. The expansion was measured from Demec studs mounted in the beams' surfaces using a Demec dial gage at different locations and directions, as shown in Figure 5.9(b). Measured expansions are shown in Figure 5.30. It can be seen that the expansion of both 5R1 and 5N1 beams (at all locations) were at the level of about 0.018% immediately after the beams were immersed in water. The author explained this initial expansion was caused by the absorption of moisture in concrete as well as the increase in exposure temperature. This expansion, hence, was considered to be a form of thermal expansion without any reduction in the concrete's mechanical properties. In addition, concrete cylinders were prepared along with the prisms for mechanical properties testings at 28-day, i.e., compressive strength, tensile strength and modulus of elasticity.

After 1-year immersion in an alkali solution, the beams were tested for their load-carrying capacity. The load-deflection curves obtained from both the 5R1 and 5N1 beams are shown in Figure 5.31. The load-deflection behaviours of these two beams are almost identical despite a certain reduction in mechanical properties of the concrete of 5R1 due to ASR. The behaviour of the non-reactive beam can be referred to as the undamaged concrete beam in comparison to the damaged reactive beam.

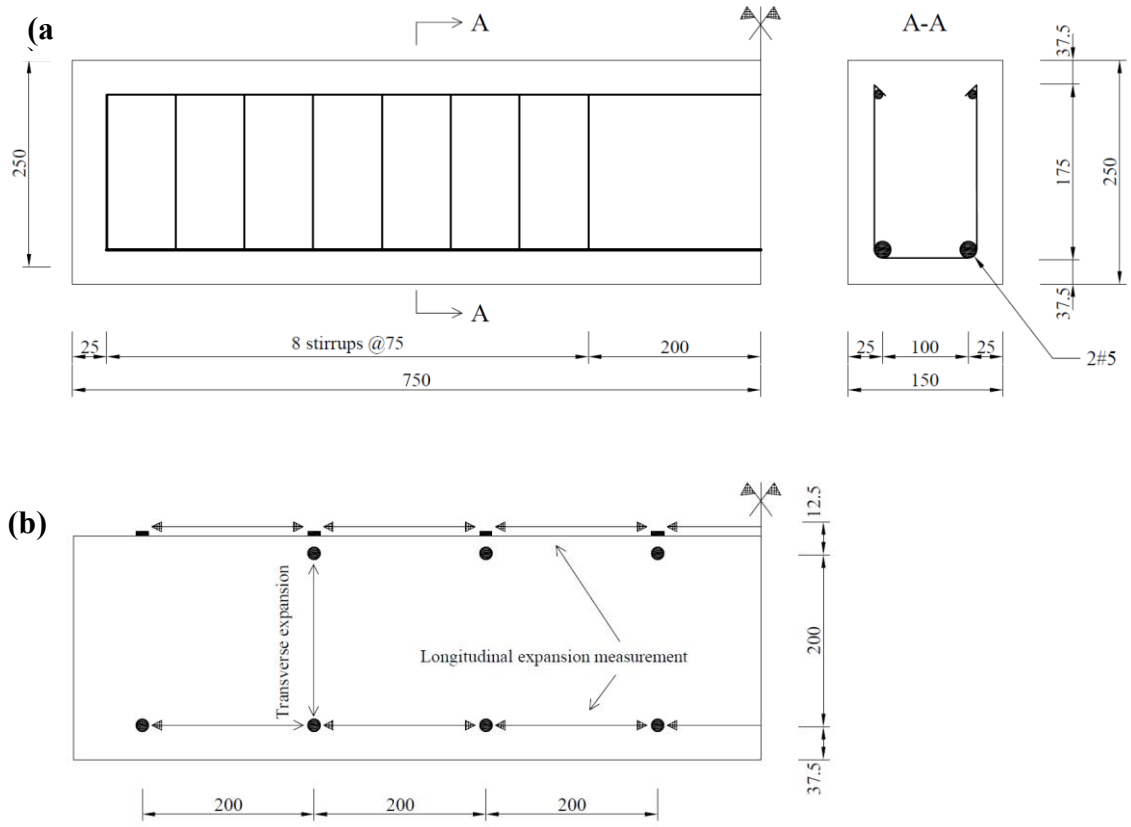

Figure 5.29: Reinforced concrete beams tested in Fan & Hanson (1998): (a) Dimensions and reinforcement configuration, (b) expansion measurements (unit: mm).

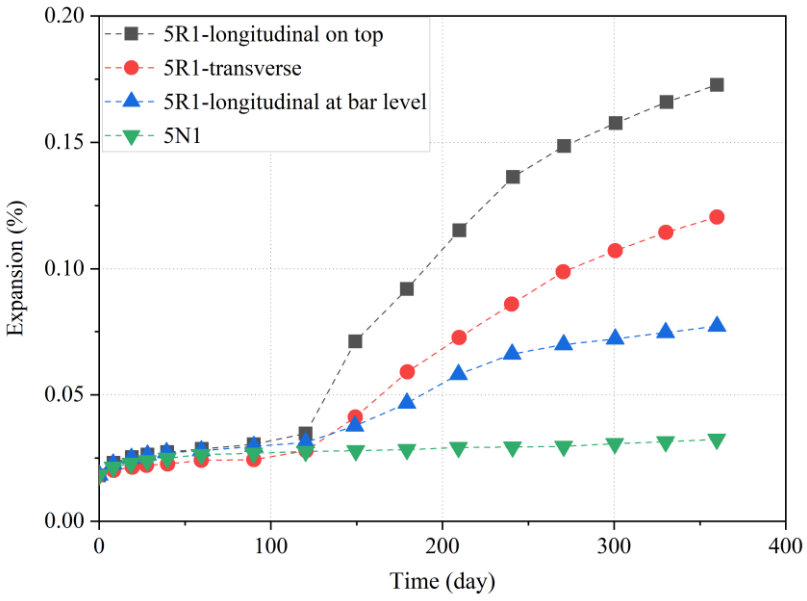

Figure 5.30: Expansion measured on the 5R1 and 5N1 beams.

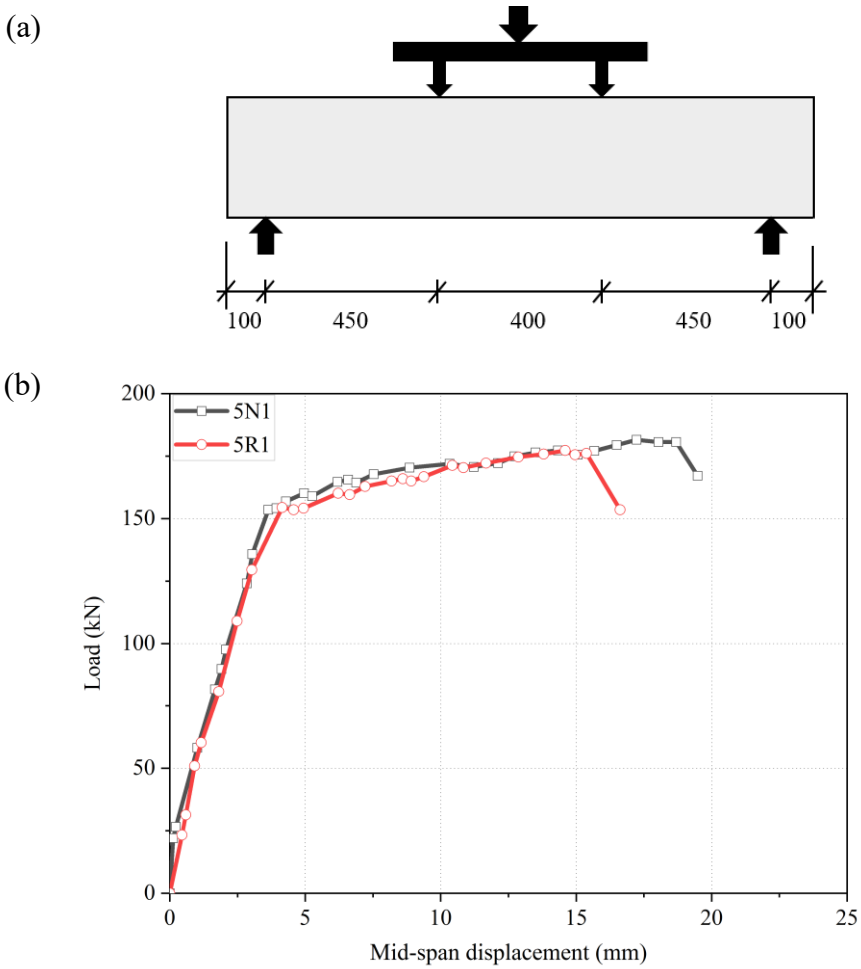

Figure 5.31: Test for load capacity of 5R1: (a) four-point bending test and (b) load-deflection behaviour.

5.7.2. Nonlinear finite–element modelling

5.7.2.1. Geometry and mesh

Due to the symmetry of the prism geometry and boundary conditions, only a quarter of the beam was simulated utilising symmetric boundary conditions as shown in Figure 5.32. 3D 8–node hexahedral elements with reduced integration (**C3D8R**), which are the most widely used in finite element modelling of reinforced concrete, was selected to model concrete. For the reinforcement, the 3D 2-node linear beam element (B31) was utilised for modelling of the reinforcement, in which the use of perfect bond model implies full

compatibility between concrete and reinforcement deformation. Mesh size of approximately 10 mm was used for all the FE analyses of the beams.

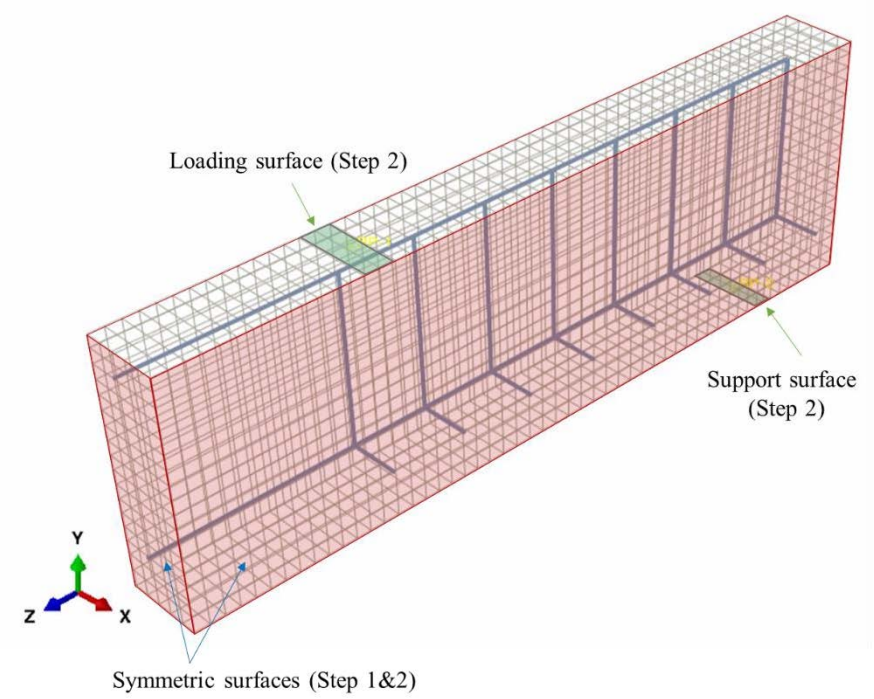

Figure 5.32: Geometry and boundary conditions of the reinforced concrete tested in Fan & Hanson (1998).

5.7.2.2. Boundary conditions and load application

FE model of the reactive beam consists of two computational steps, namely Step 1 and Step 2, for the expansion modelling and then modelling four-point bending test of the beam, respectively. Boundary conditions and loading are thus different for these two steps. As only one-fourth of the beam was modelled, symmetric boundary conditions were applied to two symmetric planes (see Figure 5.32) started from Step 1. The beam was assumed not be restrained by any end-supports at this step. To reproduce the expansion measurement on the beams, expansion strain was determined from displacement between nodes as the same locations as Demec studs (see Figure 5.29).

After completing the expansion modelling in the first step, additional boundary conditions and loadings as shown in Figure 5.32 were applied to simulate the four-point bending test. To avoid stress concentrations, a 20 mm wide surface was constrained to a reference point lying on this surface with a rigid body motion before restraining the vertical displacement only of the reference point. Likewise, loading was applied to a reference point lying on and constrained to a 30 mm wide surface on the top surface, in which a displacement–controlled strategy was used.

For the non-reactive beam, only the FE model for load-deflection behaviour was conducted, in which the boundary conditions and loading applications were similar to the second step of the FE model for the reactive beam.

5.7.2.3. Material properties

Material properties of concrete and reinforcing steel used for the FE model of both non-reactive and reactive beam are shown in Table 5.7. The constitutive models for concrete and reinforcement behaviour were discussed in Section 5.2 in this chapter. For the reactive beam, the residual mechanical properties with respect to the expansion level presented in Section 5.3 were adopted in the simulation of expansion and especially load-carrying capacity. Figure 5.33 illustrates the stress-strain behaviour of concrete under compression and tension at various representative expansion levels using mean values of the residual mechanical properties. The stress-strain behaviour of concrete defined at every 0.025% expansion level (i.e., 0%, 0.025%, 0.05%, 0.075%, 0.1%, etc.) appears to be sufficient to represent the change in the concrete mechanical properties as the expansion increases. Note that ABAQUS automatically and linearly interpolates the stress and strain at any other expansion levels based on the inputted stress-strain curves.

Table 5.7: Material properties of the concrete used for 5N1, 5R1 and reinforcing steel

	5R1 Concrete	5N1 concrete	Steel bars
Compressive strength (MPa)	34.7	35.9	–
Tensile strength (MPa)	3.21	3.28	–
Young's modulus (GPa)	32.6	32.9	200
Poisson's ratio (-)	0.2	0.2	0.3
Yield stress (MPa)	–	–	415
Ultimate strength (MPa)	–	–	720
Ultimate strain (mm/mm)			0.10
Density (kg/m^3)	2400	2400	7820

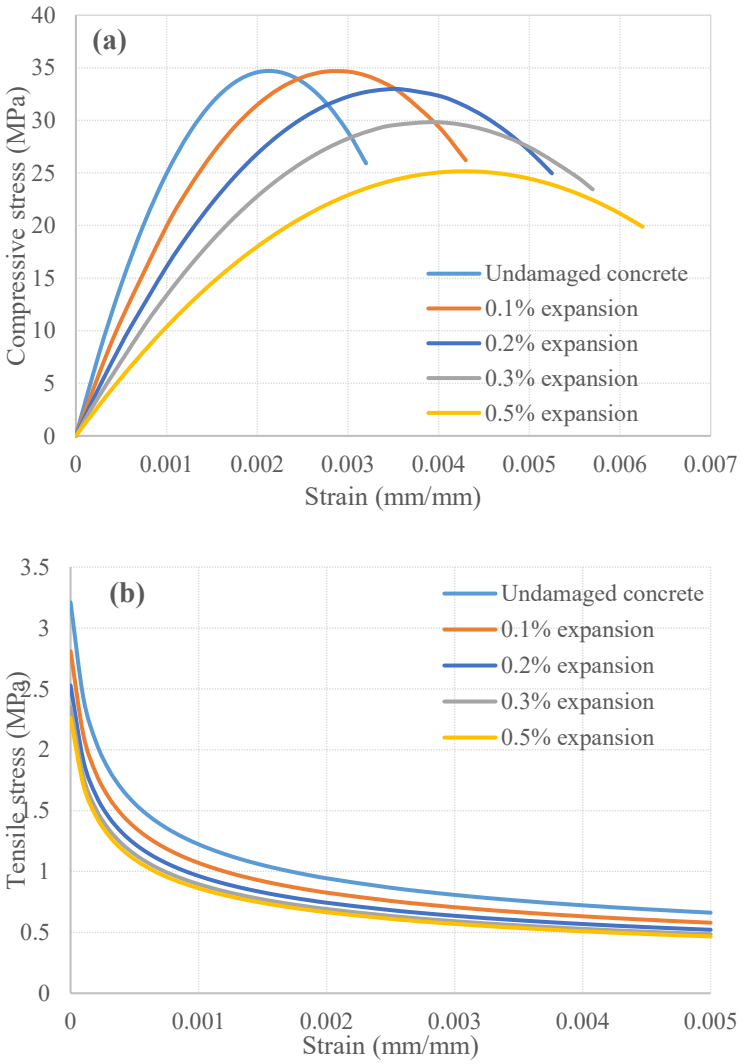

Figure 5.33: Stress-strain behaviour of concrete under (a) compression and (b) tension.

5.7.3. Results of the ASR expansion modelling

The free volumetric expansion curve used in this model is shown in Figure 5.34. This free volumetric expansion curve was assumed to obtain the same expansion of concrete measured on the top of the beam from the modelling. The main goals were to investigate the expansion under reinforcement restraints prior to modelling for load-deflection behaviour of the reinforced beams, taking into account the reduction in mechanical properties of concrete.

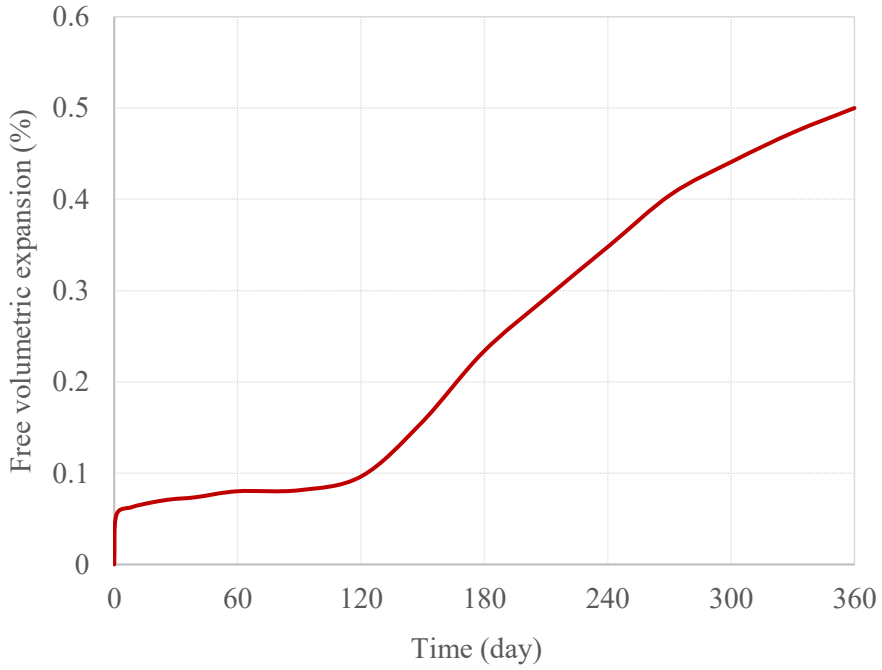

Figure 5.34: Free volumetric expansion of the concrete containing reactive aggregate

In this model, Gautam's model was adopted for measuring expansion-stress dependence in modelling expansion of the reinforced beam. Modelled results are shown in Figure 5.35, showing comparable outcomes to the measured expansions. It can be seen that the numerical results agreed well with the experimental data in the ratio of expansions in the longitudinal directions at the bar level and on top of the beam. This confirms the suitability of the proposed procedure to account for effects of reinforcement restraints.

With higher ratio of reinforcement in the longitudinal direction at the bottom, the expansions obtained at the bar level are significantly lower than at other locations. Similar to experimental observations, at the bar level, the expansion levels off after 240 days of immersion, while it keeps increasing in other less restrained directions. There is a higher expansion obtained in the transversal directions in comparison to the experimental data. This could be due to the casting direction-induced anisotropy as previously discussed.

In terms of mechanical properties effects, Figure 5.36 shows expansions obtained from three FE models using upper bound, lower bound and mean values of the residual mechanical properties with respect to the expansion level. The result shows an insignificant impact of the residual mechanical properties variations to the modelled expansion, especially for the less restrained directions such as transverse direction and longitudinal direction on top of the beam. This observation is similar to the previous application on modelling the Kingston reinforced beam.

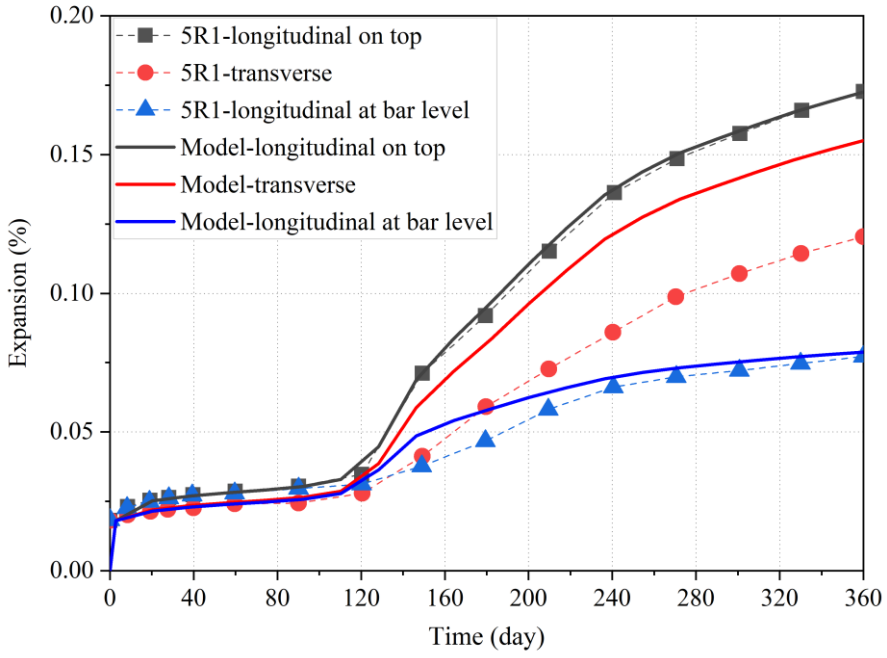

Figure 5.35: Numerical and experimental ASR expansion at different locations for the reactive beam.

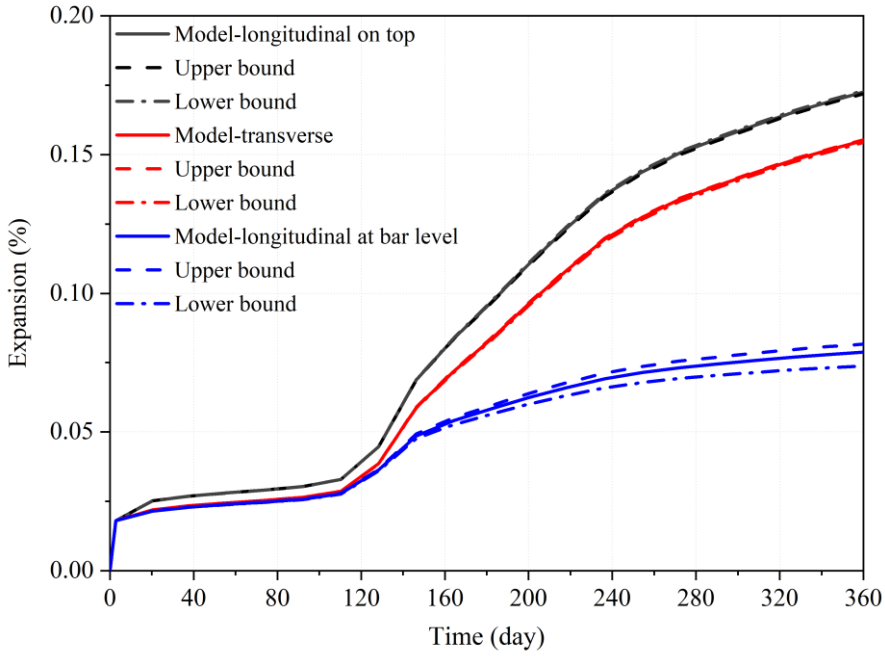

Figure 5.36: Predicted expansions using the upper bound, lower bound and mean values of residual mechanical properties.

5.7.4. Spatial distribution of stress, expansion and residual mechanical properties

Figure 5.37 shows the stresses of concrete elements in a cut section of the reactive beam at the symmetric plane. In the longitudinal direction, the compressive stress of concrete elements close to the bar level is significantly higher than other locations and directions, which is as high as 4.8 MPa. This greater compressive stress explains the lower expansion measured and computed at the bar level. Contrariwise, at the end of the beam without reinforcement, concrete elements are in tension instead of compression. Very low compressive stress levels of about 1.2 MPa are also observed in concrete elements on the top side of the beam. In the transverse direction, there is an insignificant effect of the stirrups when the highest compressive stress is only 1.8 MPa.

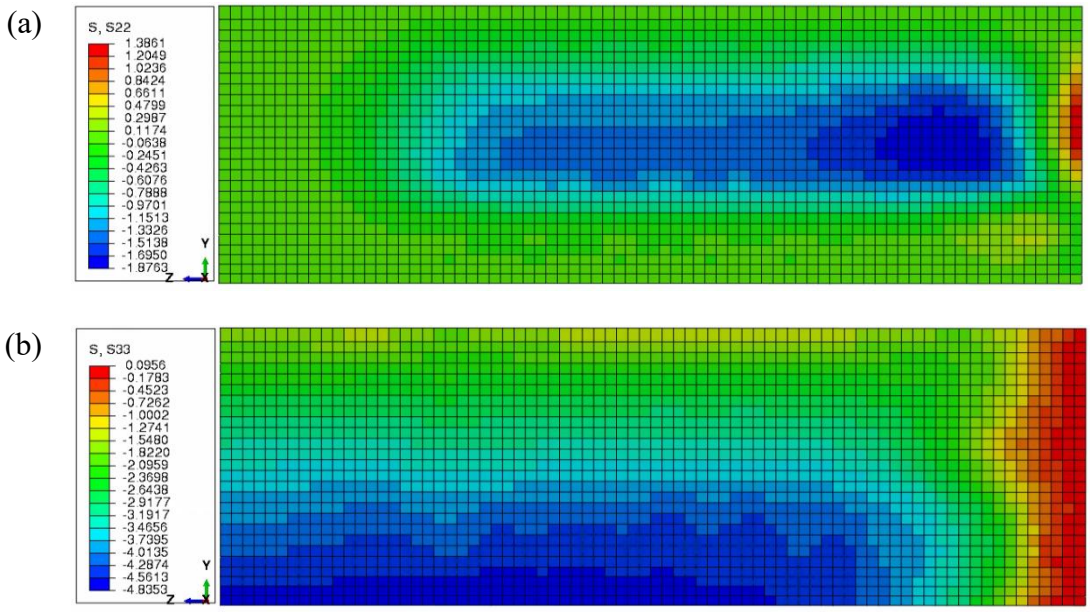

Figure 5.37: Spatial distribution of concrete stresses after 360 days: (a) S22 in the transverse direction and (b) S33 in the longitudinal direction.

The spatial compressive stress distribution could lead to the spatial distribution of the expansion and consequently to the residual mechanical properties of concrete elements in the beam, and vice versa. An example is shown in Figure 5.38 from a symmetric section of the beam for the average expansion of concrete elements from three principal directions (i.e., as one-third of the volumetric expansion). The expansion level of concrete elements around the bar level is notably lower than in other locations. Consequently, higher residual modulus of elasticity is observed in this bar level area. In general, however, the variation of the average expansion of concrete elements in the beam is insignificant. This is mainly due to the expansion transfer behaviour, as discussed in previous sections, as well as low expansion level the beam experienced.

The results of the residual mechanical properties of concrete are shown in Figure 5.39. It is noted herein that there is no change in mechanical properties of concrete elements up until 0.018% of the expansion level as previously discussed. After 360 days' exposure, the modulus of elasticity of concrete and tensile strength reduces up to about 40% and

25%, while the effect on compressive strength is negligible. Note that these observations are from the FE model adopting the mean values of the residual mechanical properties change.

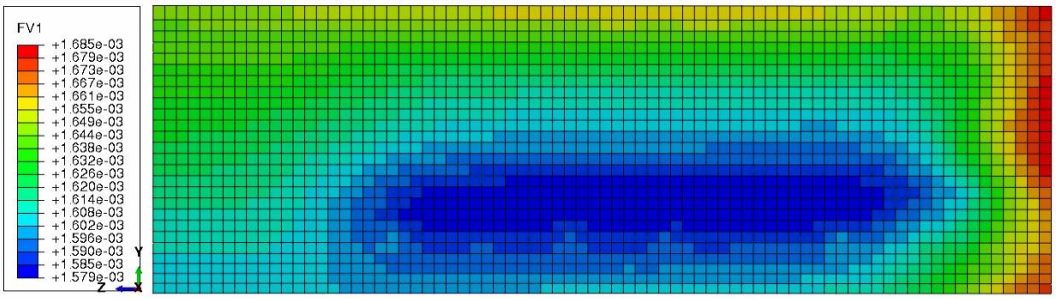

Figure 5.38: Spatial distribution of average expansion in concrete elements.

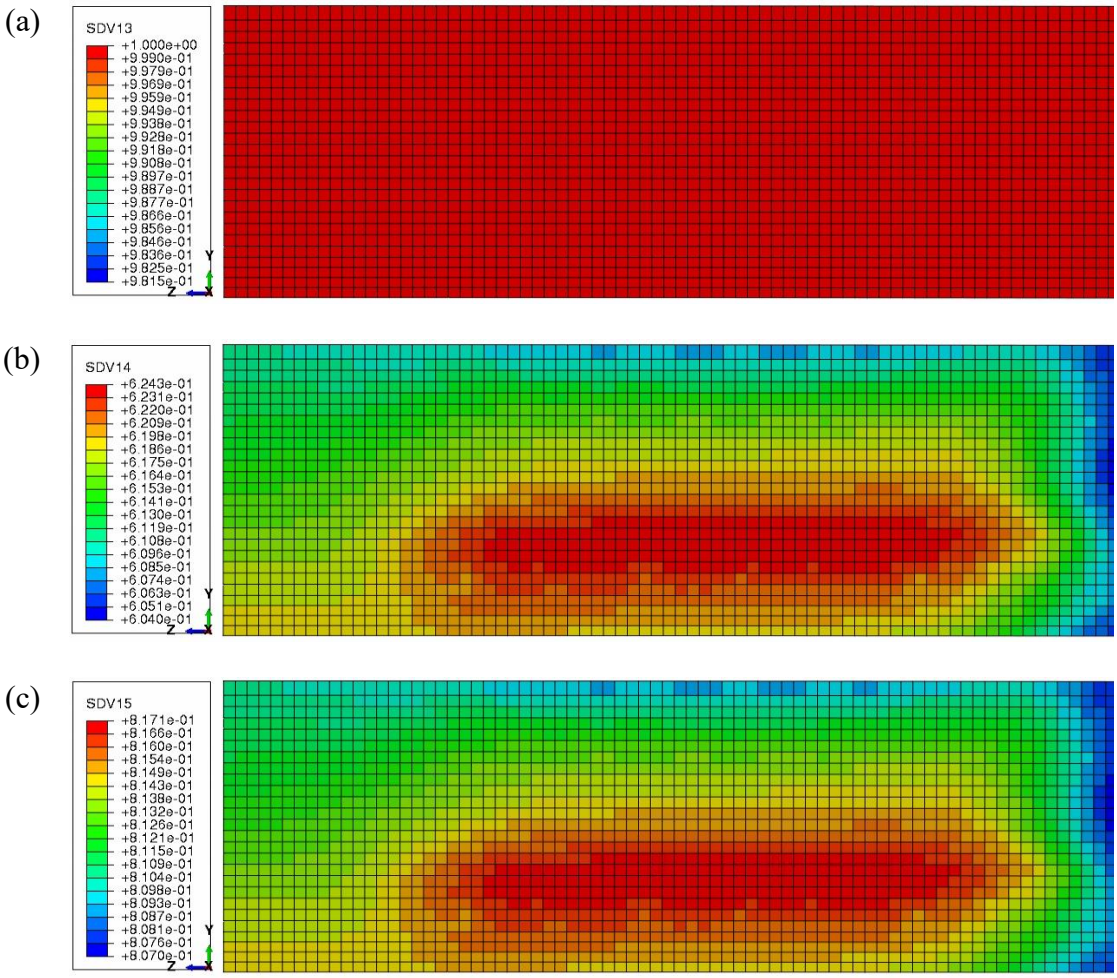

Figure 5.39: Spatial variations of the residual mechanical properties after 360 days: (a) compressive strength (SDV13), (b) modulus of elasticity (SDV14), and (c) tensile strength (SDV15).

5.7.5. Results of the capacity modelling

5.7.1.1. Comparison to experimental results

Load-deflection results for the 5N1 beam are shown in Figure 5.40. It is obvious that there is a good agreement between numerical and experimental results on the load-deflection behaviour. The numerical results of ultimate loading are about 176.3 kN in comparison to approximately 180.6 kN from the tested data, respectively. After the cracking of concrete at about 31.3 kN loading, there is a notable reduction in the beam's bending stiffness. After the reinforcement yielded, the beam failed due to crushing of concrete on the top of the beam. This good agreement between numerical and experimental results demonstrates validation of the FE model for the reinforced concrete beam in terms of material constitutive model, boundary conditions and load application prior to the modelling for the beam 5R1. It helps to minimise model uncertainties in FE modelling of the reactive beam, which covers both expansion and load-carrying capacity features.

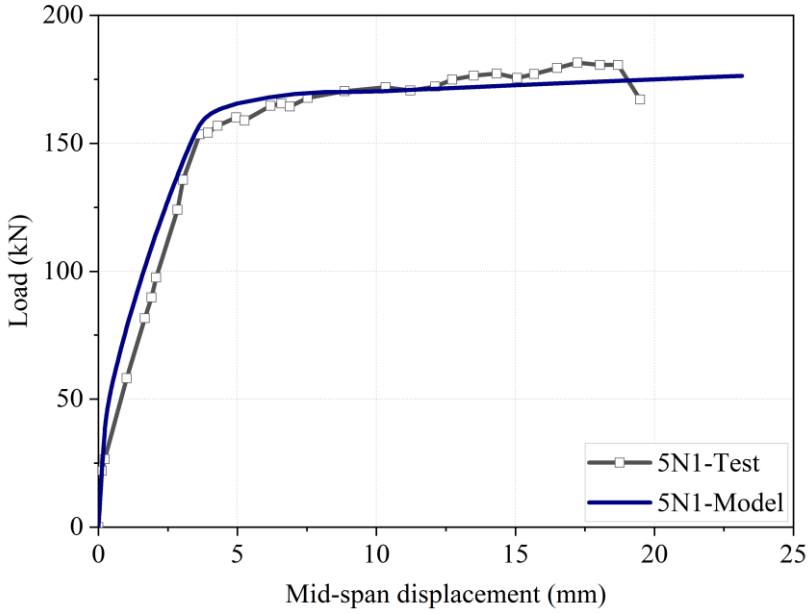

Figure 5.40: Load-deflection behaviour of the non-reactive beam.

Figure 5.41 shows the predicted load-deflection curve of the reactive beam using the mean values of residual mechanical properties. First, the numerical results are comparable to the experiment in terms of capacity. The predicted ultimate loading values of the beam are about 175.0 kN, while this value from test results is approximately 177.3 kN. Similar to the test data, the numerical results show an insignificant reduction in the capacity of the affected beam despite the reduction in mechanical properties as presented above. Second, the bending stiffness of the beam is slightly higher than the measured result despite the reduction in concrete stiffness. The observation is aligned with observations from ISE (1992), Hansen et al. (2016) and Huang et al. (2014), in which a favourable prestressing effect of the restrained ASR expansion helps to increase stiffness and capacity of several affected structures at low expansion levels. The perfect bond model between steel reinforcement and concrete provided the full potential of the prestressing stress transferred from reinforcement to concrete. Some studies, however, reported a degradation in the bond strength between steel reinforcement and concrete at high expansion levels (Huang et al. 2014; ISE 1992). Therefore, it is necessary to conduct intensive experimental testing on bond-slip behaviour between steel reinforcement and concrete, and implementation in the FE model.

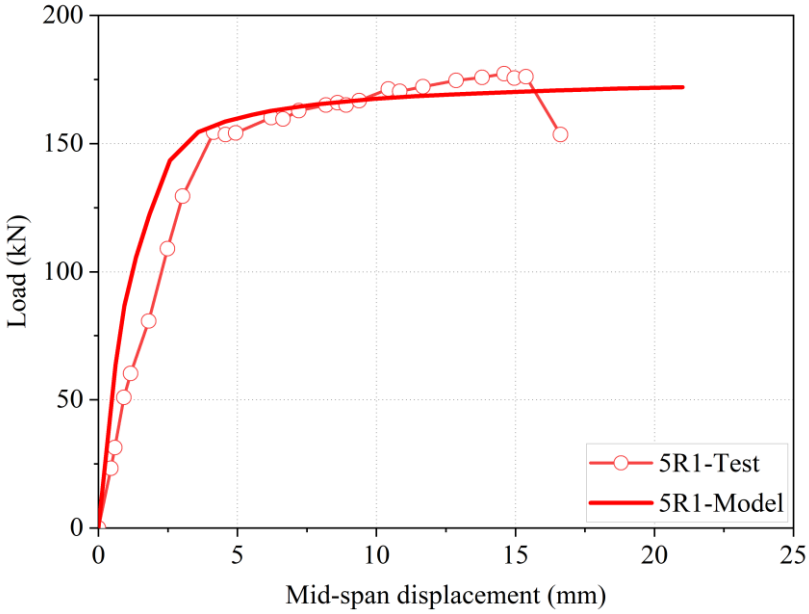

Figure 5.41: Load-deflection behaviour of the reactive beam.

5.7.1.2. Impact of uncertainties in residual mechanical properties on the load-carrying capacity

Figure 5.42 shows the results of three models using lower bound, upper bound and mean values of the residual mechanical properties in comparison to the test data. As discussed previously, there are insignificant effects of the expansion-dependent residual mechanical properties variations on ASR expansion advancement. Their effects on load-deflection behaviour are more notable. It can be seen that the overall bending stiffness and capacity of the beam was reduced from using the upper bound values to the lower bound ones. Note that the expansion level of concrete in the beam is still relatively low, and the effect of mechanical properties reduction on load capacity could become more significant at a higher expansion level. Hence, it is necessary to consider the reduction in mechanical properties and uncertainties in modelling for the capacity of the reinforced concrete structures affected by ASR.

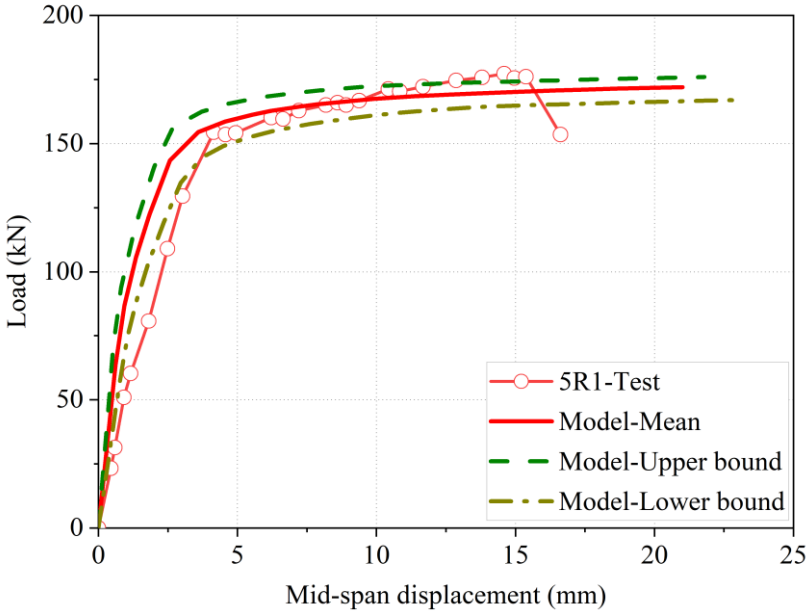

Figure 5.42: Effects of variations in residual material properties on load-deflection behaviour.

5.8. Summary

This chapter presents a numerical framework to model the ASR expansion and capacity of reinforced concrete members. For the expansion model, two models, namely Saouma's and Gautam's models, were adopted to account for restraint of reinforcement via stress dependency of the ASR expansion. The free expansion model presented in Chapter 4 and the stress dependent anisotropic expansion model formed a constitutive model for the ASR expansion modelling of reinforced concrete. The ASR expansion constitutive model along with the consideration of expansion-dependent mechanical degradation, was implemented in the FEA using different user subroutines. The model was validated by experimental data on reinforced concrete prisms at three different reinforcement ratios prior to using for modelling ASR expansion of the reinforced concrete beams at the Kingston site. The developed model proved its ability to link the free expansion of

unrestrained concrete to the expansion of the reinforced concrete. Along with the semi-empirical model proposed in Chapter 3, the model can account for different physicochemical aspects of the ASR reaction (temperature, relative humidity in concrete, restraints from reinforcement and applied stresses) to model the expansion behaviour of reinforced concrete based on laboratory measurements. The FE model could transfer the expansion modelling results such as strains, stress state, residual mechanical properties of concrete to modelling for load-carrying capacity of the affected concrete structural members, which in turn accounted for the spatial variation residual mechanical properties as well as the prestressing effect.

In general, both stress-dependency models proposed in Saouma & Perotti (2006b) - Liaudat et al. (2018) and in Gautam et al. (2017b) provided appropriate consideration for restraints from the reinforcement. Besides, it is necessary to conduct and compare their performance on expansions of reinforced concrete members in different directions. Concrete stiffness degradation due to ASR, in turn, has an insignificant effect on ASR expansion. The degradation of mechanical properties as a whole notably impacts on the load-carrying capacity. In this study, the issue of creep was not considered so future research should do so, especially for modelling of prestressed concrete members. The same strategy needs to be executed for bond-slip behaviour between steel reinforcement and concrete under ASR and confinement scenarios.

Chapter 6: Conclusions and recommendations

6.1. Conclusions

This study aimed to provide different modelling approaches for evaluating ASR effects for condition assessment and capacity evaluation of reinforced concrete structures suffering from ASR. First, degradation of mechanical properties due to ASR was evaluated using artificial neural network and computational homogenization. Then, a semi-empirical model was proposed for correlating expansion from the laboratory tests to the expansion of concrete in the field. Finally, a finite element model was developed for modelling expansion and load-carrying capacity of reinforced concrete members. The proposed models were able to forecast the expansion of concrete in the field based on laboratory measurements and evaluating mechanical properties degradation prior to assessing the structural capacity. The following conclusions were drawn from the three main chapters.

6.1.1. Degradation of mechanical properties due to ASR and evaluation of the reduction in modulus of elasticity of concrete

- Most studies on this subject show that the modulus of elasticity underwent a significant reduction compared to splitting tensile strength or compressive strength. Yet, the experimental data that has been published showed significant variations in the reduction of modulus of elasticity at any given expansion level. The lower bound of residual mechanical properties proposed by ISE (1992) is not applicable for modulus of elasticity, where many experimental testing groups provided greater reductions than the lower bound.

On the artificial neural network model:

- The proposed ANN approach was able to account for not only ASR-induced expansion but also other influential factors including cement content, proportion of reactive fine and coarse aggregate, exposure condition, total proportion of alkali content, initial compressive strength at the undamaged condition, and maximum measured expansion. In comparison to empirical models currently used, the ANN approach performed better with significantly lower mean square error and higher coefficient of determination in predicting the change in modulus of elasticity of concrete due to ASR. This approach provided a better estimation of modulus of elasticity for evaluation of ASR-affected concrete with the availability of certain important factors. The contributions of these factors have to be considered when evaluating the elastic modulus change on ASR-affected concrete.

- Based on results from the connection weights approach and partial derivatives method, the expansion level has a major impact on the modulus of elasticity of ASR-affected concrete among the 8 input variables in the ANN model. In addition, the maximum measured expansion, temperature, alkali content and fine reactive aggregate also make significant contributions, while cement content and proportion of reactive aggregate have less impact on the modulus of elasticity of ASR-affected concrete.

On the computational homogenization model:

- The computational homogenization procedure was developed to determine the effective stiffness of ASR-affected concrete mixtures using cracking

measurements in concrete damaged by ASR such as crack development patterns and density information. The model was able to model the impact of the ASR-induced cracking to concrete stiffness at various expansion levels. Based on the insights generated in this study, the meso-scale RVE-based computational homogenization procedure can be applied to a wider range of concrete mixtures presenting distinct aggregate natures and reactivity (i.e., potential to reach different and higher expansion levels). The proposed crack development scheme can serve as a basis in model updating strategies for damage detection purposes. For residual load capacity predictions of ASR-affected structures, the meso-scale RVE modelling approach can be adopted within a two-scale structural analysis framework.

6.1.2. Modelling unrestrained ASR expansion of concrete in the field

- Observations from several comparative laboratory-field studies in the past showed that the behaviour of concrete mixtures incorporating similar reactive aggregates vary greatly in the laboratory and in the field. It is often reported that field specimens such as exposed concrete clocks display significantly higher expansion than laboratory specimens. The main reason for this difference is the significant leaching of alkalis from the laboratory specimens, which is often much smaller in size and exposed a more “leaching-preferable” condition when compared to the field members.

- The leaching of alkalis is significant in the laboratory testing on small samples affecting not only the ultimate expansion but also the time constants (i.e., characteristic and latency times) of the concrete, whereas, it is minimal in the field

concrete blocks/members. By using the expansion curve and leaching at 1 year measured from laboratory testings, the proposed model is capable of estimating an ideal expansion curve without leaching to reproduce the field concrete expansion, which was well-calibrated using the different reliable laboratory test results. In comparison to the prediction without considering the leaching, forecasting of the field expansion using the proposed model shows significant improvement in forecasting expansion of non-reinforced concrete beam exposed at the Kingston site for 27 years and concrete blocks kept at CANMET for 20 years. In particular, the model results of Spratt concrete closely matched the field observations from both Kingston and CANMET specimens. Measurement of the alkali leaching emerges as very important to increase the reliability of the CPT in appraising maximum potential expansion and damage of the field concrete.

- For long-term exposed concrete, the total alkali content of the concrete is contributed not only from the cement but also possibly from the aggregates. A remarkable amount of alkali released from Sudbury reactive aggregate measured in (Bérubé et al. 2002) was adopted to raise the total alkali content of this concrete mixture for long-term expansion estimation. The good agreement between the model outcomes and measurement results of the 20-year exposed concrete blocks containing Sudbury reactive aggregate at CANMET site highlighted the significance of alkali contribution from aggregates to the long-term expansion of concrete in the field.
- The effect of environmental conditions (ambient temperature and relative humidity, precipitation) in this study are considered indirectly through concrete temperature and relative humidity. The model successfully reproduced the

expansion of both Spratt and Sudbury concrete blocks at CANMET and UT sites (i.e., the same mixture composition) using the same set of laboratory test results and their environmental conditions. This is crucially important in forecasting and correlating the expansion of concrete members using the same reactive aggregates and mixture exposed to different environmental conditions in a country. It is important to note that the concrete temperature highly influences the expansion rate, whereas the relative humidity wields a great impact on the ultimate expansion. In addition, the model outcomes reveal that the assumption of high internal RH such as 95-100% is reasonable for the concrete blocks kept in relatively high ambient RH and high precipitation environmental conditions such as at CANMET-Ottawa and UT-Texas.

6.1.3. Numerical modelling of ASR expansion and load-carrying capacity reinforced concrete

- The presence of reinforcement in concrete reduces the ASR expansion in the direction along the reinforcement, yet it may increase expansion in other directions. The numerical model is a finite element-based model, which was developed in the commercial FEA package ABAQUS using different developed user subroutines and the concrete damaged plasticity model. The numerical model was proposed by considering the impact of the reinforcement indirectly through expansion-stress dependency.
- Both expansion-stress dependency models proposed in Saouma & Perotti (2006b) - Liaudat et al. (2018) and in Gautam et al. (2017b) provided appropriate consideration for restraints from the reinforcement. In addition, concrete stiffness

degradation due to ASR have an insignificant effect on the ASR expansion evolution.

- The developed FE model proved its capability to link the free expansion of unrestrained concrete to the expansion of the reinforced concrete, such as modelling ASR expansion of reinforced concrete prisms at various reinforcement ratios. In addition, the numerical model was able to use free expansion results from the semi-empirical model for predicting expansion of the reinforced concrete beams in the Kingston site.
- The FE model was capable of transferring the expansion modelling to modelling of load-carrying capacity, which able to account for the spatial variation residual mechanical properties as well as the prestressing effect. The degradation of mechanical properties at whole induces more notable impact on the load-carrying capacity.

6.2. Recommendation for future works

Based on the outcomes of this thesis, several themes are recommended for future research to improve our scientific knowledge about diagnosis and prognosis of existing structures affected by ASR using modelling approaches. Suggestions are explained in more detail below:

- Even though the proposed ANN approach is able to gain insight into ASR effects on the change in modulus of elasticity, additional experimental data on the modulus of elasticity of ASR-affected concrete is desirable to improve the model accuracy as well as to enhance the evaluation of influencing factors effects. Especially, a comprehensive database from both laboratory and field exposed

samples/members are required for extending the model to evaluation of ASR-affected concrete in the field.

- Based on the insights gained from computational homogenization modelling, the meso-scale RVE-based computational homogenization procedure can be extended to a wider range of concrete mixtures presenting distinct aggregate natures and reactivities (i.e. potential to reach different and higher expansion levels). Uncertainties in the stiffness properties, aggregate volume fractions and crack patterns can be accounted for by utilising probabilistic approaches. The proposed crack development scheme can be used as a basis in model updating strategies for damage detection purposes. For residual load capacity predictions of ASR-affected structures, the meso-scale RVE modelling approach can be adopted within a two-scale structural analysis framework.
- The proposed simplified empirical model provides a practical, yet effective tool for forecasting ASR expansion of non-reinforced concrete in the field based on laboratory test results. However, additional reliable experimental data on ASR expansion, alkali leaching and alkali releasing from aggregates from both the laboratory and field contexts are essential to refine the proposed model. Additional test data of field concrete varying according to the types of reactive aggregate, levels of alkali, and exposed environmental conditions are necessary to provide more comprehensive confirmation of the proposed model. It is also important to further develop and apply the model for concrete with SCM to evaluate efficiency of the SCM in preventing ASR.
- In the FE model for ASR expansion of reinforced concrete, the current validation and applications in this study were mainly conducted to explore the expansion in

the main reinforcement direction. This is because the test data on expansion in other orthogonal directions were not available. Therefore, available test data of expansion to the three dimensions will ensure the reliability of the proposed model prior to application to field structures.

- The issue of creep was not explored in this thesis, so it should be the subject of future research, especially for modelling of prestressed concrete members. Bond-slip behaviour between steel reinforcement and concrete under ASR and confinements, and its impact on the expansion progress and structural capacity also need to be investigated.

References

2011, A.P., *Practice for Determining the Reactivity of Concrete Aggregates and Selecting Appropriate Measures for Preventing Deleterious Expansion in New Concrete Construction*, American Association of State Highway and Transportation Officials.

AASHTO, T. 2019, '380, Standard Method of Test for Potential Alkali Reactivity of Aggregates and Effectiveness of ASR Mitigation Measures (Miniature Concrete Prism Test, MCPT)', American Association of State and Highway Transportation Officials.

Abu-Obeidah, A., Hawileh, R. & Abdalla, J. 2015, 'Finite element analysis of strengthened RC beams in shear with aluminum plates', *Computers & Structures*, vol. 147, pp. 36-46.

Ahmed, T., Burley, E. & Ridgen, S. 1999, 'Effect of alkali-silica reaction on tensile bond strength of reinforcement in concrete tested under static and fatigue loading', *Materials Journal*, vol. 96, no. 4, pp. 419-28.

Allford, M.T. 2016, 'Expansion behavior of reinforced concrete elements due to alkali-silica reaction', University of Texas at Austin.

Altarazi, S., Ammouri, M. & Hijazi, A. 2018, 'Artificial neural network modeling to evaluate polyvinylchloride composites' properties', *Computational Materials Science*, vol. 153, pp. 1-9.

Aryan, H., Gencturk, B., Hanifehzadeh, M. & Wei, J. 2020, 'ASR Degradation and Expansion of Plain and Reinforced Concrete', *Structures Congress 2020*, American Society of Civil Engineers Reston, VA, pp. 303-15.

AS-1141.60.1 2014, *Methods for Sampling and Testing Aggregates Part 60.1: Alkali Aggregate Reactivity-Accelerated Mortar Bar Method*, Sydney.

AS-1141.60.2 2014, *Methods for Sampling and Testing Aggregates Part 60.2: Alkali Aggregate Reactivity-Concrete Prism Method*, Sydney.

Ashteyat, A.M. & Ismeik, M. 2018, 'Predicting residual compressive strength of self-compacted concrete under various temperatures and relative humidity conditions by artificial neural networks', *COMPUTERS AND CONCRETE*, vol. 21, no. 1, pp. 47-54.

ASTM-C1293 2015, *Standard Test Method for Determination of Length Change of Concrete Due to Alkali-Silica Reaction*, ASTM International, West Conshohocken, PA, <www.astm.org>.

Bach, F., Thorsen, T.S. & Nielsen, M. 1993, 'Load-carrying capacity of structural members subjected to alkali-silica reactions', *Construction and Building Materials*, vol. 7, no. 2, pp. 109-15.

Bal, L. & Buyle-Bodin, F. 2013, 'Artificial neural network for predicting drying shrinkage of concrete', *Construction and Building Materials*, vol. 38, pp. 248-54.

Belytschko, T. & Black, T. 1999, 'Elastic crack growth in finite elements with minimal remeshing', *International journal for numerical methods in engineering*, vol. 45, no. 5, pp. 601-20.

Belytschko, T., Liu, W.K., Moran, B. & Elkhodary, K. 2014, *Nonlinear Finite Elements for Continua and Structures*, John Wiley & Sons, Incorporated, New York.

Berra, M., Faggiani, G., Mangialardi, T. & Paolini, A.E. 2010, 'Influence of stress restraint on the expansive behaviour of concrete affected by alkali-silica reaction', *Cement and concrete research*, vol. 40, no. 9, pp. 1403-9.

Bérubé, M.-A., Duchesne, J., Dorion, J. & Rivest, M. 2002, 'Laboratory assessment of alkali contribution by aggregates to concrete and application to concrete structures affected by alkali–silica reactivity', *Cement and Concrete research*, vol. 32, no. 8, pp. 1215-27.

Burden, F. & Winkler, D. 2008, 'Bayesian regularization of neural networks', *Artificial neural networks*, Springer, pp. 23-42.

C1778, A. 2016, *Standard guide for reducing the risk of deleterious alkali–aggregate reaction in concrete*, ASTM International, United States.

Capra, B. & Bournazel, J.-P. 1998, 'Modeling of induced mechanical effects of alkali-aggregate reactions', *Cement and Concrete Research*, vol. 28, no. 2, pp. 251-60.

Carse, A. 1993, 'The identification of ASR in the concrete cooling tower infrastructure of the Tarong Power Station', *Construction & building materials*, vol. 7, no. 2, pp. 117-9.

Carse, A. 2003, 'The assessment of the residual expansion strain due to alkali-silica reaction in bridge structures', *Australian journal of civil engineering*, vol. 1, no. 1, pp. 45-50.

Chopperla, K., T. Drimalas, J. Tanesi, A. Ardani, M. Laskey, M. Thomas, K. Folliard, and J. Ideker 2019, 'Benchmarking the Miniature Concrete Prism Test and the Concrete Cylinder Tests to Field Exposure Blocks for Mitigation of Alkali-Silica Reaction', paper presented to the Proc., 15th International Congress on the Chemistry of Cement, Prague, Czech Republic.

Comby-Peyrot, I., Bernard, F., Bouchard, P.-O., Bay, F. & Garcia-Diaz, E. 2009, 'Development and validation of a 3D computational tool to describe concrete behaviour at mesoscale. Application to the alkali-silica reaction', *Computational materials science*, vol. 46, no. 4, pp. 1163-77.

Comi, C., Fedele, R. & Perego, U. 2009, 'A chemo-thermo-damage model for the analysis of concrete dams affected by alkali-silica reaction', *Mechanics of materials*, vol. 41, no. 3, pp. 210-30.

Comi, C., Kirchmayr, B. & Pignatelli, R. 2012, 'Two-phase damage modeling of concrete affected by alkali–silica reaction under variable temperature and humidity conditions', *International Journal of Solids and Structures*, vol. 49, no. 23, pp. 3367-80.

Comit, E.E.-I.D.B.E.C.A. 1990, *CEB-FIP model code 1990 : design code*, T. Telford, London.

Costa, U., Mangialardi, T. and Paolini, A.E. 2017, 'Minimizing alkali leaching in the concrete prism expansion test at 38° C', *Construction and Building Materials*, vol. 146, pp. 547-54.

Courtier, R. 1990, 'The assessment of ASR-affected structures', *Cement and Concrete composites*, vol. 12, no. 3, pp. 191-201.

De Normalisation, C.E. 2004, 'Eurocode 2: Design of concrete structures—Part 1-1: General rules and rules for buildings', *Brussels, Belgium*.

Dede, T. & Ayvaz, Y. 2009, 'Nonlinear analysis of reinforced concrete beam with/without tension stiffening effect', *Materials & Design*, vol. 30, no. 9, pp. 3846-51.

Deschenes, D.J., Bayrak, O. & Folliard, K.J. 2009, *ASR/DEF-damaged bent caps: shear tests and field implications*, Citeseer.

Deschenes Jr, R.A., Giannini, E.R., Drimalas, T., Fournier, B. & Hale, W.M. 2018, 'Effects of moisture, temperature, and freezing and thawing on alkali-silica reaction', *ACI Materials Journal*, vol. 115, no. 4, pp. 575-84.

Dimopoulos, Y., Bourret, P. & Lek, S. 1995, 'Use of some sensitivity criteria for choosing networks with good generalization ability', *Neural Processing Letters*, vol. 2, no. 6, pp. 1-4.

Doug Hooton, R., Rogers, C., MacDonald, C.A. & Ramlochan, T. 2013, 'Twenty-Year Field Evaluation of Alkali-Silica Reaction Mitigation', *ACI Materials Journal*, vol. 110, no. 5.

Drolet, C., Duchesne, J. & Fournier, B. 2017, 'Validation of the alkali contribution by aggregates to the concrete pore solution', *Cement and Concrete Research*, vol. 98, pp. 10-23.

Duan, Z.-H., Kou, S.-C. & Poon, C.-S. 2013, 'Using artificial neural networks for predicting the elastic modulus of recycled aggregate concrete', *Construction and Building Materials*, vol. 44, pp. 524-32.

Dunant, C.F. & Scrivener, K.L. 2010, 'Micro-mechanical modelling of alkali–silica-reaction-induced degradation using the AMIE framework', *Cement and concrete research*, vol. 40, no. 4, pp. 517-25.

Dunant, C.F. & Scrivener, K.L. 2012, 'Effects of uniaxial stress on alkali–silica reaction induced expansion of concrete', *Cement and concrete research*, vol. 42, no. 3, pp. 567-76.

Earij, A., Alfano, G., Cashell, K. & Zhou, X. 2017, 'Nonlinear three–dimensional finite–element modelling of reinforced–concrete beams: Computational challenges and experimental validation', *Engineering failure analysis*, vol. 82, pp. 92-115.

Erkmen, R.E., Gowripalan, N. & Sirivivatnanon, V. 2017, 'Elasto-plastic damage modelling of beams and columns with mechanical degradation', *Computers and Concrete*, vol. 19, no. 3, pp. 315-23.

Esposito, R., Anaç, C., Hendriks, M.A. & Çopuroğlu, O. 2016, 'Influence of the alkali-silica reaction on the mechanical degradation of concrete', *Journal of Materials in Civil Engineering*, vol. 28, no. 6, p. 04016007.

Esposito, R. & Hendriks, M.A.N. 2016, 'A multiscale micromechanical approach to model the deteriorating impact of alkali-silica reaction on concrete', *Cement & concrete composites*, vol. 70, no. C, pp. 139-52.

Fan, S. & Hanson, J.M. 1998, 'Effect of alkali silica reaction expansion and cracking on structural behavior of reinforced concrete beams', *ACI Structural Journal*, vol. 95, pp. 498-505.

Feng, D.-C., Ren, X.-D. & Li, J. 2018, 'Softened damage-plasticity model for analysis of cracked reinforced concrete structures', *Journal of Structural Engineering*, vol. 144, no. 6, p. 04018044.

Ferche, A.C., Panesar, D.K., Sheikh, S.A. & Vecchio, F.J. 2017, 'Toward Macro-Modeling of Alkali-Silica Reaction-Affected Structures', *ACI Structural Journal*, vol. 114, no. 5, p. 1121.

Folliard, K., Barborak, R., Drimalas, T., Du, L., Garber, S., Ideker, J., Ley, T., Williams, S., Juenger, M. & Fournier, B. 2006, 'Preventing ASR/DEF in new concrete: Final report', *Center for Transportation Research, University of Texas at Austin. Federal Highway Administration Report FHWA/TX-06/0-4085-5*.

Foresee, F.D. & Hagan, M.T. 1997, 'Gauss-Newton approximation to Bayesian learning', *Proceedings of the 1997 international joint conference on neural networks*, vol. 3, Piscataway: IEEE, pp. 1930-5.

Fournier, B. & Bérubé, M.-A. 2000, 'Alkali-aggregate reaction in concrete: a review of basic concepts and engineering implications', *Canadian Journal of Civil Engineering*, vol. 27, no. 2, pp. 167-91.

Fournier, B., Berube, M.-A., Folliard, K.J. & Thomas, M. 2010, *Report on the diagnosis, prognosis, and mitigation of Alkali-Silica Reaction (ASR) in transportation structures*.

Fournier, B., Bilodeau, A., Bouzoubaa, N. & Nkinamubanzi, P.-C. 2019, 'Field and Laboratory Investigations on the Use of Fly Ash and Li-Based Admixtures to Prevent ASR in Concrete', paper presented to the International Conference on Durability of Concrete Structures.

Fournier, B., Ideker, J.H., Folliard, K.J., Thomas, M.D., Nkinamubanzi, P.-C. & Chevrier, R. 2009, 'Effect of environmental conditions on expansion in concrete due to alkali–silica reaction (ASR)', *Materials characterization*, vol. 60, no. 7, pp. 669-79.

Fournier, B., Lindgård, J., Wigum, B.J. & Borchers, I. 2018, 'Outdoor exposure site testing for preventing Alkali-Aggregate Reactivity in concrete–a review'.

Fournier, B. & Malhotra, V. 1996, 'Inter-laboratory study on the CSA A23. 2-14A concrete prism test for alkali-silica reactivity in concrete', *Proceedings of the 10th International Conference on Alkali-Aggregate Reaction in Concrete, Melbourne, Australia*, pp. 302-9.

Fournier, B. & Rogers, C. 2008, 'Multi-laboratory study of accelerated mortar bar test and concrete prism expansion tests at 38 C and 60 C', *Proc., Ibid*, vol. 16, no. 10.

Gandomi, A.H., Alavi, A.H., Shadmehri, D.M. & Sahab, M. 2013, 'An empirical model for shear capacity of RC deep beams using genetic-simulated annealing', *Archives of Civil and Mechanical Engineering*, vol. 13, no. 3, pp. 354-69.

Gao, X.X., Multon, S., Cyr, M. & Sellier, A. 2011, 'Optimising an expansion test for the assessment of alkali-silica reaction in concrete structures', *Materials and structures*, vol. 44, no. 9, pp. 1641-53.

Gautam, B.P. & Panesar, D.K. 2017, 'The effect of elevated conditioning temperature on the ASR expansion, cracking and properties of reactive Spratt aggregate concrete', *Construction and Building Materials*, vol. 140, pp. 310-20.

Gautam, B.P., Panesar, D.K., Sheikh, S.A. & Vecchio, F.J. 2017a, 'Effect of coarse aggregate grading on the ASR expansion and damage of concrete', *Cement and Concrete Research*, vol. 95, pp. 75-83.

Gautam, B.P., Panesar, D.K., Sheikh, S.A. & Vecchio, F.J. 2017b, 'Multiaxial Expansion-Stress Relationship for Alkali Silica Reaction-Affected Concrete', *ACI Materials Journal*, vol. 114, no. 1.

Gevrey, M., Dimopoulos, I. & Lek, S. 2003, 'Review and comparison of methods to study the contribution of variables in artificial neural network models', *Ecological modelling*, vol. 160, no. 3, pp. 249-64.

Giaccio, G., Zerbino, R., Ponce, J. & Batic, O.R. 2008, 'Mechanical behavior of concretes damaged by alkali-silica reaction', *Cement and Concrete Research*, vol. 38, no. 7, pp. 993-1004.

Giannini, E.R. 2012, 'Evaluation of concrete structures affected by alkali-silica reaction and delayed ettringite formation', University of Texas at Austin.

Gorga, R., Sanchez, L. & Martín-Pérez, B. 2018, 'FE approach to perform the condition assessment of a concrete overpass damaged by ASR after 50 years in service', *Engineering Structures*, vol. 177, pp. 133-46.

Gorga, R., Sanchez, L., Martín-Pérez, B., Fecteau, P., Cavalcanti, A. & Silva, P. 2020, 'Finite Element Assessment of the ASR-Affected Paulo Afonso IV Dam', *Journal of Performance of Constructed Facilities*, vol. 34, no. 4, p. 04020065.

Goshayeshi, N. 2019, 'Contribution to the development of analytical models to forecast alkali-aggregate reaction (AAR) kinetics and induced expansion', University of Ottawa.

Graff, D. 2017, 'Environmental and Reinforcement Effects on Concrete Expansion Undergoing Accelerated Alkali-Silica Reaction', in V. Saouma, M.-A. Hariri-Ardebili, M. Hubler, S. Multon & Y. Xi (eds)ProQuest Dissertations Publishing.

Grimal, E., Sellier, A., Multon, S., Le Pape, Y. & Bourdarot, E. 2010, 'Concrete modelling for expertise of structures affected by alkali aggregate reaction', *Cement and Concrete Research*, vol. 40, no. 4, pp. 502-7.

Hansen, S.G., Barbosa, R.A., Hoang, L.C. & Hansen, K.K. 2016, 'Shear capacity of ASR damaged structures–In-depth analysis of some in-situ shear tests on bridge slabs', *Proceedings of 15th International Confrence on Alkali-Aggregate Reaction*.

Hariri-Ardebili, M.A. & Saouma, V.E. 2018, 'Sensitivity and uncertainty analysis of AAR affected reinforced concrete shear walls', *Engineering Structures*, vol. 172, pp. 334-45.

Hariri-Ardebili, M.A., Saouma, V.E. & Merz, C. 2018, 'Risk-Informed Condition Assessment of a Bridge with Alkali-Aggregate Reaction', *ACI Structural Journal*, vol. 115, no. 2.

Hawileh, R. 2015, 'Finite element modeling of reinforced concrete beams with a hybrid combination of steel and aramid reinforcement', *Materials & Design (1980-2015)*, vol. 65, pp. 831-9.

Hayes, N.W. 2020, 'Effect of Alkali-Silica Reaction on Confined Reinforced Concrete', The University of Tennessee, Knoxville.

HB79, S. 2015, *Alkali aggregate reaction : guidelines on minimising the risk of damage to concrete structures in Australia*, Cement and Concrete Association of Australia, and Standards Australia, North Sydney, N.S.W.

Heaton, J. 2008, *Introduction to neural networks with Java*, Heaton Research, Inc.

Hiroi, Y., Yamamoto, T., Toda, Y., Manabe, H. & Miyagawa, T. 2016, 'Experimental and analytical studies on flexural behaviour of post-tensioned concrete beam specimen deteriorated by alkali-silica reaction (ASR)', *15th International Conference on Alkali-Aggregate Reaction, Sao Paulo Brazil*, pp. 03-7.

Hodhod, O.A., Said, T.E. & Ataya, A.M. 2018, 'Prediction of creep in concrete using genetic programming hybridized with ANN', *Computers and Concrete*, vol. 21, no. 5, pp. 513-23.

Hognestad, E. 1951, *Study of combined bending and axial load in reinforced concrete members*, University of Illinois at Urbana Champaign, College of Engineering ….

Holmes, M.H. 2013, *Introduction to Perturbation Methods*, vol. 20, Springer, New York.

Huang, Q., Gardoni, P., Trejo, D. & Pagnotta, A. 2014, 'Probabilistic model for steel–concrete bond behavior in bridge columns affected by alkali silica reactions', *Engineering Structures*, vol. 71, pp. 1-11.

Ideker, J.H., Bentivegna, A.F., Folliard, K.J. & Juenger, M.C. 2012, 'Do current laboratory test methods accurately predict alkali-silica reactivity?', *ACI Materials Journal*, vol. 109, no. 4, p. 395.

ISE 1992, 'Structural effects of alkali-aggregate reaction: technical guidance on the appraisal of existing structures'.

Iskhakov, T., Timothy, J.J. & Meschke, G. 2019, 'Expansion and deterioration of concrete due to ASR: Micromechanical modeling and analysis', *Cement and concrete research*, vol. 115, pp. 507-18.

Islam, M.S. & Ghafoori, N. 2018, 'A new approach to evaluate alkali-silica reactivity using loss in concrete stiffness', *Construction and Building Materials*, vol. 167, pp. 578-86.

Jawed, I. & Skalny, J. 1978, 'Alkalies in cement: a review: II. Effects of alkalies on hydration and performance of Portland cement', *Cement and concrete research*, vol. 8, no. 1, pp. 37-51.

Jones, A. & Clark, L. 1998, 'The effects of ASR on the properties of concrete and the implications for assessment', *Engineering structures*, vol. 20, no. 9, pp. 785-91.

Jones, A.E.K. & Clark, L.A. 1996, 'The effects of restraint on ASR expansion of reinforced concrete', *Magazine of concrete research*, vol. 48, no. 174, pp. 1-13.

Kagimoto, H. & Kawamura, M. 2011, 'Measurements of strain and humidity within massive concrete cylinders related to the formation of ASR surface cracks', *Cement and Concrete Research*, vol. 41, no. 8, pp. 808-16.

Kagimoto, H., Yasuda, Y. & Kawamura, M. 2014, 'ASR expansion, expansive pressure and cracking in concrete prisms under various degrees of restraint', *Cement and Concrete Research*, vol. 59, pp. 1-15.

Kanit, T., Forest, S., Galliet, I., Mounoury, V. & Jeulin, D. 2003, 'Determination of the size of the representative volume element for random composites: statistical and numerical approach', *International journal of solids and structures*, vol. 40, no. 13, pp. 3647-79.

Kawabata, Y., Seignol, J.-F., Martin, R.-P. & Toutlemonde, F. 2017, 'Macroscopic chemo-mechanical modeling of alkali-silica reaction of concrete under stresses', *Construction and Building Materials*, vol. 137, pp. 234-45.

Kawabata, Y., Yamada, K., Ogawa, S., Martin, R.P., Sagawa, Y., Seignol, J.F. & Toutlemonde, F. 2016, 'Correlation between laboratory expansion and field expansion of concrete: Prediction based on modified concrete expansion test', *ICAAR 2016-15th international conference on alkali aggregate reaction*.

Kim, J.-K., Han, S.H. & Song, Y.C. 2002, 'Effect of temperature and aging on the mechanical properties of concrete: Part I. Experimental results', *Cement and Concrete research*, vol. 32, no. 7, pp. 1087-94.

Kim, S.-M. & Abu Al-Rub, R.K. 2011, 'Meso-scale computational modeling of the plastic-damage response of cementitious composites', *Cement and concrete research*, vol. 41, no. 3, pp. 339-58.

Kong, L., Chen, X. & Du, Y. 2016, 'Evaluation of the effect of aggregate on concrete permeability using grey correlation analysis and ANN', *Computers and Concrete*, vol. 17, no. 5, pp. 613-28.

Kubo, Y. & Nakata, M. 2012, 'Effect of Reactive Aggregate on Mechanical Properties of Concrete Affected by Alkali–Silica Reaction', *14th International Conference on Alkali–Aggregate Reaction*.

Larive, C. 1997, 'Apports combinés de l'expérimentation et de la modélisation à la compréhension de l'alcali-réaction et de ses effets mécaniques', École Nationale des Ponts et Chaussèes, Paris.

Larsson, F., Runesson, K., Saroukhani, S. & Vafadari, R. 2011, 'Computational homogenization based on a weak format of micro-periodicity for RVE-problems', *Computer methods in applied mechanics and engineering*, vol. 200, no. 1-4, pp. 11-26.

Lee, J. & Fenves, G.L. 1998, 'A plastic-damage concrete model for earthquake analysis of dams', *Earthquake Engineering & Structural Dynamics*, vol. 27, no. 9, pp. 937-56.

Liaudat, J., Carol, I., López, C.M. & Saouma, V.E. 2018, 'ASR expansions in concrete under triaxial confinement', *Cement & concrete composites*, vol. 86, pp. 160-70.

Lindgård, J., Andiç-Çakır, Ö., Fernandes, I., Rønning, T.F. & Thomas, M.D. 2012, 'Alkali–silica reactions (ASR): literature review on parameters influencing laboratory performance testing', *Cement and Concrete Research*, vol. 42, no. 2, pp. 223-43.

Lindgård, J., Sellevold, E.J., Thomas, M.D., Pedersen, B., Justnes, H. & Rønning, T.F. 2013, 'Alkali–silica reaction (ASR)—performance testing: Influence of specimen pre-treatment, exposure conditions and prism size on concrete porosity, moisture state and transport properties', *Cement and Concrete Research*, vol. 53, pp. 145-67.

Lindgård, J., Thomas, M.D., Sellevold, E.J., Pedersen, B., Andiç-Çakır, Ö., Justnes, H. & Rønning, T.F. 2013, 'Alkali–silica reaction (ASR)—performance testing: influence of specimen pre-treatment, exposure conditions and prism size on alkali leaching and prism expansion', *Cement and Concrete Research*, vol. 53, pp. 68-90.

Liu, S.-H., Bracci, J.M., Mander, J.B. & Hurlebaus, S. 2017, 'Performance of D-Regions Affected by Alkali-Silica Reaction: Experimental and Analytical Study', *Journal of Structural Engineering*, vol. 143, no. 9, p. 04017109.

M.-A. Bérubé, M.P., N. Dupont, J. Frenette, M. Langlois 1992, *Expansion test methods for mass concrete exposed to alkali-aggregate reaction*, Canadian Electrical Association, Montreal.

MacKay, D.J. 1992, 'Bayesian interpolation', *Neural computation*, vol. 4, no. 3, pp. 415-47.

Martin, R.-P., Sanchez, L., Fournier, B. & Toutlemonde, F. 2017, 'Evaluation of different techniques for the diagnosis & prognosis of Internal Swelling Reaction (ISR) mechanisms in concrete', *Construction and Building Materials*, vol. 156, pp. 956-64.

Melenk, J.M. & Babuška, I. 1996, 'The partition of unity finite element method: Basic theory and applications', *Computer methods in applied mechanics and engineering*, vol. 139, no. 1, pp. 289-314.

Miehe, C. & Koch, A. 2002, 'Computational micro-to-macro transitions of discretized microstructures undergoing small strains', *Archive of applied mechanics (1991)*, vol. 72, no. 4, pp. 300-17.

Mirkhalaf, S.M., Andrade Pires, F.M. & Simoes, R. 2016, 'Determination of the size of the Representative Volume Element (RVE) for the simulation of heterogeneous polymers at finite strains', *Finite elements in analysis and design*, vol. 119, no. C, pp. 30-44.

Mohammed, T.U., Hamada, H. & Yamaji, T. 2003, 'Relation between Strain on Surface and Strain over Embedded Steel Bars in ASR Affected Concrete Members', *Journal of Advanced Concrete Technology*, vol. 1, no. 1, pp. 76-88.

Monette, L., Gardner, N. & Grattan-Bellew, P. 2002, 'Residual strength of reinforced concrete beams damaged by alkali-silica reaction—Examination of damage rating index method', *Materials Journal*, vol. 99, no. 1, pp. 42-50.

Morenon, P., Multon, S., Sellier, A., Grimal, E., Hamon, F. & Bourdarot, E. 2017, 'Impact of stresses and restraints on ASR expansion', *Construction & building materials*, vol. 140, pp. 58-74.

MTO 2018, *Kingston Outdoor Exposure Site for ASR – 27 Year Update*, Soils and Aggregates Section, Materials Engineering and Research Office, Ontario Ministry of Transportation.

Multon, S. 2003, 'Evaluation expérimentale et théorique des effets mécaniques de l'alcali-réaction sur des structures modèles', Universitè de Marne-la-Vallèe (in collaboration with LCPCEDF), Champs sur Marne.

Multon, S. & Sellier, A. 2016, 'Multi-scale analysis of alkali–silica reaction (ASR): impact of alkali leaching on scale effects affecting expansion tests', *Cement and Concrete Research*, vol. 81, pp. 122-33.

Multon, S., Sellier, A. & Cyr, M. 2009, 'Chemo–mechanical modeling for prediction of alkali silica reaction (ASR) expansion', *Cement and concrete research*, vol. 39, no. 6, pp. 490-500.

Multon, S. & Toutlemonde, F. 2006, 'Effect of applied stresses on alkali–silica reaction-induced expansions', *Cement and Concrete Research*, vol. 36, no. 5, pp. 912-20.

Nayıra, S., Erdoğdu, Ş. & Kurbetcib, Ş. 2017, 'Effectiveness of mineral additives in mitigating alkali-silica reaction in mortar'.

Ng, K. & Clark, L. 1992, 'Punching tests on slabs with alkali-silica reaction', *Structural Engineer*, vol. 70, pp. 245-52.

Nielsen, A., Gottfredsen, F. & Thøgersen, F. 1993, 'Development of stresses in concrete structures with alkali-silica reactions', *Materials and Structures*, vol. 26, no. 3, pp. 152-8.

Olden, J.D. & Jackson, D.A. 2002, 'Illuminating the "black box": a randomization approach for understanding variable contributions in artificial neural networks', *Ecological modelling*, vol. 154, no. 1-2, pp. 135-50.

Olden, J.D., Joy, M.K. & Death, R.G. 2004, 'An accurate comparison of methods for quantifying variable importance in artificial neural networks using simulated data', *Ecological Modelling*, vol. 178, no. 3-4, pp. 389-97.

Ongpeng, J., Soberano, M., Oreta, A. & Hirose, S. 2017, 'Artificial neural network model using ultrasonic test results to predict compressive stress in concrete', *Comput. Concr*, vol. 19, pp. 59-68.

Özesmi, S.L. & Özesmi, U. 1999, 'An artificial neural network approach to spatial habitat modelling with interspecific interaction', *Ecological Modelling*, vol. 116, no. 1, pp. 15-31.

Pleau, R., Bérubé, M., Pigeon, M., Fournier, B. & Raphaël, S. 1989, 'Mechanical behaviour of concrete affected by ASR', *8th International Conference on Alkali-Aggregate Reaction*, pp. 721-6.

Pourbehi, M.S., van Zijl, G.P.A.G. & Strasheim, J.A.v. 2019, 'Analysis of combined action of seismic loads and alkali-silica reaction in concrete dams considering the key chemical-physical-mechanical factors and fluid-structure interaction.(Report)', *Engineering Structures*, vol. 195, p. 263.

Poyet, S., Alain Sellier, Bruno Capra, Geneviève Thèvenin-Foray, Jean-Michel Torrenti, Hélène Tournier-Cognon, and Eric Bourdarot 2006, 'Influence of water on alkali-silica reaction: Experimental study and numerical simulations', vol. 18, no. 4, pp. 588-96.

Poyet, S., Sellier, A., Capra, B., Foray, G., Torrenti, J.-M., Cognon, H. & Bourdarot, E. 2007, 'Chemical modelling of alkali silica reaction: influence of the reactive aggregate size distribution', *Materials and structures*, vol. 40, no. 2, p. 229.

Puatatsananon, W. & Saouma, V. 2013, 'Chemo-Mechanical Micromodel for Alkali-Silica Reaction', *ACI Materials Journal*, vol. 110, no. 1, pp. 67-77.

Reinhardt, H. & Mielich, O. 2011, 'A fracture mechanics approach to the crack formation in alkali-sensitive grains', *Cement and Concrete Research*, vol. 41, no. 3, pp. 255-62.

Rezakhani, R., Alnaggar, M. & Cusatis, G. 2019, 'Multiscale Homogenization Analysis of Alkali–Silica Reaction (ASR) Effect in Concrete', *Engineering (Beijing, China)*, vol. 5, no. 6, pp. 1139-54.

Rezakhani, R., Zhou, X. & Cusatis, G. 2017, 'Adaptive multiscale homogenization of the lattice discrete particle model for the analysis of damage and fracture in concrete', *International journal of solids and structures*, vol. 125, pp. 50-67.

Roth, S.-N. 2020, 'Benchmark Study Results: Hydro-Québec', *Diagnosis & Prognosis of AAR Affected Structures*, Springer Nature, pp. 439-59.

Sanchez, L. 2014, 'Contribution to the assessment of damage in aging concrete infrastructures affected by alkali-aggregate reaction', Université Laval.

Sanchez, L., Fournier, B., Jolin, M., Bedoya, M., Bastien, J. & Duchesne, J. 2016, 'Use of Damage Rating Index to Quantify Alkali-Silica Reaction Damage in Concrete: Fine versus Coarse Aggregate', *ACI Materials Journal*, vol. 113, no. 4.

Sanchez, L., Fournier, B., Jolin, M. & Duchesne, J. 2015, 'Reliable quantification of AAR damage through assessment of the Damage Rating Index (DRI)', *Cement and Concrete Research*, vol. 67, pp. 74-92.

Sanchez LF, F.B., Mitchell D, Bastien J 2020, 'Condition assessment of an ASR-affected overpass after nearly 50 years in service', *Construction and Building Materials*, vol. 236, p. 117554.

Sanchez, L.F.M., Fournier, B., Jolin, M., Mitchell, D. & Bastien, J. 2017, 'Overall assessment of Alkali-Aggregate Reaction (AAR) in concretes presenting different strengths and incorporating a wide range of reactive aggregate types and natures', *Cement and Concrete Research*, vol. 93, pp. 17-31.

Saouma, V. & Perotti, L. 2006a, 'Constitutive model for alkali-aggregate reactions', *Materials Journal*, vol. 103, no. 3, pp. 194-202.

Saouma, V. & Perotti, L. 2006b, 'Constitutive model for alkali-aggregate reactions', *ACI materials journal*, vol. 103, no. 3, p. 194.

Saouma, V.E. 2014, *Numerical modeling of AAR*, CRC Press, Boca Raton.

Saouma, V.E. 2020, *Diagnosis & Prognosis of AAR Affected Structures : State-of-the-Art Report of the RILEM Technical Committee 259-ISR*, Springer, Cham.

Sargolzahi, M., Kodjo, S.A., Rivard, P. & Rhazi, J. 2010, 'Effectiveness of nondestructive testing for the evaluation of alkali–silica reaction in concrete', *Construction and Building Materials*, vol. 24, no. 8, pp. 1398-403.

Seignol, J.F., Baghdadi, N. & Toutlemonde, F. 2009, 'A macroscopic chemo-mechanical model aimed at re-assessment of delayed ettringite formation affected concrete structures', *The*

first International Conference on Computational Technologies in Concrete Structures (CTCS'09), pp. 422-40.

Sellier, A., Bourdarot, E., Multon, S., Cyr, M. & Grimal, E. 2009, 'Combination of structural monitoring and laboratory tests for assessment of alkali-aggregate reaction swelling: application to gate structure dam', *ACI materials journal*, vol. 106, no. 3, pp. 281-90.

Shayan, A. & Ivanusec, I. 1989, 'Influence of NaOH on mechanical properties of cement paste and mortar with and without reactive aggregate', paper presented to the 8th International Conference on Alkali-Aggregate Reaction, Kyoto, Japan.

Sims, I. & Poole, A.B. 2017, *Alkali-Aggregate Reaction in Concrete: A World Review*, CRC Press

Sinno, N. & Shehata, M.H. 2019, 'Effect of sample geometry and aggregate type on expansion due to alkali-silica reaction', *Construction and Building Materials*, vol. 209, pp. 738-47.

Sirivivatnanon, V., Mohammadi, J. & South, W. 2016, 'Reliability of new Australian test methods in predicting alkali silica reaction of field concrete', *Construction and Building Materials*, vol. 126, pp. 868-74.

Smaoui, N., Bérubé, M.-A., Fournier, B. & Bissonnette, B. 2004, 'Influence of specimen geometry, orientation of casting plane, and mode of concrete consolidation on expansion due to ASR', *Cement, concrete and aggregates*, vol. 26, no. 2, pp. 1-13.

Smaoui, N., Bérubé, M., Fournier, B., Bissonnette, B. & Durand, B. 2005, 'Effects of alkali addition on the mechanical properties and durability of concrete', *Cement and concrete research*, vol. 35, no. 2, pp. 203-12.

Smaoui, N., Bissonnette, B., Bérubé, M.-A., Fournier, B. & Durand, B. 2005, 'Mechanical properties of ASR-affected concrete containing fine or coarse reactive aggregates', *Journal of ASTM International*, vol. 3, no. 3, pp. 1-16.

Sonebi, M., Grunewald, S., Cevik, A. & Walraven, J. 2016, 'Modelling fresh properties of self-compacting concrete using neural network technique', *Computers and Concrete*, vol. 18, no. 4, pp. 903-20.

Stanton, T.E. 1940, 'Expansion of Concrete through Reaction between Cement and Aggregate', paper presented to the Proceedings, American Society of Civil Engineers.

Stark, D. 1991, 'The moisture condition of field concrete exhibiting alkali-silica reactivity', *Special Publication*, vol. 126, pp. 973-88.

Steffens, A., Kefei Li, and Olivier Coussy 2003, 'Aging approach to water effect on alkali–silica reaction degradation of structures', *Journal of engineering mechanics*, vol. 129(1), pp. 50-9.

Sukumar, N., Chopp, D.L., Moës, N. & Belytschko, T. 2001, 'Modeling holes and inclusions by level sets in the extended finite-element method', *Computer methods in applied mechanics and engineering*, vol. 190, no. 46, pp. 6183-200.

Swamy, R.N. & AlL-Asali, M. 1989, 'Effect of alkali-silica reaction on the structural behavior of reinforced concrete beams', *Structural Journal*, vol. 86, no. 4, pp. 451-9.

Systèmes, D. 2014, 'ABAQUS 6.14 analysis user's manual', Dassault Systems Inc Waltham, USA.

Thomas, M., Fournier, B., Folliard, K., Ideker, J. & Shehata, M. 2006, 'Test methods for evaluating preventive measures for controlling expansion due to alkali–silica reaction in concrete', *Cement and Concrete Research*, vol. 36, no. 10, pp. 1842-56.

Thomas, M.D., Fournier, B. & Folliard, K.J. 2008, *Report on determining the reactivity of concrete aggregates and selecting appropriate measures for preventing deleterious expansion in new concrete construction*, United States. Federal Highway Administration.

Ulm, F.-J., Coussy, O., Kefei, L. & Larive, C. 2000, 'Thermo-chemo-mechanics of ASR expansion in concrete structures', *Journal of engineering mechanics*, vol. 126, no. 3, pp. 233-42.

Wang, T. & Hsu, T.T.C. 2001, 'Nonlinear finite element analysis of concrete structures using new constitutive models', *Computers & structures*, vol. 79, no. 32, pp. 2781-91.

Winnicki, A. & Pietruszczak, S. 2008, 'On mechanical degradation of reinforced concrete affected by alkali-silica reaction', *Journal of engineering mechanics*, vol. 134, no. 8, pp. 611-27.

Wriggers, P. & Moftah, S.O. 2006, 'Mesoscale models for concrete: Homogenisation and damage behaviour', *Finite elements in analysis and design*, vol. 42, no. 7, pp. 623-36.

Yu, Y., Li, W., Li, J. & Nguyen, T.N. 2018, 'A novel optimised self-learning method for compressive strength prediction of high performance concrete', *Construction and Building Materials*, vol. 184, pp. 229-47.